Transurethral shear wave elastography for prostate cancer

Antonio Jesús Gómez Fernández

A dissertation submitted in partial fulfillment

of the requirements for the degree of

Doctor of Philosophy

of

University College London.

Department of Mechanical Engineering

University College London

June 13, 2018

I, Antonio Jesús Gómez Fernández, confirm that the work presented in this thesis is my own. Where information has been derived from other sources, I confirm that this has been indicated in the thesis.

Abstract

Prostate cancer remains a major healthcare issue. Limitations in current diagnosis and treatment monitoring techniques imply that there is still a need for improvements. The efficacy of prostate cancer diagnosis is still low. High intensity focused ultrasound ablation is an emerging treatment modality, which enables the noninvasive ablation of pathogenic tissue. Successful focal ablation treatment of prostate cancer is critically dependent on accurate diagnostic means and would be greatly benefited by a monitoring system. While magnetic resonance imaging remains the gold standard for prostate imaging, its wider implementation remains prohibitively expensive. Conventional ultrasound is currently limited to guiding biopsy. Elastography techniques are emerging as a promising imaging method, as cancer nodules are usually stiffer than adjacent healthy tissue, and even stiffer in the case of thermally ablated tissue. In this thesis, a novel transurethral elastography approach is proposed for the diagnosis of prostate cancer and its focal ablation monitoring, based on the transmission and detection of shear waves through the urethral wall. A viscoelastic wave propagation model is developed, using a finite difference time domain technique and based on a Kelvin-Voigt fractional derivative constitutive law. Validation of the model is achieved by high-speed camera tests carried out on translucent tissue-mimicking media. A Reverse Time Migration and a Genetic Algorithm techniques are proposed for reconstructing the parameters of the stiff lesion. A comparative study of the two techniques is presented. The Reverse Time Migration method finds the stiff lesion area in short computational time. The Genetic Algorithm provides full reconstruction of the location, size and stiffness

of the lesion, however the computation time is much longer. A combination of both techniques achieves improved results by combining the speed of the Reverse Time Migration and the full reconstruction capacity of the Genetic Algorithm. Preliminary results support the feasibility of the method and encourage further investigation.

Research Impact Statement

The diagnosis of prostate cancer is a real hot topic in the cancer research field. Various medical imaging modalities have been proposed and others are under research, but further developments must be pursued if the scientific community aims to provide men with a more widely accessible and efficient method for diagnosis and treatment monitoring.

This thesis summarises the work done over the past three years to study and develop a novel Transurethral Shear Wave Elastography (TU-SWE) technique for the diagnosis of prostate cancer and the monitoring of thermal focal ablation of such tumours. The new elastography approach uses shear waves, which are propagated into the prostate by applying oscillatory rotational forces on the urethral wall. The presence of stiff lesions perturbs the propagation, generating reflections that travel back to the urethral wall where they can be sensed. Viscoelastic properties and features of the lesion can be extracted by solving the inverse problem.

Although the development of a functional TU-SWE medical imaging device falls beyond the scope of this thesis, it must be mentioned that preliminary plans for developing new sensing elements of mechanical waves have already been taken into account as a part a short-term research strategy. The TU-SWE technique can be considered a minimally invasive method. It can be designed with a disposable probe, which would spare complex sterilization processes and favour its easy implementation, key factors for less developed regions. The TU-SWE technique could be accessible to healthcare providers as either additional modular units to existing ultrasound imaging platforms, or as a new fully integrated medical device

system comprising the probe, hardware platform and software.

In the long-term, the development of a functional TU-SWE medical imaging device would be an extraordinary innovative advance in the use of elastography for the detection and diagnosis of prostate cancer, permitting the use of various enhanced imaging possibilities never used before. For the first time, this device would allow an experimental study of the use of elastography for monitoring and assessing localised therapies in the prostate, a key factor for unlocking their potential benefits. Finally, the development of new sensing components for detecting mechanical waves would open new possibilities for the whole medical imaging community.

Developing a reliable alternative to the expensive Magnetic Resonance Imaging (MRI) for diagnosis of prostate cancer would undoubtedly have a huge impact in the developing world. In developed countries such as the UK, the impact of TU-SWE could be felt not just in changing the diagnosis and risk stratification pathway, but could also hugely impact the efficacy of a range of focal therapies entering the clinic by providing a powerful treatment monitoring tool.

Acknowledgements

There is beauty in the way nature connect us to transcend beyond the individual achievements, because there is no human achievement without collaboration, support and fellowship.

I consider myself a very fortunate person, a person who has been surrounded by excellent people. For this reason, I would like to dedicate this thesis work to all the people that have guided me on reaching this point in my life, those who left and those who stay.

First, I would like to express my gratitude to my academic supervisors. I will be eternally grateful to my supervisor Nader Saffari, for believing in me and guiding me through this challenge. For teaching me the rigour, thoroughness and excellency that every scientific work must possess, for his invaluable assistance and friendship. I will be also eternally grateful to Guillermo Rus, my secondary supervisor, for introducing me into the fascinating world of science, for giving me the opportunity of pursuing a scientific career and for being an example of creativity and enthusiasm. I am also very grateful to Pierre Gelat for the rigorous proofreading of this thesis work. Thanks for your advices and your thorough discussions, they have been incredible valuable.

Second, I would like to thank my beloved family. Mum, you have given me everything even when there was little to offer. I am who I am because of you. Lourdes and Javi, my sister and brother, together we overcame the difficult times and together we will be forever. Aunt Ani, thanks for always being with us. Thanks also to my family-in-law: Encarni, Manolo and Laura, you have widened my world

and illustrated me with so many important things in life. And finally most of all I want to thank Lydia, my loved wife, you have supported and accompanied me in this challenge, moving far from the comfort of home and dealing with a totally new experience in a different culture. You represent all the best in my life, you complete me making me a better person, and now, providing me with an own family. Ainhoa, my sweet lovely daughter, I promise I will support and guide you on all your projects in life as everybody has done with me.

Third, I would like to thanks to my work colleagues from London and Granada. Thanks Reza, Ki Joo and Santiago for making me feel a part of the group since the first day and for so many useful work discussions. Thanks to Antonio C. and Miguel for their assistance with the high-speed camera tests. Thanks to Laura, Juanma, Juan and Manuel, for welcoming and guiding me on my very first steps in research. Thanks also to Sofía, Sogol, Celine, Paul, Hasnaa, Mat, Remy and Eva, for so many good moments in and out the office. Finally, I would like to thanks also all the support of my close relatives and friends from Granada: Patri, Javi, Iker, Yeray, Pepe, Loli, Antonio O., Bea, Irene, Antonio J., Sonia, Antonio, Pablo and Migue. Everything was easier after enjoying your company in London and Granada.

List of Acronyms

SWE	Shear Wave Elastography
TU-SWE	Transurethral Shear Wave Elastography
HIFU	High Intensity Focused Ultrasound
PZ	Peripheral Zone
CZ	Central Zone
TZ	Transitional Zone
PSA	Prostatic-Specific Antigen
TRUS	Transrectal Ultrasound
MRI	Magnetic Resonance Imaging
BPH	Benign Prostatic Hyperplasia
mpMRI	Multi-parametric MRI
FDTD	Finite Difference Time Domain
KVFD	Kelvin-Voigt Fractional Derivative
RTM	Reverse Time Migration
GA	Genetic Algorithm

SE	Strain Elastography
DE	Dynamic Elastography
ARF	Acoustic Radiation Force
ARFI	Acoustic Radiation Force Impulse
pSWE	Point Shear Wave Elastography
TR-SWE	Transrectal Shear Wave Elastography
SDUV	Shear wave Dispersion Ultrasound Vibrometry
CWS	Crawling Wave Spectroscopy
SNR	Signal-to-Noise Ratio
ROI	Region of Interest
FDA	Food and Drug Administration
DWI	Diffusion-Weighted MRI
CE-MRI	Contrast-Enhanced MRI
TCM	Tissue Change Monitoring
RF	Radio Frequency
KV	Kelvin-Voigt
KVFD	Kelvin-Voigt Fractional Derivative
DMA	Dynamic Mechanical Analysis
PDE	Partial Differential Equation
PML	Perfectly Matched Layer
RAM	Random Access Memory

FD	Finite Difference
FEM	Finite Element Method
GL	Grünwald-Letnikov
PLA	Polylactic Acid
FFT	Fast Fourier Transform
RMSE	Root-mean-square error
RMS	Root-mean-square
HFVS	Hyper-Frequency Viscoelastic Spectroscopy

List of Symbols

E	Young's modulus
ν	Poisson's ratio
G	Shear modulus
ρ	Mass density
c_s	Shear wave velocity
σ	Stress
ε	Strain
μ	KVFD elastic parameter associated to the complex shear modulus
η	KVFD viscous parameter associated to the complex shear modulus
α	Order of the fractional derivative associated to the KVFD shear modulus
G^*	Complex shear modulus
ω	Angular frequency
E^*	Complex Young's modulus
E_0	KVFD elastic parameter associated to the complex Young's modulus
η_E	KVFD viscous parameter associated to the complex Young's modulus

α_E	Order of the fractional derivative associated to the KVFD Young's modulus
$\mathbf{u}$	Vector of displacements
λ	First Lamé's parameter
$\mathbf{f}$	Vector of external body forces
u_i	Displacement field in the i direction
σ_{ij}	Stress field in the ij plane
t	Time
x_j	Spatial j variable
f_i	External body force in the i direction
ε_{ij}	Strain field in the ij plane
δ_{ij}	Kronecker delta
α_k	Absorption law
α_0	Constant absorption coefficient
y	Power law exponent of the absorption law
k^*	Complex wave number
$\varnothing$	Diameter
θ	Spatial angular variable
r	Spatial radial variable
z	Spatial depth variable
η_P	Bulk KVFD viscous parameter
η_S	Shear KVFD viscous parameter

Δr	Spatial step according the r coordinate
Δz	Spatial step according the z coordinate
Δt	Time step
n	Integer counter for time discretisation
g	Arbitrary differentiable function
Δx	Arbitrary spatial step
N	Maximum value of n
L	Effective memory length
r_d	Radial dimension of the model spatial domain
z_d	Depth dimension of the model spatial domain
r_u	Radius of the urethra
G'	Storage shear modulus
G''	Loss shear modulus
λ_s	Wavelength of shear wave
n_e	Number of emitters
l_e	Length of each emitter
f_e	Centre frequency of the excitation
a_e	Maximum amplitude of the excitation
n_r	Number of receivers
Δz_r	Distance between receivers
l_r	Length of each receiver

t_T	Total time of simulation
t_L	Time reference for the effective memory length
n_{PML}	Number of PML elements
z_e	z coordinate of the location of the emitter
r_c	r coordinate of the centre of the tumour
z_c	z coordinate of the centre of the tumour
$\varnothing_c$	diameter of the tumour
$\Delta\phi$	Phase change
$r_{Pearson}$	Pearson correlation coefficient
R^2	Coefficient of determination
e_m	m^{th} emitter
F_m	Displacement field for the forward propagation from emitter m
t_n	Time step n for correlation process in RTM
n	Integer counter for time
N	Maximum value of n
R_m	Displacement field for the reverse propagation with emitter m
I	Final reconstruction image for RTM
I_c	RTM reconstruction image according to the Claerbout method
I_s	RTM reconstruction image according to the Source illumination method
I_r	RTM reconstruction image according to the Receiver illumination method
I_{ratio2}	RTM reconstruction image according to the Square ratio method

I_{prop}	RTM reconstruction image according to the new proposed method
u_{exp}	Pseudo-experimental displacement measurements
r_h	r coordinate of the centre of the HIFU lesion
z_h	z coordinate of the centre of the HIFU lesion
u_{mod}	Simulated displacement measurements
r_{lesion}	r coordinate of the centre of the stiff lesion
z_{lesion}	z coordinate of the centre of the stiff lesion
$\varnothing_{lesion}$	Diameter of the stiff lesion
μ_{ratio}	Stiffness contrast ratio between stiff lesion and normal tissue
η_{ratio}	Viscosity contrast ratio between stiff lesion and normal tissue
p_{lesion}	Chromosome vector for the GA method
f	Cost function according its initial definition
f^L	Cost function according the definitive definition
R	Residual for the cost function definition
ε	Non-dimensional value for the cost function definitive definition

Contents

List of Figures

List of Tables

Chapter 1

Introduction

1.1 Motivation

Prostate cancer is the most common cancer in men in the UK. It is also the second cause of cancer death after lung cancer. It represents around 13 % of all cases of cancer and accounts for 7 % of all UK cancer deaths (Cancer Research UK, 2014). This means that about 1 in 8 men will be diagnosed with prostate cancer at some point in their lives. Prostate cancer also shows genetic and ethnicity dependency. The chances of developing prostate cancer multiply by two and a half times if a first-degree relative has been diagnosed, and is doubled for men of African or Afro-Caribbean origin. In addition, the incidence of prostate cancer increases with age, affecting mainly men over 50 years of age (The Prostate Cancer Charity UK, 2015).

The increase in longevity and awareness of the disease are leading to more men requesting screening, which is in turn increasing the number of patients diagnosed with prostate cancer. The paradox of prostate cancer lies in the relation between the high rate of positive diagnostics and the large number of patients who can live with the condition and do not die due to it. The aim of prostate cancer management is now to identify, treat and cure patients with aggressive cancers that may lead to a fatal end but to avoid the over-treatment of those where the cancer is unlikely to be life threatening (Abdellaoui et al., 2011).

The efficacy of prostate cancer detection is still low. Prostate cancer diagnosis requires advances despite many improvements achieved over the last decades. Many international research groups are focusing on the development of innovative techniques that change the current panorama. Paraphrasing Good et al. (2014), if the future diagnosis devices become cheaper and smaller, a larger range of applications will be possible, e.g. detection of prostate cancer in primary care, staging of advanced confined prostate cancer or for use in laparoscopic/robotic surgery.

New focal treatment modalities for the prostate are emerging. Focal therapy can be seen as the middle ground between active surveillance and radical therapy. High Intensity Focused Ultrasound (HIFU) ablation is one of these focal therapies (Marshall and Taneja, 2015). Successful treatment of prostate cancer using this type of focal therapy is critically dependent on accurate diagnostic means and may be benefited greatly by a real-time monitoring system for tissue damage during treatment.

Elastography is used to measure variations in tissue elasticity which might be associated with pathologies such as prostate cancer. Since tissue stiffness also increases locally due to coagulative necrosis, this method could be developed for the diagnosis of prostate cancer as well as for monitoring thermal ablation in the prostate to guide focal therapies.

1.2 Background

1.2.1 Prostate cancer diagnosis

The prostate is a gland of the male reproductive system. It surrounds the urethra just below the urinary bladder. It is about the size of a chestnut, and its most important function is the production of a fluid that, together with sperm from the testicles and fluids from other glands, makes up semen.

According to McNeal (1981), the human prostate can be divided into one non-glandular zone: the Anterior Fibro-muscular Zone, and three glandular zones: the Peripheral Zone (PZ), the Central Zone (CZ) and the Transitional Zone (TZ). The last three zones represent 70 %, 25 % and 5 %, respectively over the total glandular volume of a healthy human prostate (Figure 1.1).

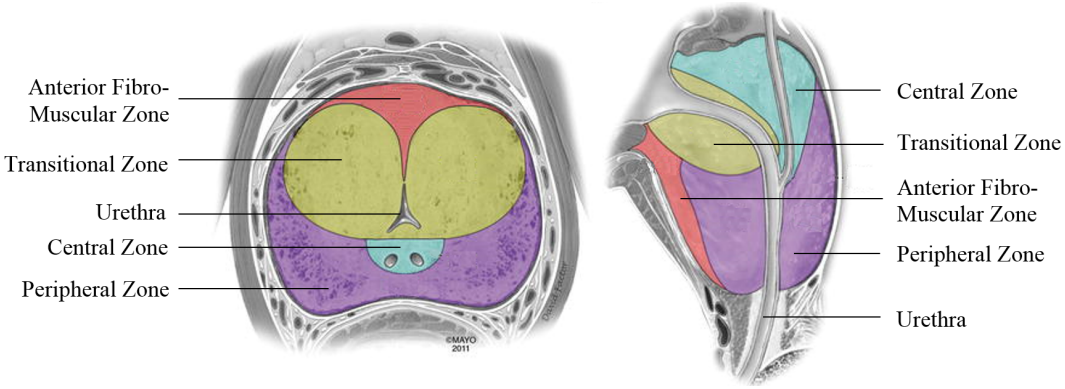

Figure 1.1: McNeal's anatomic division of the prostate. Source: Mayo Foundation for Medical Education and Research

The spatial occurrence of prostate cancer over the different zones has been analysed by some authors (Cohen et al., 2008, Lee et al., 2011a, McNeal et al., 1988). In general, the highest rate of cancerous tumours is found in the PZ, followed by the TZ, and the lowest in CZ (Table 1). However, it was found that the tumours originated at the CZ tend to be more aggressive and more likely to develop an extracapsular extension and invade the seminal vesicles (Cohen et al., 2008).

Table 1.1: Zonal occurrence of prostate cancer

Prostate zones	McNeal et al. (1988)	Cohen et al. (2008)	Lee et al. (2011a)
Peripheral Zone	68.0 %	63.7 %	70.0 %
Transitional Zone	24.0 %	33.8 %	25.0 %
Central Zone	8.0 %	2.5 %	5.0 %

Prostate carcinoma is often suspected when the serum Prostatic-Specific Antigen (PSA) is elevated or an abnormal digital rectal examination is noted. However, PSA screening leads to a substantial number of unnecessary biopsies in patients with no or indolent cancer who do not need immediate treatment (Kelloff et al., 2009). Histopathological evaluation of systematic biopsy cores is used to confirm or rule out cancer, and is normally carried out with conventional Transrectal Ultrasound (TRUS) as a guidance tool.

Despite the low specificity of PSA testing and the uncertainty after negative systematic biopsies, these techniques remain the standard for prostate cancer diagnosis, mainly due to their high availability and low cost (Junker et al., 2014). The systematic biopsy method can generate under- and over-diagnosis, as well as over-treatment of microscopic tumour foci (Giannarini et al., 2009, Pepe et al., 2010).

Conventional TRUS B-mode imaging is known for its limited sensitivity and specificity (between 40 % and 50 %) for prostate cancer detection, and it is not significantly improved by Colour/Power Doppler ultrasound (Tsutsumi et al., 2010). Contrast-Enhanced ultrasound may improve biopsies, but it is still under evaluation (Aigner et al., 2009, Tang et al., 2007).

Current research is investigating whether other modern imaging techniques can identify the site of a tumour, allowing targeted biopsy, focal therapy and improved management for low-risk patients on active surveillance strategies (Abdellaoui

et al., 2011). There are two main streams that are showing promising results: MRI and elastography techniques.

Multi-parametric MRI (mpMRI) combines T2-weighted imaging with functional sequences such as Diffusion sequence, Dynamic Contrast-Enhanced sequence and Spectro-MRI. mpMRI has become an important modality for tumour detection and staging (Lemaitre et al., 2009, Lim et al., 2009, Ahmed et al., 2017), however, mpMRI performance varies depending on which combination of features is selected (Langer et al., 2009).

A novel academically developed MR/US fusion device for guiding targeted transperineal prostate biopsy is currently available (SmartTarget Ltd., London, UK). The method produces a 3D deformable model of the gland from MRI scans. Real-time TRUS images are fused with the 3D model for tracking the suspicious areas during the biopsy (Dickinson et al., 2013, Hu et al., 2015). A paired blinded trial demonstrated that there was no overall difference in the capacity of detection of prostate tumours between visual estimation and the MR/US image fusion method, nevertheless, the authors suggested the simultaneous use of both techniques for optimal cancer detection (Donaldson et al., 2017).

In general, additional limitations of MRI-based methods include cost, limited availability, contra-indication to MRI and contrast agents, and the fact that the very large majority of biopsies are ultrasound guided (Correas et al., 2013a).

Elastography is an emerging imaging modality, which consists of the evaluation of tissue elasticity. It has been shown that prostatic cancerous nodules are usually stiffer than adjacent normal prostatic tissue. This is the basis for digital rectal examination. It has been reported that the stiffness contrast ratio of prostate cancer to normal healthy prostatic tissue suggests great potential for elastography imaging methods to identify prostate cancer (Zhai et al., 2010b, Correas et al., 2011).

Prostate tumour growth and the subsequent progression into surrounding tissue may be regarded as a disruption of normal tissue homeostasis (Hoyt et al., 2008).

Analogous to the cellular processes of wound repair, it is generally believed that normal tissue stroma responds in an effort to repair damage due to carcinoma cell invasion (Tuxhorn et al., 2001). It has been concluded that the stromal reaction is also characterised by elevated collagen deposition (Tuxhorn et al., 2002). Furthermore, research suggests that increasing tumour aggressiveness is coupled with increased amounts of collagen accumulation in the local benign tissue. Since increasing collagen deposition leads to an increase in the tumour rigidity, this suggests that quantitative stiffness estimations may prove to be an effective biomarker for assessing prostate cancer grade and identification of more aggressive cancers (Burns-Cox et al., 2001). However, as stated by Correas et al. (2013b), all elastography techniques are "subject to the same intrinsic limitations: not all cancers are stiff, and all stiff lesions are not cancers". Benign Prostatic Hyperplasia (BPH) presents also a higher stiffness than normal tissue but presents lower stiffness than prostatic carcinoma, although considerable overlap between the two frequently occurs (Correas et al., 2015, Ginat et al., 2009).

A detailed analytical review of elastography techniques for prostate cancer is developed in Chapter 2.

1.2.2 HIFU thermal ablation of prostate cancer

Radical surgery and whole-gland therapies remain controversial for treatment of localised prostate cancer due to the possibility of genitourinary and rectal side-effects as a consequence of damaging contiguous tissues. Focal therapies are emerging as suitable methods for treating localised unifocal and multifocal cancer lesions in the prostate while reducing side-effects. One example is HIFU, also known as Focused Ultrasound (FUS) ablation, which is providing encouraging results (Ahmed et al., 2012). However, despite the promising future of HIFU ablation for localized prostate cancer, the final target is usually meant to be the whole or half volume of the gland (Ahmed et al., 2011, Crouzet et al., 2014),

likely to guarantee the success of the treatment against possible scenarios of under-diagnosis.

HIFU is based on the concentrated effect of focused ultrasound on a target area. HIFU thermal ablation aims the irreversible damage of tissue by two different physical mechanisms: thermal and mechanical.

Thermal damage is achieved due to the ultrasound energy absorbed by the targeted tissue and transformed into heat. The focused ultrasound waves rapidly induce a high increase of temperature at the focal area, around 70 °C to 100 °C in a few seconds (Chaussy et al., 2013). A thermal dose, which depends not only on the temperature but also on the time of exposure, that exceeds a certain threshold, will cause tissue coagulation leading to coagulative necrosis (ter Haar, 2000).

The mechanical effects of HIFU are produced by the effects of negative pressure of the ultrasound wave. The negative pressure causes the formation and growth of bubbles in the targeted area. High pressure levels are reached when the formed bubbles suddenly collapse, causing damage to adjacent tissue (Chaussy and Thüroff, 2010).

It is well known that the stiffness of the treated soft biological tissue suffers a dramatic increase during thermal lesion formation (Arnal et al., 2011a). This suggests a potential role of elastography techniques for monitoring and assessing the lesion formation during and immediately after the treatment.

1.3 Proposed Transurethral Shear Wave Elastography technique

Patients with regions of elevated stiffness in the prostate are suspected of presenting with prostate cancer, as stated in Section 1.2. Additionally, thermal ablation of prostate cancer increases the stiffness of the treated tissue, thus generating a stiffness contrast between treated and non-treated tissue. For these two reasons, the detection and characterisation of the mechanical properties of stiff regions within the prostate can be used for the diagnosis of prostate cancer and the monitoring of focal thermal ablation of such tumours. Shear waves are sensitive to changes in the elastic properties of the tissue, therefore, imaging techniques based on the analysis of the propagation of shear waves throughout the prostate are particularly well suited for detecting and characterising regions of elevated stiffness in the prostate.

Current elastography techniques for prostate are transrectal. Given the fact that HIFU treatments for prostate are transrectally delivered, alternative elastography approaches that use different delivering channels are needed. In this thesis, a TU-SWE technique for the diagnosis of prostate cancer and the HIFU ablation monitoring of such tumours is proposed. One of the advantages of the proposed TU-SWE technique offers a solution to the delivering channel issue by using the urethra to reach the prostate. Therefore, TU-SWE is well suited for achieving the detection and characterisation of stiff areas within the prostate while keeping the rectal passage free for transrectal therapies. Further details on the advantages of TU-SWE against other elastography techniques will be provided in Section 2.3.

Current MR-based techniques are providing satisfactory results for the diagnosis of prostate cancer as detailed in Section 1.2, however these techniques are limited by their high cost and low availability, particularly in less developed countries. TU-SWE can be fabricated as an affordable device with disposable attachments by using micro-manufacturing processes that will considerably reduce

the cost of the device, thus making it accessible for use in the clinic and as a diagnosis tool in less developed countries.

Figure 1.2 shows the conceptual idealisation of the TU-SWE technique. The principles of the TU-SWE technique are based on the transmission of shear waves into the prostate by applying oscillatory rotational forces on the urethral wall, thus generating a pseudo-spherical propagation pattern of shear waves. Imaging is based on the reception of shear wave echoes generated by shear impedance variations within the gland. Shear impedance variations are due to the changes in the shear modulus distribution of the prostatic tissue, which can be associated with the presence of a lesion, as either a prostate tumour or a thermal lesion.

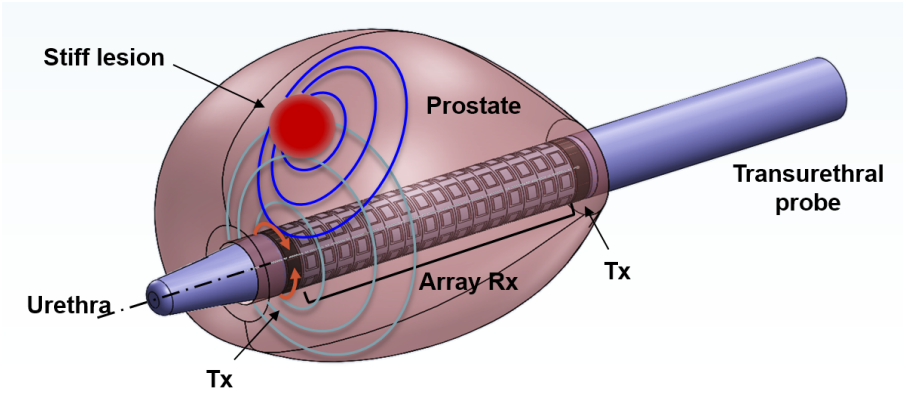

Figure 1.2: Conceptual idealisation of the TU-SWE approach for diagnosis of prostate cancer and thermal ablation monitoring in the prostate. A transurethral probe is inserted through the urethra until reaching the prostatic urethral section.

The design of the transmission and reception elements (Tx and Rx, respectively, in Figure 1.2) is still under investigation and it has been considered beyond the scope of this thesis. Nevertheless, some basic design features of both elements have already been addressed. Emitters and receivers will be mounted on a 6.5 mm diameter transurethral probe, the number and arrangement of each type will be analysed in Chapter 5. A basic laboratory version of the emitter is composed of a 6.5 mm diameter disk attached to a rotational motor. Receivers will be arranged as a distributed 1D array, thus covering the entire surface of the probe that is not

occupied by the emitters. Different tactile-based technologies for designing the receivers are being investigated in a parallel study to the work presented in this thesis.

The measured signals at the array of receivers carry information about the medium of propagation and the reflectors located within it, i.e., features of the stiff lesion, such as location, size and viscoelastic properties. The values of those features can be reconstructed by processing the signals and solving the inverse problem.

1.4 Aims and objectives

The aims of this thesis are to develop the concept of the TU-SWE method and demonstrate its feasibility as a medical imaging technique for prostate cancer diagnosis and for focal thermal ablation monitoring in prostate. By doing so, the method will move from the basic idea to a preliminary stage of proof-of-concept, thus providing significant evidence to pursue further development of the method, for instance, by producing a laboratory prototype. To succeed, specific objectives must be accomplished. These are as follows:

- To develop a numerical model representing the TU-SWE method for the propagation of shear waves through a prostate-like medium.
- To implement into the numerical model a generic viscoelastic constitutive law that represents the viscoelastic behaviour of the prostate.
- To experimentally validate the numerical model of shear wave propagation against *in vitro* observations.
- To develop methods for solving the inverse problem and thus, to reconstruct the parameters of the stiff lesion.
- To obtain an optimum TU-SWE device configuration, in terms of the number and distribution of emitters and receivers.

1.5 Thesis outline

This thesis has been divided in six chapters according to the following structure:

- Chapter 1. This chapter introduces the concept idea of the TU-SWE technique, explores the problems and needs concerning prostate cancer diagnosis and focal treatment monitoring, and details the objectives and the original contributions of the thesis.

- Chapter 2. This chapter analyses the literature on elastography applications for prostate cancer diagnosis, as well as literature about monitoring of HIFU thermal ablation in prostate and other tissues. A comparative analysis between TU-SWE and the reviewed elastography techniques is also presented. Finally, literature concerning viscoelastic parameters and mechanical models for prostate is reviewed.

- Chapter 3. This chapter is dedicated to the numerical method for shear wave propagation according to developing the TU-SWE technique. A short review concerning the most typical forms of wave equations and constitutive laws used for shear wave propagation modelling in soft tissue is presented. Finally, some simulations are shown, thus illustrating examples of shear wave propagation and its interaction with the mechanics of prostate-like media.

- Chapter 4. This chapter describes the experimental work carried out for validating the wave propagation model developed in Chapter 3. Short reviews concerning elastography tissue-mimicking materials and optical techniques for capturing particle vibration due to wave propagation are presented. Phantom fabrication and rheological characterisation of the tissue-mimicking materials are also described.

- Chapter 5. This chapter is dedicated to the development of the reconstruction methods used for solving the inverse problem. First, a short review and a

comparative analysis of various reconstruction methods are carried out. Then, after the description of the proposed methods, some examples illustrate the application of the new reconstruction methods in diagnosis and treatment scenarios. Finally, a combination of the two methods of reconstruction is proposed and evaluated.

- Chapter 6. This chapter reports the general conclusions of the thesis, as well as details the proposed future work.

1.6 Statement of original contributions

The achieved original contributions of this thesis are listed as follows:

1) A new conceptual technique in elastography for prostate, TU-SWE, based on a transurethral approach for the transmission and detection of shear waves generated by applying oscillatory rotational forces on the urethral wall.

2) A numerical model based on FDTD for shear wave propagation in 2D for the TU-SWE technique.

3) Adaptation of the viscoelastic KVFD constitutive law to a 2D FDTD wave propagation model for elastography.

4) An experimental technique for observing the true displacement field due to shear wave propagation in translucent elastography tissue-mimicking materials, combining high-speed camera tests and a custom particle tracking method.

5) Adaptation of a seismic migration technique such as Reverse Time Migration (RTM) to a medical imaging method based on elastography.

6) A new correlation condition for RTM algorithms.

7) A reconstruction method for solving the inverse problem in the TU-SWE technique, based on the combination of a migration technique such as RTM and a randomised search method such as Genetic Algorithms (GAs).

1.7 Chapter summary

In this chapter, the main motivations of the thesis were described. First, the size and importance of prostate cancer as a worldwide healthcare issue were stated. The urgent need for advancing in prostate cancer diagnosis techniques due to the low current efficacy was discussed. In addition, new focal therapies were also mentioned, as well as their need for accurate monitoring systems.

Second, the chapter introduced the basic principles of elastography imaging and its potential role in prostate cancer diagnosis and monitoring of focal thermal therapies.

Third, a new concept in elastography imaging for prostate was presented, the TU-SWE technique, an elastography imaging approach based on the transurethral transmission and reception of shear waves for detecting the presence of stiffer areas within the prostate.

Finally, the thesis outline was described after enumerating the main objectives and original contributions of the thesis.

Chapter 2

Literature review

Technology evolves with the aim of overcoming the limitations of previous techniques. The objective of this chapter is to review all the relevant material from the literature in order to provide a better understanding of the background of the thesis and to identify areas that require further research.

This chapter describes some current elastography techniques associated with prostate cancer diagnosis and investigates the latest research concerning the role of elastography for the monitoring of thermal ablation. This chapter also reports a brief analysis of the inherent advantages of TU-SWE with respect of the reviewed elastography techniques. Finally, a review of the literature concerning viscoelastic parameters and mechanical models for prostate is carried out.

2.1 Elastography for diagnosing prostate cancer

Palpation, as a technique for evaluating hardness due to abnormal tissues, has been known since ancient times (Garra, 2015). Writings in the Edwin Smith papyrus (Allen, 2005) concerning the use of palpation as a diagnostic tool have been attributed to the physician, priest and architect Imhotep who lived between 3000 and 2500 BCE in Egypt (Breasted, 1930). Whilst palpation is still a valuable technique, its application is limited to accessible organs, with low detectability and spatial discrimination, and is of course exposed to subjective interpretation (Bamber et al., 2013).

First elastography techniques were developed in the late 1980s to early 1990s with the aim of improving the ultrasound-based imaging methods (Lerner and Parker, 1987, Lerner et al., 1988, Ophir et al., 1991, O'Donnell et al., 1994). Since the above first publications, further developments have been reported in elastography. Currently, elastography methods can be divided into two main groups: Strain Elastography (SE) or quasi-static elastography and Dynamic Elastography (DE) (Bamber et al., 2013, Doherty et al., 2013). In the following subsections, the review will be focused on prostate applications of the different elastography techniques.

2.1.1 Strain Elastography

SE of the prostate is performed transrectally and is based on the comparative analysis of tissue deformation. SE exploits the fact that stiffer tissue experiences less deformation than normal tissue. A colour map of relative strain is plotted using signal processing techniques, revealing the zones where the strain is lower and therefore with high stiffness. No quantitative elastic values are available. Relative variations in the strain between zones work as a guide to the existence of suspect pathological nodules (Ophir et al., 2002). This technique is currently commercially

available on several clinical ultrasonic platforms (Bamber et al., 2013).

Some studies evaluated the use of SE in prostate cancer detection. Salomon et al. (2008) compared findings from SE in *in vivo* prostates with results from hystology after radical prostatectomy. They observed potential in SE for increasing the ultrasound-based cancer detection, however, they stated that further studies were needed in order to obtain final conclusions and to evaluate whether tumour detection can be increased by elastography-guided biopsies. Later, Brock et al. (2012) experienced improved sensitivity to detect prostate cancer using SE in addition to conventional ultrasound during prostate biopsy. Good et al. (2014) produced a comprehensive summary of SE results from several prostate cancer detection studies from 2002 to 2012, obtaining sensitivity and specificity values from 51.0 % to 74.5 % and from 62.2 % to 97.7 %, respectively.

According to Correas et al. (2013a) SE provides an improvement for prostate cancer detection, however the studies are not yet conclusive for pathology diagnosis. Some experienced limitations of SE were (Correas et al., 2013a):

- The lack of uniform compression over the entire gland.
- Intra- and inter-operator dependency.
- Penetration issues in large prostate glands.
- Artefacts due to slippage of the compression plane.

2.1.2 Dynamic Elastography

DE in prostate cancer detection has been performed mainly by Acoustic Radiation Force (ARF) methods, namely Acoustic Radiation Force Impulse (ARFI) imaging, Point Shear Wave Elastography (pSWE), Transrectal Shear Wave Elastography (TR-SWE), Shear Wave Dispersion Ultrasound Vibrometry (SDUV) and Crawling Wave Spectroscopy (CWS). These methods can be classified according to the temporal duration of the applied ARF excitation and the setting of the tracking beams used to measure the deformation response (Doherty et al., 2013). These

methods will be reviewed in the next sections.

2.1.2.1 Acoustic Radiation Force Impulse

ARFI imaging conserves the same principle as SE but using ARF as an excitation source. Instead of applying an external compression or vibration, ARFI delivers high-intensity focused acoustic beams inside the tissue to generate ARF which deforms the tissue in the beam axis direction. Then, the method plots zones of different rigidity by monitoring the resultant displacement responses.

Compared to SE images, ARFI images show a better resolution in phantoms, suffer less from stress concentration artefacts, exhibit improved signal-to-noise ratio (SNR) and are less influenced by the presence of slip movement anterior to the imaged region (Melodelima et al., 2007). However, and as in SE, ARFI imaging does not provide quantitative values.

Only two works were found in the literature using ARFI imaging for prostate cancer detection: an *ex vivo* (Zhai et al., 2010b) and an *in vivo* test (Zhai et al., 2012), both studies used Virtual Touch™ Imaging (Siemens, Erlangen, Germany). The results demonstrate that ARFI imaging can be applied to visualize internal structures and to detect suspicious lesions in the prostate, but to the date of this thesis no studies of sensitivity for prostate cancer detection have been found.

2.1.2.2 Point Shear Wave Elastography

ARF techniques create a transient shear wave propagating with cylindrical symmetry away from the axis of the pushing beam, being strongest at the position of the focus. The pSWE technique takes advantage of this effect. The method uses either correlation tracking or Doppler technique to measure the speed of the shear wave by detecting its time of arrival at lateral positions. Although ultrasound imaging is used to guide the placement of the Region of Interest (ROI), no elasticity images are produced, solely the shear wave speed value for the ROI (Tanter et al., 2008). This technique can be also found in the literature under the

name of ARFI quantification. Two commercial systems with this capability are currently available: Virtual Touch™ Quantification (Siemens, Erlangen, Germany) and ElastPQ (Philips, Amsterdam, Netherlands).

Two studies using pSWE were found in the literature. Zhai et al. (2010a) reconstructed the shear moduli values from excised human prostates. They obtained a stiffness contrast ratio of 2.2 between cancerous tissue and normal tissue, although a limitation of the study was the low spatial resolution of 6.5 mm. Zheng et al. (2012) presented an *in vivo* study. They claimed that pSWE could effectively measure the stiffness of prostate nodular lesions with better discrimination between prostate cancer and BPH, with diagnostic sensitivity and specificity of 71.93 % and 87.5 %, respectively. However they compared the results against digital rectal examination which, although widely used, is a subjective method and therefore cannot be considered as a reference technique for prostate cancer detection. In addition, they specified that the limited detected depth and the fixed box dimension of the target ROI could hamper the wider application of the technology.

2.1.2.3 Transrectal Shear Wave Elastography

TR-SWE for prostate cancer detection has been tested mainly by the Aixplorer® ultrasound system (SuperSonic Imagine, Aix-en-Provence, France). More recently, SWE has also been released for Siemens platforms and is named Virtual Touch™ IQ (Siemens, Erlangen, Germany). However, studies using the Virtual Touch™ IQ system regarding prostate elastography have not been found at the time of this thesis.

When using TR-SWE by Aixplorer® the ARF focus is swept down along the beam axis faster than the shear wave speed, generating tissue displacement at all positions along the acoustic axis almost simultaneously. This produces a cone-shaped shear wave featuring a small inclination, and is known as the Mach cone. The shear wave travels away from the pushing beam and decays less rapidly with distance than when using a single pushing focus. An ultrafast scanner achieves

a frame rate of up to 20 kHz by transmitting a plane wave. This allows shear waves to be followed in real-time in 2D, and echo tracking over a grid of points produces a displacement recording from which a small map of shear wave time-of-arrival can be created (Bercoff et al., 2004b). SE imaging and ARFI imaging present better spatial resolution but SWE elastograms are quantitative. Furthermore, the dispersion curve of the shear wave velocity over the range of frequencies could add new and potentially interesting information for general diagnostic applications (Tanter et al., 2008).

Recent studies on prostate cancer diagnosis using TR-SWE presented very promising results (Ahmad et al., 2013, Barr et al., 2012, Boehm et al., 2015, Correas et al., 2015, Woo et al., 2015), showing sensitivity and specificity values for prostate cancer detection from 80.9 % to 96.2 % and from 69.1 % to 96.2 %, respectively, which is a major improvement in the detection efficiency compared to other techniques.

However, as with all technologies, TR-SWE presents some limitations. Some of these are listed below (Correas et al., 2013a):

- The pressure artefacts induced by the transducer, as the end-fire design of the probe requires bending to image mid prostate and apex.
- The slow frame rate, i.e. one image per second.
- The limited size of the ROI (only half of the prostate is covered).
- The delay to stabilize the signals at each acquisition plane.
- The signal attenuation in large prostates making the evaluation of the anterior TZ of the prostate (Figure 1.1) difficult or impossible (Zhang et al., 2013a).

2.1.2.4 Shear Wave Dispersion Ultrasound Vibrometry

SDUV combines vibro-acoustography for generating the shear wave and pSWE for tracking the off-axis propagation. Vibro-acoustography is a technique that generates harmonic shear waves using either a single amplitude-modulated continuous excitation or two radiation force excitations transmitted simultaneously with

slightly offset frequencies and focused at the same location. This offset produces monochromatic shear waves with known frequency. By applying this technique over a range of excitation frequencies, a quantitative estimate of tissue stiffness and viscosity can be derived using a model-based approach (Doherty et al., 2013).

Mitri et al. (2011) used SDUV in *ex vivo* human prostates over a range of excitation frequencies. A quantitative estimation of tissue stiffness and viscosity at different points in the prostates was derived using a Kelvin-Voigt (KV) model-based approach. Details are shown in Section 2.4. However, no discrimination between healthy and malignant tissue was shown. Further studies were not found in the literature.

2.1.2.5 Crawling Wave Spectroscopy

In CWS, a slow-moving crawling wave is generated due to the interaction of shear waves generated by two physically separated ARF sources or mechanical actuators with slightly offset frequencies. The crawling wave can be monitored in real-time, since its speed is slow enough for using conventional ultrasound techniques. The speed of the crawling wave is related to the mechanical properties of the tissue and can be used to form a quantitative estimation of stiffness (Hazard et al., 2012).

An et al. (2011) applied the method in excised prostates obtaining 62.18 % sensitivity and 90.77 % specificity. However, this techniques experiences a major issue: the spatial requirement for placing both excitation sources poses significant difficulties for *in-vivo* application to prostate cancer detection.

2.2 Monitoring of HIFU thermal ablation in the prostate

HIFU thermal ablation for treating prostate cancer is used transrectally (see Figure 2.1). At the date of this thesis, only two HIFU systems are commercially available and recently approved by the Food and Drug Administration (FDA) for treatment in the prostate: Sonablate® (SonaCare Medical, Charlotte, NC, USA) and Ablatherm® (EDAP TMS, Lyon, France). There is a third system, Exablate® (InSightec, Tirat Carmel, Israel), only available for research use in the case of prostate tissue ablation. Thermal ablation in the prostate can be also performed by transurethral thermal ablation (Chopra et al., 2012), technique that recently obtained CE marking under the name of TULSA-PRO™ (Profound Medical Corp., Mississauga, Canada). This technique is not based on HIFU, instead, it uses plan waves at high frequency and is currently intended for whole gland ablation (Chin et al., 2016).

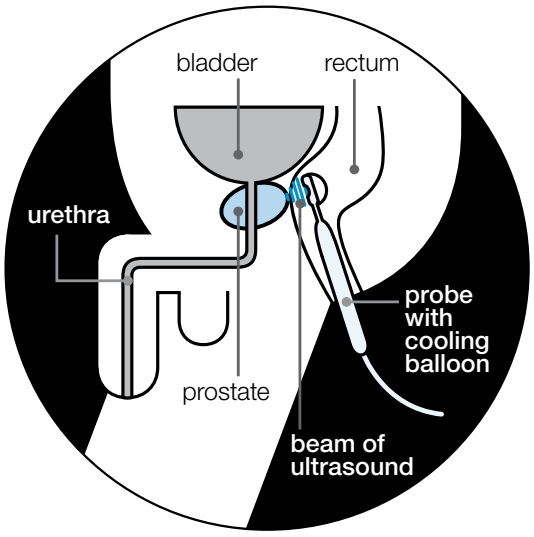

Figure 2.1: Schematic representation of the HIFU ablation procedure for prostate cancer treatment by a generic transrectal HIFU system. HIFU probe is transrectally placed facing the posterior side of the prostate. Source: The Prostate Cancer Charity UK (2017).

The HIFU ablation of the prostate is delivered via a transrectal probe. Such probes are introduced through the rectal passage and the transducer is placed facing the posterior side of the prostate (see Figure 2.1). A balloon surrounding the transducer is filled with either degassed water (Sonablate®) or acoustic coupling gel (Ablatherm®), which simultaneously works as a rectal wall cooling system. These two systems present some differences in terms of their functionality. The Sonablate® system includes two acoustic lenses with different focal length which can generate ellipsoidal lesions of $12\times3\times3$ mm and $10\times3\times3$ mm size that are delivered at three consecutive coronal layers for full- and hemi-ablation of the prostate. Both lenses can be used for B-mode imaging. On the other hand, the Ablatherm® system comprises only a single acoustic lens for therapy, which generates ellipsoidal lesions of $24\times1.7\times1.7$ mm size in only one coronal layer, in which case, the B-mode imaging can be performed via a transducer located at the centre of the HIFU transducer.

Treatment guidance is key to successfully performing localised treatments with such transrectal HIFU systems. When analysing image guidance it is important to state the difference between monitoring and assessing treatment response. Treatment monitoring is defined as the process of observing the therapy effects during the treatment as changes in the image, whilst immediate treatment assessment occurs right after the application of the treatment and its objective is the evaluation of the extent of the ablated lesion compared with the tumour area (Goldberg et al., 2009).

Real-time monitoring of thermal ablation therapies for prostate cancer is a research field of major interest. Detecting the induced lesion in the prostate as soon as it appears and monitoring its size are important requirements to avoid damage to surrounding healthy tissue and extra therapy sessions (Curiel et al., 2005). In the particular case of HIFU ablation of prostate cancer, controlling the formation and evolution of the treated volume is crucial for sparing sensitive areas such as the neurovascular bundles and the rectal wall where damage might generate significant

side-effects.

Some imaging techniques have been investigated for monitoring localised thermal ablation in different organs. In the case of prostate ablation, this includes MRI and ultrasound based techniques, which will be discussed further in Sections 2.2.1 and 2.2.2, respectively.

2.2.1 MRI-based monitoring techniques

At the present, the commercial application of MRI for real-time guidance is limited to MR thermometry. Two techniques make use of it, the transurethral thermal ablation system by TULSA-PRO™ and the transrectal thermal ablation system by Exablate® (Napoli et al., 2013). In fact, the Exablate® equipment is integrated in an MRI system. Although all of the MRI parameters show some form of temperature dependence, the most widely used one is the proton resonance frequency (Lewis et al., 2015).

Apart from the usual limitations of MRI, such as high cost and the fact that the equipment and room must be MR-compatible, a panel of experts in 2014 (Muller et al., 2014) decided not to recommend the use of MRI for monitoring thermal focal therapies of prostate cancer due to the un-resolved challenges of target movements. These are virtually impossible to avoid in transrectal ablation. For instance, Hazle et al. (2002) experienced erroneous temperature rises when using MR thermometry during transurethral ultrasound thermal ablation in canine experiments due to movements in the prostate of the order of few millimetres.

Studies using MRI contrast agents yielded good results for the post-treatment assessment of HIFU ablation in the prostate. In dynamic Contrast-Enhanced T1-weighted MRI (CE-MRI) right after treatment, the HIFU lesion is shown as a non-enhanced nucleus due to coagulation necrosis, surrounded by an enhanced peripheral rim (3-8 mm thick) due to inflammation and partial necrosis (Hazle et al., 2002, Rouvière et al., 2001). A similar phenomenon is observable in other thermal

ablation techniques such as laser, Radio-Frequency (RF) and even in cryotherapy (Rouvière et al., 2001). After treatment, the surrounding rim may either result in chronic necrosis or represent surviving tissue. For this reason, the above referred panel of experts agreed that a follow-up MRI of the prostate should be undertaken 6 months after thermal therapy (Muller et al., 2014).

Regarding other types of MRI, such as unenhanced T1-weighted and T2-weighted, results do not depict accurately the lesion extent. Unenhanced T1-weighted MRI shows slightly hyperintense foci within the target area, likely due to interstitial haemorrhage, but for a better delineation of the lesion the contrast agent is needed. Using T2-weighted MRI, a poorly defined hypointense region appears at the centre of the lesion but not clearly distinguishable from the pre-existent hypointense cancer areas (Rouvière et al., 2001). Diffusion-Weighted MRI (DWI) has been also investigated. Chen et al. (2008) compared DWI results with CE-MRI in transurethral thermal ablation of canine prostates. The authors claimed that DWI produced similar results to CE-MRI although no histological analysis was performed. More studies are needed in order to confirm the suitability of using DWI for monitoring HIFU ablation of human prostates.

2.2.2 Ultrasound-based monitoring techniques

When monitoring HIFU treatment by ultrasound imaging, it is common to see hyperechoic zones in the ablated area caused by the formation of gas bubbles. Sanghvi et al. (1995) confirmed the observation of this phenomenon in *in vivo* HIFU ablation of canine prostates. However, they reported that the hyperechoic region underestimated the extent of necrosis.

Tissue Change Monitoring (TCM) is the commercial name of the monitoring software currently implemented in the Sonablate® system. This method measures the energy of the backscattered signals coming from the focal point of ablation. The method uses the increment in backscattered energy between pre- and post-ablation

measurements as an estimator for tissue changes caused by high tissue temperatures during HIFU treatment (Chen et al., 2011). *In vivo* HIFU ablation experiments in human prostate by Chen et al. (2012) yielded a good correlation between temperature and TCM reading below 50 °C but not above 67 °C. According to the authors, this lack of correlation was due to the effects that tissue expansion and cavitation have on the TCM readings. High values of TCM readings could ensure that destructive temperature levels were reached, but this may imply over-treatment of the tumour due to excessive high temperature, with an increased likelyhood of side-effects and with longer duration of the ablation procedure. Other disadvantages of TCM are the impossibility of contouring the thermal lesion and the loss of tracking position of the lesion if body movement occurs.

2.2.3 Elastography for monitoring HIFU thermal ablation

After HIFU thermal ablation, the ablated tissue possesses greater stiffness than the surrounding non-ablated tissue (Arnal et al., 2011a). The stiffness contrast between ablated and non-ablated tissue provides the basic principle for using elastography to image the extent of the lesion. Therefore, elastography may be used for immediate post-treatment assessment of HIFU thermal ablation. Furthermore, elastography may also be used for treatment monitoring, since it has the potential for imaging single HIFU lesions, such as the initial lesion, thus providing crucial information for the correct application of the treatment.

The studies in the literature regarding the monitoring and assessment of HIFU ablation of prostate cancer are limited to SE. Two studies, Souchon et al. (2003) and Curiel et al. (2005), evaluated the feasibility of using SE for assessment of HIFU thermal ablation of prostate cancer using the Ablatherm® device. The ablated regions appeared to be stiffer in the elastograms with a reduction in average strain of 50% compared to strains measured before treatment (Souchon et al., 2003). However, differences in the measured volume with T1-weighted MRI were

observed (Curiel et al., 2005). According to the authors, this mismatch may have been reduced if MRI and SE had been performed consecutively and using a higher frame rate and wider bandwidth ultrasound scanner. The volume of the HIFU lesions observed by MRI may have changed over time because of the formation of edema and/or reabsorption of necrosed tissues as reported by Rouvière et al. (2001). Xia and Thittai (2014) carried out a study using SE for monitoring the variation of stiffness during the HIFU exposure in *ex vivo* porcine liver. According to the authors, the results indicated that SE not only provided the visualisation and measurement of a single lesion, but also provided real-time feedback to visualise untreated regions between two lesions.

TR-SWE has been extensively used in feasibility studies for prostate cancer diagnosis as reported in Section 2.1.2.3. Yet, there exists no published data of its use for the assessment of HIFU thermal ablation in the prostate. In addition, monitoring HIFU thermal ablation of prostate cancer using TR-SWE is currently impractical since both these modalities, imaging and therapeutic, are performed transrectally. Nonetheless, the feasibility of using SWE for assessment of thermal ablation in other soft tissue has been investigated, with promising results. Some examples are HIFU thermal ablation of *in vivo* rabbit liver (Anquez et al., 2012), RF ablation of *in vivo* porcine liver (Mariani et al., 2014) and HIFU thermal ablation of *ex vivo* porcine cardiac tissue (Kwiecinski et al., 2015). All these studies were carried out using SWE, with the Aixplorer® ultrasound system.

2.2.4 Stiffness as a possible thermal damage biomarker

The measurement of temperature rise during thermal therapy may provide an accurate estimate of the thermal damage that will occur in the treated area. The relationship between history of heating, i.e. temperature and exposure time, and cellular death has been confirmed in numerous studies on cells and on excised tissue, and *in vivo*, in animals and humans (Lewis et al., 2015, Rieke and Pauly,

2008). One commonly used model describing this relationship is the thermal dose model (Sapareto and Dewey, 1984), where the quantification of thermal damage is related to an equivalent heating time at 43 °C. For biological tissue, the observed thermal dose required for reaching total necrosis ranges from 25 to 240 minutes at 43 °C (Dewhirst et al., 2003).

Tissue stiffness varies with temperature (Bercoff et al., 2004a, Kiss et al., 2009, Sapin-de Brosses et al., 2010, Mariani et al., 2014, Shi et al., 2015). This highlights the possibility of using stiffness as a potential biomarker for assessing and quantifying thermal damage. The reason why stiffness changes during heating is still not perfectly understood. It is thought that collagen denaturation is the responsible phenomenon for the irreversible stiffness changes (Lepetit, 2007, Wall et al., 1999, Wright and Humphrey, 2002). This transformation is assumed to begin at about 60 °C (Lepetit, 2007, Wall et al., 1999, Wright and Humphrey, 2002). As temperature increases, collagen fibres contract moving from their native triple helical structure into a randomly coiled structure (Lepetit, 2007). Nevertheless, moderate heat, i.e. below 60 °C, can result in reversible changes in the collagen fibres, with local unfolding within the collagen and restoration of the native structure when temperature reduces back to body temperature (Wright and Humphrey, 2002).

At the tissue macro-scale, there is currently no model that describes the change in tissue elasticity due to heating. Whilst experimental studies have been carried out in soft tissue, no studies on the prostate have been reported in the literature. Some examples of these experimental studies are detailed below.

Using MR Elastography, Wu et al. (2001) observed that HIFU thermal ablation of *ex vivo* porcine muscle produced a three-fold increase in the shear modulus at 200 Hz, and its dispersion, increasing to five-fold at 500 Hz. Similar results were obtained for *ex vivo* bovine muscle samples in the same study. In addition, Wu et al. (2001) reported good reproducibility of a three-stage pattern when slowly heating bovine muscle. Firstly, reversible decrease in the shear modulus when increasing

temperature from 20 °C to 60 °C, secondly, an irreversible quick increase from 60 °C to 75 °C, and finally, a reversible (for tissues that have previously undergone irreversible thermal damage) increase of shear modulus when cooling from 75 °C back to 20 °C. These results appear to be aligned with the reversible/irreversible denaturation of collagen fibres theory reported by Lepetit (2007), Wall et al. (1999), Wright and Humphrey (2002).

Bercoff et al. (2004a) presented for the first time the use of SWE for detecting HIFU thermal lesions, observing a stiffness contrast ratio of 2.6 between necrotic and untreated tissue in *ex vivo* chicken breast.

Kiss et al. (2009) mechanically obtained the complex Young's modulus of *ex vivo* canine and porcine livers at a range of frequencies between 0.1 Hz and 50 Hz and at temperatures ranging from 40 °C to 90 °C. Two different heating methods were used to achieve the required temperature rise: RF thermal ablation and a thermo-regulated bath. Both methods showed good agreement with one another. A local maximum of Young's modulus at 70-75 °C was observed in all tissue samples and heating methods. After this temperature, the modulus decreased before finally increasing to overcome the local maximum at 70-75 °C. According to the authors, the trend of the Young's modulus that they observed differed from what had previously been reported in the literature, mainly due to the fact that most of the published tests had been carried out in skeletal muscle. The authors speculated that the peak point at 70-75 °C represented the point where liver tissue had shrunk to its minimal size, yielding an increase in the stiffness. For temperatures above this threshold, they hypothesised that the decrease in Young's modulus was likely due to the fact that the collagen content was being denatured to gelatin. The stiffness values between 40 °C and 60 °C were not recorded, therefore the reduction in the stiffness as observed in Wu et al. (2001) could not been ascertained. This study is somewhat inconclusive due to the incomplete range of temperature, and statistically not significant to draw conclusions.

Sapin-de Brosses et al. (2010) studied the temperature dependence of the shear

modulus in *ex vivo* bovine liver and muscle tissue in a thermo-regulated bath, using SWE generated and acquired by the Aixplorer® system. Results from the bovine muscle tests showed a similar three-stage trend of shear modulus variation with temperature to that reported by Wu et al. (2001) and described earlier in this Section. The same trend was not found in tests on bovine liver, where the shear modulus remained constant up until 45 °C, after which it increased exponentially until 68 °C. However, only three samples of liver were tested and only one was heated up to 68 °C before the cooling stage. This last result was not carried out on a large enough sample size for it to be statistically significant and to draw conclusions. However, it exhibits a similar behaviour compared with that observed in *ex vivo* canine and porcine livers in Kiss et al. (2009), at temperatures lower than 70-75 °C. After cooling down the liver samples that did not get heated to 68 °C (these had reached 50-55 °C), these samples resulted in a final modulus of three times the reference value at room temperature.

Tests in liver tissue produced different stiffness responses against temperature when compared with muscle tissue. Further studies are needed to conclusively state the different behaviour of these tissues as a function of temperature rise, and to extrapolate it to other glandular tissue, e.g. the prostate.

A follow-up study to Sapin-de Brosses et al. (2010) was published a year later (Sapin-de Brosses et al., 2011), which described *in vivo* experiments in rat leg muscle. Temperature values ranging from 38 °C to 48.5 °C were maintained constant so as to analyse the effect of cumulative thermal dose in muscle stiffness. Despite very different time exposures, a strong rise in stiffness was observed at the same thermal dose value in all experiments. At 202 min (cumulative equivalent minutes at 43 °C) an eight-fold rise in stiffness was found. The cumulative equivalent minutes at 43 °C, as introduced by Sapareto and Dewey (1984), is a concept that translates all different temperature-time histories to a single number representing a thermal isoeffect dose. The value of 202 min is close to the well-accepted thermal dose threshold of 240 min for thermal necrosis in muscle

found by Sapareto and Dewey (1984). Despite these encouraging results, studies with a wider range of temperatures must be considered in order to extract consistent conclusions.

Arnal et al. (2011a,b) proposed to use SWE as a thermometry method for monitoring HIFU ablation after analysing a relationship between temperature and shear modulus of around -1.0 kPa/°C in the range of 30-40 °C. However, the range of temperatures spanned by this study represents only a small subset of the temperatures encountered during HIFU treatment. Further work is therefore required in order to characterise the behaviour of the shear modulus with temperature during more clinically relevant thermal scenarios.

Mariani et al. (2014) conducted *in vivo* experiments for assessing RF thermal ablation of porcine livers using SWE. A Young's modulus threshold of 20 kPa, which was double the Young's modulus of pre-treatment liver, was selected to predict tissue necrosis with a positive predictive value of 0.83 and a sensitivity of 0.8. Positive predictive value was defined as the fraction of pixels in the elastography image with Young's modulus higher than 20 kPa that actually developed coagulation necrosis. Sensitivity was defined as the fraction of pixels correctly detected as necrosed tissue.

Shi et al. (2015) performed a series of experiments in *ex vivo* and *in vivo* porcine livers for monitoring RF thermal ablation using SWE. Tissue softening was observed during *ex vivo* tests but not observed in *in vivo*. According to the authors, the cooling effect of perfusion may have had a significant influence on the different outcomes. *In vivo* tests resulted in similar lesion sizes for measurements immediately after the ablation and measurements after several minutes of cooling time. However, *ex vivo* tests immediately after treatment underestimated the size of the lesion compared with the cooled measurement. Due to the limited number of studies available, it cannot be stated with certainty whether the softening is related to the perfusion state of the tissue sample.

Overall, more studies are needed in order to rigorously assess the feasibility

of using stiffness as a biomarker for coagulative necrosis generated by thermal therapies. Furthermore, the fact that no studies in prostatic tissue have been found highlights a big research opportunity in this field, mostly encouraged by the promising results of thermal therapies for treating prostate cancer and the need for accurate monitoring techniques.

Nonetheless, variation in the viscoelastic properties of the prostatic tissue will occur during the formation of the thermal lesion, with a remaining irreversible increase in stiffness with respect to the pre-treatment situation after the lesion formation. The location and extent of the lesion can be found as a local variation of the tissue stiffness in a particular region of the gland. The evolution of the viscoelastic parameters and the degree of the irreversible changes in prostatic tissue are unclear for now and will require extensive investigation. Nevertheless, an estimate of the irreversible increase in stiffness for the development of the model shown in Chapter 3 was considered by using the findings of studies reviewed in this chapter for other glandular tissue, such the liver (Shi et al., 2015, Kiss et al., 2009, Sapin-de Brosses et al., 2010). According to these studies a likely irreversible increase in prostate stiffness might be between 3 and 6 times.

It is also important to remember that the biological state and the extent of the necrotic lesion will evolve with time after the treatment due to natural healing processes (Rouvière et al., 2007, Chaussy et al., 2013). This evolution will have an impact on the tissue stiffness value and its spatial distribution in the gland, which for now is unclear, therefore further investigation on this will be required.

The formation of the HIFU lesion in the prostate is on the order of a few seconds, for instance 3 seconds of exposure and 6 seconds of pause in the case of the Sonablate® system (Illing and Emberton, 2006), which is a short time to allow the monitoring of the creation of every single lesion by any potential monitoring technique. However, the build-up of the global ablated area can be monitored by localising and characterising individual HIFU lesions after their formation one after another. The time requirements of the TU-SWE technique for creating the image of

the lesion are still unknown. Further development and optimisation of the system must be achieved before moving into the clinical research stage.

2.3 Transurethral Shear Wave Elastography

The two most commonly employed elastography techniques for prostate imaging are the SE and the TR-SWE by the Aixplorer® system, which were described in Section 2.1. Both techniques are commercially available and implemented in clinical ultrasound imaging systems, and both use transrectal probes for imaging the prostate.

Major drawbacks in the diagnosis of prostate cancer when using SE and TR-SWE come from their intra- and inter-operator dependency, specifically in terms of the pressure applied over the gland from the rectal wall by the operator (Correas et al., 2013b). The nonlinear nature of the prostatic tissue produces variability in the measurements of the shear wave velocity in the case of SWE depending on the degree of precompression applied and creates artefacts in both SE and SWE images when exceeding certain level of precompression on the gland (Barr and Zhang, 2012). Additionally, uneven stress over the face of the transducer, stiff lesions within soft tissues and tissue mobility can also produce artefacts in SE (Dietrich et al., 2017). Artefacts in SWE can also show up from reflections originated by large variations of shear wave velocity, nevertheless, filtering methods for the direction of propagation are providing reduction of this type of artefacts (Lipman et al., 2016).

Although the full design and prototyping of the TU-SWE probe is beyond the scope of this work, it can be stated that the TU-SWE probe will be introduced through the urethra until reaching the prostatic urethra, then, a slight suction will be applied through uniformly distributed orifices along the surface of the probe thus ensuring a good uniform mechanical contact between probe and prostatic urethral wall. An example of this method for ensuring the mechanical contact between a transurethral probe and the prostate is detailed in the work of Chopra et al. (2009). Afterwards, the manipulation of the TU-SWE probe by the operator should be minimal, therefore reducing the operator-dependency of the imaging technique.

In addition to the above detailed drawbacks, current SE and TR-SWE devices

cannot be used for the monitoring of HIFU ablation of prostate cancer since SE and TR-SWE use the rectal passage to reach the position for imaging the prostate, the same channel that the HIFU probes use for delivering the treatment. In this case, TU-SWE presents a major advantage against SE and TR-SWE for monitoring HIFU treatment of prostate cancer since the probe will use the urethra channel for imaging the prostate leaving the rectal passage for the HIFU probe.

Furthermore, other inherent advantages of TU-SWE over other elastography techniques for prostate are apparent:

- The TZ and the CZ of the prostate (Figure 1.1) remain less accessible when using techniques that operate from the rectal passage. The urethral approach makes these zones more reachable. The TR-SWE studies are limited to the PZ (Figure 1.1) due to the difficulty of reaching the anterior zones of the prostate (Barr et al., 2012). In the case of SE, it has been found that the sensitivity of prostate cancer detection decreases when the prostate volume exceeds 50 ml (Miyagawa et al., 2009).

- The possibility of using higher frequencies, e.g. above 500 Hz, compared with other dynamic elastography techniques. This is due to the use of mechanical actuators as an excitation source. This type of source is not constrained by the ARF setting to maintain the thermal index under a safe threshold. Higher frequencies allow finer spatial resolution, thus enhancing the imaging quality and the capacity of detecting smaller lesions. In the case of TU-SWE, the upper limit of the frequency range will be determined by the attenuation of the medium and the sensitivity of the detecting elements.

- Due to the geometrical disposition of the emitters and receivers on the TU-SWE probe, the whole gland volume could be scanned simultaneously, providing the opportunity for 3D imaging (Figure 1.2). Current elastography techniques require several scans to cover the whole gland. Body movements can occur, thus complicating the creation of a true 3D geometry

reconstruction. For instance, TR-SWE by the Aixplorer® system covers only half the section of the prostate at every 2D scan. In the case of SE, although a complete 2D section of the prostate may be covered, there are problems with covering the whole gland due to the challenge of keeping the pressure constant at every scan.

- The probe could be designed to be flexible, thus producing less distortion and compression of the gland compared with transrectal approaches. This advantage would generate less imaging artefacts and would result in a more realistic geometry when mapping the desired mechanical parameters.

- In comparison with ARF techniques, lower levels of energy are expected, and therefore a lower thermal index.

Not a single medical imaging technique is without possible weaknesses. The main possible drawbacks of TU-SWE compared to SE and TR-SWE are listed below:

- The fact that the TU-SWE technique uses the urethra as the channel for introducing the probe could increase the risk of urinary infection if the probe is not properly sterilised. Moreover, the use of the urethra might be resisted by patients as it can be seen as a more invasive way of access compared with the rectal passage.

- The image reconstruction methods proposed for the TU-SWE technique (detailed in Chapter 5), use a forward model of the shear wave propagation in the prostate, which needs to be realistic and accurate in order to produce high quality image reconstructions.

- A slipping or incomplete mechanical contact between emitters and receivers and the prostate would impede the correct transmission and detection of shear waves.

Nevertheless, some improvements can be developed in order to reduce the effect of the enumerated disadvantages. For instance, the TU-SWE probe could be fabricated with affordable disposable attachments that would comprise the part of the probe in contact with the body of the patient, thus reducing the risk of urinary infection and allowing the use of the TU-SWE technique for diagnosis of prostate cancer in clinics, as opposed to a sterile operating theatre environment. The possible mechanical contact issue can be solved by the application of a slight suction through an uniform distribution of orifices on the surface of the probe. By applying suction the prostatic tissue will collapse onto the probe, thus ensuring the needed mechanical contact between probe and urethral wall in order to transmit and detect the shear waves (Chopra et al., 2009, Arani et al., 2011).

To the best of the author's knowledge, SWE for prostate by using the urethra as the excitation transmission channel has solely been investigated by one research group. Chopra et al. (2009) and Arani et al. (2011), among other articles from the same research group, evaluated the capability of transmitting shear waves into the prostate by mechanical contact through the urethral wall in phantoms and *in vivo* canine experiments. A longitudinal piezoceramic actuator connected to a 6.35 mm diameter micro-perforated solid brass rod was used as excitation source, thus generating cylindrical shear waves with particle displacement parallel to the bar axis, i.e. to the urethra. MRI elastography was used for measuring the amplitude of displacements, thus detecting regions in phantoms of elevated stiffness with diameter ranging from 5 mm to 15 mm. Chopra et al. (2009) and Arani et al. (2011) also obtained values of the shear modulus between 3.9 kPa and 8.0 kPa in *in vivo* canine experiments. Although results were encouraging, the group abandoned the idea in order to pursue the development of a transurethral ablation method, which resulted in the commercially available TULSA-PRO™ device.

The studies by Chopra et al. (2009) and Arani et al. (2011) support the idea of using the urethra as a channel of transmission for shear waves. However, there are features of the TU-SWE technique proposed here that makes it more

attractive. For instance, the fact that the TU-SWE concept does not require an external technique for sensing the shear waves makes it highly advantageous. In any case, investigation of the TU-SWE approach is needed. Furthermore, methods for solving the inverse problem and reconstruction of the features of the stiff lesions must also be developed.

2.4 Mechanical properties of the prostate

2.4.1 The elastic case simplification

It is common to consider soft tissues as an elastic media in commercial applications of elastography. Therefore, the frequency dependence of the elastic moduli is ignored, velocity dispersion effects are not considered and the group and phase velocities are assumed to be equivalent. This simplification has been accepted for most elastography applications, and can be considered valid as long as the spatial region to be analysed is small. The simplification allows the use of time-of-flight-based methods for measuring the group velocity.

Bearing in mind the above assumptions, large variations in values of the elastic modulus of the prostate are found in the literature. This is likely due to the strong dependence of the mechanical properties on the tissue condition, the frequency of excitation, the type of pathology, the measurement method and the experimental conditions (Sahebjavaher et al., 2013).

Among all the elastography techniques that provide quantitative elasticity results at present, TR-SWE by Aixplorer® is the most prolific in terms of the number of publications. Within the TR-SWE literature it is common to find elasticity represented by Young's modulus E. In order to obtain E, TR-SWE techniques first measure the velocity of propagation of the generated shear wave. Then, Equation 2.2 is used to calculate the shear elastic modulus G, after assuming that soft tissue may be locally considered as an isotropic, homogeneous and purely elastic medium for reduced volumes. Soft tissue is, in general, nearly incompressible as the Poisson's ratio ν is approximately 0.5. Therefore, E can be estimated as 3 times G according to Equation 2.1.

$$E = 2G(1+\nu) \tag{2.1}$$

$$G = \rho {c_s}^2 \tag{2.2}$$

Where ρ is the mass density and c_s is the shear wave velocity.

Table 2.1 shows Young's modulus values of prostatic tissues from *in vivo* elastography studies using TR-SWE by the Aixplorer® system. Whilst the frequencies of excitation are omitted, the frequency range is expected to be between 50 Hz and 450 Hz according to other TR-SWE publications (Tanter et al., 2008). Due to inconsistencies in the way in which these results were reported, these results should be interpreted with caution.

By analysing the results in Table 2.1, differentiation between benign and malignant tissue in terms of stiffness is not a trivial matter since ranges of values overlap. In order to discriminate malignant tissues from benign tissues using TR-SWE, Correas et al. (2015) and Barr et al. (2012) proposed Young's modulus thresholds of 35 and 37 kPa respectively. According to their conclusions, these thresholds provided additional criteria for prostate cancer detection and biopsy guidance, and enabled a substantial reduction in the number of biopsies. Additional studies are required for establishing a criterion for the appropriate elasticity thresholds to discriminate cancerous tissue from normal tissue and benign pathologies.

It can be seen in Table 2.1 that the values obtained by Ahmad et al. (2013) for both benign and cancerous tissue were around 2.5 times higher compared with those obtained in other studies also summarised in Table 2.1. In the case of benign tissue, these differences could be due to the fact that no effort was made to differentiate samples with a benign conditions from normal tissue samples. However, no satisfactory explanation for these differences could be found in the case of cancerous tissue. Significant evidence in terms of test protocols, number and condition of patients, etc. was not found. This variability reflects the need for further multicentre studies on a large number of samples.

In addition to the results shown in Table 2.1, Barr et al. (2012) carried out a study involving 53 patients where the stiffness values of normal tissue,

Table 2.1: Young's modulus values (mean ± SD) of *in vivo* prostatic tissue by using TR-SWE.

Reference	Quantitative results: E (kPa)	
(Woo et al., 2014)	Normal tissue: 33.2 ± 16.7	Cancerous tissue: 54.6 ± 46.0
(Zhang et al., 2013a)	PZ normal tissue: 24.1 ± 4.9	TZ with BPH: 32.2 ± 5.9
(Barr et al., 2012)	Normal tissue: 21.2 ± 11.8	Cancerous tissue: 58.0 ± 20.7
(Correas et al., 2011)	PZ normal tissue: 18.0 ± 9.0	Cancerous tissue: 55.0 ± 45.0
(Ahmad et al., 2013)	Benign tissue †: 74.9 ± 47.3	Cancerous tissue: 133.7 ± 57.6

†According to Ahmad et al. (2013) benign tissue terminology comprises normal tissue and other benign pathologies, namely atrophic parenchyma, acute and chronic inflammation.

referred to as benign tissue in the publication, were analysed. Whilst several benign conditions were considered, i.e. atypia, acute inflammation and chronic inflammation (see Table 2.2), the authors did not mention the BPH condition of the patient. However, it is possible that BPH may have been implicit under the label of "chronic inflammation". Although chronic inflammation resulted in higher tissue stiffness than normal tissue, the authors declared that this result was not statistically significant. The remainder of the benign conditions exhibited similar mean values of stiffness to normal tissue. The fact that stiffness values of tissues with benign conditions fall within, or are close to, the normal tissue stiffness range, and do not fall within the range of malignant tissue, is encouraging in terms of reducing the number of false positive results in prostate cancer diagnosis when using elastography.

Zheng et al. (2012) presented an *in vivo* study on 107 patients, using pSWE for measuring the shear wave velocity of three types of prostatic tissue: normal, BPH

Table 2.2: Reproduction of Young's modulus values (mean ± SD) obtained from *in vivo* prostatic tissue using TR-SWE by Barr et al. (2012).

Reference	Pathological tissue type	Quantitative results: E (kPa)
(Barr et al., 2012)	Normal (benign) tissue	21.2 ± 11.8
	Atypia	20.6 ± 4.9
	Cancer	58.0 ± 20.7
	Acute inflammation	19.5 ± 5.5
	Chronic inflammation	27.3 ± 15.5

and cancer. The authours obtained good discrimination between prostate cancer and BPH. Although stiffness contrast ratio between the different tissue types were in agreement with Barr et al. (2012) (around 1.8 between BPH and normal tissue and 3.0 between cancerous and normal tissue) absolute stiffness values were near 50% lower compared with those provided by Barr et al. (2012). (Equation 2.2 was used for making the comparison). These differences could be due to the use of different techniques for measuring the velocity of shear waves. In the case of Zheng et al. (2012) a pSWE technique by Virtual Touch™ Quantification was used, whilst TR-SWE by Aixplorer® was used in the case of Barr et al. (2012) and the remainder of studies shown in Table 2.1. No studies comparing both techniques were found at the date of this thesis.

Regarding the zonal division of prostate, the PZ and TZ in normal samples were found to have similar values of stiffness, while the CZ tended to be stiffer. A stiffness contrast ratio of 1.8 between CZ and PZ/TZ was observed by Zhai et al. (2010a,b) in *ex vivo* prostates using ARFI imaging by Virtual Touch™ Imaging.

Other investigations focused on the search of correlation between stiffness and the Gleason score of tumours. The Gleason score is a grading system (from 2 to 10) used to evaluate the prognosis of men with prostate cancer. The higher the score, the more aggressive the tumour. Correas et al. (2015) identified that prostate

cancer elasticity values could be matched with Gleason score results and appeared linked to cancer aggressiveness, especially for elevated Gleason scores (≥ 7). Woo et al. (2014) observed that aggressive prostate cancer showed significantly higher values of stiffness than indolent prostate cancer, and this correlation followed a linear trend. On the other hand, Ahmad et al. (2013) could not find a statistical correlation. Nonetheless, the authors admitted that further studies involving a larger number of cases should be addressed for statistical relevance.

2.4.2 Viscoelasticity of the prostate

Soft tissue is well known for behaving as a viscoelastic medium. Viscosity has important effects on wave propagation, increasing attenuation and generating frequency dispersion. Shear wave dispersion properties have been gaining interest in the medical community for the additional characterisation of pathologies that they may provide (Holm and Sinkus, 2010). Some examples of elastography studies that have included the effects of viscosity when modelling shear wave propagation can be found in Taylor et al. (2001), Bercoff et al. (2004c) and Caenen et al. (2015).

The mechanical response of soft tissue is generally represented by rheological models comprising combinations of springs and dashpots. Apart from the three basic linear viscoelastic models (Maxwell, Kelvin-Voigt and Zener), other linear, quasi-linear or nonlinear models have also been employed to describe the mechanical behaviour of soft tissue. In the case of the prostate, the Kelvin-Voigt (KV) is the most used. The KV model is typically represented as a parallel arrangement of a spring and a dashpot. One other rheological model is recently gaining interest, the fractional derivative generalisation of the KV model, the Kelvin-Voigt Fractional Derivative (KVFD). The KVFD model consists of a similar arrangement whereby the dashpot is replaced by a fractional element commonly named spring-pot (Grzesikiewicz et al., 2013). The schematic representation of the two models is shown in Figure 2.2, where μ is the elastic component, η is the

viscous component and α the order of the fractional derivative. Further discussion on the KVFD is provided later in Section 3.1.2.

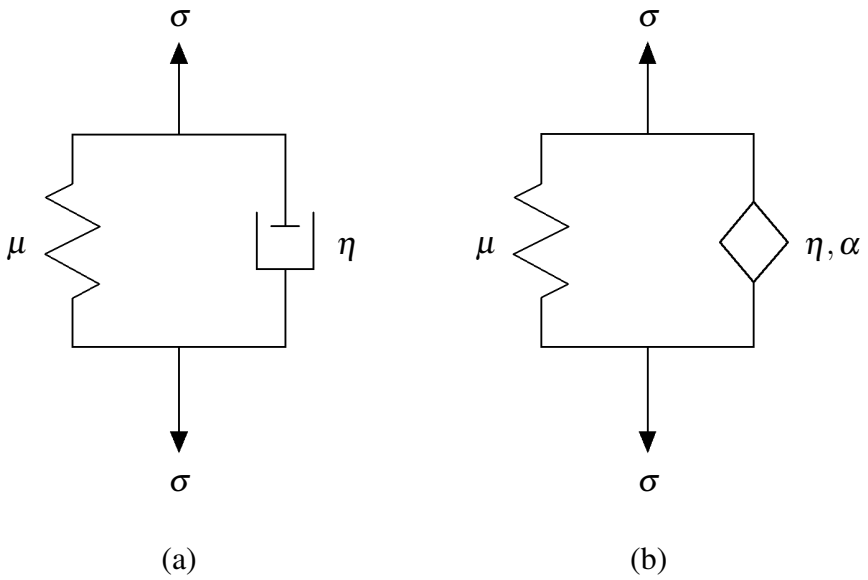

Figure 2.2: (a) Schematic representation of the KV rheological model as a combination of a spring in parallel with a dashpot. (b) Schematic representation of the KVFD rheological model. The dashpot of the KV model is replaced by a fractional element of order α, commonly named spring-pot.

The stress on the dashpot is equal to the fractional derivative of order α of strain. This means that when $\alpha = 0$, the fractional element acts as a spring and the model becomes purely elastic, whilst when $\alpha = 1$, the fractional element works as a perfect dashpot and the model becomes a KV model. Considering this relation between models, the complex shear and Young's moduli according to both models can be expressed as Equations 2.3 and 2.4. For convenience and consistency of symbols throughout this thesis, the parameters of the complex shear modulus have not been expressed with subscripts unlike the parameters of the complex Young's modulus.

$$G^*(\omega) = \mu + \eta(i\omega)^\alpha \tag{2.3}$$

$$E^*(\omega) = E_0 + \eta_E (i\omega)^{\alpha_E} \tag{2.4}$$

Where, E_0, η_E and α_E are the elastic parameter, the viscous parameter and the order of the fractional derivative associated to the complex Young's modulus.

Mitri et al. (2011) used the KV model to characterise *ex vivo* prostatic tissue. Shear wave velocity data from SDUV experiments were fitted using the KV model for obtaining the values of the KV shear parameters for frequencies between 50 and 400 kHz (see Table 2.3). No distinction in terms of pathological condition was applied. These data prove the viscoelastic nature of the properties of prostatic tissue. The data were obtained by fitting a KV law, a singular case of a more generalised law, the KVFD constitutive law. These data were not directly used for developing the wave propagation model for the study of the TU-SWE technique since a KVFD constitutive law was chosen for such a purpose. Further details on this will be shown in Chapter 3.

Table 2.3: Viscoelastic parameters of *ex vivo* prostatic tissue using KV as rheological model

Reference	Method	Frequency of excitation	Quantitative results	
			μ (kPa) †	η (Pa·s) ‡
(Mitri et al., 2011)	SDUV	50 - 400 Hz	Whole prostate, no distinction regarding tissue pathological conditions	
			1.31 - 12.81	1.10 - 6.82

†Shear elastic modulus according KV model
‡Shear viscosity according KV model

Zhang et al. (2008) and Hoyt et al. (2008) used the KVFD for measuring the variation of the complex Young's modulus E^* between normal and cancerous prostatic tissue.

Zhang et al. (2008) extracted the complex Young's modulus by fitting data from a Dynamic Mechanical Analysis (DMA) test to a KVFD model (see Table

2.4). The DMA was a non constrained compressional stress relaxation test. Contrast ratios from 2.6 and 2.8 were obtained for the absolute value of the complex Young's modulus between cancerous and normal tissue.

Hoyt et al. (2008) carried out a comparative study between CWS and the same DMA test used by Zhang et al. (2008) for two samples of a human excised prostate. Results showed relative similarities between techniques with errors below 12%. In any case, the sample sizes were too small to be statistically significant, specially in the study by Hoyt et al. (2008).

Table 2.4: KVFD parameters for the complex Young's modulus E^* of *ex vivo* prostatic tissue.

Reference	Method	KVFD E^* parameter †	Quantitative results	
			Normal tissue	Prostate cancer
(Zhang et al., 2008)	DMA	η_E (kPa·s^α) ‡	3.61 ± 1.25	8.65 ± 3.40
		α_E ‡	0.215 ± 0.042	0.225 ± 0.03

†The elastic parameter E_0 of the KVFD complex Young's modulus was not included in the table because fitting results provided values approaching zero.
‡N.B. that in this case, η and α refer to the complex Young's modulus (E^*), and not to the complex shear modulus (G^*).

The published data in the studies of Zhang et al. (2008) and Hoyt et al. (2008) were obtained by fitting a KVFD constitutive law, however, the mechanical parameter analysed was the Young's modulus, therefore these data could not be directly used for the development of the wave propagation model for TU-SWE, where the required mechanical parameters are related to the shear modulus.

As can be observed, very little literature concerning the viscoelastic characterisation of human prostatic tissue is available. Furthermore, no studies regarding the characterisation of the shear KVFD parameters of prostatic tissue were found. Further studies are required in this topic if accurate viscoelastic models for elastography, and particularly TU-SWE, are needed.

2.5 Discussion and conclusion

In the literature reviewed in this chapter it has been proven that elastography shows great potential for detecting stiff areas within the prostate. These stiff areas can be associated with cancer, thus making elastography an affordable potential alternative to MR-based techniques for the diagnosis of prostate cancer.

Numerous elastography techniques have been proposed for imaging the prostate, among them, the two techniques most employed are SE and TR-SWE (or simply called SWE). Both techniques have been demonstrated to improve the sensitivity and specificity of detection of prostate cancer, when used in addition to conventional ultrasound during prostate biopsy (Good et al., 2014, Correas et al., 2013b). However, both techniques have limitations in terms of operator dependency, mainly due to the level of pre-compression applied manually by the operator, which produces artefacts and no consistent measurements of shear wave velocity (Barr and Zhang, 2012, Dietrich et al., 2017).

In this thesis, a new elastography technique called TU-SWE has been proposed for the diagnosis of prostate cancer. The technique uses the urethra channel for imaging the prostate. It is believed that the TU-SWE technique will have a lower operator dependency since the probe will not need to be held by the operator over the imaging process. Some other possible advantages of TU-SWE against SE and TR-SWE are detailed in Section 2.3, such as the capacity of scanning the whole gland simultaneously and an expected low thermal index. Nonetheless, the main advantage of the TU-SWE technique is the possibility of monitoring transrectal thermal ablation treatments of prostate cancer, which is not possible with current SE and TR-SWE devices.

Quantitative elastography of prostate, such TR-SWE, provides local values of elasticity of the gland. The mechanical behaviour of the tissue when using commercial quantitative elastography techniques is considered purely elastic, which allows the elastic moduli (Young's modulus or shear modulus) to be obtained by

using simple expressions (see Equations 2.1 and 2.2). Although the consideration of pure elasticity for soft tissue for measuring elastic properties is widely used and accepted, the real response of soft tissues is viscoelastic. One of the most commonly employed viscoelastic models in soft tissue is the KV law, which is a particular case of a more generalised constitutive law, the KVFD. In this thesis, a KVFD constitutive law was chosen for developing a wave propagation model for the TU-SWE. Details on this will be shown in Chapter 3.

A review of the characterisation of the shear properties of prostatic tissue with different conditions (normal, cancerous, BPH, etc) was carried out. Most of the published data were obtained by considering the elastic assumption, as expected. Only three studies that considered the viscoelastic behaviour of prostate were found: (Mitri et al., 2011, Zhang et al., 2008, Hoyt et al., 2008). These studies proved the viscoelastic behaviour of prostatic tissue. Unfortunately, none of these studies provided useful relevant data for the development of the wave propagation model for TU-SWE. In the case of the study carried out by Mitri et al. (2011), the viscoelastic law employed was the KV. In the case of the other two studies (Zhang et al., 2008, Hoyt et al., 2008) the obtained KVFD mechanical parameters were related to Young's modulus, which is not totally useful for the TU-SWE wave propagation model, since in principle, there is not a direct known relationship between the three KVFD parameters of the Young's modulus (E_0, η_E and α_E) and the corresponding KVFD parameters of the shear modulus (μ, η and α). Due to the lack of relevant data for the development of the wave propagation model for TU-SWE, a range of possible values were proposed based on experimental results and calculations from several studies reviewed in this chapter. Further detail on this will be shown in Chapter 3.

2.6 Chapter summary

Overall, this chapter was dedicated to reviewing all of the fundamental literature concerning the use of elastography for prostate cancer diagnosis and measuring the elasticity of prostatic tissue.

Literature about elastography applications for prostate cancer diagnosis was analysed. There are several elastography techniques used for this purpose in the prostate. The two more widely used techniques in commercially available systems are SE and TR-SWE. In general terms, many studies concluded that the use of elastography for targeted biopsies can improve the efficacy of the diagnosis of prostate cancer. However, larger multicentre studies are needed in order to obtain conclusive results.

Literature about the monitoring of HIFU thermal ablation in the prostate and other tissues was also reviewed. Thermal ablation elevates tissue stiffness due to the denaturation of collagen fibres. This change in stiffness demonstrates the potential for elastography to play a key role in monitoring and assessing thermal therapies. Furthermore, stiffness may also be used as a thermal damage marker. The large number of recent publications in this topic suggests that it is of rapidly increasing interest.

A comparative analysis of the expected inherent advantages of the TU-SWE concept and the reviewed elastography techniques was presented.

Finally, literature concerning elasticity of prostatic tissue and pathological conditions was reviewed. Although it seems clear that malignant prostatic tissue experiences higher stiffness compared to benign tissue, further studies are necessary in order to establish an appropriate criterion concerning values of elasticity thresholds to discriminate malignant from benign tissue. In addition, it was shown that the prostate, as with most soft tissues, behaves viscoelastically. However, very little literature is available on this topic, hence requiring further investigation on more realistic mechanical models.

Chapter 3

A numerical model for shear wave propagation in the prostate

From a physical perspective, the TU-SWE technique is based on the transurethral transmission and detection of transient shear waves travelling throughout the prostate. Shear waves are mechanical disturbances where the particles of the medium oscillate perpendicularly to the propagation path. As mechanical waves, they interact with the mechanics of tissue and its spatial variability. Due to the complexity of the problem, numerical methods are normally used for solving the equations of wave propagation.

This chapter describes the development of a 2D numerical model for shear wave propagation in prostate-like media according to the TU-SWE approach. A brief literature review is also carried out in order to select the required tools for developing the model.

3.1 Mechanical wave equations in soft tissue

The equations that govern the propagation of mechanical waves are well known. They are usually represented as Partial Differential Equations (PDE) where the unknown function is the displacement field of particles within the medium. The most common example of this is the classical Navier equation for mechanical waves in an isotropic elastic solid medium (Graff, 1991), in vector notation:

$$\rho \frac{\partial^2 \mathbf{u}}{\partial t^2} = (\lambda + \mu) \nabla (\nabla \cdot \mathbf{u}) + \mu \nabla^2 \mathbf{u} + \mathbf{f} \tag{3.1}$$

where ρ is the local density of the medium, $\mathbf{u}$ is the vector of displacements, λ and μ are the first and second Lamé's parameter respectively and $\mathbf{f}$ is the external body force vector. μ is also known as the shear modulus.

It can be demonstrated that Equation 3.1 can be obtained by combining three different types of equations: linear momentum conservation (Equation 3.2), the strain-displacement linear relationship (Equation 3.3) and the constitutive law (also known as the material law or rheological law) for an elastic medium (Equation 3.4). The following index notation will be hereinafter used.

$$\frac{\partial^2 u_i}{\partial t^2} = \frac{\partial^2 \sigma_{ij}}{\partial x_j} + f_i \tag{3.2}$$

$$\varepsilon_{ij} = \frac{1}{2} \left(\frac{\partial u_j}{\partial x_i} + \frac{\partial u_i}{\partial x_j} \right) \tag{3.3}$$

$$\sigma_{ij} = \lambda \delta_{ij} \varepsilon_{kk} + 2\mu \varepsilon_{ij} \tag{3.4}$$

where i, j are the index components, u is the displacement field, σ is the stress tensor, x represents the spatial variables, f is the external body force, ε is the strain tensor, and δ is the Kronecker delta.

However, soft tissues are viscoelastic media, implying that the mechanical response of tissue will be viscoelastic. Therefore, the elastic constitutive law

(Equation 3.4) is not suitable and viscoelastic laws are required.

3.1.1 Kelvin-Voigt model

As mentioned in Chapter 2, one of the most used viscoelastic constitutive laws for modelling transient shear wave propagation in tissue is the KV model.

Bercoff et al. (2004c) derived an analytical formulation using the Green's function for the viscoelastic KV version of the Navier's equation. The formulation was used to numerically calculate the shear wave propagation field generated by ARF. The model was proved to be valid for the near field. However, for distances larger than a shear wavelength, the experimentally observed attenuation values were inconsistent with the theoretically predicted attenuation using KV. According to the authors, this discrepancy was due to the omission of some viscous terms in the analytical solution. This simplification made viscosity to solely affect the wave amplitude, but not the wave velocity. This means that the method was unable to model the velocity dispersion due to viscosity (Bercoff et al., 2004b). It seems clear that the proposed technique by Bercoff et al. (2004c) is not suitable for the TU-SWE approach, due to the fact that the TU-SWE technique requires the modelling of long propagation paths. Further developments of the initial model were proposed. Most recent examples involve an extension for transversally anisotropic viscoelastic media (Chatelin et al., 2015), and a correction to take into account the wave diffraction (Budelli et al., 2017).

Other examples of the use of the KV model can be found in Orescanin et al. (2011). The authors modelled the wave propagation generated by a needle vibrating in soft tissue-like media, with the aim of imaging stiff areas within tissue-like phantoms. A Finite-Difference Time Domain (FDTD) method was used to solve the wave equation, assuming a KV constitutive law. The system of equations was simplified by neglecting all the normal components and solely leaving the deviatoric (shear) components. According to the authors, the simplification did not seem to

affect the results, due the low level of normal pressure generated by the vibrating needle.

3.1.2 Kelvin-Voigt Fractional Derivative model

Many studies have suggested the use of the KVFD constitutive law to model shear wave propagation in elastography.

It is well known that absorption for both compressional and shear waves often follows a power law as expressed in Equation 3.5 (Holm and Sinkus, 2010):

$$\alpha_k(\omega) = \alpha_0 \omega^y \tag{3.5}$$

where $\alpha_k(\omega)$ is the absorption law as a function of frequency, α_0 is the absorption coefficient at a linear frequency $f = 1/(2\pi)$, ω is the angular frequency and y is the power law exponent. The subscript k is used to differentiate it from the order of the fractional derivative α that is used later in this section (k denotes that α_k is the imaginary part of the complex wavenumber k^*).

The classical integer order wave equations can only model limited values of exponents for power-law absorption (Chen and Holm, 2003). The KV wave equation models absorption with $y = 2$ for the low-frequency region, and $y = 0.5$ for the high-frequency region. Fractional order wave equations have been proved to fill these gaps and produce models that fit well experimental absorption laws with variable values between 0 and 2 (Holm and Näsholm, 2011). In addition, Holm and Näsholm (2014) demonstrated that some of the most used fractional wave equations, such as the fractional Szabo equation and the fractional Laplacian wave equation, are low-frequency approximations of the KVFD, and the more general fractional Zener wave equation. Some examples for modelling wave propagation in biological applications using the KVFD can be seen in the studies by Caputo et al. (2011) and Zhang and Holm (2016).

Caputo et al. (2011) developed a numerical algorithm based on FDTD for

modelling compressional wave propagation in biological applications, assuming a KVFD constitutive law. The model was successfully tested obtaining good agreement with an analytical solution in a homogeneous breast fatty tissue-like medium. Zhang and Holm (2016) used a time fractional wave equation to simulate the shear wave propagation in different viscoelastic media generated by ARF. The authors estimated the stiffness by using a time-to-peak technique, as it is done in SWE. The results showed that the technique worked well in lossless media or in media with small losses. However, in the case of highly lossy media the time-to-peak technique produced biased estimations.

Fractional models for mechanical wave propagation were initially motivated by a requirement to match experimentally observed attenuation. However, as it is obvious, the models must also be able to correctly model the viscous dispersive effects. Amador et al. (2015) used a KVFD model to successfully fit shear wave dispersion curves from *in vitro* tests using SWE and the so-called Hyper-Frequency Viscoelastic Spectroscopy (HFVS) (HFVS is an advanced rheological characterisation technique involving frequencies up to 2 kHz). Interestingly, it has been proven that in some cases, fractional models better model dispersion effects compared with their homologous integer counterpart models. Examples of this can be seen in the experimental *ex vivo* canine liver work by Kiss et al. (2004) and in the *in vivo* MR elastography studies in human liver and brain by Klatt et al. (2007).

In this thesis, a KVFD model was chosen for implementation into the wave propagation model as the constitutive law. This was due to its ability to accurately model absorption and dispersive effects, based on the results from the literature reviewed. KVFD equations are shown in detail in Section 3.2.

3.2 Model geometry and equations

A simplified prostate-like medium was geometrically modelled as a solid cylinder containing a coaxial straight urethra-like conduit. Following the TU-SWE concept, an oscillatory rotational disk was placed into the urethra in contact with the urethral wall as an emitter (Figure 3.1). Note that the number of emitters can vary.

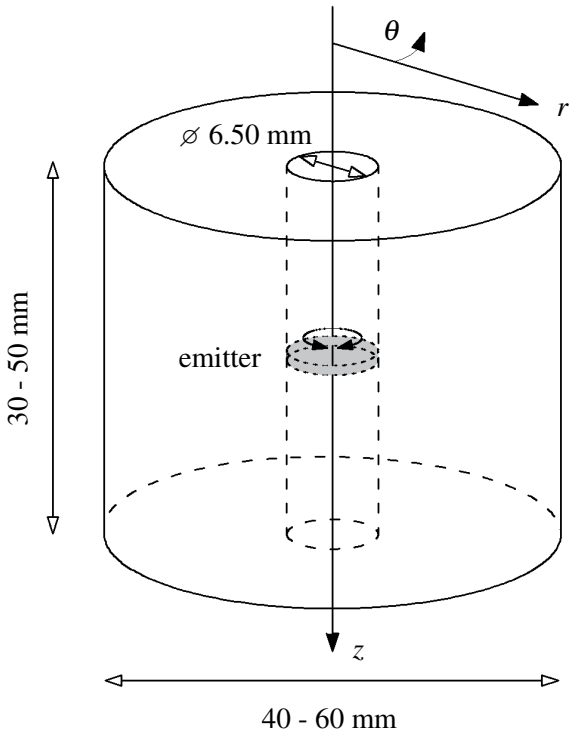

Figure 3.1: Geometrical arrangement for the wave propagation model in a prostate-like medium. Dimensions according to the size of real human prostate. The oscillatory rotational emitter (in grey colour) is placed at a middle height into the urethra. A cylindrical system of coordinates is shown.

The dimension ranges were chosen according to the expected size of human prostates with pathological conditions (Zhang et al., 2013b, Eri et al., 2002). It is well-known that the diameter of the human male urethra is variable along the luminal length (from 4 mm to 10 mm, approximately). However, in this thesis, the

diameter was fixed at 6.50 mm along the whole urethra-like conduit length. Similar values have been used in previous experimental studies using transurethral actuators (Chopra et al., 2009, Arani et al., 2011).

The geometrical arrangement allows the use of a cylindrical coordinate system (r,θ,z). The distribution of stresses and strains on an infinitesimal cylindrical element is shown in Figure 3.2.

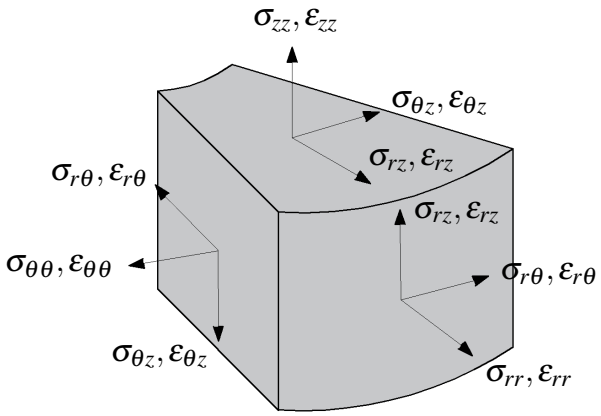

Figure 3.2: Infinitesimal element according to a cylindrical coordinate system (r,θ,z). Representation of stresses (σ) and strains (ε).

The conservation of momentum equations in cylindrical coordinates are as follows (see also Figure 3.2).

$$\frac{\partial^2 u_r}{\partial t^2} = \frac{\partial \sigma_{rr}}{\partial r} + \frac{1}{r}\frac{\partial \sigma_{r\theta}}{\partial \theta} + \frac{\partial \sigma_{rz}}{\partial z} + \frac{1}{r}(\sigma_{rr} - \sigma_{\theta\theta}) + f_r \tag{3.6}$$

$$\frac{\partial^2 u_\theta}{\partial t^2} = \frac{\partial \sigma_{r\theta}}{\partial r} + \frac{1}{r}\frac{\partial \sigma_{\theta\theta}}{\partial \theta} + \frac{\partial \sigma_{\theta z}}{\partial z} + \frac{2}{r}\sigma_{r\theta} + f_\theta \tag{3.7}$$

$$\frac{\partial^2 u_z}{\partial t^2} = \frac{\partial \sigma_{rz}}{\partial r} + \frac{1}{r}\frac{\partial \sigma_{\theta z}}{\partial \theta} + \frac{\partial \sigma_{zz}}{\partial z} + \frac{1}{r}\sigma_{rz} + f_z \tag{3.8}$$

The strain-displacement relationships are as follows (see also Figure 3.2):

$$\varepsilon_{rr} = \frac{\partial u_r}{\partial r} \tag{3.9}$$

$$\varepsilon_{\theta\theta} = \frac{1}{r}\frac{\partial u_\theta}{\partial \theta} + \frac{u_r}{r} \tag{3.10}$$

$$\varepsilon_{zz} = \frac{\partial u_z}{\partial z} \tag{3.11}$$

$$\varepsilon_{r\theta} = \frac{1}{2}\left(\frac{1}{r}\frac{\partial u_r}{\partial \theta} + \frac{\partial u_\theta}{\partial r} - \frac{u_\theta}{r}\right) \tag{3.12}$$

$$\varepsilon_{rz} = \frac{1}{2}\left(\frac{\partial u_z}{\partial r} + \frac{\partial u_r}{\partial z}\right) \tag{3.13}$$

$$\varepsilon_{\theta z} = \frac{1}{2}\left(\frac{\partial u_\theta}{\partial z} + \frac{1}{r}\frac{\partial u_z}{\partial \theta}\right) \tag{3.14}$$

And the KVFD constitutive law for a linear viscoelastic medium:

$$\sigma_{rr} = \left(\lambda + \eta_p \frac{\partial^{\alpha_p}}{\partial t^{\alpha_p}}\right)(\varepsilon_{rr} + \varepsilon_{\theta\theta} + \varepsilon_{zz}) + 2\left(\mu + \eta_s \frac{\partial^{\alpha}}{\partial t^{\alpha}}\right)\varepsilon_{rr} \tag{3.15}$$

$$\sigma_{\theta\theta} = \left(\lambda + \eta_p \frac{\partial^{\alpha_p}}{\partial t^{\alpha_p}}\right)(\varepsilon_{rr} + \varepsilon_{\theta\theta} + \varepsilon_{zz}) + 2\left(\mu + \eta_s \frac{\partial^{\alpha}}{\partial t^{\alpha}}\right)\varepsilon_{\theta\theta} \tag{3.16}$$

$$\sigma_{zz} = \left(\lambda + \eta_p \frac{\partial^{\alpha_p}}{\partial t^{\alpha_p}}\right)(\varepsilon_{rr} + \varepsilon_{\theta\theta} + \varepsilon_{zz}) + 2\left(\mu + \eta_s \frac{\partial^{\alpha}}{\partial t^{\alpha}}\right)\varepsilon_{zz} \tag{3.17}$$

$$\sigma_{r\theta} = 2\left(\mu + \eta_s \frac{\partial^{\alpha}}{\partial t^{\alpha}}\right)\varepsilon_{r\theta} \tag{3.18}$$

$$\sigma_{rz} = 2\left(\mu + \eta_s \frac{\partial^{\alpha}}{\partial t^{\alpha}}\right)\varepsilon_{rz} \tag{3.19}$$

$$\sigma_{\theta z} = 2\left(\mu + \eta_s \frac{\partial^{\alpha}}{\partial t^{\alpha}}\right)\varepsilon_{\theta z} \tag{3.20}$$

where, λ is the first Lamé's parameter at zero frequency, η_p is the bulk KVFD viscous parameter, α and α_p is the order of the fractional derivative for the deviatoric and normal components of the equation respectively, μ is the shear modulus at zero frequency, and η_s is the shear KVFD viscous parameter. The range for α is between 0 and 2, but mostly, it is less than 1 for elastography (Zhang and Holm, 2016).

The shear waves according to the TU-SWE technique follow a pseudo-spherical propagation pattern. Moreover, the interaction of the pseudo-spherical wave with

the different areas of the prostate will produce reflection and refraction, which also will be propagating in a 3D space. Therefore, a 3D model of the wave propagation will be required. Nevertheless, one of the principal aims of this thesis is the preliminary evaluation of the feasibility of the TU-SWE technique, and that requires solving the inverse problem associated with the TU-SWE technique. In this thesis, image reconstruction methods based on forward modelling were used to solve the inverse problem (these methods will be described in detail in Chapter 5). Fast forward models are preferred since a significant number of iterations of the forward simulations are needed. 3D models are highly computationally expensive. For this reason, 2D simplifications are greatly beneficial for preliminary studies while keeping most of the physics unaltered. In this case, absolute axial symmetry was taken into account in order to simplify the geometry to a 2D case. The wavefront generated by an oscillatory rotational source is propagated axisymmetrically in a pseudo-spherical distribution (see emitter in Figure 3.1). This fact, together with the axisymmetric geometry of the model, produces a reduction in the displacement field to only one component, the angular displacement u_θ (Expressions 3.21). Besides, all of the derivatives regarding the variable θ will be zero.

$$u_r = 0; \quad u_\theta = u_\theta(r,z,t); \quad u_z = 0; \tag{3.21}$$

An r-z plane was selected as the 2D domain for developing the wave propagation model (see the red dashed contour in Figure 3.3). Obviously, any stiff inclusion in the 2D geometry model is translated to the 3D space as toroidal shapes. Although toroidal geometries are not representative of prostate tumours or HIFU lesions, they were considered acceptable for the initial stage of development of the model.

Therefore, after applying the aforementioned axisymmetric simplification, and neglecting the external forces, the system of equations of conservation of momentum was reduced to Equation 3.22, the strain-displacement relationships

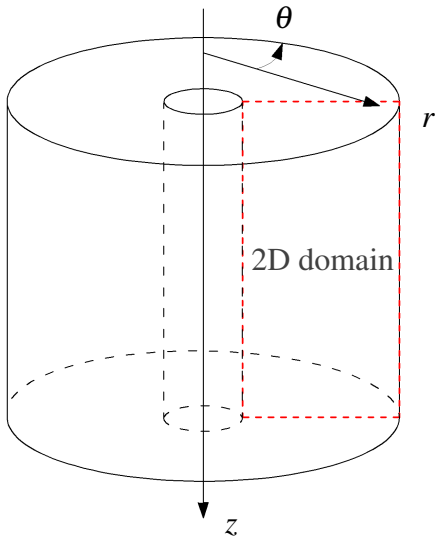

Figure 3.3: From the 3D model to a 2D model in cylindrical coordinates. 2D section contour in red dashed line.

were reduced to Equations 3.23 and 3.24, and the KVFD constitutive law was reduced to equations 3.18 and 3.20.

$$\frac{\partial^2 u_\theta}{\partial t^2} = \frac{\partial \sigma_{r\theta}}{\partial r} + \frac{\partial \sigma_{\theta z}}{\partial z} + \frac{2}{r}\sigma_{r\theta} \tag{3.22}$$

$$\varepsilon_{r\theta} = \frac{1}{2}\left(\frac{\partial u_\theta}{\partial r} - \frac{u_\theta}{r}\right) \tag{3.23}$$

$$\varepsilon_{\theta z} = \frac{1}{2}\frac{\partial u_\theta}{\partial z} \tag{3.24}$$

The boundary conditions of the problem were the excitation source at certain points in the urethral wall (Expression 3.25) and the absence of shear stress on the rest of the urethral wall as a free boundary (Expression 3.26).

$$u_\theta\left(r_{\text{urethral\_wall}}, z_{\text{emitter}}, t\right) = u_{\theta,\,\text{excitation}}\left(t\right) \tag{3.25}$$

$$\sigma_{r\theta}\left(r_{\text{urethral\_wall}}, z_{\text{no\_emitter}}, t\right) = 0 \tag{3.26}$$

The value of the KVFD parameters (μ, η_s and α) depended on the condition

of the tissue: normal, cancerous or thermally ablated tissue. Details are provided later in Section 3.4. For convenience, the KVFD shear viscous parameter will be hereinafter denoted as a simple η.

3.3 Numerical method

Numerical methods are predominantly used to solve equations of physical phenomena when analytical methods are either impractical or impossible to obtain. In addition, the fast development of high performance computing system, combined with the decrease in computing cost, is favouring the broad use of numerical methods for solving all types of physical problems. Nowadays, the two most popular numerical techniques for simulating wave propagation phenomena are the Finite Difference (FD) method and the Finite Element Method (FEM).

3.3.1 Finite Difference Time Domain method

In this thesis, a FDTD technique was chosen to model the propagation of shear waves according the TU-SWE approach. FDTD is a FD method developed in the time domain. The choice was made from a practical point of view, after considering that a 2D FDTD algorithm offers simplicity, speed and flexibility for implementing a singular constitutive law such as the KVFD model. The time domain was preferred due to the transient nature of the wave propagation.

The FD method is based on the standard definition of the derivative in elementary calculus. For fine discretisation of the domain, derivatives can be approximated by their discrete definition. The FDTD method was first introduced by Yee (1966) to discretise the differential Maxwells equations in isotropic media. The algorithm was applied for the first time to elastic equations by Madariaga (1976).

3.3.2 Space-time grid discretisation

Gomez et al. (2016) developed an FDTD elastic wave propagation model using a velocity-stress formulation adapted from a previous work by Virieux (1986). This

approach reduced the amount of time derivatives, and therefore the computational overhead. However, in this case, the displacement field must be stored as a requirement for the successful implementation of one of the reconstruction methods detailed later in Chapter 5 (see Subsection 5.2.1). For this reason, a displacement-stress formulation, composed by Equations 3.18, 3.20, 3.22, 3.23 and 3.24, was chosen. Strain-displacement relationship equations (Equations 3.23 and 3.24) were fused into the KVFD constitutive equations (Equations 3.18 and 3.20), thus reducing the memory required for computing the algorithm.

Spatial discretisation was achieved using the staggered grid illustrated in Figure 3.4 (Gomez et al., 2016). The displacement component is placed at grid positions that are offset by a half-step from the corresponding stress and strain components. Space was uniformly sampled, with $r = i\Delta r/2$ and $z = j\Delta z/2$ for integers i, j and space step of discretisation Δr and Δz.

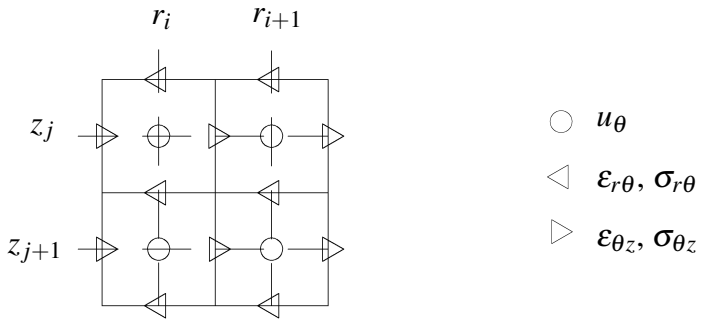

Figure 3.4: Staggered grid discretisation showing the locations of variables: displacements (u_θ), stresses ($\sigma_{r\theta}$, $\sigma_{\theta z}$) and strains ($\varepsilon_{r\theta}$, $\varepsilon_{\theta z}$).

The classical time-staggering approach is often used in FDTD literature to discretise variables in time. This means that stress and strain components are calculated in a half-step time instant from the corresponding time instant of the displacements. However, in this case, an alternative method was chosen based on the work of Orescanin et al. (2011). All stress, strain and displacement components are computed at the same time interval, thus providing verifiable magnitudes at each time step. Time was uniformly sampled via $t = n\Delta t$ for an integer n and a time step

Δt.

Medium properties, such as density and KVFD viscoelastic parameters, were introduced into the model by setting their values at the grid cells of the discretised space domain.

3.3.3 Approximation of derivatives

In order to apply the FD method to the system of equations (Equations 3.18, 3.20, 3.22, 3.23 and 3.24), the expressions 3.27, 3.28, 3.29 and 3.30 were used. These expressions are derived from Taylor series expansions and details can be found in basic FD literature.

The centred finite difference scheme was chosen for derivatives with respect to one of the spatial variables. In this case, the staggered grid produces a second order approximation of the derivative:

$$\left.\frac{\partial g(x,t)}{\partial x}\right|_{x_i,t_n} = \frac{g\left(x_{i+\frac{1}{2}},t_n\right) - g\left(x_{i-\frac{1}{2}},t_n\right)}{\Delta x} + O\left(\Delta x^2\right) \tag{3.27}$$

Where g is an arbitrary differentiable function within the domain of interest, x represents one of the spatial variables r and z, t represents time, and Δx is one of the spatial steps used for the spatial discretisation.

For first and second order time derivatives, backward finite differences were chosen, since during the computation, future states are unknown.

$$\left.\frac{\partial g(x,t)}{\partial t}\right|_{x_i,t_{n+1}} = \frac{g\left(x_i,t_{n+1}\right) - g\left(x_i,t_n\right)}{\Delta t} + O\left(\Delta t\right) \tag{3.28}$$

$$\left.\frac{\partial^2 g(x,t)}{\partial t^2}\right|_{x_i,t_{n+1}} = \frac{g\left(x_i,t_{n+1}\right) - 2g\left(x_i,t_n\right) + g\left(x_i,t_{n-1}\right)}{\Delta t} + O\left(\Delta t\right) \tag{3.29}$$

For fractional derivatives of order α, a backward difference formulation based on the Grünwald-Letnikov (GL) approximation was chosen following the work of Podlubny (1999) and Carcione et al. (2002). The derivation of the expression can

be found in Carcione et al. (2002).

$$\left.\frac{\partial^{\alpha} g(x,t)}{\partial t^{\alpha}}\right|_{x_i,t_{n+1}} = \frac{1}{\Delta t^{\alpha}} \sum_{k=0}^{N} (-1)^k \binom{\alpha}{k} g\left(x_i, t_{n-k+1}\right) + O\left(\Delta t\right) \tag{3.30}$$

Where N is the maximum value for n.

As can be noticed by analysing Equation 3.30, the approximated value of the derivative is given in terms of the summation of all previous states of the function $g(x,t)$. However, this summation of states leads to an iterative and storing process that may result in huge memory consumption. However, the binomial coefficients that appear in the expression are negligible for k exceeding an integer J. This allows the application of the so-called short-memory principle, through which the summation can be truncated at $k = L$, with $L \leq N$ being the so-called effective memory length (Podlubny, 1999).

Higher order approximations for the derivatives could have been used to reduce truncation errors. However, higher order schemes require the computation of more space-time grid nodes. This generates complications around the boundaries, where extra grid nodes have to be added to satisfy the high order approximation scheme. Nevertheless, by using small enough values of the space and time steps, Δx and Δt, the truncation errors are also reduced, as can be deduced from Equations 3.27, 3.28, 3.29 and 3.30.

The discrete equations derived from the application of the FD expressions (Equations 3.27, 3.28, 3.29 and 3.30) to the equations of the wave propagation problem (Equations 3.18, 3.20, 3.22, 3.23 and 3.24) can be found in AppendixA.

3.3.4 Stability conditions

In general terms, a trade-off between accuracy and computational cost must be reached. Two types of numerical errors may occur when modelling with FDTD methods.

The first type is linked to the spatial steps of the discretisation and generates

phase errors known as numerical dispersion. In this case, group and phase velocity are functions of the spatial discretisation parameters. These errors cannot be eliminated, but can be reduced to an acceptable level if the shortest wavelength is sufficiently sampled in space (Leutenegger and Dual, 2004). Different sampling rates have been suggested in the literature. For instance, Gomez et al. (2016) considered a conservative rate of a minimum of 20 space intervals per wavelength λ. However, the FDTD model employed was elastic. In viscoelastic cases, since viscoelasticity naturally shows dispersion effects, an appropriate verification test for numerical dispersion errors must be carried out. This verification is shown in Section 3.4.2.

The second type is linked to the time step of the temporal discretisation. It affects the stability of the wave amplitude during the simulation. If Δt is not chosen small enough, the wave amplitude increases exponentially with every time step and the system becomes unstable (Leutenegger and Dual, 2004). This leads to a stability criterion that defines the maximum Δt as a function of the geometrical, material and space discretisation parameters (Gsell et al., 2004). The numerical stability criterion of non-fractional differential equations is usually derived by using Von Neumann analysis (Orescanin et al., 2011). In the case of fractional derivatives the inference of the criterion is not immediate and requires a thorough mathematical development. One example found in the literature is the work of Yuste and Acedo (2005), who developed a stability condition for fractional diffusion equations. The mathematical development of a stability condition was considered beyond the scope of this thesis. As an alternative, a trial-and-error approach was used, with a reference starting value for Δt deduced from Expression 3.31 for integer derivatives (Leutenegger and Dual, 2004, Gomez et al., 2016).

$$\Delta t < \frac{1}{\max\left(c_s\right)} \left(\frac{1}{\Delta r^2} + \frac{1}{\Delta z^2} \right)^{-\frac{1}{2}} \tag{3.31}$$

Apart from the two main sources of numerical error associated with FDTD

methods, another source of error exists. As indicated in Section 3.3.3, the use of the Grünwald-Letnikov (GL) approximation (Equation 3.30) for the fractional derivative allows the application of the so-called short-memory principle. This principle reduces the temporal series of summation by truncating it at a certain value, and therefore reduces the computational overhead of the simulation. However, a wrong effective memory length L can increase the truncation errors of the approximation. Therefore, an appropriate analysis must be carried out in order to avoid errors due to a poor implementation of the short-memory principle. This analysis is carried out in Section 3.4.3.

3.3.5 Boundary conditions

The boundary conditions described in Expressions 3.25 and 3.26 were set into the discretised space-time grid as follows:

- The excitation signal was introduced by setting the values of $u_{\theta,\,\text{excitation}}(t_n)$ for each time step n, at the grid points that represent the place where the emitter is in direct contact with the urethral wall.
- The grid points on the urethral wall that were not used for the above boundary condition, were set with $\sigma_{r\theta} = 0$, in order to represent a non-constrained boundary.

A third boundary condition was set on the remaining boundaries. A Perfectly Matched Layer (PML) was incorporated surrounding the spatial domain, with the exception of the urethral wall side (Figure 3.5) for absorbing incoming reflections from the outer boundaries. The PML scheme was adapted from the formulation in cylindrical coordinates developed by Liu (1999) and was directly merged with the discrete equations of the problem. Details of the PML formulation incorporated into the discrete equations can be observed in Appendix A.

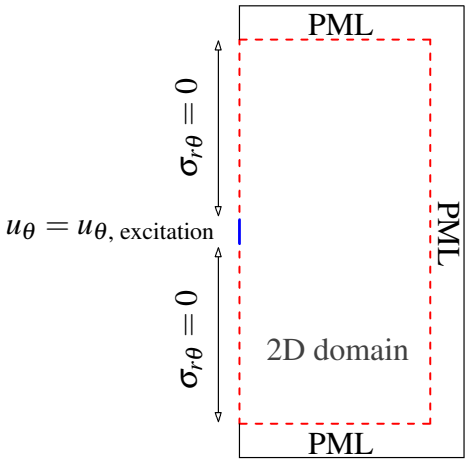

Figure 3.5: Spatial distribution of the boundary conditions of the model. 2D main domain contoured by red dashed lines. PML surrounding it. Urethra wall at left side where boundary conditions for u_θ (blue line) and $\sigma_{r\theta}$ are set.

3.3.6 Emission and reception elements

Emission and reception elements were not physically modelled. Instead, for the emission case, the excitation signal was directly implemented as the value of the displacement field of the mesh elements on the urethral wall in physical contact with the emitters' locations. In a similar fashion, measurements were simulated by saving the displacement values at the mesh elements in physical contact with the receivers' locations.

3.3.7 FDTD algorithm

As mentioned in Section 3.3.3, the mathematical expressions of the discrete equations are shown in Appendix A. The algorithm was developed using MATLAB® (Release 2017a, MathWorks, Natick, United States). The algorithm code can be found in Appendix B.

3.4 FDTD model results

In this section, several different scenarios were simulated by using the FDTD model described in Sections 3.2 and 3.3. The generic geometrical distribution of elements of the model is shown in Figure 3.6. The description and values of the different parameters from Figure 3.6 are displayed in a series of tables throughout this section.

The simulations were carried out on a quad-core 3.60 GHz, 16 GB RAM, desktop computer, using MATLAB® (Release 2017a) and Parallel Computing Toolbox™ (Release 2017a, MathWorks, Natick, United States).

The model parameters related to the size of the domain remained unchanged throughout all simulated scenarios. These values are shown in Table 3.1.

Table 3.1: Values of invariable geometrical parameters of the FDTD model throughout all scenarios simulated.

Parameter	Description	Value (mm)
r_d	Radial dimension of the domain	20.00
z_d	Depth dimension of the domain	40.00
r_u	Radius of the urethra	3.25

Before carrying out simulations of these different scenarios, the KVFD shear parameters of the different tissue conditions and the stability conditions of the model were considered. These considerations are detailed in Sections 3.4.1 and 3.4.2, respectively.

3.4.1 Viscoelastic properties used in this work

Values of the KVFD shear parameters (μ, η and α) for normal, cancerous and thermally ablated prostatic tissue, were required for the wave propagation model.

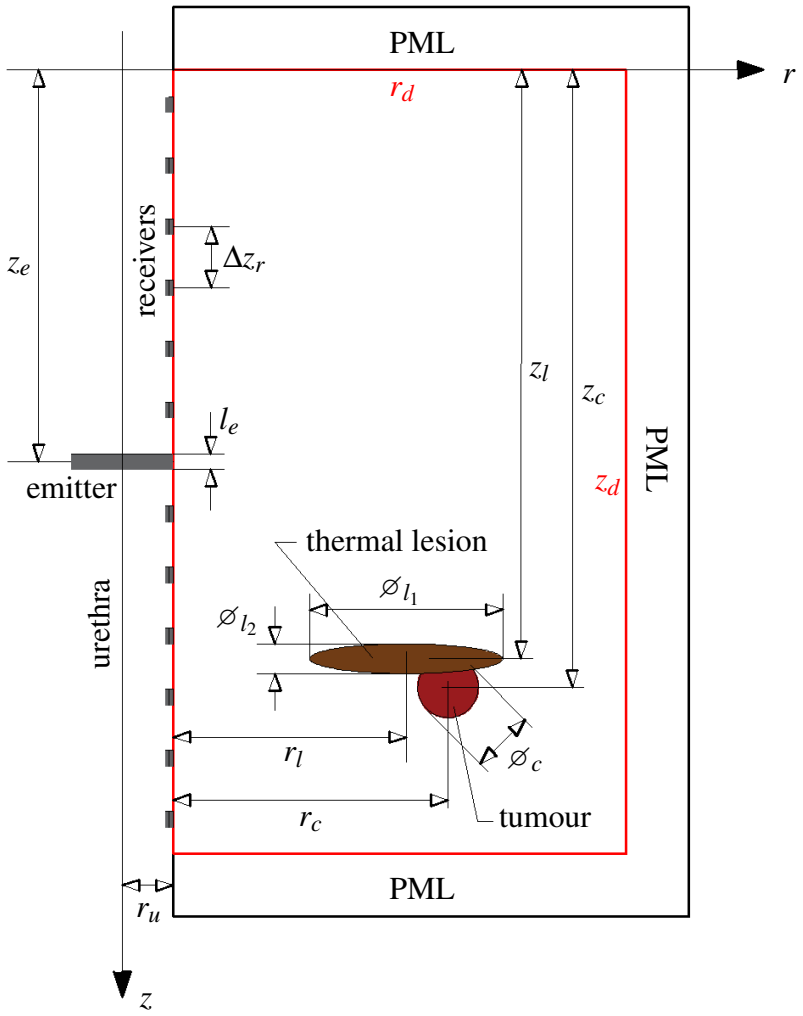

Figure 3.6: Scheme of the geometrical parameters of the wave propagation model. Real spatial domain contoured in red. PML surrounds the boundary domain with the exception of the urethral wall. Rounded tumour coloured in red, thermal lesion in brown. Emitter rotating disk in grey.

In Section 2.4, the latest studies concerning the characterisation of mechanical properties of prostatic tissue were reviewed. However, no consistent data were found for the KVFD shear parameters, or at least, data that allow their calculation. For this reason, a range of possible values was proposed based on results from several studies (Zhang et al., 2008, Mitri et al., 2011, Barr et al., 2012, Mariani et al., 2014, Correas et al., 2015, Zhang and Holm, 2016).

The shear modulus of normal tissue, taken as the absolute value of the complex shear modulus G^* (see Equation 2.3), can be expected to be within the range of 2 to 10 kPa. This range was chosen based on the data available in the literature shown in Tables 2.1 and 2.2. It should be noted that, throughout this thesis, the shear modulus is also denoted as the shear stiffness, or simply as the stiffness.

As can be seen in Equation 2.3, the KVFD expression for the complex shear modulus is a function of the three KVFD shear parameters. By making specific assumptions, plausible values of each parameter can be inferred. These assumptions are detailed below.

The parameter α was set as 0.35, which is representative of the findings of Zhang et al. (2008) and Zhang and Holm (2016). The rest of the KVFD shear parameters were obtained by using Equation 2.3 for matching the expected range of the shear modulus (2 - 10 kPa). In the studies by Zhang and Holm (2016) and Mitri et al. (2011), the ratio of the elastic μ and viscous η parameters was found to be of two orders of magnitude. For this reason, and also to produce a velocity dispersion curve resembling that provided by Mitri et al. (2011), μ was chosen to be 3.0 kPa and η 35 Pa·s$^{\alpha}$.

The phase shear velocity of a monochromatic plane shear wave according the KVFD model can be derived from the combination of Equations 3.32, 3.33 and 3.34.

$$c_s(\omega) = \sqrt{\frac{2\left(G'^2(\omega) + G''^2(\omega)\right)}{\rho\left(G'(\omega) + \sqrt{G'^2(\omega) + G''^2(\omega)}\right)}} \tag{3.32}$$

with:

$$G'(\omega) = \mu + \eta\,\omega^{\alpha}\cos\left(\frac{\alpha\pi}{2}\right) \tag{3.33}$$

$$G''(\omega) = \eta\,\omega^{\alpha}\sin\left(\frac{\alpha\pi}{2}\right) \tag{3.34}$$

where G' and G'' are the real and imaginary parts of the complex shear modulus G^*, respectively.

The combination of the three KVFD parameters produces values of the shear

modulus ranging from 3.2 to 3.6 kPa (according to Equation 2.4) and velocities from 1.8 to 1.9 m/s (according to Equation 3.32) for frequencies between 100 and 1000 Hz (see Figure 3.7), which is in agreement with the reviewed studies (Zhang et al., 2008, Mitri et al., 2011, Barr et al., 2012, Mariani et al., 2014, Correas et al., 2015, Zhang and Holm, 2016). Tissue density was considered to be 1000 kg/m^3.

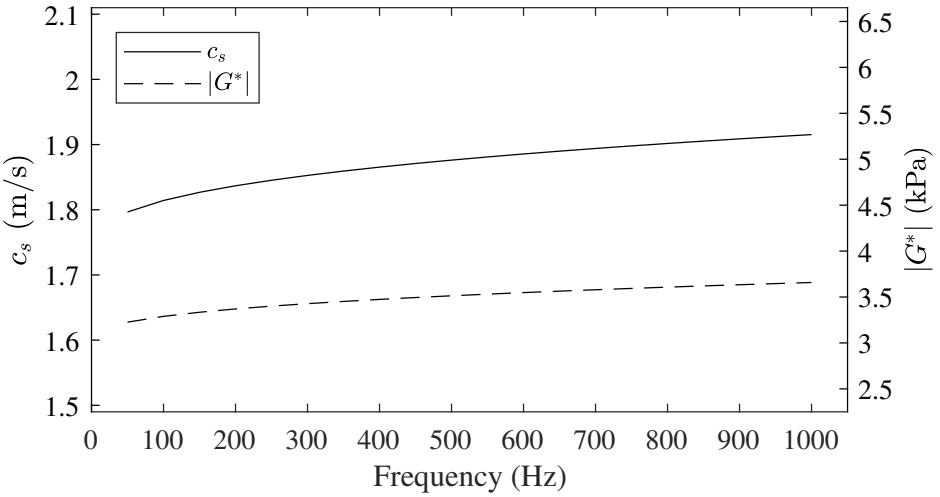

Figure 3.7: Shear velocity dispersion curve c_s and absolute value of the complex shear modulus G^* for normal prostatic tissue, generated by using the estimated KVFD parameters in Equations 2.3 and 3.32.

The shear modulus contrast ratio between cancerous and normal tissue was chosen to be 3.0, based on data from different studies using TR-SWE by Aixplorer® (see Tables 3.2 and 2.2) (Barr et al., 2012, Correas et al., 2015). At the time of writing this thesis, no study of the elastic values of thermally ablated prostatic tissue could be found. However, some studies for other types of tissue were available. Among them, liver was estimated to show certain degree of similarity in terms of viscoelastic properties. A reasonable value of 5.0 was assumed for the shear modulus contrast ratio between thermally ablated and normal tissue based on the results in *in vivo* porcine liver by Mariani et al. (2014).

From the DMA results by Zhang et al. (2008), it can be seen that α is nearly the same for normal and cancerous tissue. No information about change in the other

two KVFD parameters, μ and η, was found. For this reason, α was assumed to remain constant for all the tissue conditions, and both μ and η were proportionally increased by the assumed contrast ratio of 5.0.

It was assumed that no change in viscosity occurs between thermally ablated and cancerous tissue. Nevertheless, this assumption has no fundamental reasoning. It was applied due to the lack of relevant information and therefore it should be addressed in further studies. Accordingly, the full increment in stiffness due to thermal ablation was assumed to affect only the elastic parameter μ.

The values proposed for the KVFD shear parameters are summarised in Table 3.2.

Table 3.2: Values for the three KVFD shear parameters proposed for modelling all the tissue conditions in the FDTD wave propagation model.

KVFD parameter	Type of tissue		
	Normal	Cancerous	Thermally ablated
μ (kPa)	3.0	9.0	15.0
η (Pa·s$^{\alpha}$)	35.0	105.0	105.0
α	0.35	0.35	0.35

3.4.2 Analysis of numerical dispersion and stability.

Soft tissue shows natural wave velocity dispersion due to its viscoelastic behaviour, i.e. phase velocity of propagation depends on the frequency. Numerical modelling of wave propagation in viscoelastic materials inevitably produces numerical dispersion added to the natural dispersion of the medium. Therefore, a revision of velocity dispersion was required to ensure that the numerical dispersion errors were kept below a reasonable threshold.

The number of discretisation elements per wavelength is the key factor in controlling numerical dispersion. Therefore, the shorter the wavelength, the smaller the elements required to correctly form the wave. Accordingly, normal prostatic tissue was assumed as the medium of propagation. Normal prostatic tissue experienced the lowest shear velocity, hence also the shortest wavelength at every frequency.

Using the 2D FDTD wave propagation model developed in Section 3.3 of this thesis, cylindrical monochromatic shear waves were propagated through a normal prostatic tissue medium (mechanical properties in Table 3.2). Axisymmetric cylindrical shear waves in 3D are the equivalent of plane shear waves in the 2D model (see Figure 3.8). Therefore, in order to analyse the numerical dispersion generated, the shear group velocity measured in the model can be compared with the values of shear phase velocity analytically obtained (shown in Figure 3.7) .

The frequencies of excitation used varied between 400 Hz and 1000 Hz. The spatial step size in the axial direction Δz was set to be the same as that in the radial direction, Δr. The range for these quantities was set from 70 μm to 1500 μm. Δt was set as 20 μs after an initial estimate using Equation 3.31 and the theoretical shear velocity values shown in Figure 3.7. The effective memory length L was set at its maximum value, in this case 1000 since the total time of propagation was 20 ms. The pursuit of an optimised L parameter will be carried out later in this thesis, in Section 3.4.3.

2D FDTD simulations were carried out under the described setup. No instabilities were observed during the simulations. Shear velocity was calculated by using a time-to-peak technique at two points located in a radial line passing through a centred z coordinate (dashed black line in Figure 3.8). The two points were located at 5 and 15 mm respectively from the urethral wall.

The calculated shear velocity from the time-to-peak measurements in the 2D model was normalised by the theoretical KVFD shear velocity (Equation 3.32). These normalised values were expressed as a function of the number of Δr elements

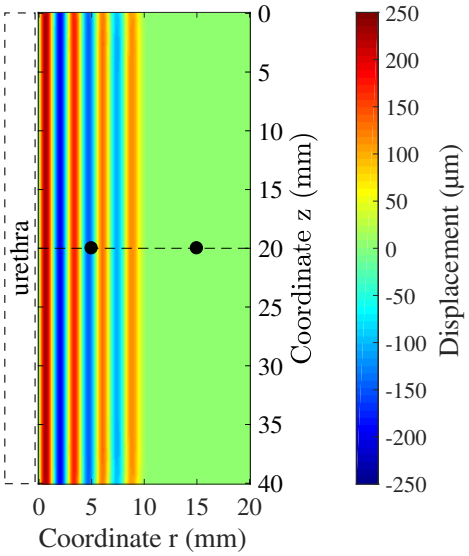

Figure 3.8: Example of snapshot taken at 5 ms of the start of the propagation, showing the displacement field when a monochromatic plane shear wave is propagated at 700 Hz from the urethral wall. In order to transmit the 2D plane wave, the emitter occupies the whole urethral length. The displacement measurements were taken at the two black points located on the dashed line at $z = 20$ mm.

per wavelength ($\lambda/\Delta r$) at four frequencies: 400, 600, 800 and 1000 Hz. Results are shown in Figure 3.9.

The numerical dispersion effect is clearly observable in Figure 3.9. Numerical errors decrease when increasing the number of elements per wavelength, with an identical tendency at all frequencies tested. Values ranging from 18 elements per wavelength showed acceptable low levels of errors. Specifically, 18 and 25 elements per wavelength yielded errors below 0.40% and 0.25% respectively.

Similarly to Δr and Δz, the accuracy of the model also depends directly on the time discretisation parameter Δt. As mentioned in Section 3.3.4, the smaller the value of Δt, the more accurate the finite-difference approximation of the time derivatives. However, Δt has a huge impact on the computational overhead of the method. For this reason, a trade-off between accuracy and computational cost was sought. Several values of Δt were tested considering the most computationally

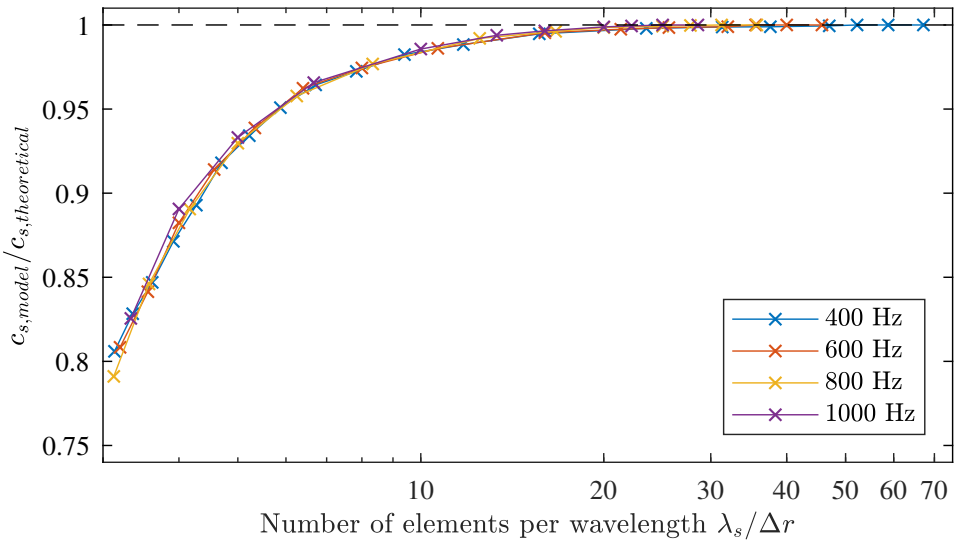

Figure 3.9: Numerical shear wave velocity dispersion produced by using 2D FDTD model as a function of the number of elements per wavelength ($\lambda/\Delta r$). Cross marks represent the normalised measurements by the theoretical velocity value according Equation 3.32. The medium was chosen as homogeneous and isotropic, with the KVFD properties of normal prostatic tissue. Shear waves were simulated at several frequencies.

demanding scenario: propagation in thermally ablated tissue and at the highest frequency (in this case 1000 Hz). Both Δr and Δz were set to generate a spatial discretisation with a minimum of 18 elements per wavelength. Equation 3.31 were used to obtain a starting Δt reference value. By a trial-and-error process, the stability of the model was secured by using Δt values equal to or smaller than 25 µs.

3.4.3 Analysis of the short-memory principle

Another numerical parameter that affects the accuracy of the model is the memory parameter L (see Section 3.3.3). L has a special impact on the computational cost of the simulation, by establishing the number of summation elements of the series of the GL approximation for the time fractional derivatives (Equation 3.30). However, a poorly chosen L parameter can increase the truncation error in the fractional derivative approximation.

In order to select an optimised value of L, a convergence study of simulations with respect L was carried out. The short-memory parameter L varied from 0 to N, the total number of time discretisation elements. Thus, $L = 0$ meant that none of the previous states was used for calculating the fractional derivative approximation, whereas $L = N$ meant that all the previous states were used. The convergence was studied by analysing the trend of the Euclidean distance (also known as l^2-*norm*) between measurements from simulations using variable L values and the case of using $L = N$.

Four simulations were performed for each of the three types of tissue (normal, cancerous and thermally ablated), using frequencies from 400 to 1000 Hz and time duration of 20 ms. Plane shear waves were propagated, and measurements of the displacement generated were taken at 15 mm from the urethral wall on the centred line, similarly to the previous study of numerical dispersion (see Figure 3.8). Δr and Δz were once again set to generate a spatial discretisation with a minimum of 18 elements per wavelength. Δt was set as 20 µs.

Results from the convergence study are shown in Figure 3.10. Results from the average of the twelve simulated scenarios were expressed as the error of the approximation relative to simulations with $L = N$ (100% of the total duration of the simulation) using the three types of tissue. The L parameter was expressed in terms of time. The approximation errors converged to 0% between 1.6 and 1.8 ms for all the different combinations of tissue types and frequency.

3.4.4 Wave propagation simulations

A preliminary demonstration of the wave propagation model described in this chapter is shown in this section. This demonstration aims to show the wave propagation features associated with the TU-SWE technique. Validation of the results against other numerical or analytical studies was not carried due to the lack of published work with a similar model configuration to the TU-SWE technique

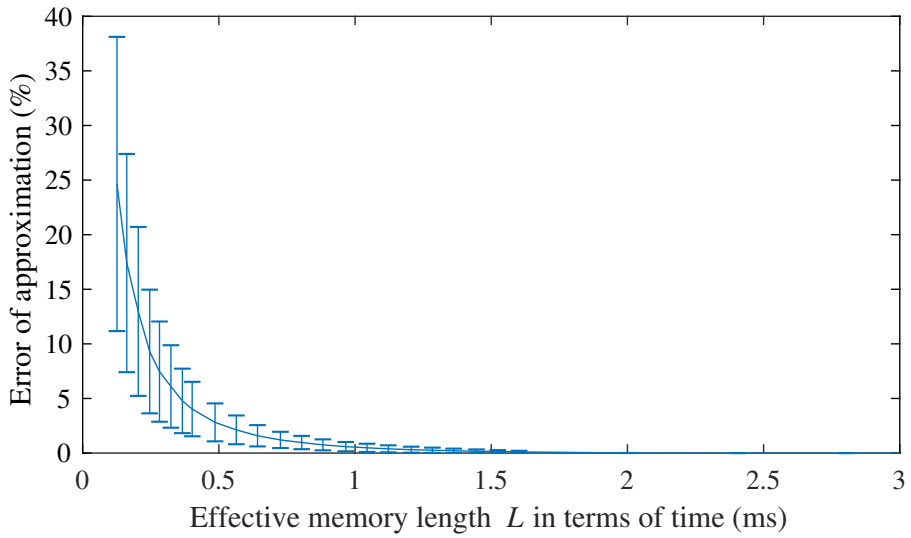

Figure 3.10: Results from the convergence study for optimising the value of the effective memory length L. Results expressed as the error of approximation due to L relative to simulations with $L = N$. Values were averaged from simulations using four different frequencies from 400 to 1000 Hz and the three types of tissues. Time step Δt set as 20 µs. Total duration of the simulations was 20 ms, however, solely results from 0 to 3 ms are shown for visual convenience. Data is shown in terms of mean and standard deviation values.

that allows the comparison.

Two types of likely clinical scenarios were simulated: pre-ablation scenarios and post-ablation scenarios. Nevertheless, some model parameters were kept invariable for all simulations. These invariable parameters were grouped into three categories: the probe setup, numerical discretisation, and mechanical parameters of tissue.

The probe setup parameters are related to the arrangement of emitters and receivers and the features of the excitation source. A generic probe setup was chosen, comprising one emitter at a variable z position on the urethral wall and 20 receivers uniformly distributed along the urethral wall (see Figure 3.6).

As indicated in Section 3.3.6, no physical emitters and receivers were modelled. Instead, values of displacement were implemented for the emission, and measured for the detection, on the grid elements that constitute the contact

between the urethral wall and the emitter and receivers. The excitation signal was a Gaussian monocycle with a centre frequency of 700 Hz and maximum amplitude of 0.3 radians, which is equivalent to 1 mm of displacement at the emitter surface of contact. The probe setup parameters are summarised in Tables 3.3 and 3.4.

Table 3.3: Invariable values of emitters parameters for all scenarios simulated by using the FDTD model.

Parameter	Description	Value
n_e	Number of emitters	1
l_e	Length of the emitter	1.00 mm
f_e	Centre frequency of the excitation	700 Hz
a_e	Maximum amplitude of the excitation	0.30 rad

Table 3.4: Invariable values of receivers parameters for all scenarios simulated by using the FDTD model.

Parameter	Description	Value
n_r	Number of receivers	20
Δz_r	Distance between receivers	1.90 mm
l_r	Length of each receiver	0.50 mm

The parameters of the time and space discretisation of the model are listed in Table 3.5. As shown in previous sections, numerical dispersion effects were kept under reasonable threshold by using 18 elements or more per wavelength. Because of that, Δr and Δz were both set at 150 µm. This value ensured a minimum of 18 elements per wavelength in all simulated scenarios. Conversely, the value of 20.00 µs chosen for Δt ensured stability of the simulation. The selected L parameter was shown to not generate additional truncation error for the fractional derivative approximation in the cases simulated in this section (see section 3.4.3). The number

of PML elements, n_{PML} was set to 60, which was sufficient to eliminate incoming reflections from the boundary domain.

Table 3.5: Invariable values of the discretisation parameters for all scenarios simulated by using the FDTD model.

Parameter	Description	Value
Δr	r spatial dimension interval	150.00 µm
Δz	z spatial dimension interval	150.00 µm
Δt	time interval	20.00 µs
t_T	Total time of simulation	35.00 ms
t_L	Time reference for L parameter	2.00 ms
n_{PML}	Number of PML elements	60

The third group of invariable parameters were the mechanical parameters of the three tissue types. The values of these parameters are shown in Table 3.2.

The remainder of the model parameters were varied in accordance with the scenario simulated. Values are listed in Table 3.6 for pre-treatment scenarios.

Table 3.6: Values of the variable model parameters for the 3 pre-treatment scenarios simulated by using the FDTD model.

Parameter	Description	Value (mm)		
		Scenario 1	Scenario 2	Scenario 3
z_e	z coordinate of the emitter	0.50	20.00	39.50
r_c	r coordinate of the tumour centre	10.00	14.00	16.00
z_c	z coordinate of the tumour centre	20.00	18.00	28.00
$\varnothing_c$	diameter of the tumour	4.00	6.00	8.00

Snapshots of the displacement field u_θ resulting from shear wave propagation in the pre-treatment scenarios are shown in Figures 3.11, 3.12 and 3.13. The

displacements were tangent to the out-of-plane direction and contained within planes perpendicular to the urethra (axis z). The corresponding measurements at the receivers' locations are shown in Figures 3.14,3.15 and 3.16.

The second snapshot of each scenario represents an instant after the emission of the shear wave.

The third snapshot of each scenario shows an instant after the impact of the wave against the tumour and the first moments of the propagation backwards of a reflected wavefront. In all the three scenarios, it can be noticed that the wave accelerates as it propagates through the tumour. This is due to the increase in stiffness with respect the normal tissue surrounding the tumour. The generation of a reflected wave from the far side of the tumour can also be observed, as well as signs of constructive interactions near the tumour contour.

The fourth snapshot of each scenario shows another instant of the propagation, where the reflections can be easily observed moving towards the urethral wall, where the receivers can detected them. The amplitude of the ongoing wave was altered after leaving the tumour behind. The sections with higher amplitude result from previous constructive interactions on the lateral sides of the tumour (observed in the third snapshot). The central section was highly attenuated due to the previous reflections and refractions, and the higher absorption in the tumour. Incoming reflections from the PML boundary were not discernible by eye.

The graphs on Figures 3.14, 3.15 and 3.16 show measurements of the displacements at the receivers for the three pre-treatment scenarios. The measurements were deliberately stacked for visual convenience. The section of the wave travelling along the urethral wall, here referred to as the direct wave, is clearly noticeable in the graphs as an oblique perturbation with decreasing amplitude from the emitter position towards the receivers. The reflected waves from the tumours are seen as two consecutive curved perturbations after the arrival of the direct wave. In all cases, the first curve perturbation was due to the reflection of the wave against the front side of the tumour, whereas the second one was due to the reflection

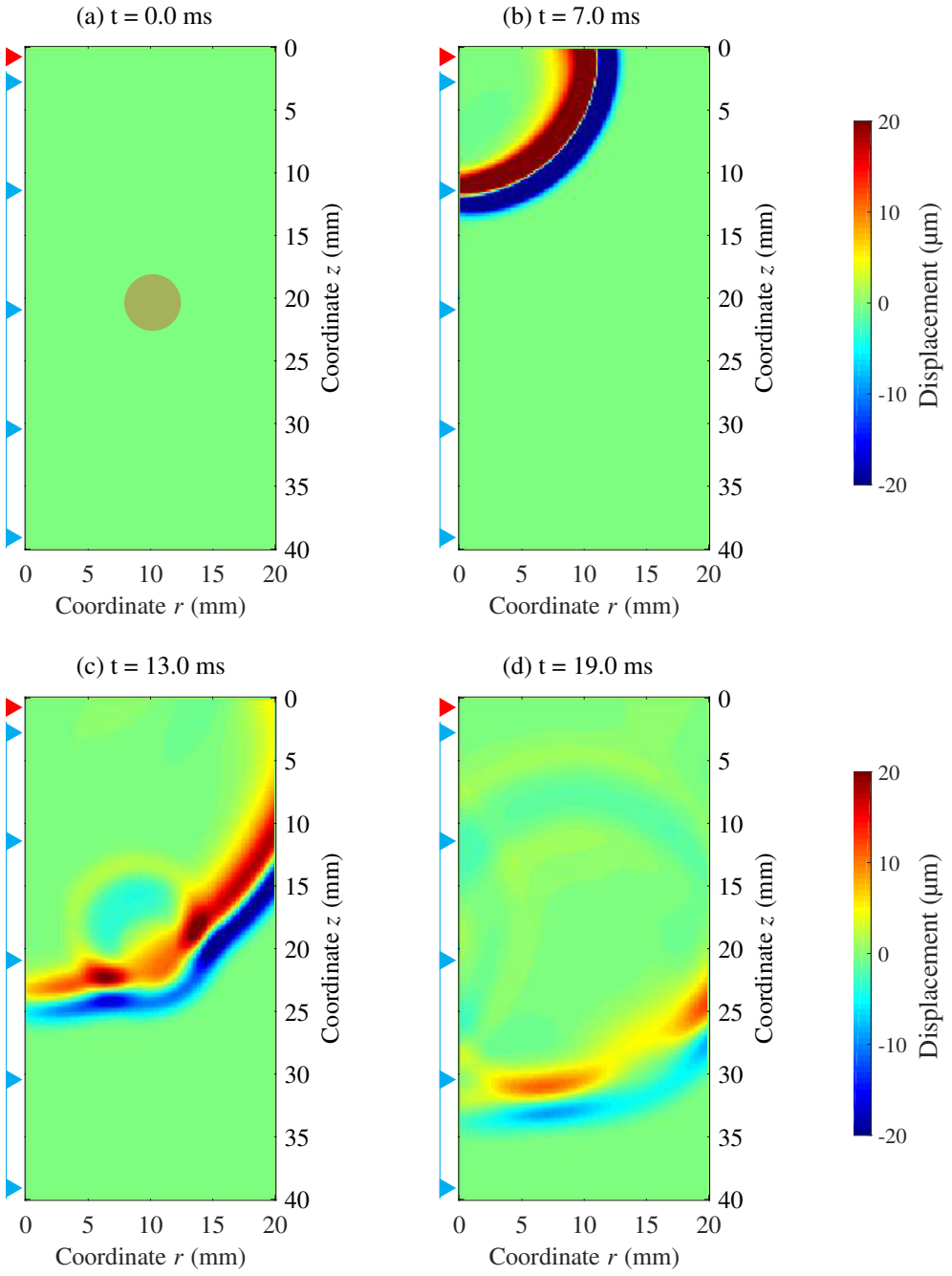

Figure 3.11: Four snapshots of the displacement field during the wave propagation for the scenario 1 simulated using the FDTD model at different time instants (a) 0.0 ms, (b) 7.0 ms, (c) 13.0 ms and (d) 19.0 ms. Location of the emitter (red triangle) at the top section of the urethral wall, the 20 receivers (blue triangles) uniformly distributed along the urethral wall and a rounded tumour (dark shaded circle) of 4.0 mm in diameter (details are shown in Table 3.6). Figures (b), (c) and (d) show other instants of the wave propagation. Measurements at the receivers' location are shown in Figure 3.14.

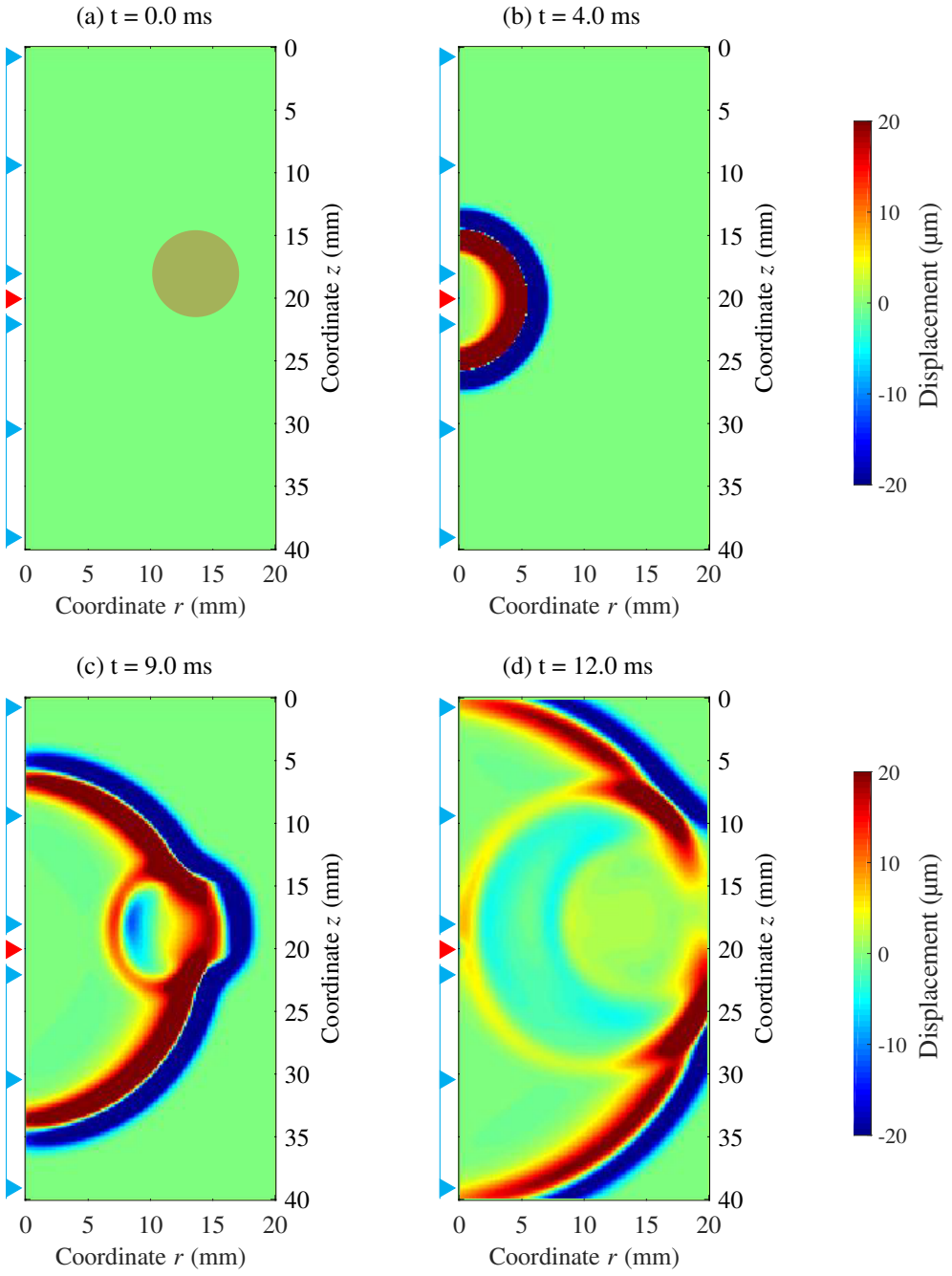

Figure 3.12: Four snapshots of the displacement field during the wave propagation for the scenario 2 simulated using the FDTD model at different time instants (a) 0.0 ms, (b) 4.0 ms, (c) 9.0 ms and (d) 12.0 ms. Location of the emitter (red triangle) at the middle section of the urethral wall, the 20 receivers (blue triangles) uniformly distributed along the urethral wall and a rounded tumour (dark shaded circle) of 6.0 mm in diameter (details are shown in Table 3.6). Figures (b), (c) and (d) show other instants of the wave propagation. Measurements at the receivers' location are shown in Figure 3.15.

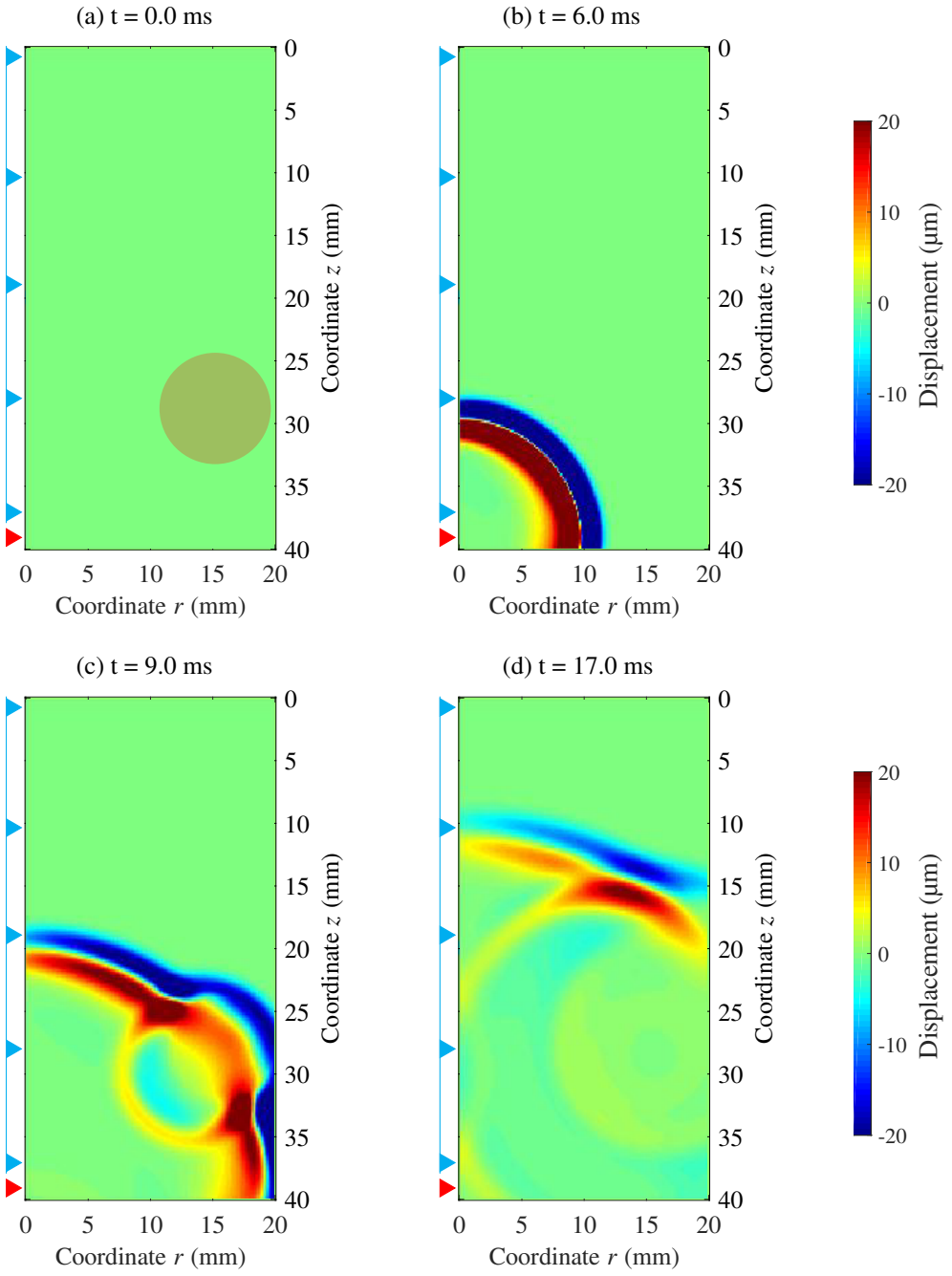

Figure 3.13: Four snapshots of the displacement field during the wave propagation for the scenario 3 simulated using the FDTD model at different time instants (a) 0.0 ms, (b) 6.0 ms, (c) 9.0 ms and (d) 17.0 ms. Location of the emitter (red triangle) at the bottom section of the urethral wall, the 20 receivers (blue triangles) uniformly distributed along the urethral wall and a rounded tumour (dark shaded circle) of 8.0 mm in diameter (details are shown in Table 3.6). Figures (b), (c) and (d) show other instants of the wave propagation. Measurements at the receivers' location are shown in Figure 3.16.

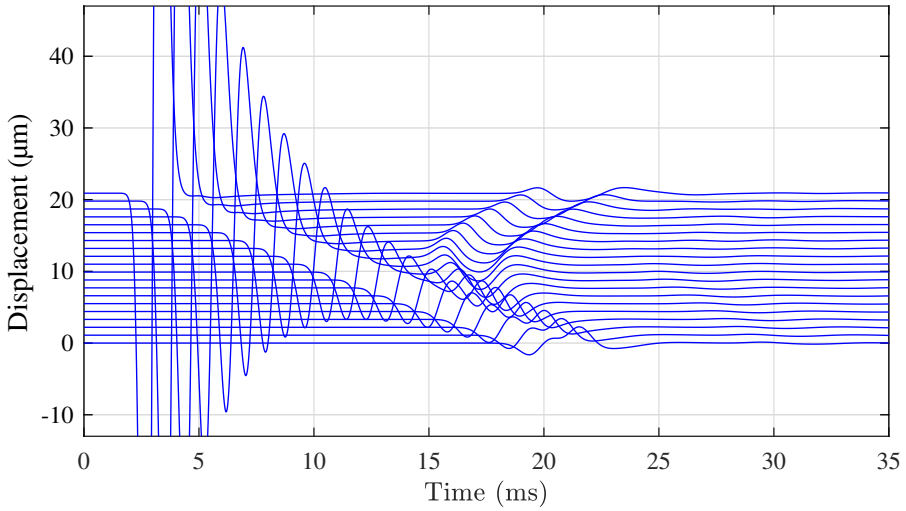

Figure 3.14: Measured displacement at the 20 receivers from scenario 1 (details in Table 3.6, scenario 3)

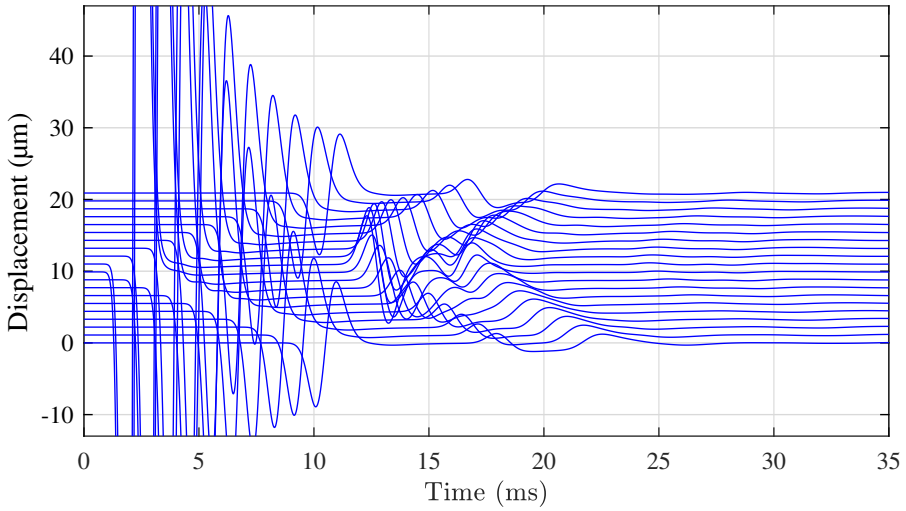

Figure 3.15: Measured displacement at the 20 receivers from scenario 2 (details in Table 3.6, scenario 3)

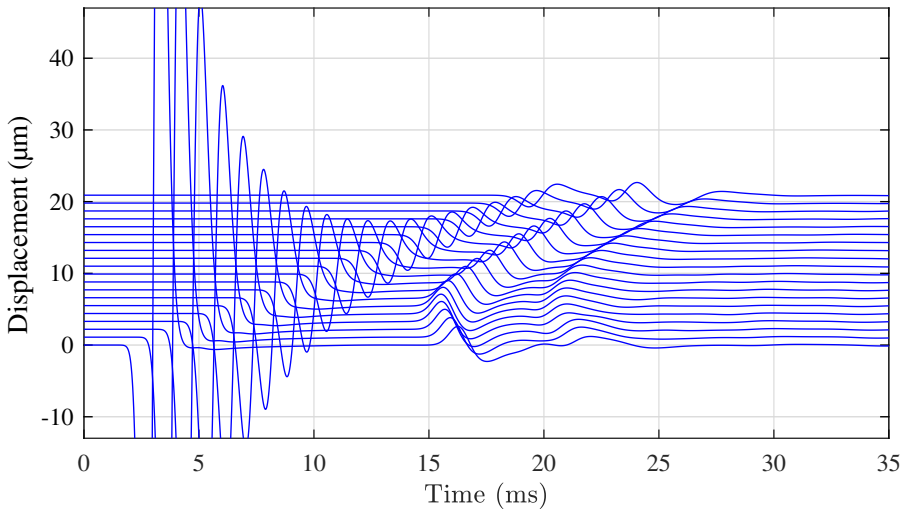

Figure 3.16: Measured displacement at the 20 receivers from scenario 3 (details in Table 3.6, scenario 3)

against the far side of the tumour. As expected, it can be seen that the larger the tumour the longer the time of arrival between the first and the second reflection.

Scenario 3 was used as the initial pre-treatment situation for showing two examples of treatment assessment scenario. Scenario 4 simulated the assessment of a first HIFU lesion, as a practical situation for checking the treatment delivery position. Scenario 5 simulated the assessment at the end of the ablation process after covering the totality of the tumour area. Elliptic thermal lesions of $10\times3\times3$ mm size produced by the Sonablate® system were selected as HIFU lesions in the model. Figure 3.17 shows the features of treatment scenarios 4 and 5.

The displacement measurements at the position of the receivers for treatment scenarios 4 and 5 are shown in Figures 3.18 and 3.19.

When comparing displacement measurements from scenario 4 (Figure 3.18) with measurements from pre-treatment scenario 3 (Figure 3.16), some differences could be noticed as a result of the HIFU lesion presence. In scenario 4, the reflected wavefront arrives earlier at the receiver positions located closer to the emitter. In general, the amplitude of the reflection was higher compared with the pre-treatment scenarios, since the mechanical impedance change between normal tissue and

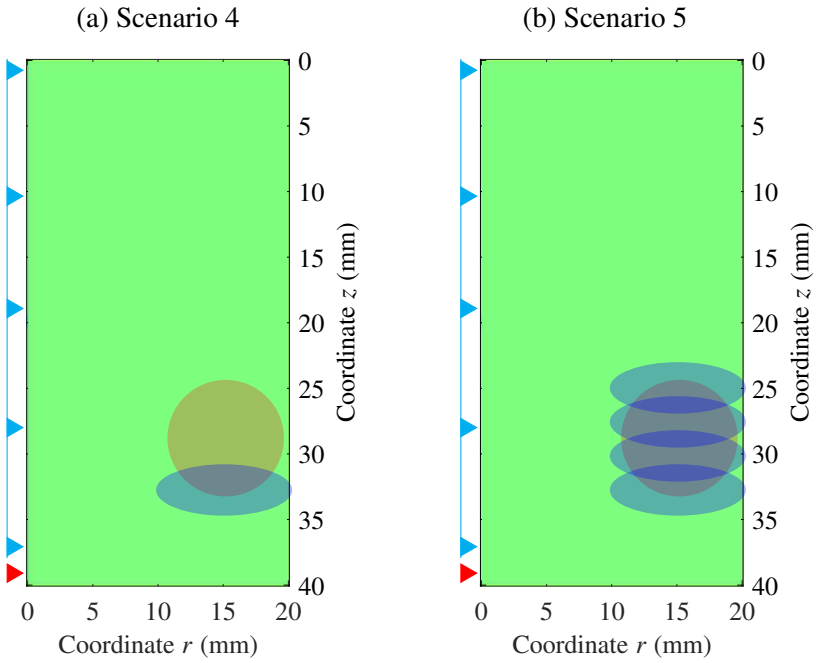

Figure 3.17: Schematic representation of the treatment scenarios 4 and 5. The arrangement of emitter and receivers, as well as the tumour features, were the same that in scenario 3. Scenario 4 contained only a single HIFU lesion (blue ellipse), thus resembling an initial stage of the HIFU ablation procedure. Scenario 5 contained 4 stackable HIFU lesions covering the whole tumour, thus resembling the final stage of the HIFU ablation procedure (SonacareMedical, 2015).

HIFU lesion is higher compared with the impedance change between normal and cancerous tissue. Similar effects could be observed between measurements from scenario 5 (Figure 3.19) and scenario 4 (Figure 3.18). In scenario 5, the reflected wavefronts arrived earlier at the receivers on the upper half of the urethral wall, and experienced higher amplitude compared with scenario 4.

Overall, it could be seen from the examples simulated that the presence of stiffer lesions (tumours or HIFU lesions) produced perturbations. These perturbations travelled back to the urethral wall, where they were measured. Different scenarios, concerning the probe setup and the distribution of lesions, generated different patterns of measurements, thus providing specific information

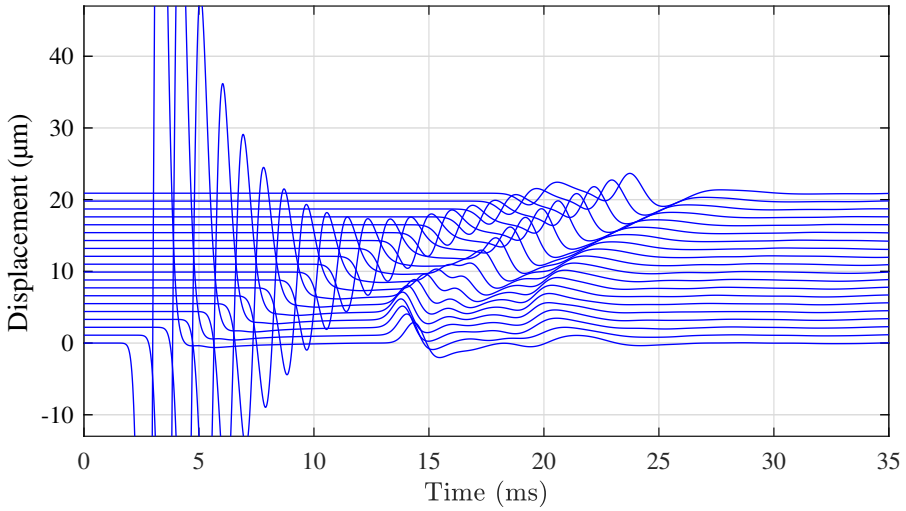

Figure 3.18: Measured displacement at the 20 receivers from scenario 4 (details in Table 3.6)

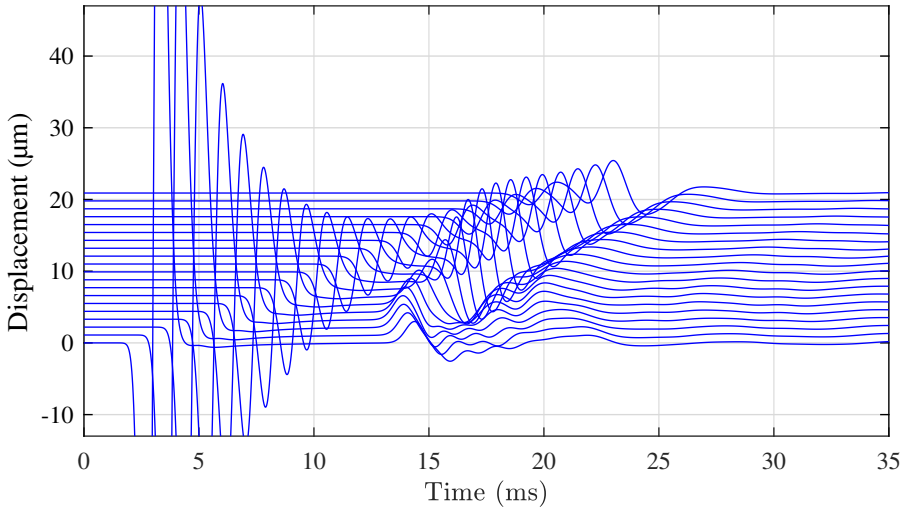

Figure 3.19: Measured displacement at the 20 receivers from scenario 5 (details in Table 3.6)

about the characteristics and distribution of the lesions. The described model will be used used later in Chapter 5, as a forward model for two different reconstruction techniques.

3.5 Discussion and conclusion

Various assumptions were taken into account for developing the wave propagation model for the TU-SWE technique described in this chapter. These model assumptions are summarised as follows:

1) The prostate was idealised as a cylinder with the urethra as a coaxial cylindrical hole.

2) A cylindrical coordinate system was used for creating the mesh.

3) The initial 3D model configuration was simplified to a 2D configuration by assuming axial symmetry.

4) The wave propagation is governed by a wave equation based on a KVFD material constitutive law.

5) The KVFD mechanical properties were indirectly estimated by using data from different published studies of characterisation of the viscoelastic properties of prostate.

The three first assumptions listed above implied a geometrical approximation different from the real anatomy of the prostate. Nevertheless, these assumptions aimed to simplify the geometrical complexity of the problem, with the purpose of creating a 2D model, close enough to reality and simultaneously efficient. Nevertheless, a more anatomically realistic 3D geometry will be needed in future steps of development of the TU-SWE technique.

The two last assumptions listed above are related to the mechanical behaviour of prostatic tissue. In general, soft tissue behaves viscoelastically under external loading or deformation. For this reason, wave equations based on viscoelastic material constitutive laws are well suited for describing the mechanical phenomenon of wave propagation. In this work, a wave equation based on a KVFD

constitutive law has been used to model the propagation of shear waves according to the TU-SWE technique. The KVFD constitutive law is a generalisation of the KV model. The KVFD law is a three parameters model and can model frequency power law absorption with variable exponent, which is the main advantage against the KV based models that only produce frequency squared absorption laws. On the other hand, there is a clear need for characterisation studies of the viscoelastic properties of prostatic tissue with different pathological conditions. At this stage, it is not possible to estimate to what extent the KVFD mechanical properties used for the different prostatic tissues in the model are realistic. Real values of KVFD properties are needed so that the results produced by the model can be properly evaluated and related with the actual possibilities of the TU-SWE technique.

The 2D wave propagation model was not validated against other numerical or analytical studies, due to the limited number of published work with a similar configuration to the TU-SWE technique, in terms of geometrical and mechanical characteristics. In fact, only one study was found that modelled in 1D the propagation of shear waves using a KVFD constitutive law (Zhang and Holm, 2016). However, the shear waves were generated by ARF, thus presenting a vertical direction of particle vibration. This type of shear wave differs from the shear wave generated in TU-SWE, which presents an angular out-of-plane direction of vibration. Under these circumstances, an experimental approach was undertaken for the validation of the wave propagation model. This will be described in Chapter 4.

The results shown in Section 3.4.4 illustrated a few possible clinical scenarios. The expected pseudo-spherical propagation of the wave was clearly observable from a 2D perspective. Refraction and reflection phenomena were also noticeable. The reflected waves were detected at the receivers' positions. Mode conversion of waves was indirectly disabled in the equations of the problem after imposing the axial symmetry simplification. Longitudinal waves travel much faster than shear waves in the prostate, nevertheless, this type of wave can alter the measurements of the future

receivers, therefore, further investigation of the effect of mode conversion will be addressed by developing the 3D wave propagation model. Apart from the stiff tumours and HIFU lesions, no other type of heterogeneity was added. Therefore, no background noise was measured and an estimate of the SNR was not possible. This point will need to be addressed in further work since it will be a determining factor for realistically analysing the clinical feasibility of the TU-SWE technique.

3.6 Chapter summary

Overall, this chapter was dedicated to describing the development of a wave propagation model for the TU-SWE technique.

First, the equations of the wave propagation problem were established. Since soft tissue is well known to behave viscoelastically, a brief review about wave equations based on viscoelastic constitutive laws was carried out. An approach based on the KVFD wave equation was chosen.

Subsequently, the development of the model was initiated by setting up a simplified cylindrical geometry for the prostate. The system of equations was formulated according to a 2D simplification based on cylindrical coordinates and axial symmetry.

An FDTD method was chosen to numerically solve the system of equations. FD schemes were selected for approximating the time and space derivatives. A displacement-strain-stress formulation was then developed according to the proposed time-space discretisation and FD schemes. Stability criteria and boundary conditions of the problem were described and implemented.

Finally, after setting up the model parameters, results from the wave propagation model were reported. Stability and numerical errors were analysed. Three examples of simulations for the diagnosis application and two for the treatment monitoring application were shown. As expected, it could be seen that the presence of stiffer lesions generated increasing perturbations of the incoming wavefront. These perturbations travelled back to the urethral wall where they were evaluated, thus simulating a measurement. Different patterns of measurements were simulated involving the probe setup and the distribution of lesions, thus providing specific information about the characteristics and distribution of the lesions.

Chapter 4

Experimental validation

Validation is a crucial step within any research project that involves computational modelling of physical phenomena. Validation of computational models can be achieved by different means, for instance by experimental work. Experimental work objectively proves the capacity of the model to simulate the physical phenomenon. Well-established alternative techniques can be used to measure certain features of the physical phenomenon that can be compared with model simulations. The model is validated when a certain level of agreement is reached between model simulation results and experimental measurements.

This chapter describes the experimental work carried out for validating the wave propagation model for TU-SWE presented in Chapter 3. Translucent elastography phantoms were fabricated as media for the experimental propagation of shear waves according the TU-SWE approach. A high-speed camera technique was used to obtain measurements of the displacement generated by the wave propagation through the phantom. Experimental measurements were compared with model simulations in order to validate the FDTD wave propagation model.

4.1 Background

4.1.1 Review of elastography phantoms

Most elastography researchers have used phantoms composed of tissue-mimicking materials in their work. Phantoms enable the investigation of elastography techniques before initial clinical trials (Madsen et al., 2003). There exists a vast amount of elastography studies involving the use of tissue-mimicking phantoms. Madsen et al. (1983) was one of the first studies that analysed the elastic properties of tissue-like materials widely used in manufacturing phantoms for ultrasound research. A follow-up study by Madsen et al. (2003) was dedicated to review the initial investigations dealing with tissue-mimicking materials and *ad hoc* phantoms for elastography. In that review, Hall et al. (1997) is referred to as the first study thoroughly dedicated to elastography phantoms. The study was focused on addressing the long-term stability of tissue-mimicking materials, such as gelatine and agar, for elastography research.

A large variety of phantom recipes have reportedly been studied in the last two decades (Nguyen et al., 2014). It is usual to find phantoms based on gelatine, agar or a mixture of both. Apart from these basic components, additives can be added to provide the phantom with other specific features, for example to increase viscosity or to control the proliferation of fungi and bacteria (Madsen et al., 2003).

Generic phantoms can be tuned in order to get the desired final properties of the mimicked tissue by varying the ingredients and their concentrations as specified in the original recipes. Madsen et al. (2005) created an elastography phantom recipe after a thorough analysis of previous studies, aimed to provide long-term stable heterogeneous phantoms with not solely soft tissue elastic properties, but also MR tissue properties. Increased levels of agar concentration were used to create the heterogeneities while keeping the gelatine concentration at the same level compared with the background mixture. This combination ensured long-term stability of the

heterogeneities' shape.

Dunmire et al. (2013) adapted the recipe by Madsen et al. (2005) to produce agar/gelatin phantoms for image guided dosing and feedback control of HIFU. However, further improvements are still required, since the phantom response to temperature was not in good agreement with that of the human tissue. Another example of interest can be found in Amador et al. (2015). They designed a gelatine-based viscoelastic phantom to compare results from SWE with the HFVS technique. A KVFD model was used to fit the data. To vary the viscous properties, the authors added different concentrations of Vanicream Lite (Pharmaceutial Specialties, Inc., Rochester, MN, USA). HFVS can be seen as an improved rheometer with an extended frequency range up to 2 kHz.

Madsen et al. (2003) also proposed oil-in-gelatine solutions for elastography phantoms. In follow-up studies, Madsen et al. (2006a,b) studied oil-in-gelatine anthropomorphic phantoms mimicking breast glandular tissue. In these studies, the acoustic and elastic properties, as well as the stability, of such phantoms were investigated in depth. Later, Pavan et al. (2010, 2012) concluded that adding oil to an agar/gelatine mixture decreases the stiffness of the gels and also reduces the nonlinear behaviour of agar gels described by Hall et al. (1997). Another example of using oil-in-gelatine phantoms was described by Nguyen et al. (2014). They mixed a gelatine base with castor oil at different concentrations to obtain phantoms with variations in viscoelastic properties measured by SWE.

Many different recipes designed for elastography applications in the prostate can also be found in the literature. For example, Salcudean et al. (2006) fabricated a gelatine-based prostate phantom to check a vibro-elastography technique. Similarly, Chopra et al. (2009) used a gelatine-based prostate phantom to detect inclusions by using MR elastography and shear waves created by a transurethral vibrating bar. The inclusions were fabricated by increasing the concentration of gelatine. Cao et al. (2013) studied different materials to fabricate phantoms for the detection of prostate cancer using SWE. The authors obtained suitable elastic and

ultrasound properties by using polyacrylamide for prostate tumours and agar for the normal prostate background. Thörmer et al. (2013) used a multi-modality prostate phantom (053-MM, CIRS Inc., Norfolk, VA, USA) to test a novel modality of MR elastography using a modified endorectal coil as an actuator. Elastic properties of the background and inclusions were within the range of those found in human prostate.

Specific features related to the type and conditions of the experiment must be taken into account at the time of choosing a phantom recipe. In this case, a gelatine-based recipe from a modified combination of recipes by Chopra et al. (2009) and Dunmire et al. (2013) among others, was chosen. The motivation for doing so and along with further details are described in Section 4.2.1.

4.1.2 Optical techniques for shear wave detection

The objective of the experimental work described in this chapter was to validate the 2D FDTD wave propagation model, described in Chapter 3, developed for the TU-SWE method. To achieve this validation, it was required to obtain measurements of shear wave propagation from TU-SWE-based phantom experiments, feasible to be simulated by the 2D axisymmetric model.

Optical techniques using lasers have been previously used to detect and measure the properties of shear waves generated in elastography phantoms by ARF. In one of the first reported experimental observations of shear waves generated by ARF, Andreev et al. (1997) used a laser beam to successfully detect the waves and measure their velocity. The laser beam was partially focused on the edge of an embedded particle in a rubber-like medium, so that the amount of light passing through the medium was related to the displacement of the particle due to the shear wave propagation. Later, Chen et al. (2004) used a laser vibrometer to measure the wave velocity dispersion of shear waves generated by oscillatory ARF. The laser beam measured the vibration of micro mirror particles embedded in the phantom,

thus allowing the measurement of the phase shift of narrow band shear waves between two different locations, and therefore the calculation of the shear wave velocity dispersion.

Optical tracking by high-speed camera has also been used to observe the full displacement of particles due to shear wave propagation. Bouchard et al. (2009) utilised an optical tracking method to investigate the mechanical response of a translucent tissue-mimicking phantom to ARF pulses. The optical system consisted of a microscope and an attached high-speed camera. Shear waves were successfully observed by tracking the displacement of an embedded single particle. Later, Czernuszewicz et al. (2013) employed a similar optical tracking system to experimentally confirm displacement underestimation when using ARFI, previously predicted by theory and FEM modelling. Suomi et al. (2015) used another similar optical tracking system to characterise the amplitude of the displacements and the phase shifts with respect to some ARF setup features.

The examples detailed above demonstrate that optical techniques based on laser and high-speed cameras are suitable tools to capture the shear wave propagation induced by ARF in translucent phantoms. However, in these examples, high-speed cameras were used to record the displacement of a single particle, as laser would do. This method misses the opportunity to simultaneously record several particles in a plane, which would increase the amount of information acquired and therefore improve the tracking reconstruction.

In this thesis, a high-speed camera-based technique was chosen instead of a laser-based technique, due to its simplicity of use and its capacity to directly record the true displacement field of particles located in an area. This ability is especially useful in the case of TU-SWE, where the displacements follow an angular direction within a perpendicular plane to the emitter shaft. To the best of the author's knowledge, this work represents the first attempt of using a high-speed camera technique to measure the displacement field in a 2D space, resulting from shear wave propagation induced by a mechanical actuator.

4.2 Methods for experimental validation

This section details the different methods used in the experimental validation of the wave propagation model.

4.2.1 Preparation of the tissue-mimicking phantoms

4.2.1.1 Phantom recipe

Different potential recipes for elastography phantoms were reviewed in Section 4.1.1. In principle, generic elastography recipes can be tuned to yield the desired viscoelastic response. In practice, challenges can arise. Given that a high-speed camera-based technique was chosen for recording the displacement within a prostate-mimicking phantom, this optical method requires the use of clear translucent phantoms with embedded visible particles. Such design constraints can place restrictions on the phantom design.

Translucent gelatine-based phantoms were fabricated by taking into account characteristics from the recipes by Chopra et al. (2009), Dunmire et al. (2013), Amador et al. (2015), Bouchard et al. (2009), Czernuszewicz et al. (2013). Details of the ingredients and their concentrations are shown in Table 4.1. Bovine gelatine was the gelation component. Formalin was added as a cross-linking agent, thus elevating the melting point of the gelatine (originally around 32°C) and stabilising the response of the phantom properties to room temperature variations. Potassium sorbate was included to preserve the phantom from early decay due to bacterial and fungal activity. Additives for tuning viscosity and acoustic properties were excluded after observing a drastic lack of transparency if added.

Four different batches of the gelatine solution were produced. The batch for the background of the phantom contained a 9% wt/wt concentration of gelatine. The other three batches were prepared for conforming the stiffer inclusions that simulate tumours. The amount of gelatine was increased for these new batches until stiffness

Table 4.1: Details of the ingredients of the gelatine solution for the background of the phantom.

Ingredient	Quantity	Supplier, type
Gelatine[†]	10 g	Sigma Aldrich, Bovine skin gelatine 225 bloom
Formalin	0.24 cc	Sigma Aldrich, Formaldehyde sol. 37% wt in H_2O
K-Sorbate	1.62 g	Alfa Aesar, Potassium sorbate, 99%
H_2O	100 mL	Laboratory distilled water

[†]The amount of gelatine indicated corresponds to the background mixture of the phantom. The amount was increased for the three types of stiffer inclusions, specifically 14, 17 and 20 g, while keeping the amount of the rest of ingredients the same as for the solution batch for the background.

contrast ratios (between inclusion and background) of up to approximately 4.0 were obtained. In these cases, the amount of gelatine was chosen arbitrarily as 14, 17 and 20 g, which approximately corresponded with gelatin wt/wt concentrations of 12, 14 and 16%, respectively.

Dark visible particles were embedded into the phantoms. These particles were positioned so that their centroids lay in two parallel planes. Details of this will be discussed in Section 4.2.1.3. These particles consisted of basalt microspheres (Whitehouse Scientific Ltd., Chester, UK) of sizes between 180 and 212 μm.

4.2.1.2 Phantoms design

Moulds were designed so that the phantoms resembled a 3D compatible representation of the 2D axisymmetric model described in Chapter 3. The correct 3D representation coincides with the cylindrical geometry displayed in Figure 3.1. This geometry involves a toroidal lesion whose elastic properties are stiffer than those of the surrounding medium. However, this geometry was discarded due to the difficulty in manufacturing the toroidal inclusion. Instead, a cuboid form was opted for, which resulted from extruding the 2D model in the out-of-plane direction (see Figure 4.1). Therefore, the stiffer inclusions were designed as straight cylinders.

The dimensions of the final phantoms were 60×60×60 mm. The moulds were designed and 3D-printed using polylactic acid (PLA) as separate assembling parts, thus allowing the extraction of the phantom after gelation. Two cylindrical bars were added to the mould walls in order to leave two holes in the phantom: one as the urethra-like conduit and the other for the stiffer inclusion. Plastic flat sheets were placed onto each interior face of the mould to ensure perfect flat ends.

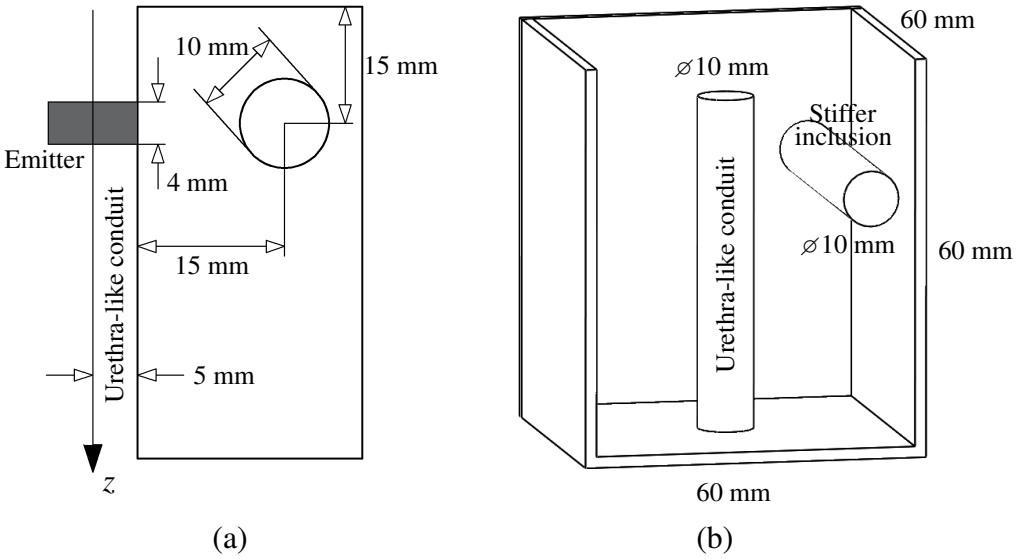

Figure 4.1: Details of the design of the mould. (a) Schematic 2D representation and dimensions of the model to be validated. (b) Final design of the mould fabricated as separated assembly parts. Solid bars for creating the cylindrical holes in the phantom for the urethra-like conduit and the stiffer inclusion. The frontal part has been removed to facilitate the visualisation of the interior.

The dimensions of the 2D model setup are shown in Figure 4.1a. The diameter of the urethra-like conduit was 10 mm, in order to allow the use of an emitter prototype fabricated by University of Granada (Spain) for another collaborative project. The diameter of the emitter was 11 mm. The difference of 1 mm ensured good mechanical contact between emitter and phantom surface. The diameter of the inclusion was also set as 10 mm, within the order of the size of prostate tumours.

According to the 2D wave propagation model for TU-SWE, the displacement

of particles is tangent to the out-of-plane direction and contained within planes perpendicular to the urethra (axis z). For this reason, the location of particles was set so that their centroids lay in two planes perpendicular to the urethra-like conduit at different z coordinate height (see Figure 4.1). Therefore two different scenarios were available for testing by moving the emitter along the urethra-like conduit and placing it at the corresponding height of each plane: one containing the inclusion (using plane A according Figure 4.1) and another not containing the inclusion (using plane B according Figure 4.1). These planes of particles were translated into the 2D axisymmetric model as two lines of constant z value (see Figure 4.2a).

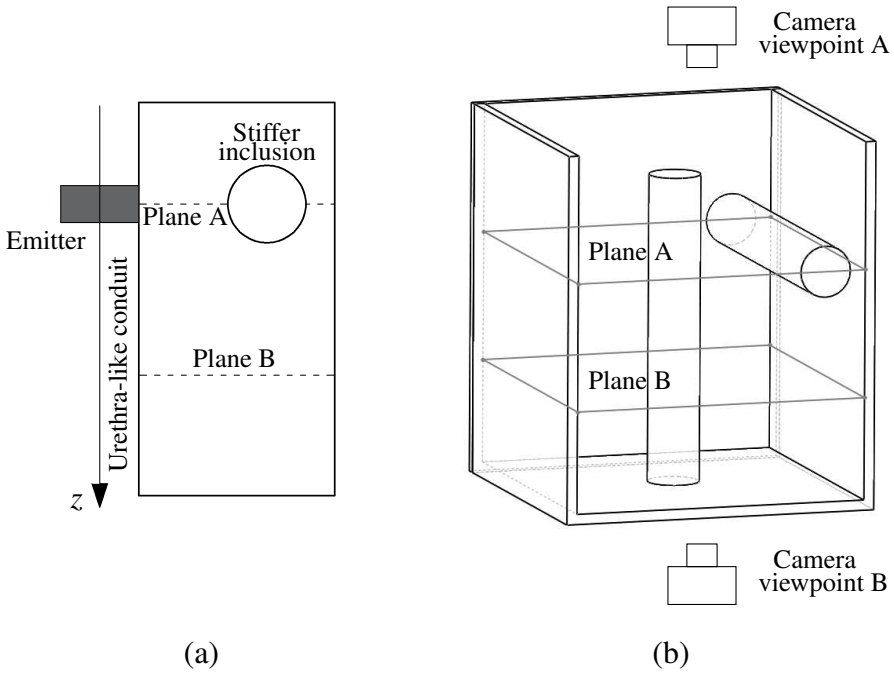

Figure 4.2: Location of the planes containing the visible particles: plane A contains a section of the inclusion whilst plane B does not. (a) 2D model showing the location of the planes of particles (dashed lines) relative to the emitter and the stiffer inclusion. (b) 3D representation of the mould showing the location of the planes contoured in dark blue and the viewpoints of the high-speed camera for recording each plane.

4.2.1.3 Steps for the phantom fabrication

Three phantoms were fabricated, i.e. one for each grade of inclusion stiffness. The steps taken for making the phantoms are listed below. These are based on a similar procedure to that detailed by Dunmire et al. (2013). The procedure of making the gelatine solution (steps 7-15) was repeated for each batch. All gelatine solutions were kept at the indicated temperature by using a controlled water bath. All mixing was conducted manually at a rate that minimised the introduction of air bubbles and the formation of clumps.

1) Place the plastic sheets over each interior side of the moulds.
2) Wrap the bars of the moulds with aluminium foil making sure there are no creases left.
3) Mount the moulds by gluing and sealing the parts using liquid PVC.
4) Leave the glued moulds to dry under a stream of hot air if possible.
5) Test the mounted moulds against leakage with distilled water.
6) Leave the moulds to dry again.
7) Weigh and prepare the ingredients used in the recipe.
8) Add the K-sorbate to the distilled water and begin mixing.
9) Heat the combined solution at a rate of approximately 1°C per minute.
10) Gradually add the gelatine powder to the combined solution.
11) Allow 5-10 minutes to verify that the gelatine is well mixed.
12) Cover and heat the solution to 85°C at a rate of approximately 1°C per minute.
13) Hold the mixture between 85°C and 90°C for 90 min.
14) Cool the mixture from 85°C to 40°C at a rate of approximately 1°C per minute.
15) Add the formalin and mix the solution gently.
16) Pour the solution into the moulds until the level of plane B of particles is reached (see Figures 4.2 and 4.3).
17) Allow 5-10 minutes for partial gelation of the surface (the gelatine solution

temperature should be of the order of 37°C- 38°C).

18) Keep the rest of solution at 40°C.
19) Carefully sprinkle the particles onto the surface of the phantoms.
20) Allow 5 minutes for fixation of particles to the surface of the phantoms.
21) Carefully pour more gelatine solution into the moulds using a syringe covering the first section created. Reach the level of plane A of particles.
22) Repeat steps 18-21.
23) Pour more gelatine solution until filling up the rest of the moulds.
24) Leave the solution to rest at room temperature until the following day.
25) The following day, unmould the phantoms by carefully removing the PVC seal (Figure 4.4).
26) Prepare the gelatine solution for the stiffer inclusions (steps 7-15).
27) Pour the new gelatine solution using a syringe into the hole for the inclusion left after removing the parts of the mould.
28) Leave the solution to rest at room temperature for 30 minutes.
29) Wrap the phantoms with plastic foil and keep them stored in a sealed container.

Figure 4.5 shows one of the final phantoms out of the mould. The inclusion does not contain basalt particles (see dashed red cylinder in Figure 4.5) due to the fabrication process of the phantom. The planes of basalt particles are formed before filling the space of the inclusion with a gelatine solution of higher concentration. While forming the planes of basal particles the space of the inclusion is occupied by a cylindrical bar attached to one of the mould's plates and wrapped with aluminium foil. The area of plane B beneath the inclusion shows less basalt particles since during the formation of the plane B of particles the cylindrical bar impedes the correct scatter of basalt particles from above the mould.

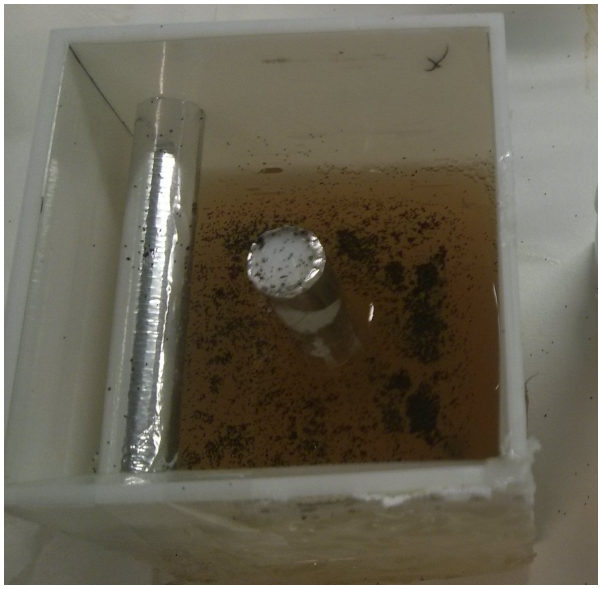

Figure 4.3: One of the 3D-printed moulds filled up with gelatine solution until the plane B boundary of particles (step 16). Basalt microspheres are on the surface. The flat plastic sheets covering the interior sides of the mould and the aluminium foil wrapping the two bars are visible.

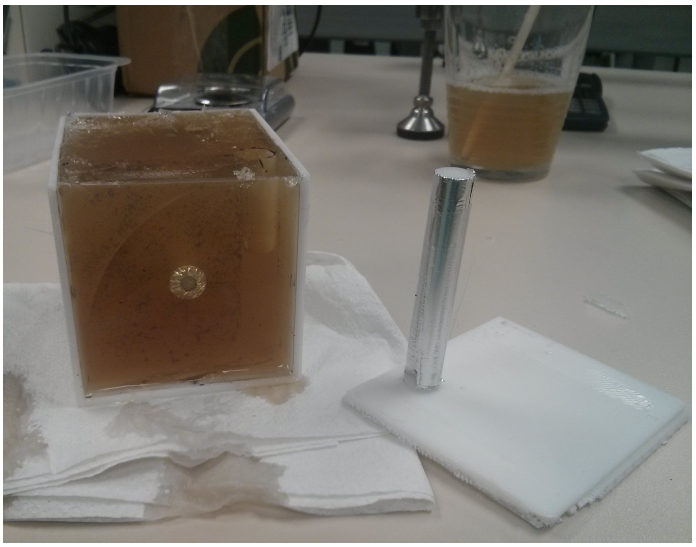

Figure 4.4: Unmoulding of one of the phantoms. After removing one of the assembling parts of the mould (right side), the remaining cavity is filled up with gelatine solution of higher gelatine concentration to create the stiffer inclusion.

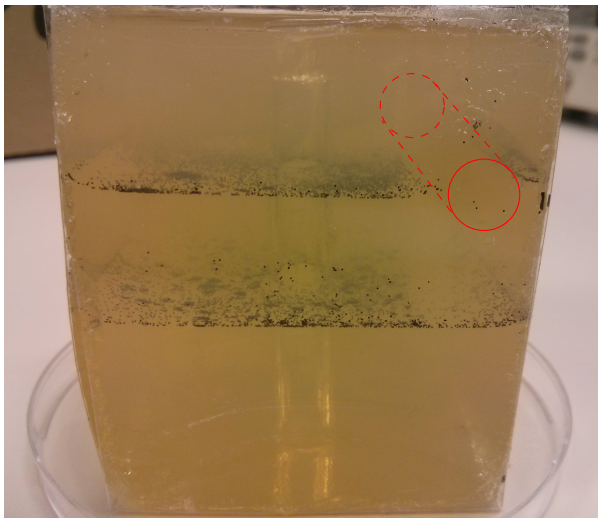

Figure 4.5: Completed phantom placed on a Petri dish. The mould has been removed and the inclusion cavity has been filled up. Both planes of particles are clearly visible, as is the urethra-like conduit which allows the insertion of the emitter, and the region where the stiffer inclusion is located (designated by the dashed red cylinder).

4.2.1.4 Rheological characterisation

Viscoelastic properties of the different gelatine solutions were characterised using a rheometer (MCR 300, Physica-Anton Paar, Graz, Austria) (see Figure 4.6). A rheometer is a device able to characterise the viscoelastic behaviour of fluids and soft solids by controlling and measuring both stress and strain. The type of rheometer used in the experiments falls into the category of shear stress-controlled rheometers. This type of rheometers measures the deflected angle in the sample produced by the torque applied.

For soft solid materials oscillatory rheometry is most common for measuring their viscoelastic properties. In oscillatory rheometry, the rheometer sets up an oscillatory excitation and measures the resulting oscillatory response. In the tests carried out, the excitation was set up in terms of strain while the response was measured in terms of stress. Since the sample is viscoelastic, there will be a time delay between excitation and response, indicated by a phase shift δ. By using

Figure 4.6: Rheometer (model MCR 300, Physica-Anton Paar, Graz, Austria) during one of the tests. Temperature control system connected. Rotating disk in contact with the sample.

the ratio between the stress σ, obtained from the applied torque, and the strain ε, obtained from the measured deflected angle, the complex shear modulus can be calculated (Equation 4.1). Then, the storage modulus G' and the loss modulus G'' can be calculated by using Equation 4.2.

$$G^* = \frac{\sigma}{\varepsilon} \tag{4.1}$$

$$\tan\delta = \frac{G''}{G'} \tag{4.2}$$

Small amounts of gelatine solution from the same batches prepared for the phantoms fabrication were poured and gelled into small Petri dishes. The day after the preparation of the phantoms, disk-shaped samples of 20 mm diameter and 2-3 mm thick were extracted from the Petri dishes for the rheometry tests (see Figure 4.7).

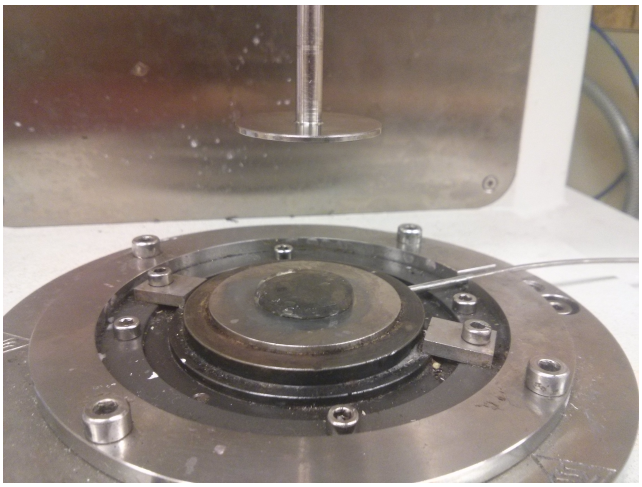

Figure 4.7: Disk-shaped sample of phantom mounted on the Peltier platform. Rotating disk plate elevated over the sample. Temperature sensor on the right side connected to the Peltier platform.

The rheometry tests were performed at a constant temperature of 20°C, the same temperature measured in the laboratory room where the optical tests were carried out. The samples were quickly extracted from their containers and immediately placed onto the rheometer. The whole preparation and testing of each sample lasted approximately 5 minutes: 2 minutes for cutting and extracting the sample from the Petri dish, 1 minute for correctly placing the sample on the rheometer, and 2 minutes for the set of preconditioning and oscillatory rheometry tests. Measures against loss of moisture were not considered necessary due to the short duration of the whole process.

In order to ensure accurate and repeatable measurements, preconditioning is considered essential prior to initiating rheometry tests (Nasseri et al., 2002, Yoo et al., 2011). Following the procedure outlined in the cited studies, preconditioning in all samples was achieved by inducing five cycles of low amplitude, 1% of shear strain, at a low shear rate, $0.1\%/\mathrm{s}$.

Two types of oscillatory rheometry tests were carried out: strain sweep oscillation and frequency sweep tests. Strain sweep oscillation tests aimed to determine the strain range of the linear viscoelastic regime, i.e. the range of strains

where the mechanical parameters measured did not depend on the value of strain. Frequency sweep tests aimed to obtain the value of the complex shear modulus G^* as a function of frequency. Three samples were tested per each type of gelatine phantom. Each sample was consecutively tested three times by lifting the upper plate and repeating the process from the beginning, i.e., from the preconditioning.

4.2.2 Optical test setup

Optical tests using a high-speed camera were carried out in order to measure the displacement of particles within a tissue-mimicking medium resulting from the propagation of shear waves generated according the TU-SWE technique. The experiments were carried in University of Jaen (Spain).

The general experimental setup is shown in Figures 4.8 and 4.9. The gelatine phantom was placed on an elevated platform with the urethra-like conduit vertically aligned. The emitter was introduced into the urethra-like conduit and held in position by a clamping structure (Figure 4.10). A source of light KL-2500-LCD (Schott North America Inc., NY, USA), guided by a flexible fibre optic bundle, was directed towards the phantom. A Fastcam SA1 high-speed camera (Photron Inc., San Diego, California, USA) with a zoom objective VZM™450i (Zoom Imaging Lens, Edmund Optics Inc.,Barrington, USA) was positioned pointing towards a 45° mirror that was placed below the platform where the phantom was held. The platform presented a centred aperture to allow the visualisation of the phantom from the bottom side. Temperature in the laboratory was kept at 20° C. Regular temperature checks were performed during the experiments.

The emitter prototype consisted of a PLA disk of 11 mm diameter and of 4 mm thickness, attached to the shaft of an electromagnetic rotational motor. The excitation signal was generated by a custom function generator, also designed and fabricated by University of Granada (Callejas et al., 2017). Dark spots were painted on the top side of the disk emitter to allow the reconstruction of its rotational

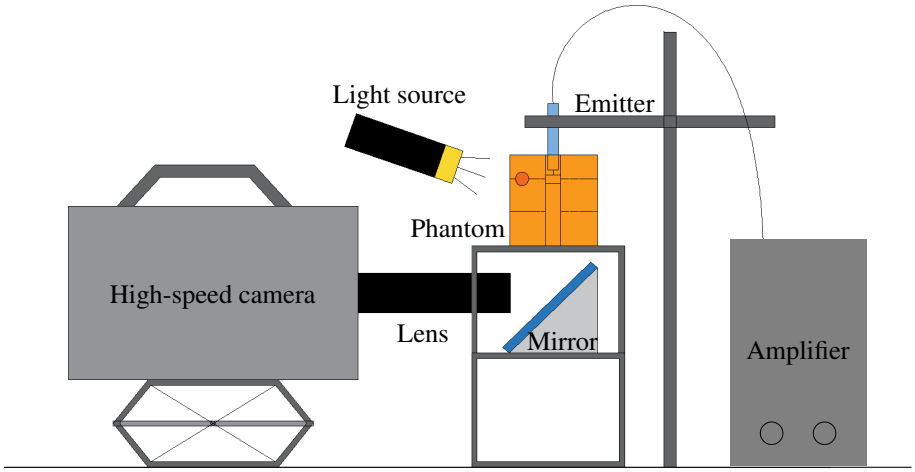

Figure 4.8: Schematic setup of the optical tests. The emitter (in blue) was held inside the phantom (in orange) through the urethra-like conduit. The emitter was connected to the amplifier. The excitation signal was created by a custom wave generator (not shown in the Figure). The function generator and the high-speed camera were synchronised. The high-speed camera pointed to the 45° mirror. The independent light source was pointed at the phantom.

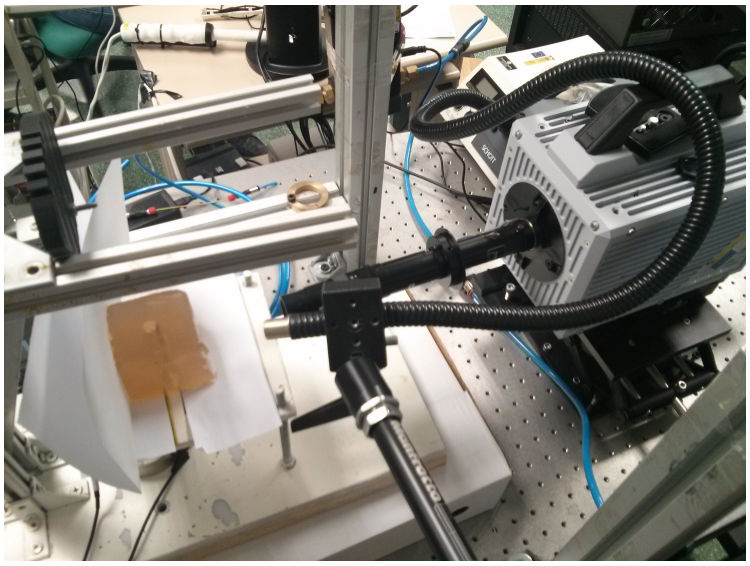

Figure 4.9: Setup for the high-speed camera-based tests. Phantom at the left side of the picture on top of the white platform. High-speed camera and light source at the right side pointing towards the phantom.

Figure 4.10: Setup for the high-speed camera-based tests. Phantom at the back side of the picture with the emitter inserted into the urethra-like conduit. High-speed camera pointing towards the 45° mirror located beneath the platform that held the phantom. A paper sheet was placed on top of the phantom to create a white contrast background for the video recording, since visible particles are black. Light source at the left side of the picture pointing towards the phantom.

displacement.

The excitation signal consisted of single sinusoidal cycles, with a fundamental frequency ranging from 100 to 300 Hz, with a pulse repetition frequency of 10 Hz. Limitations in the equipment did not permit the use of higher frequencies. The maximum voltage amplitude was set at 25 V in the function generator. Then, excitation signals were amplified three times using a low-frequency amplifier MA-25T (Fonestar Sistemas S.A., Barcelona, Spain). The function generator and the high-speed camera were synchronised. An initial 5 V spike, sent before the excitation signal, triggered the camera. The camera filmed at a rate of 10,000 fps with a resolution of 720×720 pixels. Actual spatial dimensions where obtained by recording the full frontal face of the disk emitter and measuring features with known dimensions before each test. The emitter was free to move along the urethra-like conduit in order to transmit the shear wave to each plane of

particles. Mechanical repositioning of the camera was performed using a precision 3D-positioning platform of 0.01 mm accuracy.

The high-speed camera tests were performed at a constant room temperature of 20° C, the same temperature as for the rheometry tests. Variation in the temperature of the order of a few degrees can produce changes in the mechanical properties of the gelatine phantom. However, formalin was added to the gelatine mixture, which elevates the melting point of the gelatine (originally around 32° C) and enhances the stability of the mechanical properties of the phantom against variations in the room temperature. The source of light was exclusively switched on for the filming time, i.e. 0.9 s. The distance between the main source of heat, i.e. the light source (a 250 W cold halogen lamp) and the phantom was about 80 cm. The distance between the tip of the fibre optic bundle that directed the light and the phantom was about 20 cm. The luminous flux at the tip of the fibre optic bundle was approximately 1300 lm according to the manufacturer.

Limitations in the available lab equipment at the time of the tests did not allow the measurement of the temperature of the phantom during the filming. Nonetheless, it is reasonable to consider that the phantom experienced a negligible level of temperature variation due to the experimental setup and conditions, i.e. the constant room temperature, the addition of formalin to the gelatine solutions, the considerable distance between the main source of heat, the distance between the tip of the fibre optic and the short exposure time to the light. Therefore, it can be assumed that the mechanical properties of the phantom were not affected by the source of light during the high-speed camera tests.

4.2.3 Particle tracking method

A custom particle tracking algorithm was developed in collaboration with University of Granada for extracting the true displacement from the optical tests described in Section 4.2.2. The algorithm was developed and implemented in

MATLAB® (Release 2017a, MathWorks, Natick, United States). The algorithm code can be found in Appendix C.

Before using the algorithm, image processing treatments were applied to the raw camera recordings for improving the visual quality. The open-source image processing software ImageJ was used (ImageJ, US National Institutes of Health, Maryland, USA) (Schneider et al., 2012). First, the raw recordings were decomposed frame by frame into a sequence of images over time. The raw recordings were filmed at 10,000 fps. Therefore, the time step between frames was 0.1 ms. Second, the contrast of the images was enhanced to improve the visibility of the dark particles relative to the background. Finally, the background was despeckled in order to reduce the noise of the images. Figure 4.11 shows an example of the resulting image after applying the image processing described in a frame.

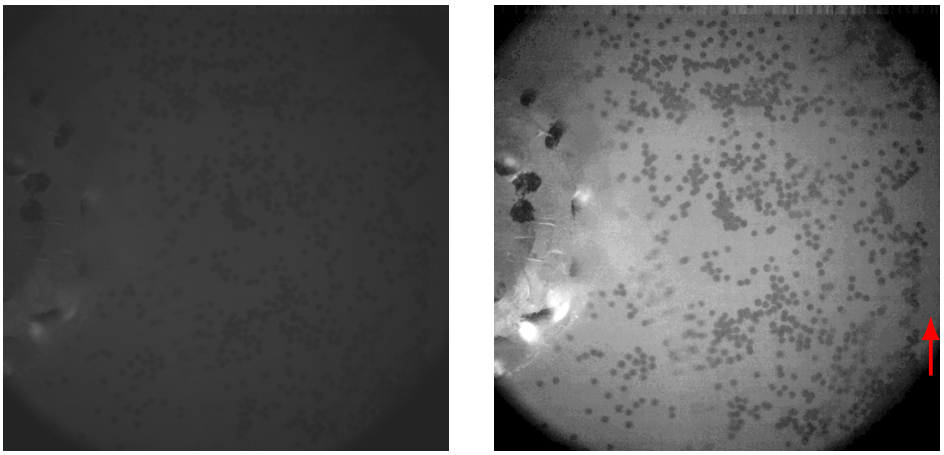

(a) (b)

Figure 4.11: Example of image processing of a frame from a high-speed camera recording on plane A. (a) Image before being processed. (b) Image after processing. Image (b) reveals a portion of the emitter disk on the left side and a blank space on the right side, corresponding to the stiffer inclusion (red arrow pointing to the blank space).

Two planes of basalt particles were set at planes A and B according Figure 4.2. These planes were not coincident with the 2D domain of the wave propagation

model, in fact, they were perpendicular to the 2D model as can be seen in Figure 4.2. For this reason, the validation of the model was based on the analysis of the intersection between both the 2D model and each plane of particles. These intersections consisted of two lines, denoted here as lines of analysis A and B, depending on which plane they were contained in (see dashed lines in Figure 4.2a. An example of a line of analysis in an image from a camera recording is shown in Figure 4.12 as a dashed blue straight line.

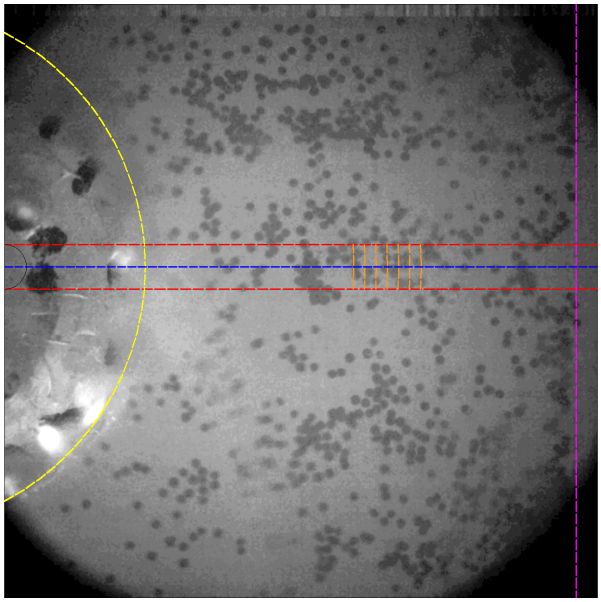

Figure 4.12: Schematic representation of the elements involved in the particle tracking method. Contour of the disk emitter in yellow. Contour of the stiffer inclusion in purple. Area of interest falls between the two red dashed lines. Blue line represents the line of analysis. Sections for calculating the cross-correlation are shown in orange.

The particle tracking method was developed based on a cross-correlation technique. First, a reference image was selected from the sequence of images, corresponding to an initial state before rotation of the emitter. Second, the axis of rotation of the disk emitter was located. Third, the area of analysis that contained the line of analysis was set (area between the 2 red dashed lines in Figure 4.12, with 1.5 mm of separation between both lines). Then, frame by frame, small quasi-rectangular sectors 0.1-0.15 mm wide (contoured in orange colour in Figure

4.12) were cross-correlated with their rotated versions from the reference image, until the entire area of analysis was covered. Rotation was applied about the axis passing through the centre of the emitter and perpendicular to the plane of particles. The angular displacement of each sector was estimated by finding the angle that yielded the maximum coefficient of correlation. This procedure was repeated for the entire sequence of images. Finally, the angular displacement was transformed into linear displacement u_θ, thus generating a time-space representation of the displacement generated by the shear wave propagation along the line of analysis.

4.2.4 Validation approach

Validation of the wave propagation model from Chapter 3 was performed by analysing its ability to replicate the observations from the optical tests.

First of all, KVFD mechanical properties of the different gelatine solutions were required. Values of the shear wave velocity derived from the optical tests, merged with the rheological viscoelastic characterisation, were used to characterise the KVFD mechanical properties.

The phase shear wave velocity c_s was calculated from the optical tests, according to the following expression (Chen et al., 2009, Mitri et al., 2011):

$$c_s(\omega) = \frac{\omega \Delta r}{\Delta \phi(\omega)} \tag{4.3}$$

where $\Delta\phi(\omega)$ is the phase change over a travelled distance Δr for an angular frequency ω. The phase change over the travelled distance was obtained by applying a Fast Fourier Transform (FFT) algorithm to the reconstructed particle displacement from the optical tests.

In the case of the rheological characterisation, values of the shear wave velocity c_s were calculated using Equation 3.32.

The full velocity dispersion curve was built up by combining values derived from both type of tests, described above. Both tests provided values at different

frequency ranges, however, as reported by (Bernal et al., 2013), the combination of both produces a wider picture of the velocity dispersion effect.

The full velocity dispersion curve was fitted by the theoretical KVFD expression for shear wave velocity (Equation 3.32) to obtain the KVFD mechanical parameters (μ, η and α). The Curve Fitting module of MATLAB® (Release 2017a, MathWorks, Natick, United States) was used.

The 2D FDTD model described in Chapter 3 was used for simulating the wave propagation observed in the optical tests. The calculated KVFD parameters and the geometrical setup shown in Figure 4.1a were used. The excitation signals were directly implemented into the model, using the displacement data of the emitter measured in each optical test. PML boundary conditions were turned off for a more realistic simulation of the phantom-air interface.

When comparing the results from the optical tests with the model simulations, some sources of uncertainty are to be expected. These include phantom manufacturing tolerances. For example, minor geometrical differences between the phantoms and model may occur. The fabrication of the inclusions could have generated a region of smooth transition between inclusion and background, thus creating a diffusive interface that could not be measured and therefore simulated in the model. Furthermore, small differences of less than 1 mm were found between dimensions of phantoms. Comparative methods able to transcend these geometrical differences were required.

Results from the optical tests and the model simulations were expressed as time-space representations of the wave propagation along the line of reference, as described in Section 4.2.3. A correlation analysis was proposed to compare both sets of results regardless of the above described differences. The denominated Pearson correlation coefficient $r_{Pearson}$ gives a measure of the linear dependency between two variables (Fisher, 1958). It has a value between +1 and −1, where 1 is total positive linear correlation, 0 is no linear correlation, and −1 is total negative linear correlation. Values of $r_{Pearson}$ close to 1 would indicate that results from the

optical tests and the model simulations have similar distribution of features such as the apparent group velocity.

A second validation approach involved a comparative analysis of the amplitude spectra from the optical tests and from the model simulations. The root-mean-square error (RMSE) normalised to the maximum amplitude value was used to quantify the difference between amplitude spectra.

4.3 Results

4.3.1 Rheological tests results

A rheological characterisation of the complex shear modulus G^* was carried out for the different gelatine batches used in the fabrication of phantoms, as described in Section 4.2.1.4. Strain sweep oscillation tests provided the strain range that ensures linear viscoelasticity in the rest of tests. Figures 4.13 and 4.14 show the resulting storage and loss moduli, respectively, from the strain sweep oscillatory tests. The four different gelatine concentration batches were tested at 1, 2 and 4 Hz with maximum strain ranging from 0.5 to 49%. Figures 4.13 and 4.14 show averaged results with standard deviation bars from tests using the three frequencies. Standard deviation bars are representative of the dependency of the storage and loss moduli for the three frequencies used.

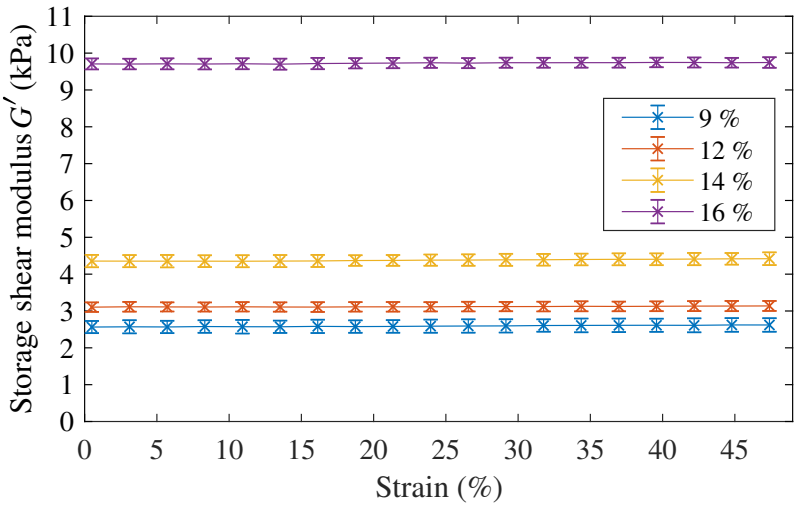

Figure 4.13: Storage shear modulus as a function of the strain for the different gelatine solutions with respect to the concentration of gelatine.

The linear viscoelastic regime is normally characterised by a plateau in graphs of the storage and loss moduli as functions of the maximum strain of the oscillations (Yoo et al., 2011). This means that the shear viscoelastic properties of the medium

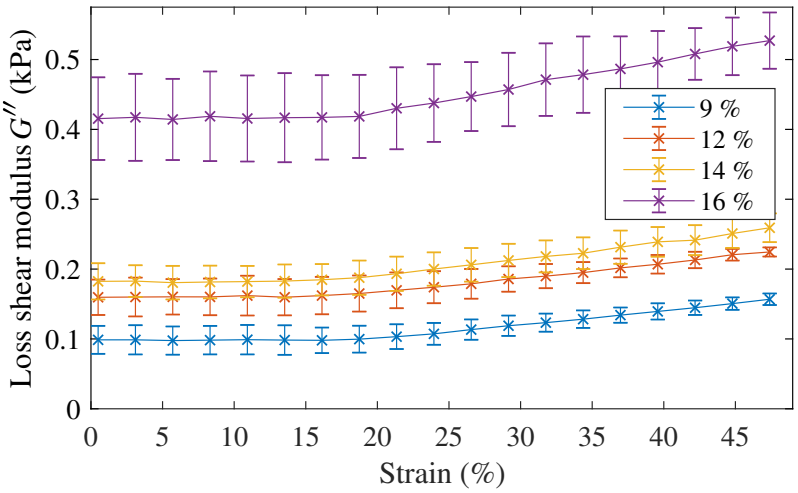

Figure 4.14: Loss shear modulus as a function of the strain for the different gelatine solutions with respect to the concentration of gelatine.

are not dependent on the strain. According to the obtained results, the storage modulus shows a steady plateau along the whole range of strain tested (see Figure 4.13). However, the plateau in the loss modulus graph (Figure 4.14) shows a point of inflexion approximately between 12 and 16% of strain. A steady ramp is noticeable after the point of inflexion for all the gelatine solutions, which means that the gelatine solutions show an increasing viscous response when increasing the strain levels over 15%. In any case, as a relatively conservative rule, the linear viscoelastic regime was maintained by using maximum strain values below 10% in the frequency sweep tests.

Frequency sweep tests aimed to characterise the complex shear modulus as a function of frequency. These tests were performed for each gelatine concentration batch, using a maximum strain of 1%, therefore within the linear viscoelastic regime, and for frequencies ranging from 0.5 to 50 Hz. Figures 4.15 and 4.16 show the real and imaginary parts of the complex shear modulus, also known as storage and loss modulus respectively. The storage modulus is related to the elastic response of the material, whilst the loss modulus is related to the viscous behaviour. Results are shown in terms of mean and standard deviation values for the three frequency

sweep tests for each of the three samples tested from each gelatine concentration batch. Standard deviation values are representative of the minor variability due to the use of different samples and the factors associated with the mechanical contact between sample and the plates of the rheometer.

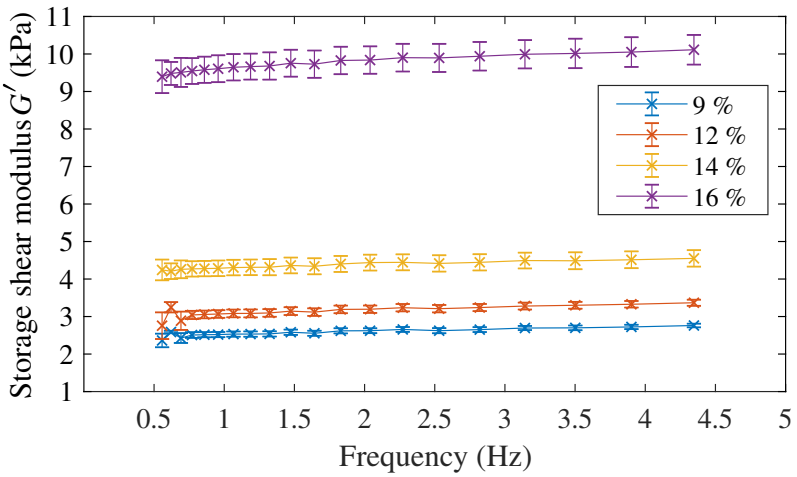

Figure 4.15: Storage shear modulus for the different gelatine solutions with respect to the concentration of gelatine.

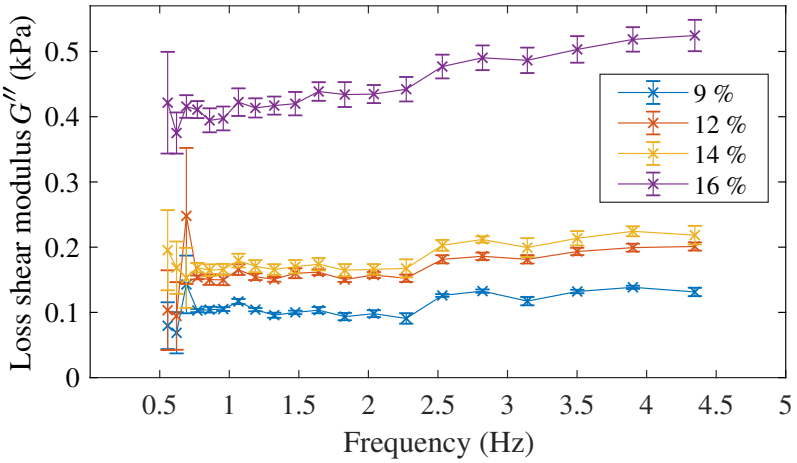

Figure 4.16: Loss shear modulus for the different gelatine solutions with respect to the concentration of gelatine.

Graphs in Figures 4.15 and 4.16 solely display results for frequencies between 0.5 and 4.5 Hz. Results at higher frequencies showed instabilities and incoherent

Table 4.2: Shear modulus contrast ratios between background and stiffer inclusions of phantoms.

	Gelatine concentration of the stiffer inclusions		
	12%	14%	16%
$\lvert G^* \rvert / \lvert G^*_{background} \rvert$	1.2	1.7	3.8

values for all the tested samples. At higher frequencies, inertial effects of the rheometer's components alter the measurements. This phenomenon has been observed in other rheological studies (Schroyen et al., 2017). Overall, higher concentrations of gelatine provided higher values of the elastic component G' of the shear modulus. The viscous component G'' also increased with higher concentrations of gelatine. Fluctuations in the values of storage and loss moduli were observed in all the graphs at frequencies below 0.7 Hz. However this phenomenon was not relevant to the general aims of the rheometry tests. The reasons for these fluctuations can be numerous. One plausible reason is the possible low sensitivity of the rheometer at very low frequencies.

Shear modulus contrast ratios between material from the background and the stiffer inclusions were calculated. Table 4.2 shows the resulting shear modulus contrast ratios after averaging for the valid range of frequencies.

4.3.2 Optical test results

Optical tests using a high-speed camera were carried out on translucent phantoms with embedded visible particles. Three phantoms were fabricated as described in Section 4.2.1, each one containing an inclusion with a different value of stiffness. The gelatine solution for the background was the same in all three phantoms. Tests were repeated six times for each phantom, specifically three times for each plane of particles. The excitation signals consisted of single sinusoidal cycles with centre frequencies ranging from 100 to 300 Hz.

The camera recordings captured the movement of dark basalt particles located in two planes, A and B, as defined in Section 4.2.3. Figures 4.11 and 4.12 show examples of the raw and treated camera recordings before applying the particle tracking method. The random pattern of marks on the disk emitter, and on the space without particles corresponding to the inclusion, were easily detected. In each phantom, the validation analysis focused on the area between the emitter and the inclusion, since the latter does not contain visible particles due to manufacturability limitations.

The particle tracking method described in Section 4.2.3 was applied to all the camera recordings. Results were obtained as a time-space representation of the displacement generated by the shear wave propagation along the line of analysis.

For the sake of brevity, all the illustrative examples that will be shown in this section were obtained from tests in the phantom that contained an inclusion with a stiffness contrast ratio of 3.8, and using an excitation signal with central frequency of 150 Hz. The analysis of the tests in this phantom with central frequency of excitation of 150 Hz will be referred to as the "example case" throughout the rest of the chapter. When other cases are shown their details will be specified.

Figure 4.17 shows an example of displacement reconstruction for the sample case in plane A. The propagation of the shear wave was recorded for 25 ms. The r coordinate ranged from 4 to 15.5 mm, with $r = 0$ corresponding with the centre of the disk emitter, and the inclusion starting at approximately $r = 15$ mm.

Although the excitation signal was a single sinusoidal cycle, the displacement of the emitter (shown in Figure 4.17 between coordinates $r = 4$ - 5.5 mm) showed a noticeable extension, due to the weak resistance of the emitter against the inertia of the phantom.

A comprehensive analysis of the emitter performance and transfer function requires a contact mechanics-based analysis. Such an analysis is beyond the scope of the work in this thesis and is proposed as a further investigation in Chapter 6.

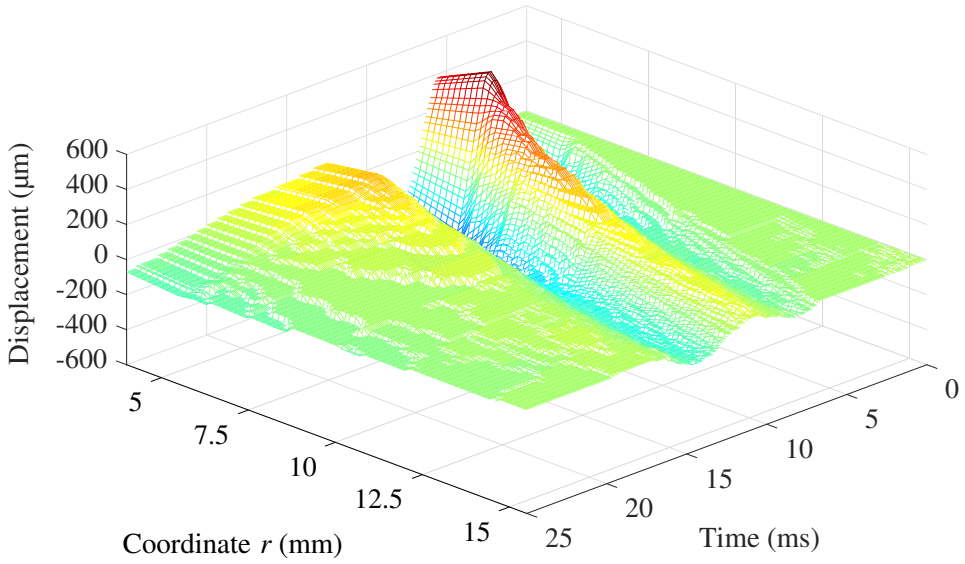

Figure 4.17: Time-space representation of the displacement due to shear wave propagation in plane A of the example case.

4.3.3 KVFD parameters of the phantom

The KVFD viscoelastic parameters of the phantom background and inclusions were required for the wave propagation model. The KVFD parameters were obtained after the reconstruction of the wave velocity dispersion curve from the optical and rheological tests.

First, phase velocities of the shear waves observed in all the optical tests were calculated. To do so, a spectral analysis of the phase variation over space was carried out by applying an FFT algorithm to the results from the optical tests. Note that space refers to the r coordinate in the line of analysis. Figure 4.18 shows the phase spectrum over space for the example case in plane B.

Phase velocity was calculated for all the optical tests using Equation 4.3. $\Delta\phi/\Delta r$ was obtained by fitting the phase variation over space with linear polynomial functions.

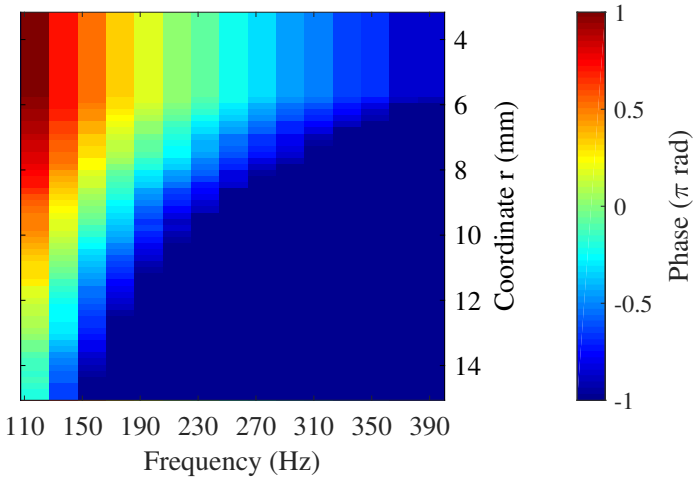

Figure 4.18: Example of phase spectrum over the line of analysis for the example case in plane B.

Subsequently, phase velocity was calculated for the low frequency range using the shear complex modulus obtained from the rheological tests in Equation 3.34.

Results from both high-speed camera-based and rheological tests were then combined in a single velocity dispersion curve. Results from all the experiments in terms of mean and standard deviation values are shown in Figure 4.19. Although the original excitation signal was monochromatic with frequencies ranging from 100 to 300 Hz, the final transmitted wave contained a wider frequency spectrum due to nonlinearities introduced by the actuator of the emitter.

Finally, the combined set of data was fitted by the KVFD expression for the shear wave velocity (Equations 3.32, 3.33 and 3.34). The obtained KVFD parameters were $\mu = 2.61$ kPa, $\eta = 205.2$ Pa$^{\alpha}$ and $\alpha = 0.2117$. The goodness-of-fit was acceptable, with $R^2 = 0.9610$.

4.3.4 Validation of the wave propagation model

The 2D wave propagation model from Chapter 3 was used to replicate the observations from the optical tests according to the methodology described in Section 4.2.4. Geometry, dimensions and boundary conditions of the model were

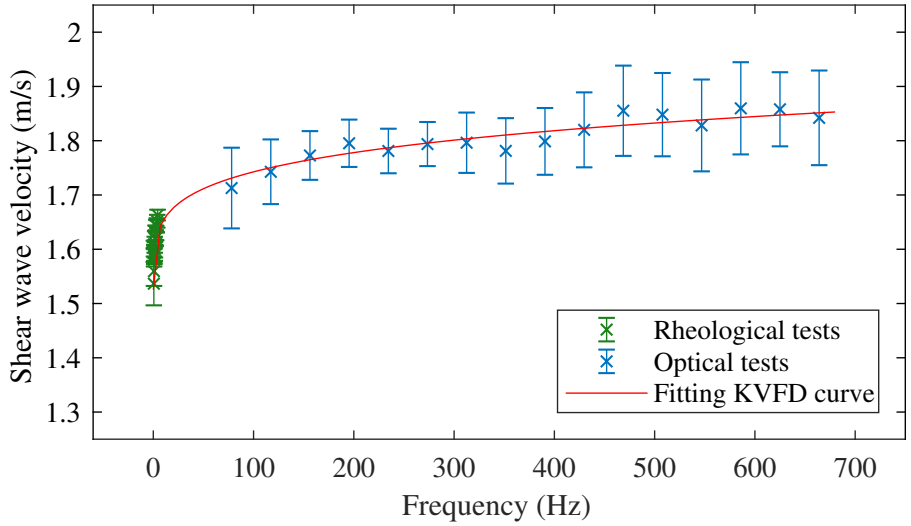

Figure 4.19: Results in terms of mean and standard deviation values.

also detailed in Section 4.2.4. KVFD mechanical parameters for the background of the medium were obtained by fitting combined data from the optical and rheological tests in Section 4.3.3.

No particles were embedded into the inclusions due to manufacturability limitations. For this reason, reconstruction of the shear velocity of the inclusions, and therefore reconstruction of their KVFD parameters, was not possible. Instead, estimates of the stiffness contrast ratio between inclusions and background of the phantom were used (Table 4.2). KVFD parameters of the inclusions were then calculated by making the same assumptions described in Section 3.4.1.

The displacement of the emitter obtained from each optical test was implemented as an excitation signal in each simulation. An example of a simulation is shown in Figure 4.20a. The simulation replicated the wave propagation for the example case and plane A. According to the figure, the urethra-like wall is located at $r = 5.5$ mm (top side of Figure 4.20a), and the interface between background and inclusion is located at $r = 15$ mm (bottom side of Figure 4.20a).

Reconstruction from the optical test for the same example is shown in Figure 4.20b. Both sets of result display common trends, in terms of distribution of features

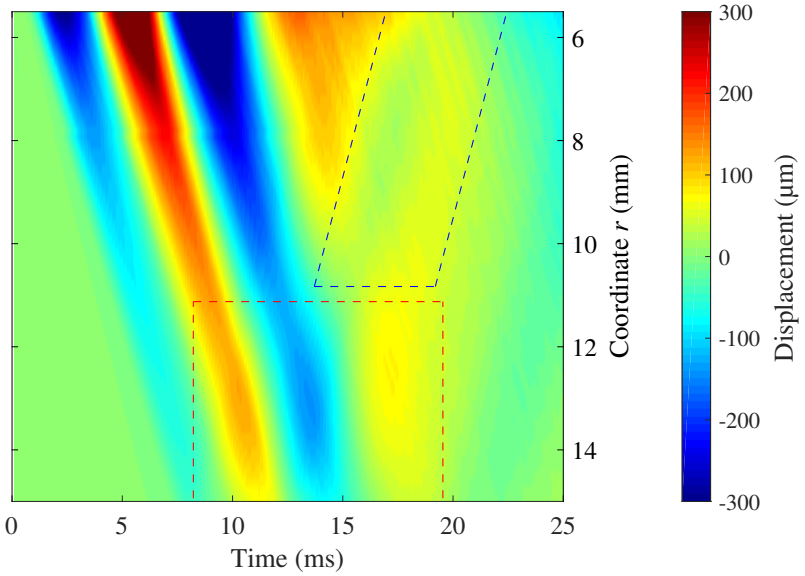

(a)

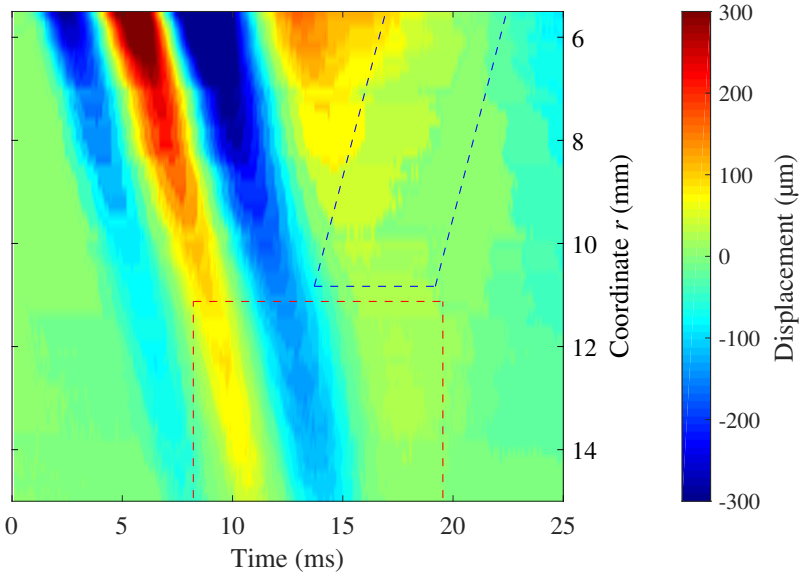

(b)

Figure 4.20: Time-space representation of the wave propagation in the example case, plane A, from (a) the model simulation and (b) the optical test. The top side of each figure is where the contact with the disk emitter is located. The bottom side of each figure corresponds with the boundary with the stiff inclusion. The reflected wave going back to the emitter is clearly noticeable within the area contoured by the dashed blue line in Figure (a). The perturbation due to the interaction between the incident wave and its reflection against the stiff inclusion is observable in both figures within the area contoured by the dashed red line. The perturbation is observed as a change in the time-space alignment of the amplitude peaks.

and amplitude. However, while the perturbation generated by the reflection was noticeable in the case of the model, it was not visible in the experimental case (compare propagations within the dashed blue contours after 15 ms in Figures 4.20a and 4.20b).

Figure 4.21b shows the reconstruction from the optical test in the same phantom but in plane B, i.e. not intersecting the inclusion. The presence of a perturbation in the apparent wave group velocity in the proximity of the inclusion can be seen (Figure 4.20b), that is not visible in the case of no-inclusion (Figure 4.21b). The apparent wave group velocity was estimated from the slope of the line fitted through the peaks of the time-space representation.

The observed perturbation was believed to result from the reflective interaction of the wave with the inclusion. Indeed, the results for plane B (Figure 4.21) do not show the perturbation, while the results for plane A (Figure 4.20) clearly do (compare the wave propagation within the dashed red contours in Figures 4.21 and 4.20). Furthermore, this type of perturbation was consistently observed in all the optical tests performed in the phantom containing the inclusion with the highest stiffness contrast ratio, whilst in the other two types of phantoms, the perturbation was less noticeable. In Figure 4.22, an example is shown which corresponds to the optical test in a phantom with an inclusion of stiffness contrast ratio of 1.2 and with an excitation with centre frequency of 200 Hz. A weaker perturbation was observable at the proximity of the inclusion (within the dashed red area).

Overall, all of the simulations in plane A showed a clear perturbation near the inclusion and a reflected wave travelling back to the emitter. On the other hand, all results from the optical tests showed weaker perturbations near the inclusions compared with the simulations, and non-perceptible reflected waves going back to the emitter. Geometrical differences between the model and the phantoms were believed to be involved in this disagreement. The inclusions produced for the optical tests were straight cylinders, whereas the 2D axisymmetric model considered toroidal inclusions when considering a 3D representation.

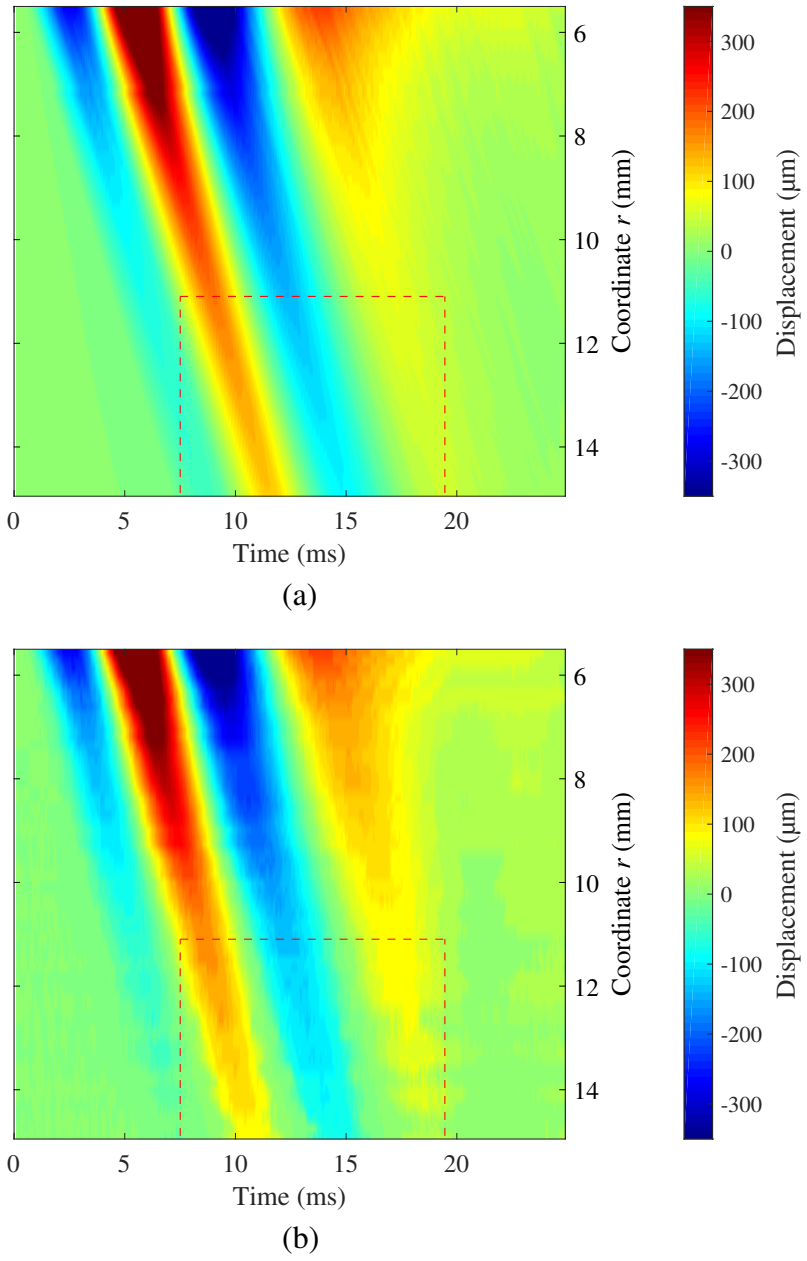

Figure 4.21: Time-space representation of the wave propagation in the example case, plane B, from (a) the model simulation and (b) the optical test. The top side of each figure is where the contact with the disk emitter is located. In this case, there is no inclusion at the bottom side of each figure since the plane of propagation is plane B, therefore, perturbations due to wave reflection are not noticeable.

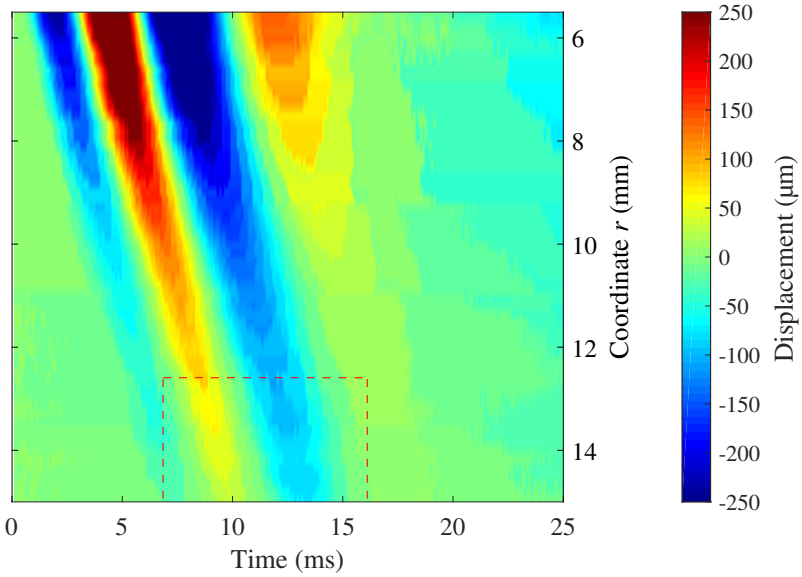

Figure 4.22: Time-space representation of the wave propagation from the optical test with inclusion of stiffness contrast ratio of 1.2. Excitation with centre frequency of 200 Hz. The top side of each figure is where the contact with the disk emitter is located. The bottom side of each figure corresponds with the boundary with the stiff inclusion. The perturbation due to the interaction between the incident wave and its reflection against the stiff inclusion is weaker than in the case of maximum stiffness contrast ratio (example in Figures 4.20) but observable within the area contoured by the dashed red line. The perturbation is observed as a change in the time-space alignment of the amplitude peaks.

By analysing the wave propagation in plane A, toroidal inclusions in the model create a concave curved interface that produces reflections converging to the emitter. In the same plane A, straight interfaces in the phantom produce reflections that diffract, therefore with added amplitude attenuation. It was believed that in the experimental cases, the attenuation due to the added diffraction reduced the amplitude of the reflections to a level below the sensitivity of the optical tests.

In any case, it can be concluded that the wave propagation before reflection was well replicated by the model. The correlation coefficient $r_{Pearson}$ was between 0.9671 and 0.9894, with a mean value of 0.9785 and standard deviation of 0.0068. These figures close to 1 indicated a high similarity between optical tests and model simulations in terms of apparent group velocity.

It can be also concluded that the amplitude attenuation of the wave before reflection was well replicated by the model. An example of amplitude spectrum from the optical test in the example case is shown in Figure 4.23a. The corresponding model simulation is shown in Figure 4.23b. It can be seen that there exists similarities between both amplitude spectra. The normalised RMSE, calculated according to Section 4.2.4 as a measure of the difference between the simulation and the experimental results, was between 2.36 and 5.77%, with a mean value of 3.76% and standard deviation of 1.20%. These values that can be considered to be relatively low.

Overall, the wave propagation model replicated the experimental observations with acceptable accuracy, hence the model was considered validated. In any case, further improvements in the experimental protocol would improve the experimental data and allow the observation of features that remained not fully proved, for instance the reflections. An improved version of the experimental protocol will be proposed as future work in Chapter 6.

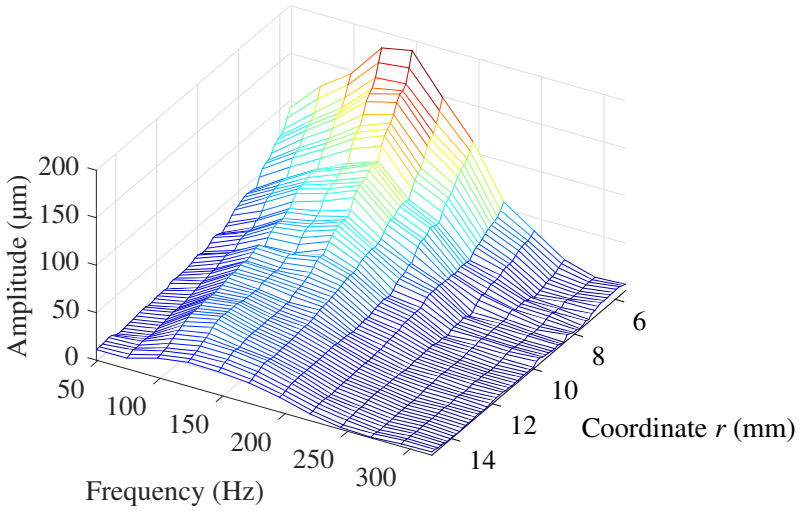

(a)

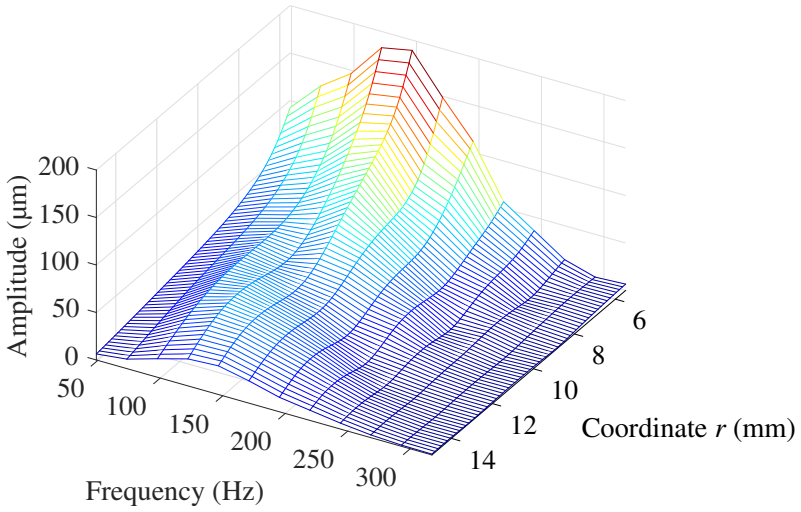

(b)

Figure 4.23: Amplitude spectrum from (a) the optical test of the example case in plane A, and (b) the model simulation of the example case in plane A.

4.4 Discussion and conclusion

The development of an experimental validation method for the TU-SWE wave propagation model (detailed in Chapter 3) has been described in this chapter. The method is based on the use of a high-speed camera setup for recording the true displacement of particles generated by a TU-SWE prototype emitter in a soft tissue-like elastography phantom. The phantom was translucent containing stiff translucent inclusions with embedded basalt particles at different planes of interest. Studies using high-speed camera for observing the displacement of single particles due to shear waves generated by ARF excitation have been published (Bouchard et al., 2009, Czernuszewicz et al., 2013, Suomi et al., 2015). However, no studies that consider more than a single particle and shear waves produced by mechanical actuators were found. To the author's knowledge, the method described in this chapter is the first attempt at using a high-speed camera technique to measure the displacement field in 2D produced by shear waves induced by a mechanical actuator.

Characterisation of the viscoelastic properties of the different gelatine solutions was achieved by combining the results at low frequency (0.5 - 4.5 Hz), from rheometry oscillatory tests, and the results at higher frequency (100 - 700 Hz), from the high-speed camera observations. The range of frequencies used in the rheometry tests was limited by the instabilities produced at high frequency (up to 100 Hz) due to inertial effects of the device. This type of instability has been commonly reported when using rheometers where the deflected angle sensor and the rotational motor are not mounted on the same shaft (Klemuk and Titze, 2010, Schroyen et al., 2017), such as the rheometer employed in this work. The use of rheometers with separated driver motor and sensor is encouraged for future work since this type of rheometer has been proven to have a better control of the inertial instabilities at high frequency (Franck, 2005).

Model simulations were carried out by setting the geometry and viscoelastic

properties of the phantoms in order to compare the wave propagation model and camera observations. Some small differences in the amplitude of the wave reflection from the stiff inclusion were observed (see Figures 4.20). These differences were proved to be due to the geometrical mismatch between the 3D geometry of the model (Figure 3.1) and the geometry of the phantoms (Figure 4.1b). The 3D geometry of the model considered axial symmetry, thus modelling stiff lesions as toroidal shapes, while the the stiff inclusions contained inside the phantoms were fabricated as straight cylinders. This mismatch implies a difference in the component of attenuation due to geometrical diffraction. In the experimental case the geometrical diffraction was due to a straight interface, however, in the case of the 3D axisymmetric model the geometrical diffraction effect was reversed since the interface between the background and the stiff inclusion was concave, thus getting a reflected wave focused back on the location of the emitter in the urethra-like conduit.

Furthermore, the fundamental frequency for the excitation used in the high-speed camera based experiments ranged from 100 to 300 Hz. This range provided information on the phase wave velocity from 100 to 700 Hz. The amplitude spectrum showed low level of energy for the highest frequencies in the range (Figure 4.23). It is encouraged to increase the upper limit of the range for the excitation signal used in the high-speed camera based experiments in order to obtain more energy at high frequencies.

Overall, the significant similarities obtained between the experimental results and the wave propagation model, specifically the apparent group velocity of the forward and reflected waves, as well as the amplitude attenuation of the forward wave, were considered sufficient to validate the wave propagation model developed for the TU-SWE technique.

4.5 Chapter summary

This chapter was dedicated to describing the experimental validation of the wave propagation model for the TU-SWE technique.

First, a brief review was carried out encompassing recipes for tissue-mimicking material for elastography applications and optical methods for capturing displacement due to shear wave propagation.

The methodology for the experimental validation was then described. The design and preparation of phantoms, as well as the optical test setup, were reported in detail. A gelatine-based recipe was used to fabricate translucent phantoms containing visible particles and stiffer inclusions. A high-speed camera-based technique was used to capture the displacements within the phantom due to shear wave propagation according the TU-SWE approach. A particle tracking algorithm was developed to extract the data from the optical tests.

Results were presented as space-time representations of the wave propagation. KVFD viscoelastic parameters of the different parts of the phantoms were extracted by fitting the wave velocity dispersion curve with its theoretical KVFD expression. The wave velocity curve was obtained by combining results from rheological tests and optical tests. Wave propagation simulations were used to replicate the observations from the optical tests.

Finally, the model was considered validated after analysing several metrics for studying the degree of agreement between simulations and experimental observations. Good results were obtained, which indicated that the wave propagation model was able to replicate the experimental observations with acceptable accuracy.

Chapter 5

Image reconstruction methods

A novel TU-SWE approach for the diagnosis of prostate cancer and the HIFU ablation monitoring of such tumours has been presented in Chapters 1 and 2 of this thesis. This novel approach is based on shear waves, which are propagated into the prostate. The presence of stiff lesions perturbs the propagation, thus generating reflections that travel back to the urethral wall where they could be sensed by an array of receivers. The measured signals carry information about the stiff lesions, such as location, size and mechanical properties.

In this chapter, methods for reconstructing the features of stiff lesions within the prostate are proposed, described and analysed. First, several approaches are reviewed. Two reconstruction methods are chosen: a Reverse Time Migration and a Genetic Algorithm technique. The wave propagation model described in Chapter 3 is used as the forward model for the two reconstruction methods. Furthermore, several device configurations regarding the arrangement of emitters and receivers are analysed in order to obtain an optimal configuration in terms of quality and efficiency of the reconstruction.

5.1 Review of various reconstruction methods

Inversion methods for image reconstruction using data collected by arrangements of receivers are commonly found in many physical applications. In this thesis, two groups of reconstructions methods that have been applied to medical imaging problems were investigated: wave migration and randomised search methods.

5.1.1 Initial considerations

Some initial conceptual design considerations for the TU-SWE probe were taken into account prior to reviewing the reconstruction methods:

- The conceptual design of TU-SWE contains an array of emitters and receivers that can cover the whole cylindrical body of the probe.
- Although the TU-SWE probe was conceptually developed to allow for a 3D scan of the prostate, a 2D simplification was used in previous chapters. Therefore, in this chapter the arrangement of emitters and receivers was solely considered along the axial direction of the probe.
- The conceptual TU-SWE probe was designed to scan the prostate from the urethra. Therefore, the length of the probe is limited by the length of the prostatic urethra, here set as 40 mm, according the assumptions detailed in Chapter 3.
- Designs of emitters and receivers may employ different transduction mechanisms, in which case, they could not swap their operational mode, i.e. emitters could not work as receivers and *vice versa*.
- Emitters and receivers have not been designed yet, nonetheless, their length was considered to be within the range of 0.5 - 2 mm.

5.1.2 Wave migration methods

Wave migration encompasses a set of imaging techniques that places reflectors within the medium. In general terms, migration methods are inversion methods that involve the rearrangement of wave information elements from time to space domain so that reflections and diffractions are plotted at their true locations (Sheriff, 2012). Two of the most widely used techniques are the back projection methods and the time reversal methods. Back projection methods are widely used in medical imaging and radar, and are known as Kirchhoff migration in geophysics and seismic imaging disciplines (Liu and Liu, 2014). A particular implementation of time reversal, called RTM, comes from geophysics literature and has recently been applied to medical imaging (Liu et al., 2013).

Kirchhoff migration propagates the source and receiver wavefields down to each potential reflector point using ray-based techniques. These ray-based techniques are high-frequency solutions of the wave equation (Farmer et al., 2009). In order to obtain the exact location of a reflector, the method redistributes the received acoustic energies from each receiver position and produces a summation in space by spatial integration. If there is a large number of receivers, the amplitude at the location of the reflector will be enhanced, otherwise the amplitudes should be minimal (Sheriff and Geldart, 1995).

RTM predicts the location of each reflector running the wave equation backwards for all receivers. The source signal is injected at the source position into a numerical model, commonly a FD method. The recorded wavefield is reintroduced into the model at the receiver locations reversed in time, i.e. from late to early times. To predict the reflectivity at each position, the estimated incident and reflected wavefields are correlated at each location for each emission shot. Then, all the correlated wavefields are merged to generate the output image, where higher values of correlation correspond with the location of reflectors (Farmer et al., 2009).

Both class of techniques require an initial estimate of the velocity field

of the medium, however, traditional back projection methods are based on the assumption that the wave velocity distribution in the medium is relatively constant. For heterogeneous media, such as for brain cerebral vascular imaging, traditional back projection algorithms results in poor reconstruction images (Wang and Jing, 2015). It has also been proven that, relative to Kirchhoff migration in seismic imaging, RTM provides more accurate reconstructions for the same level of initial information of the velocity field (Zhu and Lines, 1998). The key feature of RTM against Kirchhoff migration is that, once the source and receiver signals are injected into the model, RTM does not present limitations on propagation with direction (Farmer et al., 2009), thus improving the detection of steeply dipping interfaces or lower boundaries of reflectors (Liu et al., 2013, Müller et al., 2012).

RTM was originally introduced for the first time in seismology by Whitmore (1983). However, due to its heavy computing requirement, it was not until after 2000 that RTM became a practicable method over other less computationally demanding migration methods such as Kirchoff migration. One of the major applications of RTM is hydrocarbon exploration, as discussed by Farmer et al. (2006). Moreover, RTM has been successfully used in other applications, such as non-destructive evaluation using ultrasound for crack detection (Wang and Yuan, 2005, Zhou et al., 2007) and location of embedded elements in concrete foundations (Müller et al., 2012, Grohmann et al., 2016).

Both back projection methods and RTM have been recently compared in medical imaging applications. Liu et al. (2013) used back projection (Kirchhoff migration) and RTM for image reconstruction in *in silico* and *ex vivo* transcranial thermoacoustic tomography. The *in silico* experiments in human brain mimicking material were carried out in order to compare both reconstruction techniques. Under the same conditions, RTM provided better results in terms of geometrical accuracy and image quality. Results from experiments in an *ex vivo* monkey's head showed image reconstructions with distorted geometries of inserted needles when using both Kirchhoff migration and RTM, due to a selected wave velocity field far from

reality according to the authors. Despite this lack of accuracy, RTM provided less geometrical distortion and sharper contour of the features compared with Kirchhoff migration. In a second publication, Liu and Liu (2014) proposed an iterative method that improved the image distortion when using RTM. The iterative process updated the wave velocity field for the model used in the RTM reconstruction from previous RTM results, until the convergence of the output image was observed. Furthermore, Hristova et al. (2008) carried out a comparative study between back projection and time reversal approaches for thermoacoustic tomography. The authors observed that time reversal approaches were the least restrictive in terms of number of sources and receivers.

Another study of RTM applied to medical imaging was conducted by Wang et al. (2016). The authors presented a novel theoretical approach for optical tomography using RTM image reconstruction. They used RTM reconstruction in different *in-silico* models. The authors obtained high-quality image reconstructions with sufficient contrast and spatial resolution, thus making structure identification feasible. Moreover, the authors tested different methods for the image correlation in RTM, thus obtaining in some cases improved image quality and reduction of artefacts.

5.1.3 Randomised search methods

An inverse problem can be solved by using a previously developed model of the physical phenomenon. The model is used for finding a set of model parameters that minimises the difference between the predicted and the actual measurements of the physical phenomenon. The process of finding the set of model parameters that minimise the difference between measurements can be achieved by means of an optimisation algorithm (Gallego and Rus, 2004).

Randomised search methods such as Genetic Algorithms (GAs) and simulated annealing have been successfully applied as optimisation algorithms in the field

of non-destructive evaluation, for instance for damage detection (Rus et al., 2006). Their capacity of dealing with complex problems, and at the same time, their permanent insistence on global convergence is an advantage against other optimisation techniques such as gradient-based methods (Rus et al., 2006).

Simulated annealing was presented by Kirkpatrick et al. (1983). The name and inspiration come from annealing in metallurgy, a technique involving heating and controlled cooling of a material to increase the size of its crystals and reduce defects. Simulated annealing interprets slow cooling as a slow decrease in the probability of accepting worse solutions as it explores the solution space.

GAs were introduced by Holland (1975) and they belong to the class of evolutionary algorithms, a group of optimisation algorithms inspired by natural evolution. In a GA, a population of candidate solutions is evolved toward better solutions by using evolutionary concepts such as crossover, mutation and tournament selection.

GAs and simulated annealing can be seen as close relatives. A simulated annealing algorithm can be thought as a GA where the population size is only one, and where there is no crossover, but only mutation. While simulated annealing creates a new solution by modifying only one solution with a local move, GAs normally create solutions by combining the former best candidates. Simulated annealing has been catalogued as a "quick starter" method, since it obtains good solutions in a short time, but it is not able to improve on that given more time. Conversely, GAs have been catalogued as "slow starters" and are able to improve the solution consistently when given more time (Kohonen, 1999). However, in practice it cannot be stated that one is more advantageous than the other before comparing both under the same conditions for the same optimisation problem (Kohonen, 1999).

5.1.4 Proposed reconstruction methods

After considering the methods mentioned above, two techniques were selected: the RTM and the GA techniques.

RTM was chosen in preference to Kirchhoff migration since RTM usually provides more accurate image reconstruction under the same conditions as found in the literature review in Section 5.1.2. Moreover, RTM can directly use the previously developed wave propagation model, described in Chapter 3 and validated in Chapter 4. Using the Kirchhoff migration method would require the derivation of its mathematical expression, which is beyond the scope of this thesis. To the best of the author's knowledge, this thesis shows the first application of RTM in elastography imaging.

From the group of randomized search methods, GAs were selected over simulated annealing. Although the opposite selection might have also been suitable, the choice was supported by previous successful experiences in optimisation problems involving wave propagation models by the collaborative group of University of Granada. Gomez et al. (2013) used a GA-based method for obtaining the shear moduli of a multi-layered tissue-like medium under a rotational excitation applied to its surface. Rus et al. (2013) used a GA-based method for obtaining some relevant mechanical parameters from denatured *ex vivo* porcine corneas during the cell-culturing process in a bioreactor. Melchor et al. (2017) used a GA method for optimising the design of a rotational piezoceramic actuator for transmitting shear waves throughout the surface of a tissue-like medium modelled by FEM.

5.2 Reverse Time Migration reconstruction method

In this thesis, an RTM method was developed for image reconstruction for the TU-SWE application. The RTM methods aims to provide information concerning the location of stiff regions in the prostate that can be associated with either cancer nodules or thermally ablated tissue. Both cancer nodules and thermally ablated tissue will be referred to as stiff lesions throughout this section.

RTM localises the elements within the medium that generate wave reflections, as mentioned in Section 5.1.2. The method uses a wave propagation model, usually based on FD (Wang et al., 2016). The excitation and recovered experimental signals are propagated into the model, which approximates the wave velocity field inside the medium. The wave velocity field of the model is usually set as homogeneous or smoothed. In this thesis, the FDTD-based wave propagation model described in Chapter 3 was used. A homogeneous distribution of the wave velocity field was chosen, since information concerning the position and shear wave velocity of the stiff lesions was unknown.

The method for obtaining the initial wave velocity value for the homogeneous model was not analysed here. Nevertheless, some basic ideas could be explored in future work, such as the iterative method described by Liu and Liu (2014).

5.2.1 Description of the RTM method

Considering an experimental device configuration with M emitters and a set of P receivers distributed along the urethral wall, the RTM method yields an image reconstruction by following the procedure below (see also Figure 5.1):

1. Experiment: shear waves are transmitted by the emitter e_m (where $m = 1,2,3,\ldots M$) and detected at all P receivers' location. Signals are acquired by the receivers during sufficiently long times in order to capture all the multiple reflections from the reflectors within the medium.

2. Forward modelling: the excitation signal used in the experiment is implemented into the wave propagation model at the corresponding location of the emitter e_m. Then, the wave propagation is simulated and the displacement field $F_m(r,z)$ of the forward wave propagation is stored at every time step t_n.

3. Reverse modelling: the signal measured on each receiver during the experiment is reversed in time and implemented into the wave propagation model at the location of each corresponding receiver. Then, the wave propagation is simulated and the displacement field $R_m(r,z)$ of the reversed wave propagation is stored for every time step t_n.

4. Image correlation method: the correlation between the displacement fields from the forward modelling F_m and the reverse modelling R_m is calculated at each time step t_n.

5. Iterative process: Iteration of steps 1-4 for the combination m that considers transmission from emitter e_m and detection at all the P receivers.

6. Stacking: all the M correlation images are stacked up to produce the final reconstruction image I.

The displacement field, from both the forward and the reverse simulations, was directly stored at each time step t_n during the simulations since a displacement-strain-stress formulation was chosen for developing the wave propagation model in Chapter 3 (Section 3.3.2).

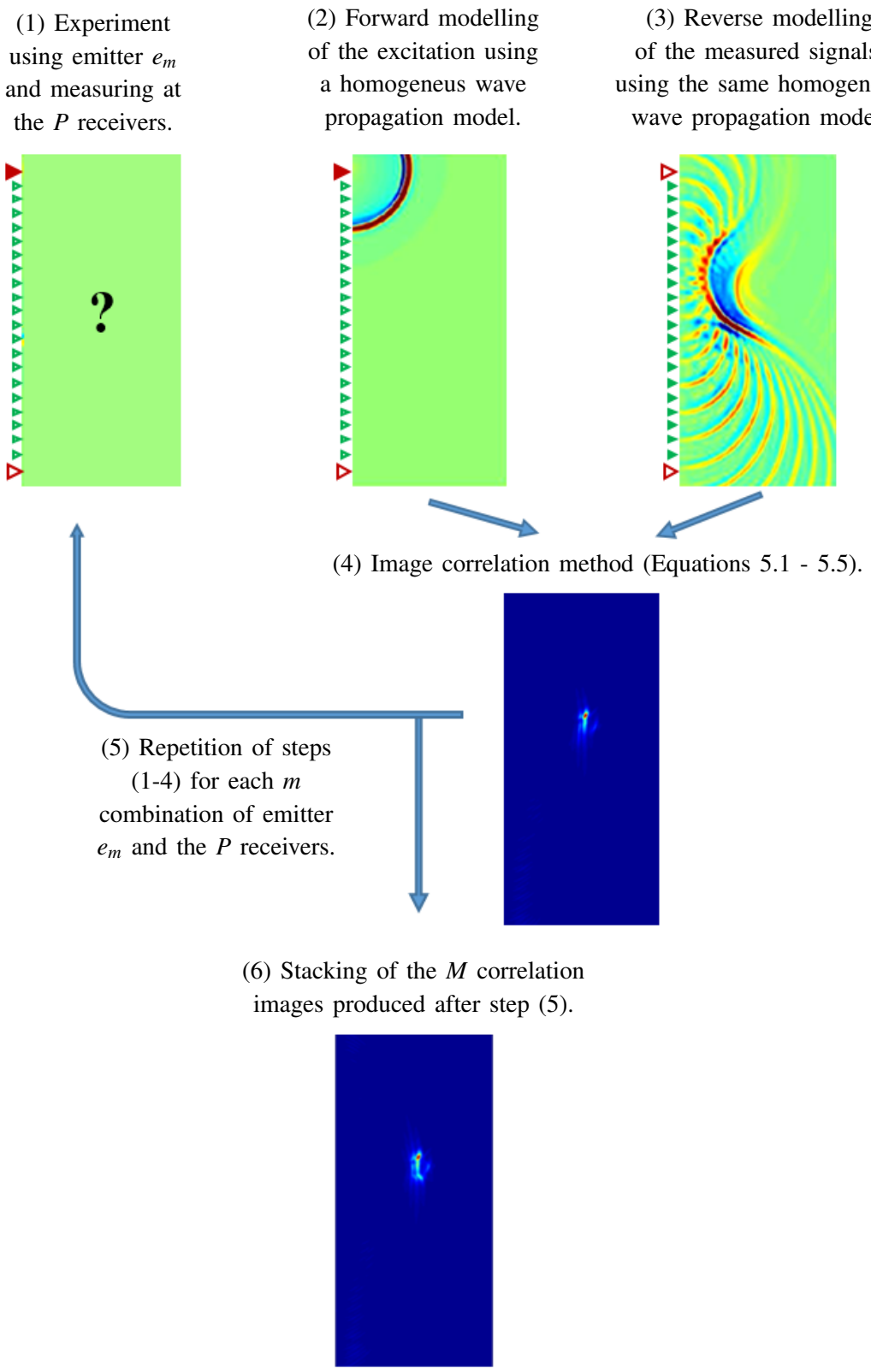

Figure 5.1: Steps of the proposed RTM method.

Artefacts and poor definition may be present in RTM reconstructed images due to a number of reasons, such as the direct wave propagated from the emitters to the receivers along the surface, low signal-to-noise ratio in the measurements and the large-amplitude, low-frequency noise in the reconstruction when using non-homogenous initial models. In order to minimise those artefacts some complementary techniques can be applied, such as filtering and wavefield decomposition as described in the literature (Liu et al., 2011, Chen and He, 2014, Wang et al., 2016), or the normalisation of the cross-correlation by the source or receiver illumination for each shot (Wang et al., 2016). This former technique is called the illumination normalisation and it will be explored in this thesis due to its relative simplicity to implement.

5.2.2 Correlation methods for RTM

The original Claerbout cross-correlation method and three correlation methods that consider different illumination normalisation approaches from the literature (Wang et al., 2016) were tested and compared. Additionally, a new correlation method with illumination normalisation was proposed and compared with the other four methods from the literature. Equations 5.1-5.5 contains the correlation expression for producing the reconstruction image $I(r,z)$ according to the five correlation methods:

- Original Claerbout cross-correlation method:

$$I_c(r,z) = \sum_{m=1}^{M} \sum_{n=1}^{N} F_m(t_n,r,z) R_m(t_n,r,z) \tag{5.1}$$

- Source illumination method:

$$I_s(r,z) = \sum_{m=1}^{M} \frac{\sum_{n=1}^{N} F_m(t_n,r,z) R_m(t_n,r,z)}{\sum_{n=1}^{N} F_m^2(t_n,r,z)} \tag{5.2}$$

- Receiver illumination method:

$$I_r(r,z) = \sum_{m=1}^{M} \frac{\sum_{n=1}^{N} F_m(t_n,r,z)R_m(t_n,r,z)}{\sum_{n=1}^{N} R_m^2(t_n,r,z)} \tag{5.3}$$

- Squared ratio method:

$$I_{ratio2}(r,z) = \sum_{m=1}^{M} \frac{\sum_{n=1}^{N} R_m^2(t_n,r,z)}{\sum_{n=1}^{N} F_m^2(t_n,r,z)} \tag{5.4}$$

- Proposed new correlation method:

$$I_{prop}(r,z) = \sum_{m=1}^{M} \frac{\sum_{n=1}^{N} F_m^2(t_n,r,z)R_m^2(t_n,r,z)}{\sum_{n=1}^{N} F_m^2(t_n,r,z)} \tag{5.5}$$

Where $F_m(t_n,r,z)$ is the displacement field of the forward propagation generated from the m^{th} emitter, $R_m(t_n,r,z)$ is the displacement field of the reverse propagation generated from the m^{th} emitter, M is the number of emitters, n is the time step index and N is the number of time steps.

5.2.3 Computational implementation of the RTM method

The algorithm for the RTM reconstruction method was developed and implemented using MATLAB® (Release 2017a, MathWorks, Natick, United States). The algorithm code can be found in Appendix D.

5.3 RTM method results

Experimental data for studying the suitability of the RTM method was not available at the time of writing this thesis, instead, *in silico* data was used. Pseudo-experimental measurements, u_{exp}, were created by adding white noise to measurements generated by the wave propagation model from Chapter 3. White noise was selected due to the lack of information concerning the nature of the background noise that will be encountered in a real experimental situation in the prostate.

5.3.1 Comparative analysis of the image correlation methods

First, a visual comparative study was carried out to obtain the most suitable image correlation method among the proposed methods in Section 5.2.2. Two different scenarios of the wave propagation model were used. The first scenario was conceived for producing the u_{exp} measurements, whilst the second scenario was used as the homogeneous wave propagation model for the RTM procedure.

The first scenario contained two stiff lesions: a circular tumour and a single HIFU lesion. These types of objects may be considered too complex for a first evaluation of the reconstruction method. However, their similarity to real lesions in the prostate can provide a first insight into the capacity of the reconstruction method from a more introductory perspective. Sensitivity studies using more common evaluation objects are encouraged for the further development of the reconstruction methods for the TU-SWE technique.

The device configuration comprised three emitters and a set of 20 receivers, all of them uniformly distributed covering the entire length of the urethral wall (see Figure 5.2a). The number of emitters and receiver elements was limited by their own size and the length of the urethral wall (reported in Tables 3.3, 3.4 and 3.1, respectively). Larger number of receivers compared with emitters were preferred,

since the forward propagation, which originates from the emitters, contains no information about the reflectors, whilst the reverse propagation, which originates from the receivers, does.

Features and dimensions of the model for the first scenario were kept the same as in Section 3.4. Figure 3.6 shows the parametric distribution of elements and dimensions. Tables 3.1, 3.2, 3.3, 3.4 and 3.5 show the values of the model parameters. Location and size of the stiff lesions, and position of the emitters are detailed in Table 5.1. The excitation signal was implemented as a Gaussian modulated wave with centre frequency of 700 Hz. The recording time was 25 ms, long enough to capture all the reflections generated by the tumour and the HIFU lesion, but not so long as to enhance artefacts due to multiple reflections (Müller et al., 2012). Displacement measurements were recorded during the wave propagation at the location of each receiver. White noise, with a maximum amplitude of 10% of the root-mean-square (RMS) value of the recorded measurements, was added to the recorded measurements to create the u_{exp} signals. The lack of experimental data or other valid information from published work led to the selection of a plausible figure for the expected level of noise. In this case, the figure of 10% of the RMS value of the recorded measurements was taken as a plausible value, however, no rigorous reason can be provided for this choice.

The direct wave propagated from emitters to receivers along the surface was removed from the all the measured signals at the P receivers. The removal was carried out in a similar way as performed by (Wang et al., 2016), i.e. by simulating a homogeneous model and subtracting the recorded signals from the u_{exp} signals.

The second scenario involved the homogeneous model, which retained the configuration of the first scenario but eliminated the presence of reflectors, thus producing a model with a homogeneous wave velocity field. The value of the wave velocity field corresponded to the wave velocity of normal prostatic tissue (see Figure 3.7). This scenario was used for performing the steps (2) and (3) of the RTM procedure, the forward modelling and the reverse modelling, respectively (Figure

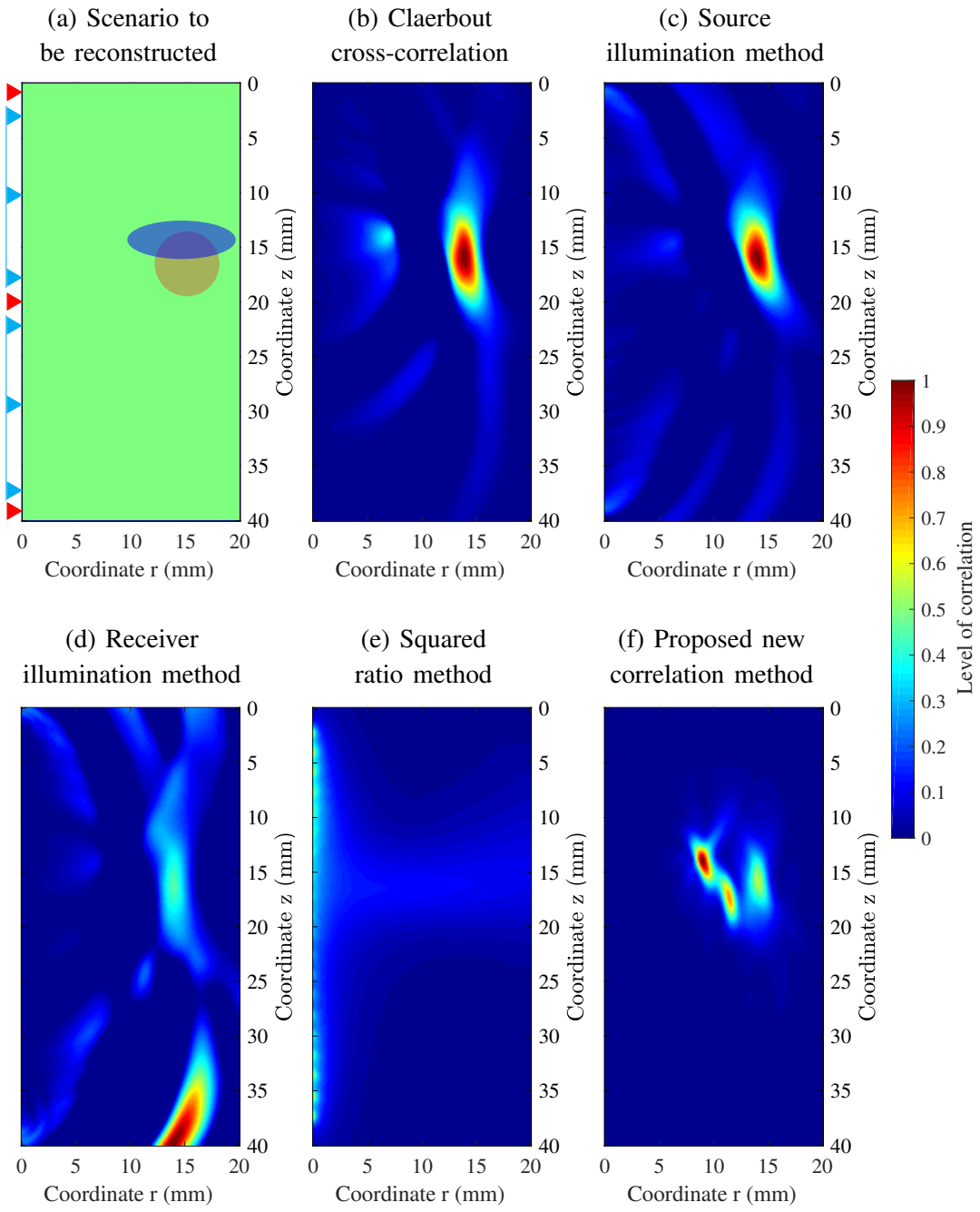

Figure 5.2: Comparative analysis of correlation methods for the RTM reconstruction method. Figure (a) shows the scenario to be reconstructed and the chosen device configuration with three emitters (red triangles) and 20 receivers (blue triangles) uniformly distributed along the urethral wall. Figures (b), (c), (d) and (e) show the reconstruction images by using five different correlation methods (Equations 5.1 - 5.5).

Table 5.1: Invariable values of the discretisation parameters for all scenarios simulated by using the FDTD model.

Parameter	Description	Value
$z_{e,1}$	z coordinate of emitter 1	1.0 mm
$z_{e,2}$	z coordinate of emitter 2	20.0 mm
$z_{e,3}$	z coordinate of emitter 3	39.0 mm
$\varnothing_c$	diameter of the tumour	6.0 mm
r_c	r coordinate of the tumour centre	15.0 mm
z_c	z coordinate of the tumour centre	17.0 mm
r_h	r coordinate of the HIFU lesion centre	14.0 mm
z_h	z coordinate of the HIFU lesion centre	14.0 mm

5.2). The device configuration, i.e. the arrangement of emitters and receivers, from the first scenario was used here. The excitation signal for the forward modelling was the same as that used in the first scenario.

The displacement fields from both forward and reverse modelling were correlated by using the five correlation methods proposed in Section 5.2.2. Figure 5.2 shows the image reconstructions produced by the five correlation methods. All the image reconstructions were normalised by their maximum value in order to allow for their comparison. As can be observed, none of the methods was able to contour the entire shape of the reflectors.

When comparing results from all the correlation methods, only the Claerbout cross-correlation method (Figure 5.2b), the source illumination method (Figure 5.2c) and the new proposed method (Figure 5.2f) provided some information about the location of the reflectors. The most valuable image reconstruction with the lowest level of artefacts was produced by the new proposed method. The new proposed correlation method highlighted the location of the front side of both reflectors, however, the far side of the reflectors was weakly highlighted and placed

in a slightly anterior region to its actual location. The Claerbout cross-correlation method weakly pointed the front side of the HIFU lesion by highlighting the anterior region close to the HIFU lesion. The Claerbout method and the source illumination method also placed the far side of the reflectors in a slightly anterior region to its actual location.

Theoretically, the RTM method provides better defined results as the wavelength of the excitation source decreases compared with the size of the reflectors (Wang et al., 2016). To reduce the wavelength, the tests must be carried out using higher frequencies. Figure 5.3 shows the reconstruction of the comparative study case, shown in Figure 5.2, using an excitation signal with centre frequency of 1000 Hz for the Claerbout cross-correlation, the source illumination and the proposed method. According to the reconstructed images, the increase in frequency did not produce any significant improvement in the level of definition in any of the revised correlation methods.

It is believed that a larger increase in frequency would be required for achieving a significant improvement in the reconstruction image. However, this option was not explored for the sake of brevity, since the wave propagation model for frequencies above 1000 Hz would require revisiting the stability analysis described in Chapter 3, Section 3.4.2.

RTM reconstruction in lossy media can be improved by some complementary techniques. Travelling waves are attenuated during both forward and reverse propagation in lossy media, the amplitude of displacements is highly degraded compared with the lossless case. Several techniques have been reported in the literature to compensate for the losses in the reverse propagation, such as amplitude compensation, inverse filtering and inverted-loss medium methods (Wang et al., 2016, Liu et al., 2011, Chen and He, 2014). The definition of the shape of the reflectors might be also improved by following the iterative process proposed by Liu and Liu (2014) that updates the wave velocity field from previous RTM results until observing convergence in the final output image reconstruction. The investigation

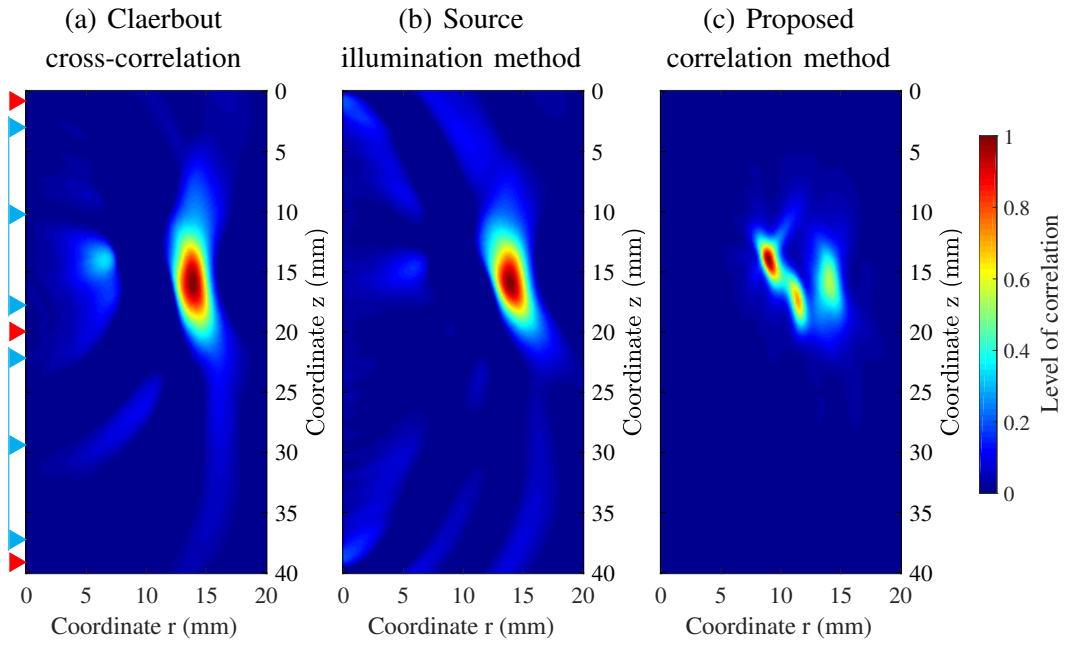

Figure 5.3: Comparative analysis of correlation methods for the RTM reconstruction method using the same case scenario from the previous comparative study (see Figure 5.2). The excitation signal was implemented as a Gaussian modulated wave with centre frequency of 1000 Hz.

of these methods is beyond the scope of this thesis and will therefore be proposed as future work in Chapter 6.

After analysing the results of the comparative study, the new proposed correlation method was found to provide the most useful image reconstruction. The centre frequency of the excitation source was kept at 700 Hz for further investigation, since the use of a higher frequency did not provide significant improvement on the definition of the reconstructed image.

5.3.2 Analysis of the device configuration for RTM reconstruction

A visual comparative study was carried out for obtaining the most suitable device configuration, in terms of arrangement of emitters and receivers, for the RTM reconstruction method. The correlation method used was the new proposed correlation method (Equation 5.5). The scenario reconstructed in Section 5.3.1 was

used here (see Figure 5.2a). Four device configurations were explored, combining configurations with 8, 16 and 32 receiving elements and 1, 3, 5 and 9 emitters (Figures 5.4, 5.5, 5.6 and 5.7). The centre frequency of the excitation source was 700 Hz.

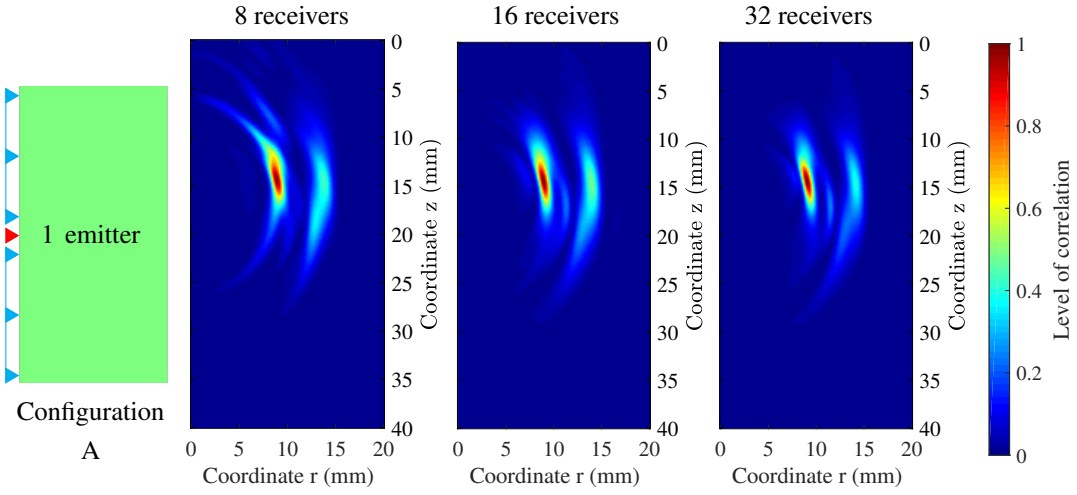

Figure 5.4: RTM reconstructions using the proposed correlation method and the device configuration A, which comprises one emitter (red triangle) and distributions of 8, 16 and 32 receivers (blue triangles).

Figures 5.4, 5.5, 5.6 and 5.7 show the RTM reconstruction results for the different device configurations. Overall, device configurations with a higher number of emitters yielded reconstructions with better definition of the shape of reflectors. The same effect was observed when increasing the number of receivers, however this was not as noticeable as the improvement when increasing the number of emitters. Moreover, a higher number of receivers reduced the intensity of the spider-shape artefacts that can be observed surrounding the highlighted areas, especially noticeable for the device configurations with three and five emitters.

The improvement in the definition of shapes was significant when moving from device configuration A to device configuration B. It was still noticeable between configurations B and C, however, the improvement was weaker when comparing the device configurations C and D. Regarding the number of receivers, the improvement

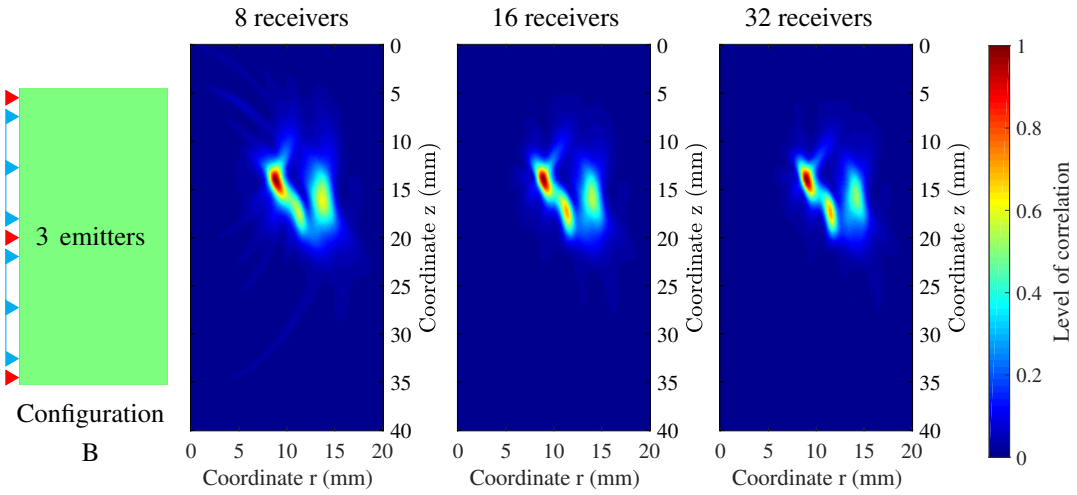

Figure 5.5: RTM reconstructions using the proposed correlation method and the device configuration B, which comprises three emitters (red triangles) and distributions of 8, 16 and 32 receivers (blue triangles).

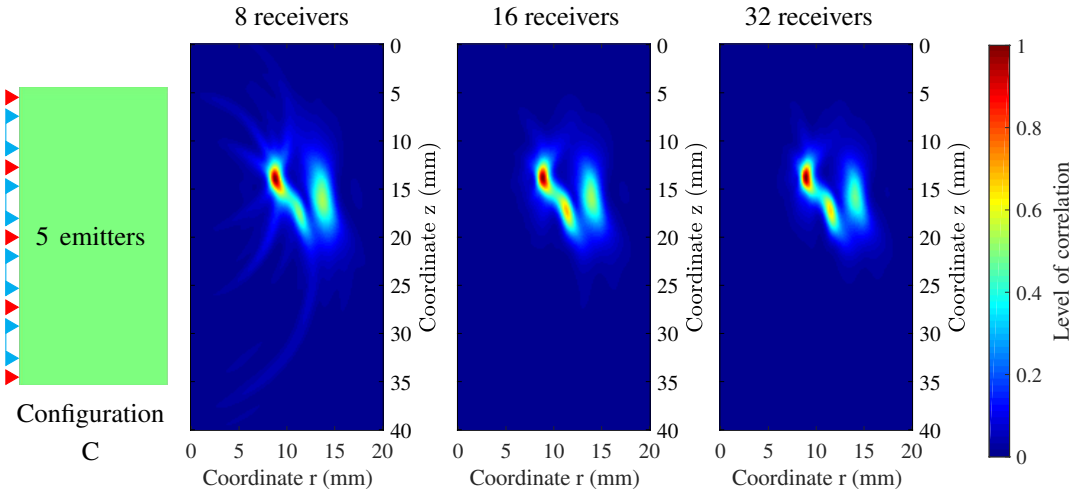

Figure 5.6: RTM reconstructions using the proposed correlation method and the device configuration C, which comprises five emitters (red triangles) and distributions of 8, 16 and 32 receivers (blue triangles).

in definition and the reduction of the spider-shape artefacts was more significant when using configurations with 16 receivers compared with configurations with eight receivers, and less noticeable when comparing with configurations with 32

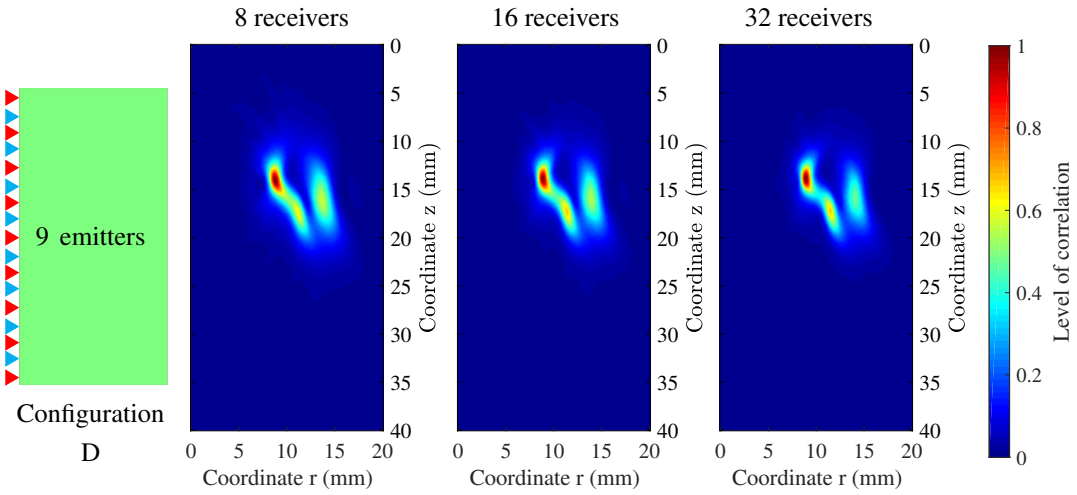

Figure 5.7: RTM reconstructions using the proposed correlation method and the device configuration D, which comprises nine emitters (red triangles) and distributions of 8, 16 and 32 receivers (blue triangles).

receivers.

It is important to recall that the number of emitters involved in the RTM reconstruction has a direct impact in the computational overhead, proportionally increasing the computing time. The memory required was around 2.1 MB, and it barely increased with the number of emitters, since after each image correlation formation (RTM step 5, Figure 5.1) the memory used was released. Table 5.2 shows the computation time of the RTM method for the different device configurations. The number of receivers barely has influence on either the computation time or the amount of memory used. Consequently, and considering the results of the comparative study between different device configurations (shown in Figures 5.4-5.7), a balanced optimum configuration might comprise three to five emitters and a number of receivers between 16 and 32, all of them uniformly distributed along the urethral wall.

The RTM method presented in this section only yielded partial reconstruction of the tumour and the HIFU lesion. Further investigation in techniques for improving the reconstruction are required. Some of these will be proposed as part

Table 5.2: Computation time of the RTM reconstruction method for the different device configurations.

Device configuration	Number of emitters	Computation time
A	1	6 min
B	3	18 min
C	5	30 min
D	9	54 min

of future work in Chapter 6. In any case, the proposed RTM method provided valuable information concerning the location of stiff regions that can be used as initial information for other reconstruction methods.

5.4 Genetic Algorithm reconstruction method

According to the description of the proposed TU-SWE technique, shear waves are transmitted into the prostate after applying an oscillatory rotational stress at specific regions of the urethra wall. Then, shear waves propagating from the interior of the prostate are detected, once again, at the urethra wall. These detected waves carry information about possible stiff lesions within the prostate, such as tumours or thermally ablated areas. The process of reconstructing the unknown features of the stiff lesions by using the information contained within the detected signals is known as solving the inverse problem. In this case, the signal denotes the measurement of displacement due to shear wave propagation measured at the receivers' locations along the urethral wall, as detailed in Chapter 3 and Section 5.3 of this chapter.

A practical way of solving an inverse problem is by minimising the discrepancy between experimental signals, u_{exp}, and others produced by a model that simulates the physics of the system, u_{mod}. In general terms, the lower the discrepancy between experimental and simulated signals, the better the fit of the properties of the theoretical model with their experimental counterparts. In this section, a reconstruction method was developed, that uses a GA for minimising the discrepancy between experimental and simulated signals. GAs are heuristic optimization techniques based on the rules of natural selection and genetics. They optimise a solution by emulating the mechanism of survival of the fittest: the superiors survive while the inferiors are eliminated. Figure 5.8 shows a diagram that details the steps of the proposed reconstruction method. The forward method used for generating the simulated signals was the wave propagation model developed in Chapter 3.

The aim of the proposed reconstruction method is to solve the inverse problem in order to obtain its causal factors, i.e. the parameters of interest that define the stiff lesions, as defined in Section 5.2 (i.e. either a tumour or a HIFU lesion). The parameters proposed were related to the location, size and mechanical properties of

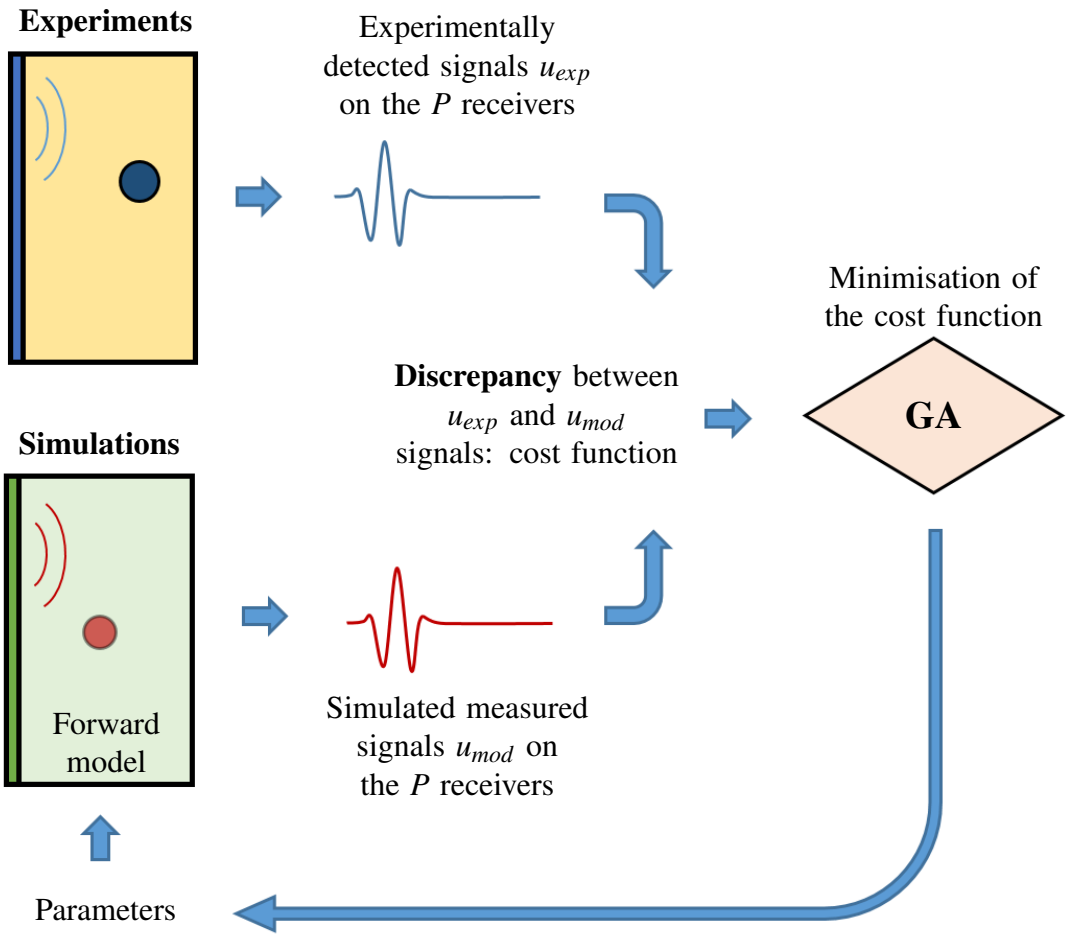

Figure 5.8: Iterative scheme of the GA for solving the IP.

the stiff lesions (see Table 5.3).

The GA method used in the work described in this thesis was developed by Gallego and Rus (2004), who previously adapted the method from a GA technique developed by Haataja (2000). The adaptation of the cost function to the problem, as well as the parametrisation and implementation of the forward model to the GA method were performed by the author of this thesis. The GA method comprises the following iterative process:

1. First, the forward model is parametrised so that it can handle a range of different values of the causal factors, i.e. the lesion parameters listed in Table

Table 5.3: Parameters of interest that define the stiff lesions.

Parameter	p_{lesion}
r coordinate of the centre of the stiff lesion	r_{lesion}
z coordinate of the centre of the stiff lesion	z_{lesion}
Diameter of the stiff lesion	$\varnothing_{lesion}$
Stiffness contrast ratio between stiff lesion and normal tissue (according the KVFD constitutive law)	μ_{ratio}
Viscosity contrast ratio between stiff lesion and normal tissue (according the KVFD constitutive law)	η_{ratio}

5.3.

2. A population of individuals, called chromosomes, is randomly generated using the parametrised forward model. These chromosomes take values from the defined ranges for the lesion parameters. These chromosomes are candidates for the solution within the domain of the problem.

3. The fitness of each chromosome as a candidate for the solution is assessed by a cost function. This cost function evaluates the discrepancy between the u_{exp} and the u_{mod} signals. The u_{mod} signals are generated by the forward model by using the lesion parameters that each chromosome contains.

4. The chromosomes are ranked according to their fitness to approximate the solution of the problem.

5. Evolutionary operators such as, tournament, crossover, mutation and selection are applied to obtain an offspring population (Gallego and Rus, 2004).

6. Then, the child chromosomes from the generated population with higher fitness replace some of the parent chromosomes.

7. The process is iterated until a stop criterion is reached. In this case, the criterion was a specific number of generations, since one of the objectives is the study of the performance of the GA method over the generations.

Values of the evolutionary operators are shown in Table 5.4. These values were chosen based on a trial-and-error approach from previous experiences (Rus et al., 2013, Gomez et al., 2016).

Table 5.4: Values of the evolutionary operators used in the GA.

Evolutionary operator	Value
Probability of mutation	0.3
Probability of crossover	0.8
Tournament probability	0.7
Mutations scale	0.1

A detailed description of the GA basic steps and terminology is beyond the scope of this thesis. For more information on this topic, the reader is referred to the basic literature available regarding GAs, for instance Mitchell (1998).

A key point in GAs is to keep a small population by comparison with the number of generations, in order to keep the influence of the randomness low, and therefore, to increase the natural selection effect (Mitchell, 1998). Table 5.5 shows the selected values for the rest of the parameters to be set for the GA method: the population of chromosomes and the number of generations, which were chosen by a trial-and-error approach.

In order to quantify the discrepancy between u_{exp} and u_{mod} signals, a residual vector $R(p_{lesion})$ is defined according to Melchor and Rus (2014), as the mismatch between both signals u_{exp} and u_{mod}, normalised by the RMS of the experimental

Table 5.5: Population of chromosomes and number of generations used in the GA method.

Parameter	Value
Population of chromosomes	8
Number of generations	50

signal (Equation 5.6).

$$R(p_{lesion}) = \frac{u_{exp} - u_{mod}(p_{lesion})}{RMS(u_{exp})} \tag{5.6}$$

Where p_{lesion} represents the vectorial form of a chromosome (Expression 5.7), which contains the lesion parameters (Table 5.3), also known as genes.

$$p_{lesion} = (r_{lesion}, z_{lesion}, \varnothing_{lesion}, \mu_{ratio}, \eta_{ratio}) \tag{5.7}$$

Then, each gene is normalised according to an interval of possible values that it can take. These search ranges were previously established in agreement with the spatial domain and the rest of lesion parameters of the forward model. Details of this will be shown in Section 5.5.

The GA requires a first population of chromosomes. This constitutes the initial guess for the optimisation algorithm. In this case, this first population is created by taking random samples from within the search ranges. The suitability of the solution generated by implementing every chromosome into the forward model then needs to be evaluated. A cost function f was established for this, and was defined as the squared norm of the residual (Equation 5.8), which is also related to the square of the Euclidean distance between the u_{exp} and the u_{mod} signals (Rus et al., 2007).

$$f(p_{lesion}) = \frac{1}{2}|R(p_{lesion})|^2 \tag{5.8}$$

An alternative definition of the cost function, f^L, (Equation 5.9) was used. This definition introduces a base 10 logarithm and a small non-dimensional value ε, set as $\varepsilon = 10^{-16}$ (Palma et al., 2009), to ensure the existence of the logarithm when f tends to zero. This particular definition was proven to enhance the convergence speed when carrying out the minimisation using GAs (Gallego and Rus, 2004).

$$f^L(p_{lesion}) = \log_{10}(f + \varepsilon) \tag{5.9}$$

The minimisation of the discrepancy, that the GA must achieve in order to obtain an approximation to the solution of the inverse problem, was formulated as follows :

$$\min_{p_{lesion}} f^L \Rightarrow p_{lesion,approximation} \tag{5.10}$$

At the time of writing this thesis, experimental data was not available for studying the feasibility of the GA reconstruction method. Alternatively, pseudo-experimental signals, u_{exp}, were generated by adding white noise to the simulated signals, as performed in the study of the RTM technique in Section 5.2.1. Further details of this will be provided in Section 5.5.

5.4.1 Computational implementation of the GA reconstruction method

The algorithm for the GA reconstruction method was implemented using MATLAB® (Release 2017a, MathWorks, Natick, United States). The core algorithm of the GA search tool was originally written by Juha Haataja, Center for Scientific Computing, Finland. Details about the author and the core algorithm can be found in Appendix E.

5.5 GA reconstruction method results

In silico tests were carried out to study the feasibility of the GA method described in Section 5.4 as a reconstruction method for the TU-SWE technique.

The scenario proposed for the analysis coincided with that used for the study of the RTM method in Section 5.3. The scenario was shown in Figure 5.2a. Tables 3.1-3.5 and 5.1 show the values of the model parameters. The scenario represents a treatment monitoring situation where it is required to locate an initial single HIFU lesion produced in the prostate during the HIFU ablation procedure of a single tumour (Figure 5.2a). The GA method will aim to reconstruct the parameters that define the HIFU lesion listed in Table 5.3.

The computing time of the GA reconstruction method is longer compared with the RTM method since larger number of simulations are required. The memory usage is similar in both methods. In addition, the total computing time of the reconstruction is proportional to the number of emitters, therefore, unlike the analysis of the RTM method in Section 5.3, device configurations with only one emitter were used. The emitter was set at the middle section of the urethral length. The increase in the number of receivers did not produce a significant rise of the total computational time, as was observed in the RTM method in Section 5.3. For this reason, device configurations with 8, 16 and 32 receivers were tested, hence, the arrangement of emitters and receivers coincided with the device configuration A shown in Figure 5.4.

As with the study of the RTM method, experimental data was not available at the time of writing this thesis. Alternatively, pseudo-experimental u_{exp} signals were generated by adding white noise to the displacement measurements detected at the receivers' locations from the simulation of the scenario to be reconstructed (see location of receivers in Figure 5.2a). Maximum amplitude of the added white noise was set as 10% of the RMS of the recorded measurements.

5.5.1 Analysis of the cost function

5.5.1.1 Known pre-treatment scenario

The proposed methodology scenario for generating the modelled signals u_{mod} was based on the scenario shown in Figure 5.9. The location, size and mechanical parameters of the tumour were assumed known as a result of a previous reconstruction process. Details of the scenario are shown in Table 5.1. The GA will use the scenario shown in Figure 5.9 for generating multiple scenarios with a single HIFU lesion by using different combinations (chromosomes) of lesion parameters (genes).

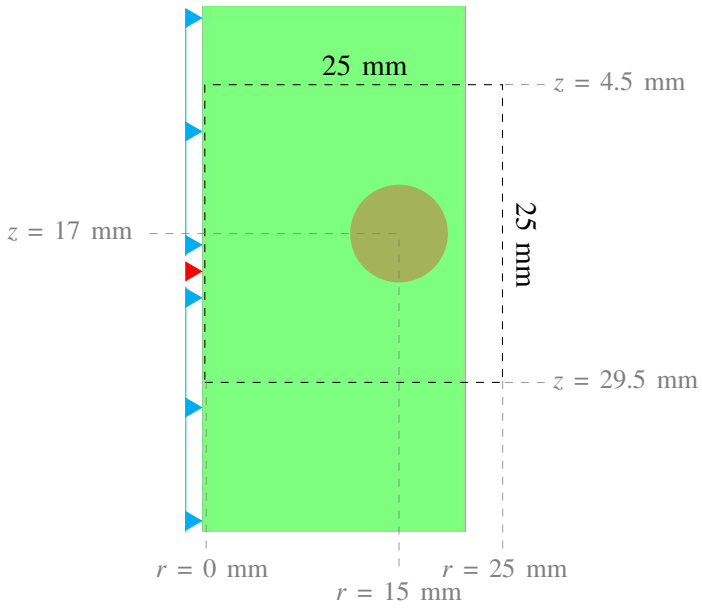

Figure 5.9: Scenario proposed as the model for generating the u_{mod} signals. The dashed contour represents a box of 25×25 mm, that contains the 6 mm diameter tumour, within which the HIFU lesion is suspected to have been formed. The box corresponds to the spatial search domain proposed for the GA method shown in Table 5.6.

Table 5.6 shows the real values of the lesion parameters from the scenario to be reconstructed and the search range proposed for each lesion parameter. The GA will take values from the search ranges for producing the different scenarios for

obtaining the u_{mod} signals. The size of the HIFU lesion was assumed to be a known parameter, specifically ellipsoidal thermal lesions of $10\times3\times3$ mm size produced by the Sonablate® system, therefore, $\varnothing_{lesion}$ was taken off the set of lesion parameters to be reconstructed, p_{lesion}.

Table 5.6: Lesion parameters to be reconstructed and search ranges for the GA method. Definition of the parameters shown in Table 5.3.

Lesion parameter	Real value	Search range
r_{lesion}	14 mm	5 - 20 mm
z_{lesion}	14 mm	6 - 28 mm
μ_{ratio}	5	2 - 6
η_{ratio}	3	2 - 4

The proposed search range for the location parameters consisted of a 2D spatial box of 25×25 mm containing the tumour of 6 mm diameter, within which the HIFU lesion was suspected to have been formed (see Figure 5.9). The alignment of the HIFU lesion with respect to the urethral wall was also assumed to be known. This quantity may in fact be known in a future clinical scenario if the position of the TU-SWE device with respect to the HIFU rectal probe is known. In any case, four lesion parameters were considered sufficient to prove the feasibility of the GA reconstruction method.

The four parameters that defined the HIFU lesion and their respective ranges (Table 5.6) generated a 4D hyperspace. The cost function can be evaluated at different points in the 4D hyperspace thus creating graphs that can provide useful information for analysing the influence of the numbers of receivers in the GA reconstruction method. In this case, the cost function defined as f^L (Equation 5.9) was evaluated on a mesh of 21^4 nodes, i.e., 21 points from each search range of the lesion parameters (Table 5.5).

Figures 5.10 and 5.11 show two planes of the cost function evaluated in the 4D

hyperspace generated by the four lesion parameters, r_{lesion}, z_{lesion}, μ_{ratio} and η_{ratio}, for the device configurations with one emitter and 8, 16 and 32 receivers.

The planes shown in Figure 5.10 were obtained by fixing the values of $\mu_{ratio} = 5$ and $\eta_{ratio} = 3$, i.e. their values for the solution of the inverse problem. Therefore, the planes in Figure 5.10 show the variation of the cost function with regards to the lesion location parameters r_{lesion}-z_{lesion}. Similarly, Figure 5.11 shows the planes with respect to the ratios of the mechanical parameters μ_{ratio}-η_{ratio} while fixing the parameters r_{lesion} and z_{lesion} at their respective solution values, $r_{lesion} = z_{lesion} = 14$ mm.

The point where the cost function has its minimum value is the absolute minimum and it represents the solution of the inverse problem. The coordinates of the absolute minimum in the 4D hyperspace provides the real values of the lesion parameters. The GA will attempt to locate the global minimum of the cost function, thus reconstructing the solution values of the lesion parameters. The mean value and standard deviation of the cost function evaluated at the solution for the lesion parameters, i.e. at the absolute minimum, after ten simulations for each device configuration was -2.3082 ± 0.0089. No significant differences between device configurations were found. Variability indicated by the standard deviation value stems from the random nature of the added white noise of the u_{exp} signals.

The absolute minimum of the cost function was clearly noticeable in the r_{lesion}-z_{lesion} planes (see Figure 5.10) in the vicinity of $r = z = 14$ mm. However, no absolute minimum was located in the μ_{ratio}-η_{ratio} planes (see Figure 5.11). Instead, a valley-shape was observed slightly aligned at $\mu_{ratio} = 5$. This valley-shape indicates that the viscosity contrast ratio η_{ratio}, in the range of proposed values (see Table 5.6), does not have as significant an impact on the generation of reflections, as the stiffness contrast ratio μ_{ratio} does. In fact, between both ratios, there is a difference of the order of 2. For this reason, no consistent satisfactory reconstructions of the parameter η_{ratio} are to be expected after the application of the GA method. Additionally, the μ_{ratio}-η_{ratio} planes showed lower cost function

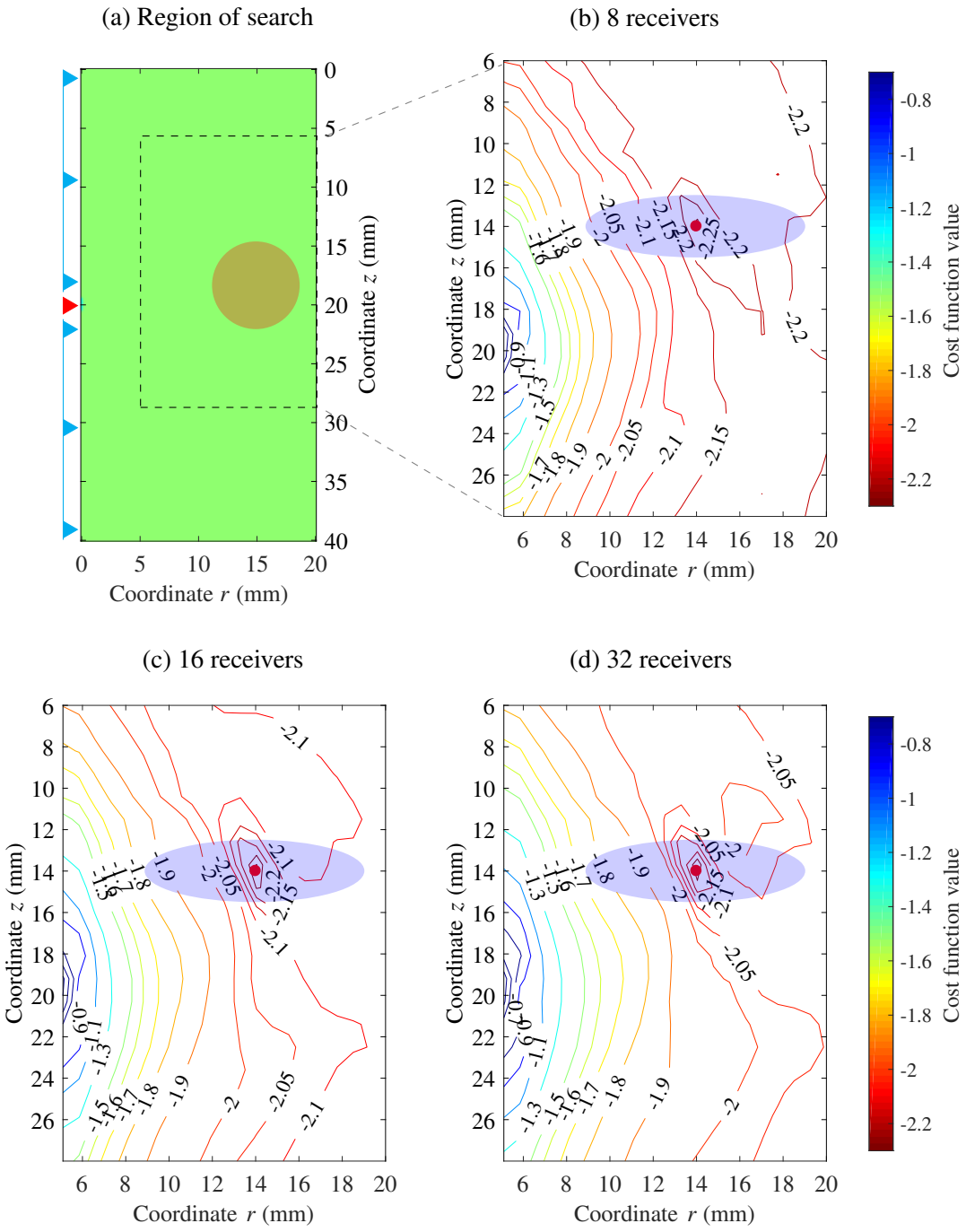

Figure 5.10: (a) Schematic representation of the region of search of the centre of the HIFU lesion (contoured by the black dashed line) inside the spatial domain of the forward model. (b), (c) and (d) r_{lesion}-z_{lesion} planes taken from the evaluation of the cost function for each device configuration in the 4D hyperspace formed by the four lesion parameters to be reconstructed and their respective search ranges shown in Table 5.6. The location of the real centre of the HIFU lesion (blue ellipse) is marked by a red dot at $r = z$ =14 mm.

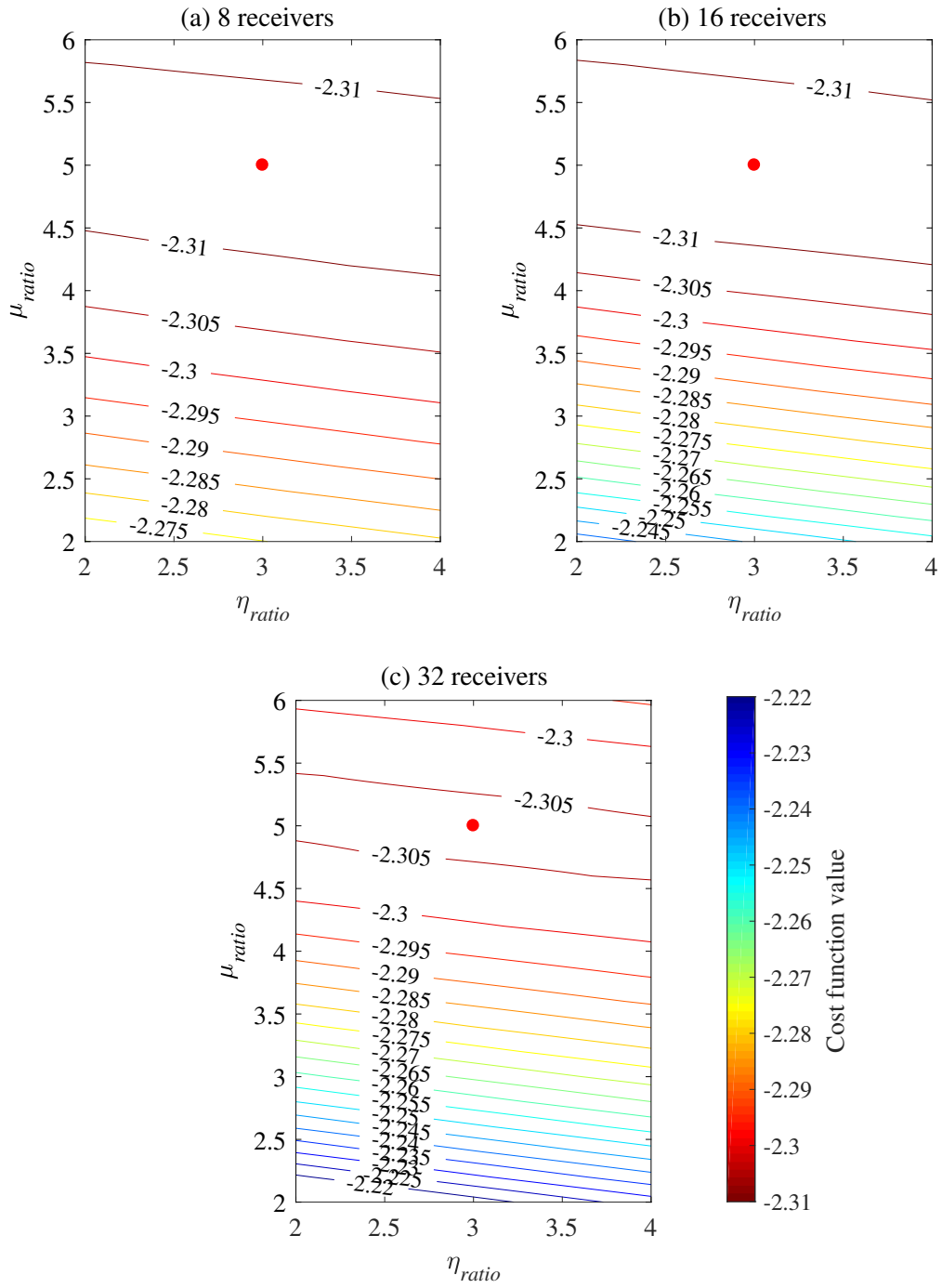

Figure 5.11: μ_{ratio}-η_{ratio} planes taken from the evaluation of the cost function for each device configuration in the 4D hyperspace formed by the four lesion parameters to be reconstructed and their respective search ranges shown in Table 5.6. The mechanical parameters of the real HIFU lesion, i.e. the μ_{ratio} and η_{ratio} parameters of the solution to the inverse problem, are marked as red dots at $\mu_{ratio} = 5$ and $\eta_{ratio} = 3$.

values compared to the r_{lesion}-z_{lesion} planes, for all the device configurations. Consequently, the GA method will provide worse approximations of the mechanical parameters and with higher variability compared with the location parameters. Furthermore, it can be observed in all of cases that the valley-shape is slightly inclined with respect to $\mu_{ratio} = 5$, so that the bottom line of the valley-shape, where the minimum values of the cost function are located, moves from values of $\mu_{ratio} \in [5.0, 5.5]$ for $\eta_{ratio} = 2$ to values of $\mu_{ratio} \in [4.5, 5.0]$ for $\eta_{ratio} = 4$ (see Figure 5.11). It is believed that this inclined bottom line comprises the pairs of values $(\mu_{ratio}$-$\eta_{ratio})$ that produce similar amplitude of the reflected wave due to the presence of the HIFU lesion in the forward model. The reflection coefficient depends on the shear velocity of the HIFU lesion and the normal tissue. The shear velocity depends on the shear modulus, which simultaneously depends on the combination of μ and η among other parameters. Different combinations of μ and η can produce similar reflection coefficients (see Equations 3.32, 3.33 and 3.34).

As mentioned in Section 5.1.3, the permanent insistence on global convergence of GAs is an advantage against other optimisation techniques such as gradient-based methods when local minima are present (Rus et al., 2006). Nevertheless, GAs may require large populations and a high number of evaluations in order to overcome local minima, therefore reducing their efficacy (Mitchell, 1998). Local minima were not visually detected in any of the planes for the different device configurations (Figures 5.10 and 5.11) studied here, nevertheless, the results from the reconstructions will be individually checked since local minima could be present at other regions within the 4D hyperspace.

When comparing r_{lesion}-z_{lesion} planes from different device configurations it can be seen that the device configuration with 32 receivers produces a better defined absolute minimum, using the definition of the absolute minimum as the value of the cost function near the absolute minimum compared with values of the cost function from the rest of the search domain. A better definition of the absolute minimum

is expected to enhance the performance of the GA method in the search for the solution. Table 5.7 shows the average value and the standard deviation of the cost function evaluated in the r_{lesion}-z_{lesion} plane for each device configuration, as well as their comparison with the value of the cost function at the absolute minimum. When using a larger number of emitters, it can be noticed in the r_{lesion}-z_{lesion} plane that the cost function yields higher values outside the absolute minimum, thus enhancing the contrast value of the cost function between the absolute minimum and the rest of the r_{lesion}-z_{lesion} plane. When comparing μ_{ratio}-η_{ratio} planes from different device configurations, a similar effect of better definition of the absolute minimum for the device configurations with more receivers can also be seen. In general, a better defined absolute minimum is expected to produce lower levels of error in the reconstruction of the lesion parameters.

Table 5.7: Mean and standard deviation of the cost function f^L evaluated in the r_{lesion}-z_{lesion} plane and cost function evaluated at the absolute minimum $f^L_{solution}$ relative to the mean value f^L_{mean} for each device configuration.

Device conf.	Mean $\pm$ SD of f^L on the r_{lesion}-z_{lesion} plane	Ratio between $f^L_{solution}/f^L_{mean}$ on the r_{lesion}-z_{lesion} plane
8 receivers	-2.0097 ± 0.1397	1.1486
16 receivers	-1.8985 ± 0.1336	1.2157
32 receivers	-1.8191 ± 0.1315	1.2619

5.5.1.2 Unknown pre-treatment scenario

The response of the GA-based method when there is no previous reliable data regarding the location and mechanical properties of the tumour was also studied. The cost function for this new situation was analysed. In this case, the forward model used for generating the u_{mod} signals consisted of a homogeneous background

with the mechanical properties of normal prostatic tissue, i.e. the model represented in Figure 5.9 without the tumour.

The GA will generate multiple scenarios using the forward model. Each one of these scenarios will contain a single HIFU lesion at different locations and with different mechanical properties. The search range of values was the same for the previous case with known tumour characteristics, shown in Table 5.6. The u_{exp} signals were generated by subtracting the pseudo-experimental signals of the pre-treatment scenario from the pseudo-experimental signals of the treatment scenario, thus reducing the weighting of the information contained in the treatment signals that concerns the tumour.

Figure 5.12 shows the r_{lesion}-z_{lesion} and μ_{ratio}-η_{ratio} planes of the cost function for this new situation involving a device configuration with a single emitter and 32 receivers.

Similarities and differences were observed when comparing the r_{lesion}-z_{lesion} and μ_{ratio}-η_{ratio} planes with those obtained in the previous case studied where the tumour features were known. Similarly to the previous case, the r_{lesion}-z_{lesion} plane (Figure 5.12a) showed a global minimum around the r and z coordinates, where the solution of the inverse problem is actually located. This demonstrates that the reconstruction of the location of the HIFU lesion is possible even without having good information about the pre-treatment situation. Nevertheless, a small local minimum was detected near the global minimum which might lead to minor errors in the approximation to the solution. In any case, due to the proximity to the absolute minimum, the presence of the local minimum should not significantly affect the search by the GA method, thus obtaining good approximations to the location parameters of the HIFU lesion.

The search range for parameters μ_{ratio} and η_{ratio} was deliberately enlarged to cover ratio values up to 8 for both μ_{ratio} and η_{ratio} (see Figure 5.12b). The variation in the range of μ_{ratio} and η_{ratio} shows a μ_{ratio}-η_{ratio} plane with a tilted valley-shape with no clear absolute minimum in the range of μ_{ratio} and η_{ratio} values

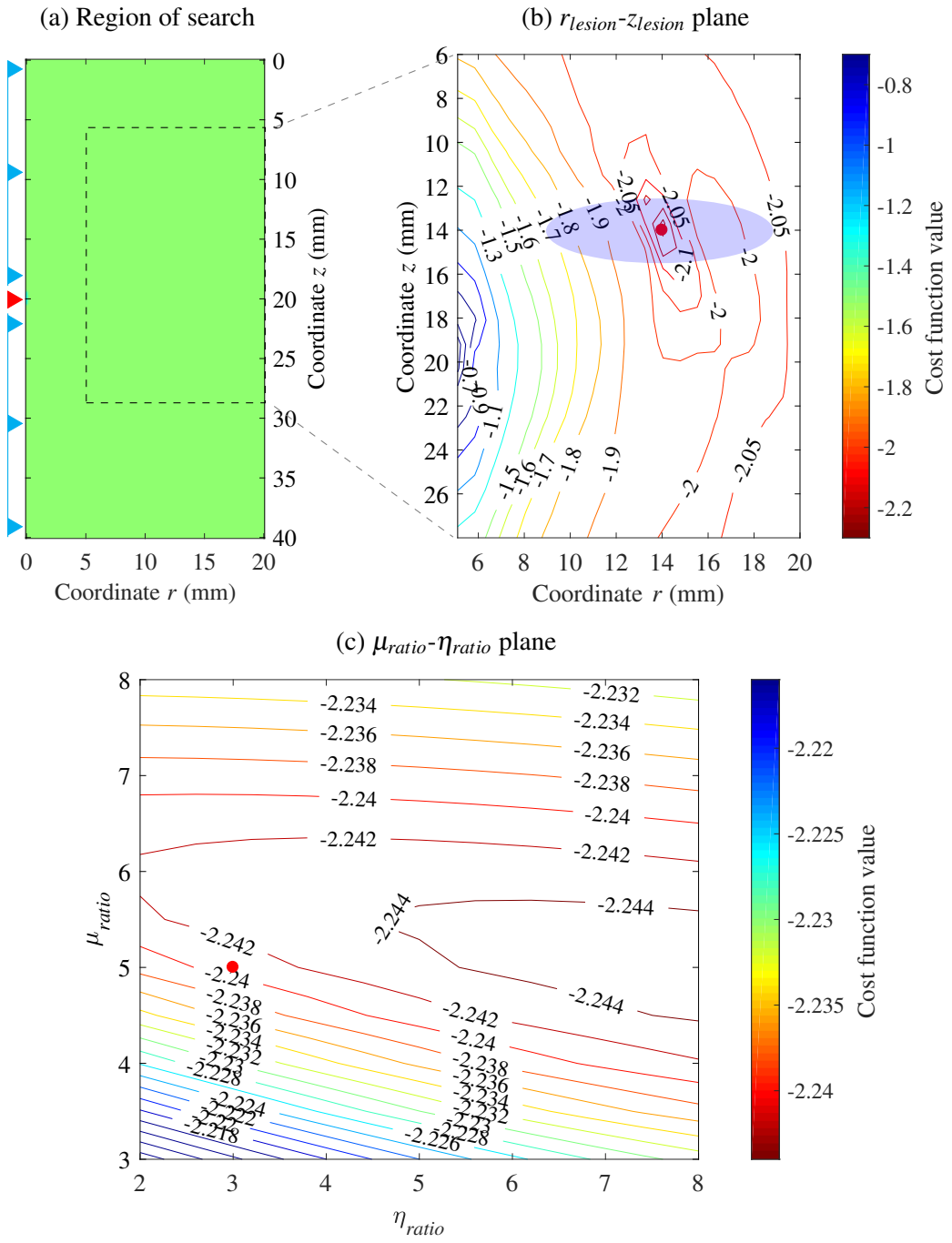

Figure 5.12: (a) Schematic representation of the region of search of the centre of the HIFU lesion (contoured by the black dashed line) inside the spatial domain of the forward model without having information regarding the tumour. (b) and (c) Planes taken from the evaluation of the cost function for the post-treatment monitoring scenario, where the characteristics of the tumour are unknown. The centre of the real HIFU lesion (blue ellipse) and its mechanical parameters, i.e. the parameters of the solution of the inverse problem, are marked as red dots at r = 14 mm, z = 14 mm in Figure (b) and at μ_{ratio} = 5 and η_{ratio} = 3 in Figure (c).

tested. Nevertheless, the alignment of the bottom of the valley shape suggests a possible absolute minimum at values of η_{ratio} higher than 8. Minimum values of cost function when η_{ratio} falls within the range of 2-5 and yields values of μ_{ratio} between 5.5 and 6, therefore, higher than the value of $\mu_{ratio} = 5$ for the solution. It is believed that this mismatch between the cost function shape and the actual solution ($\mu_{ratio} = 5$ and $\eta_{ratio} = 3$) is a way to compensate for the decrease in amplitude of the reflected wave due to the absence of the tumour in the forward model. In other words, the reconstruction of the shear modulus of the HIFU lesion, that combines both μ and η, yielded higher values than the solution shear modulus, in order to produce the same level of amplitude of the reflected wave as in the scenario that contains the tumour.

5.5.2 GA reconstruction results and analysis of errors

Several reconstruction tests were carried out to analyse the performance of the GA method. The three device configurations compared in Section 5.5.1 were employed. Ten reconstruction tests for each device configuration were carried out for the range of GA parameters indicated in Tables 5.4 and 5.5. The tests were performed using MATLAB® in conjunction with its Parallel Computing Toolbox™ (Release 2017a, MathWorks, Natick, United States). Each reconstruction procedure lasted 9 hours approximately on a quad-core 3.60 GHz, 16 GB RAM, desktop computer. The number of receivers used did not have a significant impact on computational times.

Table 5.8 shows the reconstructed values of the four lesion parameters. Values are shown in terms of the mean and standard deviation of the reconstructed results from the ten performed tests. The standard deviation provides a notion of the variability of the reconstructed values. Regarding the location parameters r_{lesion} and z_{lesion}, the device configurations with 16 and 32 receivers provided good approximations to the solution with low variability, whilst the device configuration with 8 receivers showed larger variability and less accurate approximations. The

reconstruction of the mechanical parameters μ_{ratio} and η_{ratio} was less accurate and possessed high variability, regardless of the device configuration. This result was foreseen by analysing the behaviour of the cost function in the μ_{ration}-η_{ratio} planes in Section 5.5.1.

Overall, the reconstructed location of the lesion using the device configurations with 16 and 32 receivers produced errors no larger than a tenth of a millimetre, which can be considered valuable from a tumour detection perspective. In the case of the mechanical parameters, the combination of both reconstructed μ and η values produced shear moduli of 15.85±2.42 kPa and 16.56±2.27 kPa at 700 Hz when using the 16 and 32 receivers configuration respectively (calculated according to Equation 2.3). The real shear modulus was 16.72 kPa, therefore both receivers configurations produced averaged absolute errors below 1.0 kPa with SD below 2.4 kPa. When comparing these levels of error with the shear modulus ranges for prostate cancer reviewed in Chapter 2, it can be said that the reconstruction of the mechanical properties may provide valuable information for the use in diagnosis and treatment monitoring by TU-SWE, however, further investigation on the clinical side should be accomplished in order to obtain conclusive results.

Table 5.8: Reconstructed values of the four lesion parameters by using the GA method with different device configurations. Results in terms of mean and standard deviation obtained after ten tests for each device configuration.

Device conf.	Reconstruction results (Mean ± SD)			
	r_{lesion} (mm)	z_{lesion} (mm)	μ_{ratio}	η_{ratio}
8 receivers	14.600 ± 1.802	13.769 ± 0.807	4.548 ± 0.584	2.796 ± 0.463
16 receivers	14.063 ± 0.076	14.042 ± 0.159	4.677 ± 0.691	3.162 ± 0.604
32 receivers	14.054 ± 0.082	14.041 ± 0.179	4.895 ± 0.648	3.271 ± 0.559

Table 5.9 shows the averaged absolute and relative errors of reconstruction of the four lesion parameters in terms of mean and standard deviation. The absolute

error was defined as the absolute value of the difference between the reconstructed value of each lesion parameter and its actual solution value. Relative errors were obtained by weighting the averaged absolute errors by the length of their respective search ranges.

Table 5.9: Results of the GA method using the device configuration with 8 receivers. Values and absolute errors of the reconstructed HIFU lesion parameters.

Device conf.	Absolute errors (Mean / |SD|)			
	r_{lesion} (mm)	z_{lesion} (mm)	μ_{ratio}	η_{ratio}
8 receivers	0.673 / 1.778	0.389 / 0.744	0.487 / 0.555	0.409 / 0.298
16 receivers	0.080 / 0.058	0.132 / 0.098	0.424 / 0.633	0.530 / 0.332
32 receivers	0.081 / 0.056	0.140 / 0.118	0.551 / 0.357	0.529 / 0.324
	Relative errors (Mean / |SD|)			
	r_{lesion} (%)	z_{lesion} (%)	μ_{ratio} (%)	η_{ratio} (%)
8 receivers	4.517 / 11.932	1.769 / 3.382	9.738 / 11.108	13.622 / 9.928
16 receivers	0.537 / 0.389	0.600 / 0.445	8.475 / 12.680	17.658 / 11.055
32 receivers	0.544 / 0.376	0.636 / 0.536	11.016 / 7.138	17.652 / 10.820

The lowest relative errors were found in the reconstruction of the location parameters, u_{lesion} and z_{lesion}, for the device configurations with 16 and 32 receivers. These errors were below 1.0% in both configurations. The device configuration with 8 receivers yielded higher errors with large variability for the location parameters. The errors of reconstruction of the mechanical parameters, μ_{ratio} and η_{ratio}, were larger and showed high variability compared with errors of reconstruction of the location parameters for all the device configurations. The highest level of errors with the larger standard deviation values was observed in the reconstruction of η_{ratio}, as expected after the observation of the valley-shape of the evaluation of the cost function shown in Figure 5.11.

No significant differences in the reconstructed values and errors were

found between device configurations using 16 and 32 receivers. Overall, both configurations provided good approximations of the location parameters of the HIFU lesion. Results of the reconstruction of the mechanical parameters were similar for all the device configurations, showing less accurate reconstructed values and high variability, with averaged relative errors between 9% and 11% for μ_{ratio} and between 13% and 18% for η_{ratio}. In any case, the results of the reconstructed mechanical parameters shown in Table 5.8 significantly differed from the unity value, thus representing a considerable alteration of the values of mechanical parameters of the lesion with respect the normal prostatic tissue. For this reason, although relative errors were significant, the reconstructed values of the mechanical parameters of the lesion may be considered acceptable from a treatment monitoring perspective.

Figure 5.13 shows the cost function evaluated for the chromosome with the best fitness over the selected number of generations, thus illustrating the performance of the GA method for each device configuration. Results are shown in terms of mean and standard deviation from the ten tests performed on each device configuration. It can be seen that the GA method converged for all the device configurations to values of the cost function close to the solution. However, a close cost function value to the solution is not necessarily an indicator of good approximation, especially for the mechanical parameters, as can be seen by relating the graphs from Figure 5.13 with the reconstruction results detailed in Tables 5.8 and 5.9.

The performance of the GA method shown in Figure 5.13 for each device configuration reflected the predictions based on the observations of the cost function planes in Section 5.5.1. The GA for the device configuration with eight receivers yielded low values of the cost function at the start of the optimisation process. The standard deviation, which is an indicator of the variability in the population of chromosomes, did not decrease over generations (Figure 5.13a). On the other hand, device configurations with 16 and 32 receivers (Figures 5.13b,c) resulted in higher initial values of the cost function. In both of the above cases, the GA converged

(a) Device configuration with 8 receivers

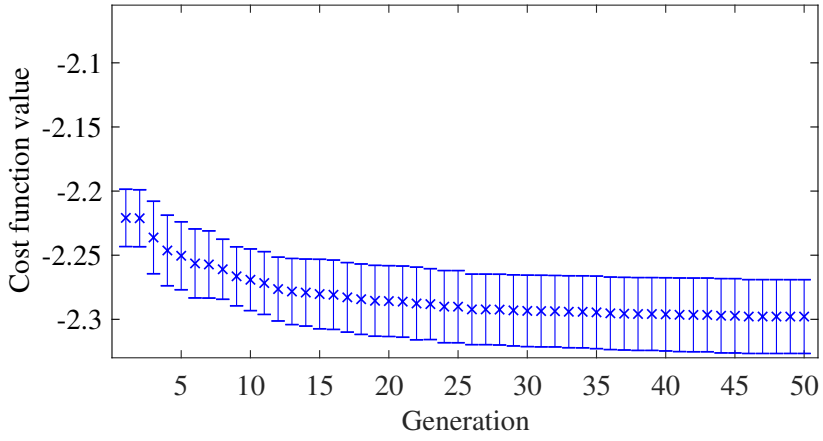

(b) Device configuration with 16 receivers

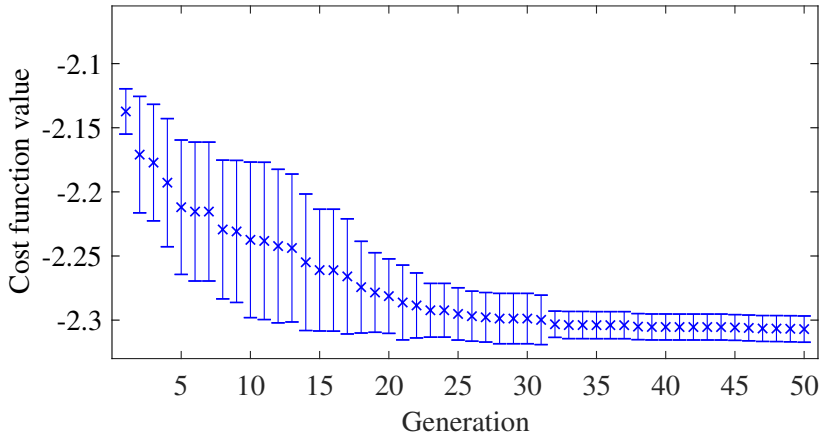

(c) Device configuration with 32 receivers

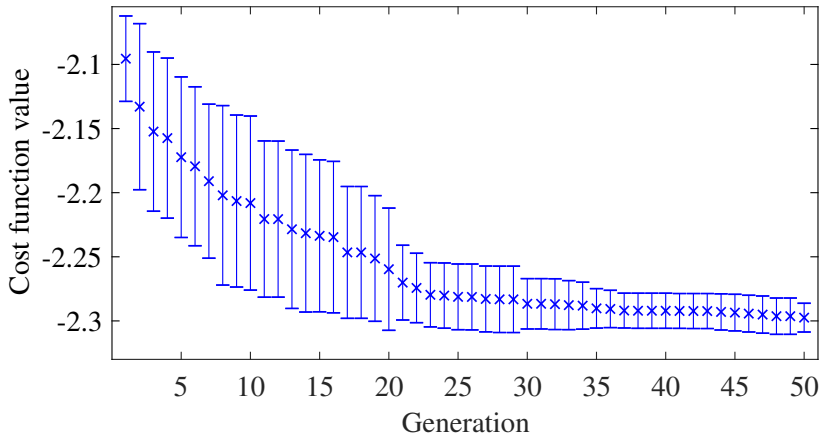

Figure 5.13: Cost function value of the fittest chromosome over the number of generations for the each device configuration. Data is shown in terms of mean and standard deviation values.

towards lower values while achieving lower standard deviation, thus improving the chances of selecting fitter chromosomes over generations. This difference in the performance of the GA method between the device configuration of 8 receivers and the other two configurations is related to the cost function for each configuration. It can be seen in the comparison of r_{lesion}-z_{lesion} planes (see Figure 5.10) that, unlike the 16 and 32 receivers cases, the eight receivers configuration presents a less defined absolute minimum, as observed by comparing the absolute minimum and the mean value for the *r*-*z* planes (see Table 5.7).

Overall, the location parameters of the HIFU lesion were better reconstructed compared with the mechanical parameters (Tables 5.8 and 5.9). The worst reconstructed parameter was the viscosity contrast ratio. This outcome was expected after observing the valley-shape in the μ_{ratio}-η_{ratio} planes in Section 5.5.1. Regarding the location parameters, the GA achieved good approximations with low errors when using the device configurations with 16 and 32 receivers. No significant differences in the reconstruction of the mechanical parameters were observed between these two cases. It can be concluded that, any device configuration with a number of receivers between 16 and 32 would achieve similar reconstruction results for the four lesion parameters.

The reconstruction of the lesion parameters for the case where the pre-treatment scenario was unknown (analysed in Section 5.5.1.2) was beyond the scope of the work in this thesis. The reconstruction results of the location parameters would be expected to be similar to those obtained for the case where the pre-treatment scenario was known, by analysing the similarities between cost function evaluations for the *r*-*z* planes (see Figures 5.10c and 5.12a). However, for the reconstruction of the mechanical parameters, the GA method would yield high levels of error for both the stiffness and the viscosity, as concluded after the analysis of the μ_{ratio}-η_{ratio} planes in Figure 5.12b.

5.6 A reconstruction approach combining RTM and GA

A two-step reconstruction approach is proposed which involves a combination of both RTM and the GA reconstruction techniques analysed in Sections 5.2 and in 5.4, respectively. The approach uses the information that RTM provides about the location of reflectors to speed up the GA-based reconstruction by reducing its spatial search space.

The scenario used for testing the RTM and the GA methods in Sections 5.3 and 5.5 (shown in Figure 5.2a) was also used for testing the proposed combined reconstruction approach.

First, RTM reconstruction images of the pre-treatment and post-treatment scenarios were compared. The device configuration B with 32 receivers was chosen. Figure 5.14 shows the images from both the pre-treatment and post-treatment scenarios. The area where the HIFU lesion was suspected is contoured with a dashed line.

The GA reconstruction method was then implemented over a reduced spatial search space. A 14×13 mm (r and z dimensions respectively) 2D spatial box was contoured, which contained the area where the difference between both RTM reconstruction images was noticed, i.e. where the HIFU lesion was suspected (see Figure 5.15). Table 5.10 shows the revised ranges for the 4D search domain. Search ranges for the mechanical parameters were kept the same as in Section 5.5. Only the emitter located at the middle section of the urethra was used. The pre-treatment scenario was assumed to be known as in the analysis of the GA method in Section 5.5.1.1.

The cost function was evaluated over a 4D mesh of 21^4 nodes formed by the new search range of lesion parameters. Figure 5.16 shows the r_{lesion}-z_{lesion} and μ_{ratio}-η_{ratio} planes of the evaluated cost function. The resulting r_{lesion}-z_{lesion} plane

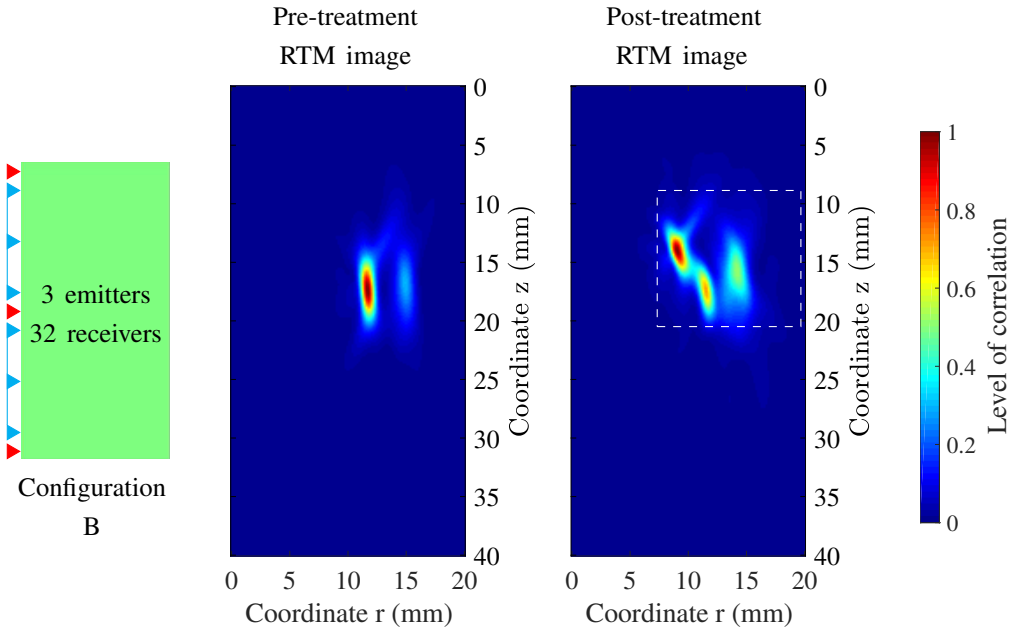

Figure 5.14: RTM reconstructions for the pre-treatment and post-treatment situations used to test the combined reconstruction method, using the proposed correlation method and the device configuration B, which comprises 3 emitters (red triangles) and a distributions of 32 receivers (blue triangles). The area where the HIFU lesion was suspected is contoured with a dashed line.

Table 5.10: Lesion parameters to be reconstructed and search ranges for the combined reconstruction method.

Lesion parameter	Real value	Search range
r_{lesion}	14 mm	12 - 16 mm
z_{lesion}	14 mm	10 - 20 mm
μ_{ratio}	5	2 - 6
η_{ratio}	3	2 - 4

resembled a zoomed section from the r-z plane obtained in Section 5.5 for the 32 receivers device configuration. The μ_{ratio}-η_{ratio} plane showed an almost unaltered distribution of cost function values for the 32 receivers configuration in Section 5.5, since the search ranges of the mechanical parameters of the lesion did not change.

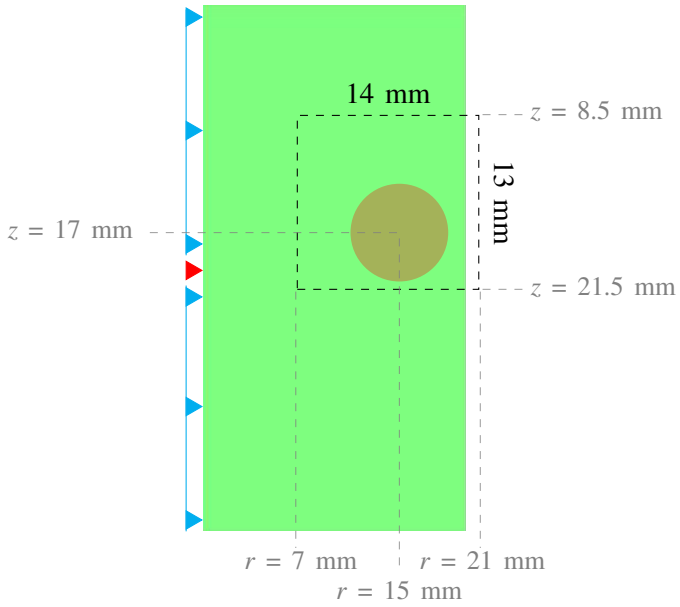

Figure 5.15: Scenario proposed as the forward model for generating the signals u_{mod}. The dashed contour represents a box of 14×13 mm, that contains the tumour of 6 mm diameter, within which the HIFU lesion is suspected to have been formed after the comparison of the RTM reconstruction results from the pre-treatment and post-treatment scenarios. The box corresponds with the domain of the reduced spatial search space proposed for the GA method.

Small differences were due to the random nature of the added white noise. The conclusions from the analysis of the cost function for the device configuration with 32 receivers performed in Section 5.5.1.1 are also valid here.

Ten reconstruction tests were carried out to analyse the performance of the GA reconstruction method after the reduction in the spatial search domain. Setting parameters of the GA were kept the same as in the GA tests from Section 5.5 (see Tables 5.4 and 5.5).

Table 5.11 details the reconstructed values for the four lesion parameters. Reconstruction results for the location parameters r_{lesion} and z_{lesion} were very close to the actual values (see Table 5.10). The reduction in the search domain provided a slightly more accurate approximation of the location parameters compared with the non-reduced spatial search domain from Section 5.5.2. The mechanical parameters were less accurately reconstructed compared with the location parameters, as

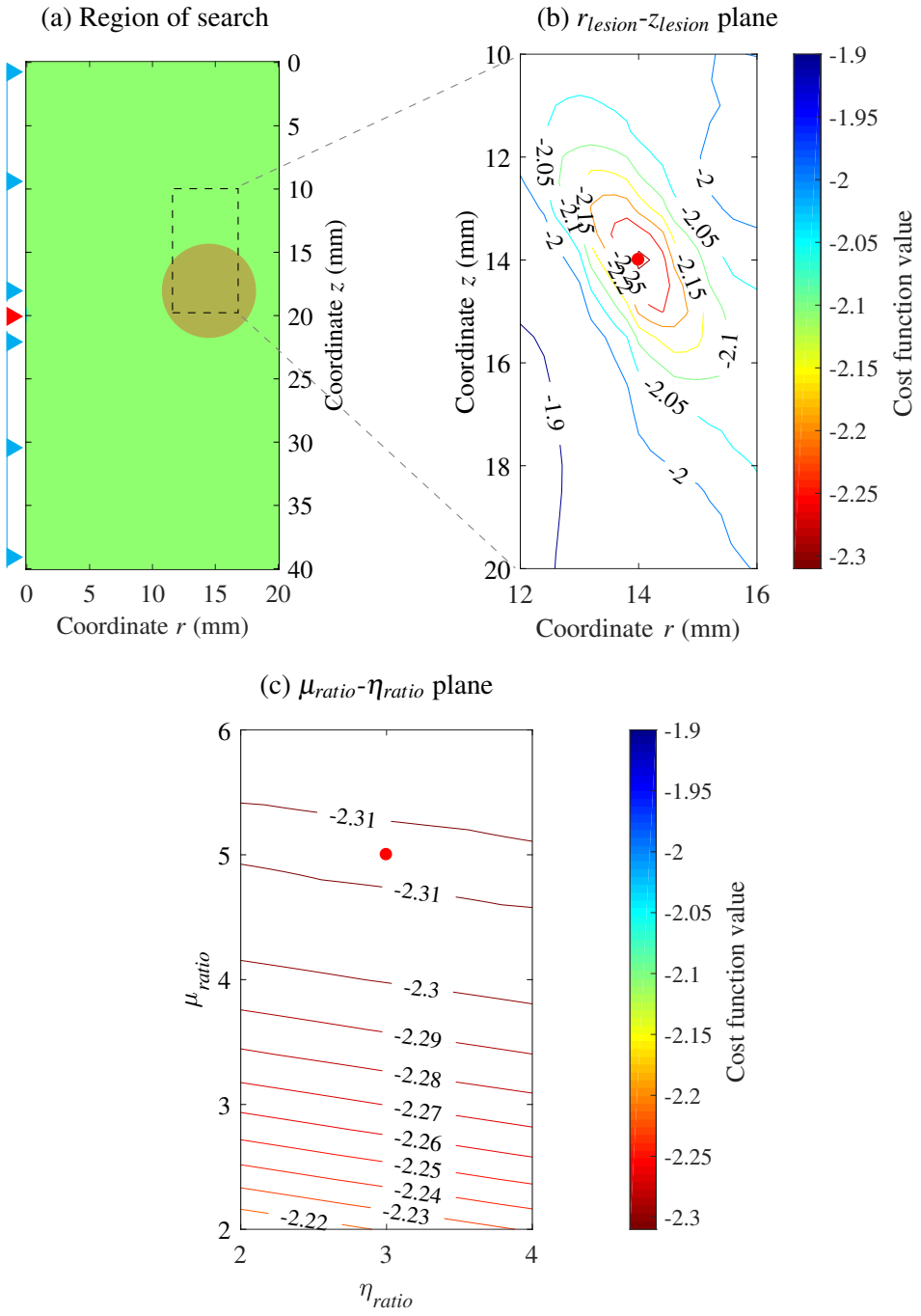

Figure 5.16: (a) Schematic representation of the reduced region of search of the centre of the HIFU lesion (contoured by the black dashed line) inside the spatial domain of the forward model. (b) and (c) r-z and μ_{ratio}-η_{ratio} planes taken from the evaluation of the cost function on the reduced 4D hyperspace formed by the four lesion parameters and their respective search ranges shown in Table 5.10. The parameters of the real HIFU lesion, i.e. the solution of the inverse problem, are marked as red dots.

Table 5.11: Reconstructed values of the four lesion parameters by using the GA method with the device configuration with 32 receivers and the reduced search domain. Results in terms of mean and standard deviation obtained after ten tests.

Configuration	Reconstruction results (Mean ± SD)			
	r_{lesion} (mm)	z_{lesion} (mm)	μ_{ratio}	η_{ratio}
32 receivers and reduced search domain	14.012 ± 0.043	14.027 ± 0.068	5.087 ± 0.131	2.940 ± 0.720

happened in Section 5.5.2.

Table 5.12 shows the averaged absolute and relative errors of the reconstructed lesion parameters. The absolute and relative errors were calculated as defined in Section 5.5. Errors in the reconstruction of the location parameters were similar to the analysed case without reduction in the spatial search domain and device configuration with 32 receivers. An improvement from 10% to 2.5% in the level of error for the μ_{ratio} parameter with a lower level of variability was achieved compared with the case without reduction in the spatial search domain. The level of error in the reconstruction of the η_{ratio} parameter was similar to the previous case without reduction in the spatial search domain.

The performance of the GA method after using the information from the RTM reconstruction images is shown in Figure 5.17. The performance of the GA improved by reaching low cost function values with low variability and in a fewer number of generations compared with the performances of the GA method in the cases with no reduction of the search domain. It is believed that this improvement in the speed of convergence is the reason for achieving a better reconstruction of the μ_{ratio} parameter, since the GA method can allocate more resources into finding a better approximation of the μ_{ratio} parameter while ensuring a good approximation of the location parameters. The low standard deviation of the errors for the μ_{ratio} parameter, i.e. the low variability within the latest generation of chromosomes,

Table 5.12: Results of the GA method using the device configuration with 32 receivers and the reduced search domain. Values and absolute errors of the reconstructed HIFU lesion parameters.

Configuration	Absolute errors (Mean / |SD|)			
	r_{lesion} (mm)	z_{lesion} (mm)	μ_{ratio}	η_{ratio}
32 receivers and reduced search domain	0.077 / 0.043	0.109 / 0.068	0.134 / 0.082	0.652 / 0.313
	Relative errors (Mean / |SD|)			
	r_{lesion} (%)	z_{lesion} (%)	μ_{ratio} (%)	η_{ratio} (%)
32 receivers and reduced search domain	0.513 / 0.285	0.497 / 0.305	2.680 / 1.638	21.723 / 10.430

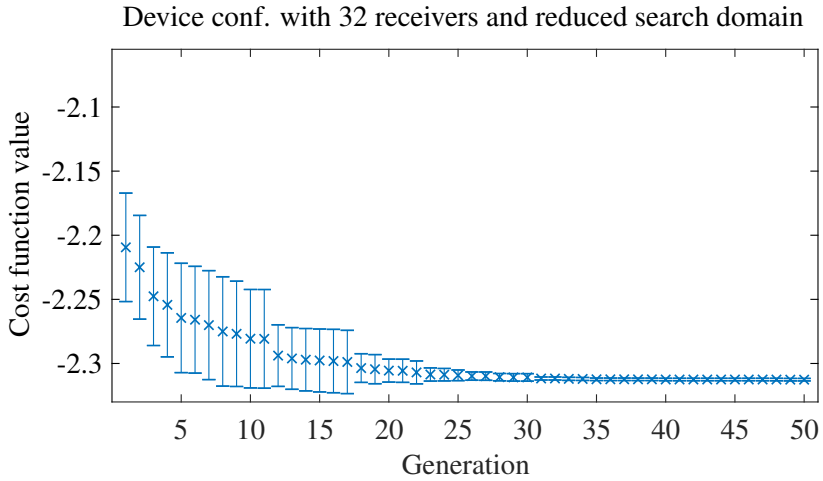

Figure 5.17: Cost function value of the best chromosome over the number of generations for a device setup with 32 receivers and taking advantage of the reduced search domain. Data is shown in terms of mean and standard deviation values.

supports this reasoning.

Overall, after comparing the reconstruction results with those from Section 5.5.2, the level of accuracy in the reconstruction of the location parameters did not improve. However, this was different for one particular mechanical parameter:

the μ_{ratio} parameter. It can be concluded that the reduction in the spatial search domain by using the information provided by the RTM reconstruction step can be used either to speed up the GA reconstruction by stopping the process at fewer generations, or to improve the accuracy of the approximation of the μ_{ratio} parameter. This improvement may not benefit the reconstruction of the η_{ratio} parameter, since it has been proved that the cost function, as defined in Section 5.4, has low sensitivity to the η_{ratio} parameter, and therefore, it is difficult to achieve accurate approximations.

In general, although mechanical parameters were less accurately reconstructed compared with the location parameters, the obtained values still may provide valuable information for the use in diagnosis and treatment monitoring by TU-SWE.

Future work could be directed towards the improvement of the sensitivity of the cost function to the viscosity parameter by exploring alternative definitions of the cost function.

5.7 Discussion and conclusion

The inverse problem for the TU-SWE technique is based on the use of the shear waves measured at the urethral wall resulting from the interaction of the transmitted shear waves with stiff lesions. Solving the inverse problem aims to detect the location of stiff lesions, as well as to reconstruct their size and viscoelastic properties. The problem has the particular characteristic that the potential sensors can be only placed on the urethral wall, thus limiting the direction of the excitation and the reconstruction of features at the far side of the stiff lesions.

Two reconstruction methods were proposed for solving the inverse problem: an RTM method and a GA-based method.

The RTM method is based on the cross-correlation of the forward modelled excitation and the reverse modelled measured signals at an array of receivers using the same wave propagation model. In principle, the RTM can only reconstruct the geometrical features of the stiff lesions. Several cross correlation methods that consider different illumination normalisation approaches were tested and compared. The preliminary results showed that the best reconstructed images with the least presence of artefacts were produced by the new proposed cross-correlation method. Different device configurations, in terms of the number and distribution of emitters and receivers were tested. Device configurations with 16-32 receivers and at least three emitters yielded the best reconstruction results.

Elliptical lesions may be considered too complex objects for a first evaluation of the reconstruction method. However, their similarity to real lesions in prostate can provide a first insight into the capacity of the reconstruction method from a more introductory perspective. Sensitivity studies using more common evaluation objects are planned for the further development of the TU-SWE technique.

Overall, the RTM method only provided partial reconstruction, highlighting the proximal face of the stiff lesions. Although the reconstructed image did not provide sufficient information to fully obtain the extension of the stiff lesions, the

partial reconstruction provided useful information regarding the location of the lesion. This feature can be used by other reconstruction methods. Although there are several improvements that can be applied to the RTM method used here, the reconstruction results produced by the RTM method can be already valuable from a clinical perspective, for instance for guiding biopsies. The ability of providing the suspicious region where stiff tumours can be located would be of great utility for directly targeting the biopsy needles, thus improving the efficiency of the biopsy process for diagnosing prostate cancer.

The GA technique was used to minimise the discrepancy between experimental data from the array of receivers and measurements on the receivers produced by model simulations of the experimental scenario. The solution to the inverse problem are the model parameters that produce the minimum discrepancy. The model parameters were defined as the location, stiffness contrast ratio and viscosity contrast ratio. The two former parameters were defined accordingly to the KVFD constitutive law implemented in the wave propagation model in Chapter 3.

Several device configurations with variable number of receivers were tested in a similar way as the analysis of the RTM method. Overall, the GA method provided the best approximations when using configurations with 16 and 32 receivers. The method yielded accurate reconstruction of the parameters related to the location of the lesion. The reconstruction of the viscoelastic parameters was less accurate compared with the location parameters, however, the shear modulus calculated by using the viscoelastic parameters yielded low errors and low variability compared with the shear modulus solution. The level of error obtained was around 2.5 % of the shear modulus for prostate cancer reviewed in Chapter 2, which indicates that the quantitative data provided by the TU-SWE method and the GA reconstruction method can be of clinical utility for measuring the elasticity of stiff nodules in prostatic tissue.

Additionally, a combined method was tested employing both the RTM method and the GA method. The use of the preliminary results from the RTM reconstruction

for reducing the spatial region of search for the GA proved to improve the performance of the GA based reconstruction method.

A direct comparative analysis between the results from the reconstruction methods employed here and elastograms from current well-established elastography techniques was not carried out. The preliminary nature of the current state of the development of the TU-SWE technique and the lack of elastography studies for thermal lesions in prostate makes such a comparison difficult.

Limitations of the reconstruction methods are mostly due to the limitations of the forward model. The reconstruction methods need realistic forward models in terms of anatomical features and then geometry, in order to achieve the level of accuracy adequate for clinical utility. Moreover, the lack of experimental data limits the available information on realistic levels of SNR and the attenuation of shear waves. A study of the reconstructed images for realistic levels of SNR and attenuation will be needed for the feasibility of the TU-SWE technique, as well as for obtaining the emitter and receiver specifications.

5.8 Chapter summary

This chapter was dedicated to describing and analysing reconstruction methods for the TU-SWE technique.

First, an initial review of reconstruction methods suitable for the TU-SWE technique, was carried out. Two methods were proposed, an RTM and a GA technique. A treatment monitoring scenario with a single HIFU lesion created over a tumour was used for testing both reconstruction methods.

An RTM reconstruction method was successfully developed. Several cross correlation methods from the literature along with a novel one were proposed. Initial tests showed that the best reconstruction images were produced by the new proposed correlation method. Different device configurations in terms of the number and distribution of emitters and receivers were tested. Device configurations with 16-32 receivers and at least three emitters yielded the best reconstruction results. Overall, the RTM method only provided partial reconstruction, highlighting the front side of the stiff lesions. Although the reconstruction image did not provide sufficient information to fully reconstruct the stiff lesions, the partial reconstruction provided useful information regarding the location of the lesion. This feature can be used by other reconstruction methods.

A GA-based reconstruction method was developed. The method aims to reconstruct the location and mechanical parameters of the HIFU lesion. The GA method was used for finding the lesion parameters that minimise a cost function that measured the discrepancy between experimental and simulated signals. Different device configurations with variable number of receivers were tested. Overall, the GA method provided the best approximations when using configurations with 16 and 32 receivers. The method yielded accurate reconstruction of the parameters related to the location of the lesion. However, less accurate reconstruction was produced for the mechanical parameters.

A combined method was tested employing both RTM and the GA method. This

method takes information provided by the RTM so that the spatial search space may be reduced when subsequently using the GA method. Overall, this method converged faster to the absolute minimum compared to the use of the GA alone. This method also achieved significantly lower levels of error in the reconstruction of the stiffness contrast ratio. The reconstruction of the location parameters was also improved, although less significantly so than for the stiffness contrast ratio. The reconstruction of the viscosity contrast ratio remained poor. Although mechanical parameters were less accurately reconstructed, the obtained values may still provide valuable information for the use in diagnosis and treatment monitoring by TU-SWE.

Chapter 6

Conclusions

This chapter is dedicated to evaluating the work described in this thesis and to identifying possible areas for further investigation.

A brief overview of the work described in each chapter of the document will be provided. The aims and objectives set out in Chapter 1 will be revised in order to assess the degree to which these have been achieved. Contributions achieved throughout this work will be summarised. Finally, those areas requiring further investigation will be analysed. New challenges arising from the work will be discussed, and possible solutions provided.

6.1 Discussion and novel contributions

The work described in this thesis was motivated by the requirement for improving the diagnosis of prostate cancer and for the monitoring of focal thermal treatments of such tumours. A brief overview of the current limitations in the diagnosis of prostate cancer was provided in Chapter 1. Additionally, the reasons as to why elastography techniques are particularly suited for the diagnosis and treatment monitoring of prostate cancer were discussed.

Previous work on the use of elastography for the detection of prostate cancer was reviewed in Chapter 2. This is an area of increasing interest in pre-clinical research. Evidence suggests that there is great potential for elastography to detect areas of elevated stiffness that might be associated with prostate cancer. Furthermore, studies on the exploration of elastography imaging for monitoring thermal therapies were also reviewed in Chapter 2. Results suggest that elastography techniques may have a potential use in the monitoring and assessment of focal thermal treatment in the prostate.

A novel transurethral shear wave elastography technique, named TU-SWE, was proposed for the diagnosis of prostate cancer and the monitoring of focal thermal treatment of such tumours. According to the TU-SWE method, the transmission of shear waves is achieved by applying oscillatory rotational forces on the urethral wall. Shear waves travelling back to the urethra have been altered by the presence of regions of elevated stiffness within the prostate. These waves can be detected at the urethral wall, providing observations that can be used for solving the inverse problem of calculating the location and viscoelastic features of the stiff lesions, the latter being defined as either tumours or thermally treated tissue. These lesion features provide the required information for developing the TU-SWE-based diagnosis and treatment monitoring application.

Results and limitations of the most common elastography techniques tested for prostate cancer detection, referred to as SE and TR-SWE in this thesis, were

discussed in Chapter 2. It was determined that the new proposed TU-SWE technique has the potential to provide improvements over SE and TR-SWE, specifically because it allows the monitoring of transrectal thermal therapies such as HIFU thermal ablation.

The principal aim of this thesis was to study the feasibility of the TU-SWE technique for the diagnosis and the monitoring of focal thermal treatment of prostate cancer.

The first achieved objective was the development of a 2D wave propagation model, which was described in Chapter 3. This model provided an insight into the mechanical response of a prostate-like medium to shear wave propagation. Moreover, the model was used as a forward model in the reconstruction methods in Chapter 5. A second objective of the work in this thesis consisted of the derivation of a wave equation based on a viscoelastic KVFD constitutive law. The reasons as to why a KVFD constitutive law is particularly suited to model shear waves in soft tissue were discussed. A FDTD method was chosen for solving the set of equations. The model assumptions were stated and justified. The mathematical description of the model was shown in Chapter 3, and further mathematical developments were detailed in Appendix A. There have been some previous work on wave modelling using the KVFD constitutive law, for example, Caputo et al. (2011) developed a FDTD model for the simulation of the propagation of compressional waves in biological applications, and Zhang and Holm (2016) used the 1D KVFD wave equation to simulate the shear displacement generated by ARF for a range of viscoelastic media. Nevertheless, to the author's knowledge, this is the first attempt at developing a 2D model based on a fractional constitutive law for propagation of shear waves in a tissue-like medium. Several scenarios with tumours and HIFU lesions were simulated using this wave propagation model, thus demonstrating its potential.

Chapter 4 was dedicated to the description of the achievement of the third objective of this work: the validation of the wave propagation model described

in Chapter 3. Tissue-mimicking materials used in prostate and elastography applications were reviewed in Chapter 4, together with several optical methods for measuring the displacements generated by shear wave propagation. Gelatine-based translucent phantoms containing visible particles were fabricated and tested using a high-speed camera based technique. The experimental setup and validation protocols were clearly detailed and justified. To the author's knowledge the work described in Chapter 4 represents the first attempt at using a high-speed camera technique to measure the displacement field in 2D produced by shear waves induced by a mechanical actuator.

The fourth objective of this work consisted of the reconstruction of features of tumours and HIFU lesion in the prostate according to the TU-SWE method. Two methods for solving the inverse problem were developed and tested in Chapter 5. First, a brief review of possible reconstruction methods was carried out. An RTM and a GA-based method were chosen. Methods and assumptions were stated and justified. To the author's knowledge this work demonstrates the first adaptation of a seismic migration technique, such as RTM, to a medical elastography method. Additionally, a new correlation method within the general RTM process was proposed and tested, achieving improved results compared with common RTM correlation methods. Although RTM reconstruction results were not conclusive, information concerning the location of stiff lesions that can be used by other reconstruction methods was obtained. The GA reconstruction method was based on previous works developed within the collaborative research group from University of Granada. Parameters related to the stiff lesion location were consistently reconstructed with low levels of error below 1.2% in all the tests for the device configurations with 16 and 32 receivers. However, parameters related to the mechanical properties of the stiff lesion were less accurately reconstructed, producing errors below 20% for the stiffness contrast ratio between the lesion and the normal tissue and 28% for the viscosity contrast ratio between the lesion and the normal tissue. A third reconstruction method, based on the combination of the

RTM and the GA methods, was proposed. The method achieved improved results compared with the GA-based method alone, yielding levels of errors below 0.8% for the location parameters, and below 4.3% for the stiffness contrast ratio. The reconstruction of the viscosity ratio yielded similar level of errors to the GA-based method alone. Overall, it can be said that the achieved reconstruction of the location and mechanical properties of the stiff lesions may provide valuable information for the clinical use in diagnosis and treatment monitoring by TU-SWE, however, further investigation on the clinical side should be accomplished in order to obtain conclusive results.

The fifth objective of this work was to obtain an optimal TU-SWE device configuration, in terms of the number and distribution of emitting and receiving elements. Since the number of emitters involved in the reconstruction bears a direct impact on the computing time, a low number of emitters was therefore desirable. On the other hand, the number of receivers barely had influence on the computation time. The results of the reconstruction methods from Chapter 5 indicated that a device configuration with at least three emitters (three emitters for the RTM method and one emitter for the GA) and 16-32 receivers yields satisfactory results while showing a balanced computational overhead. Considering such a device configuration, the maximum RAM memory used was around 2.1 MB, and the computation time was around 18 minutes for the RTM method, and around 9 hours for the GA-based method, using MATLAB® in conjunction with its Parallel Computing Toolbox™ (Release 2017a, MathWorks, Natick, United States), on a quad-core 3.60 GHz, 16 GB RAM, desktop computer.

6.2 Summary conclusion

The aim of this thesis is the evaluation of the feasibility of the proposed TU-SWE technique for the diagnosis of prostate cancer and the monitoring of the focal thermal treatments of such tumours. The main findings in relation to the aims are summarised in this section.

The determining factors for the feasibility of the TU-SWE technique have been analysed through the literature reviewed in Chapters 1 and 2. These are based on the fact that most prostate tumours are stiffer than the surrounding normal tissue, consistently proven through the elastography literature reviewed. Additionally, it has also been shown in the literature that a large increase in the tissue stiffness is expected immediately after thermal focal treatments, such as HIFU focal ablation of prostate cancer.

The first set of findings of this work is associated with the capacity of transmitting shear waves from the urethra by a mechanical actuator, and the detection of the wave reflections generated by the interaction between the transmitted waves and stiff regions inside the gland. The wave propagation model described in Chapter 3 provided some preliminary results that confirmed the possibility of transmitting and detecting the waves through the urethra by applying oscillatory rotational stress on the urethra wall. The viscoelastic parameters needed for the wave propagation model were indirectly estimated by combining results from several studies. Nevertheless, the number of studies concerning the characterisation of the viscoelastic properties of the prostate was very limited. For this reason, the suitability of the chosen values of the viscoelastic parameters can be somehow questionable. Further investigation into the shear viscoelastic parameters of prostate is needed, with particular interest in the case of thermally ablated prostatic tissue since no studies were found. Furthermore, the transmission and detection of waves were also experimentally observed in gelatine phantoms by means of a high-speed camera setup (detailed in Chapter 4). Nevertheless, further

improvements would be required since neither the wave propagation model nor the phantom were developed considering the real anatomy and heterogeneities of real prostates.

The TU-SWE technique is based on the analysis of the wave reflection from the interaction between shear waves and stiff regions within the prostate. A correct modelling of the wave amplitude is a must in order to obtain information regarding the change of shear mechanical impedance that produces the reflections, and therefore the stiffness of the suspicious lesion. For this reason, the wave equations developed for the model considered a KVFD constitutive law, which has been proven to accurately model a power law for attenuation, thus improving the modelling of attenuation compared with other common viscoelastic laws such as the KV and the Maxwell model.

The second set of findings is related to the inverse problem for the TU-SWE technique. In the case of the TU-SWE technique, the inverse problem attempts to reconstruct the solution of the location, size and viscoelastic parameters of stiff lesions (tumours and HIFU lesions) from the analysis of the signals measured by the array of receivers located at the urethral wall. These features of the stiff lesions within the prostate will be used for the diagnosis of prostate cancer and the monitoring of HIFU ablation of the prostate. Two reconstruction methods were explored in this thesis: an RTM and a GA-based method. The methods showed promising results, although further development has been suggested in order to improve both. The RTM method provides the location of the stiff lesions, an ability that can have a direct clinical utility, for instance for targeting prostate biopsies. The GA-based method is able to accurately reconstruct the location of the stiff lesions and the shear modulus contrast between the stiff lesion and the normal surrounding tissue, which can be used for the non-invasive characterisation of the elasticity of the tumours and also HIFU lesions for the treatment monitoring application. Furthermore, the combination of both the RTM and the GA-based methods has been proven to improve the speed and the accuracy of the reconstruction.

A study of the reconstruction images for realistic levels of SNR and attenuation will be required, since both factors are central to the feasibility of the TU-SWE technique. These will also be needed for specifying the required emitter amplitudes and the receiver sensitivities.

This thesis presented a novel transurethral elastography approach named TU-SWE. *In silico* tests demonstrated the feasibility of the TU-SWE technique as a tool for detecting stiff lesions within the prostate. Nevertheless, further work in all of the explored areas of this thesis work will be required to move onto a device proof-of-concept stage, which is a key step for continuing the development of the TU-SWE technique.

6.3 Future work

In Section 6.1, it has been shown that the aims and objectives outlined in Chapter 1 have been achieved, and that a number of novel contributions have been made as a result of this work. However, as indicated throughout this thesis, there are areas that will benefit from further investigation, and others that require further work in order to reach the next level of development of the TU-SWE technique.

The geometry of the model developed in this thesis was simplified in order to focus on the modelling of the viscoelastic response of the medium, and to have a basic forward model to test the performance of the reconstruction methods. Many improvements in the model are required to reach a more accurate level for the TU-SWE application, such as the adaptation to a 3D geometry with anatomical accuracy and the addition of surrounding biological structures that will influence the propagation of shear waves. Furthermore, it was noticed in Chapter 2 that there is little data concerning the viscoelastic properties of prostatic tissue, and none regarding thermally ablated prostatic tissue. Additionally, most of the reliable data available in the literature were obtained for frequencies relevant to classical rheological devices, i.e. below 100 Hz. It would be necessary to carry out a number of rheological characterisation tests, in order to provide a consistent set of realistic mechanical parameters for the different tissue and conditions to be incorporated into the improved wave propagation model. In addition, exploring new viscoelastic characterisation techniques that allow the use of higher frequencies compared with classical rheological devices would be highly relevant, for instance by using the HFVS device RheoSpectrics™ C500 (Rheolution Inc., Montreal, Canada) as carried out by Amador et al. (2015).

The method for the 3D forward model will be investigated in order to use the best suited in terms of accuracy and performance given the model assumptions: a 3D anatomical geometry and a KVFD constitutive law. FDTD and FEM are among the most commonly used methods for 3D elastodynamics (Frehner et al., 2008).

FD methods are easier to implement, however, FEMs are particularly flexible in terms of dealing with complex geometry and complicated boundary conditions (Zienkiewicz et al., 1977). For both methods, open-source and commercial packages are available. The implementation of a custom code might also be an alternative to be investigated. It is expected that a 3D model would hugely increase the computational overheads of the reconstruction methods. Therefore, a comparative study between the performance of the TU-SWE technique when using a 3D model approach against a multi-scanning 2D approach that covers the entire prostatic volume, in terms of the accuracy of the reconstruction results and the associated computational cost, would be highly relevant.

The RTM method was demonstrated to be a faster reconstruction method compared with the GA-based method. However, RTM only provided partial reconstruction of the location of the stiff lesions. There are several complementary techniques that might improve the RTM results. Travelling shear waves are highly attenuated during both forward and reverse propagation in lossy media, such as prostatic tissue. Several techniques that have been reported in the literature to compensate for the losses in the reverse propagation, could be explored. Some examples of these techniques are: amplitude compensation, inverse filtering and inverted-loss medium methods (Wang et al., 2016, Liu et al., 2011, Chen and He, 2014). Additionally, the reconstruction of the shape of the stiff lesions might be also improved by following the iterative process proposed by Liu and Liu (2014). The method consists of updating the wave velocity field from data derived from the previous RTM reconstruction until the convergence of the reconstruction image is achieved. The RTM reconstruction method would have to be adapted to the improved 3D model.

The GA reconstruction method will also require adaptation to the improved 3D wave propagation model. Alternative methods for generating model scenarios that do not require an initial assumption regarding the shape of the real lesion would be also highly relevant, for example, by clustering small circular lesions

that can approximately lead to the real shape of the lesion. Additionally, alternative definitions of the cost function can be explored in order to improve the sensitivity to the mechanical parameters. Comparative studies between the GA reconstruction method presented here, simulated annealing and gradient-based methods would also be interesting.

To speed up the reconstruction methods, the incorporation of analytical solutions can be investigated. For example, for solving homogeneous scenarios in the RTM case, the solution to the Reissner and Sagoci problem (Reissner and Sagoci, 1944, Noble and Sneddon, 1963, Gladwell, 1968) provided by the semi-analytical solver employed by (Gomez et al., 2013) can be adapted to the TU-SWE problem conditions. The so-called Reissner and Sagoci problem consists of the calculation of the displacement field generated by an oscillatory rotational disk located on the surface of a semi-infinite half homogeneous and isotropic space. Analytical solutions in homogeneous media of the wave propagation from circular or ellipsoidal sources could also be developed for accelerating the GA reconstruction method. Parallel processing methods for the simulation of propagation in 3D and for solving the inverse problem can also be investigated.

Finally, experimental proof-of-principle of the TU-SWE technique for detecting stiff regions inside the prostate will require the design and fabrication of a laboratory prototype. Several shear stress tactile technologies, such as piezoceramic technology (Yu et al., 2016, Melchor et al., 2017), capacitive designs (Cheng et al., 2010, Lee et al., 2008, 2011b) and optoelectronics devices (Missinne et al., 2011, 2012), can be tested *in silico* for ability and viability to detect shear waves. Different types of rotational electromechanical actuators, that improve upon the rotational motor used in the experimental validation in Chapter 4, can be investigated as potential emitters.

6.4 Chapter summary

Throughout this chapter it has been demonstrated that the aims and objectives outlined at the start of this thesis document have been achieved.

A 2D wave propagation model using FDTD, capable of simulating the interaction between shear waves transmitted from the urethral wall and stiff lesions, such as tumours and thermally ablated areas, was developed. The validation of the wave propagation model was achieved by comparing model scenarios with corresponding experimental results from a high-speed camera-based technique applied to gelatine phantoms.

Two reconstruction methods, a RTM and a GA-based method, were developed and tested for reconstructing the location and mechanical parameters of stiff lesions within the prostate. A third reconstruction method, which resulted from the combination of both RTM and GA methods, was tested, obtaining improving results when compared against the two methods working alone. The reconstruction of the location and the stiffness parameter of the lesion was accurate and consistent, which warrants pursuing the investigation of the TU-SWE method as a potentially suitable tool for the diagnosis of prostate cancer and for the focal thermal treatment monitoring of such tumours.

Areas of future investigation have also been identified in this chapter. An improved version of the wave propagation model capable of dealing with 3D geometries derived from anatomical data, was proposed. The reconstruction methods will correspondingly require adaptation to this new model. Finally, the design and fabrication of a laboratory prototype of a TU-SWE probe, based on several shear stress tactile technologies was suggested. This would constitute an essential step towards a physical proof-of-concept of the TU-SWE technique.

Appendix A

FDTD discrete equations

This appendix describes the derivation of the discrete equations employed in Chapter 3. The discrete equations are derived after applying the space-time discretisation to the domain (described in Section 3.3.2) and the FD expressions (described in Section 3.3.3) to the equations that describe the physical phenomenon of wave propagation in a KVFD viscoelastic medium (described in Section3.2).

First, the equations of the problem are split and the PML parameters are incorporated following the procedure for cylindrical coordinates developed by Liu (1999). The split expressions are adapted to a KVFD constitutive law, according the equations from Section 3.2.

The conservation of momentum equation in cylindrical coordinates (Equation 3.22) is as split in the following expressions:

$$a_r \frac{\partial^2 u_{\theta(r)}}{\partial t^2} + \omega_r \frac{\partial u_{\theta(r)}}{\partial t} = \frac{\partial \sigma_{r\theta}}{\rho \partial r} \tag{A.1}$$

$$A_r \frac{\partial^2 u_{\theta(\theta)}}{\partial t^2} + \Omega_r \frac{\partial u_{\theta(\theta)}}{\partial t} = 2\sigma_{r\theta} \tag{A.2}$$

$$a_z \frac{\partial^2 u_{\theta(z)}}{\partial t^2} + \omega_z \frac{\partial u_{\theta(z)}}{\partial t} = \frac{\partial \sigma_{\theta z}}{\rho \partial z} \tag{A.3}$$

Where $u_\theta = u_{\theta(r)} + u_{\theta(\theta)} + u_{\theta(z)}$ according to the notation employed by Liu (1999). a_r, A_r, a_z, ω_r, Ω_r and ω_z are the PML variables as described by Liu (1999). $a_r = a_z = 1$, whilst $A_r = 1/r$. ω_r, Ω_r and ω_z are the absorbing parameters. $\Omega_r = 0$, whilst ω_r and ω_z are 0 on the space domain of the problem and a parabolic law that shows values from 0 to 1.6ω, with ω the centre frequency of the excitation. The value of 1.6 was obtained by a trial-and-error process.

The strain-displacement relationship (Equations 3.23 and 3.24) are fused into the KVFD constitutive law equations (Equations 3.18 and 3.20), thus reducing the memory required for computing the algorithm. Then, the resulting equations are differentiated respecting time and then split in the following expressions:

$$a_r \frac{\partial \sigma_{r\theta(r)}}{\partial t} + \omega_r \sigma_{r\theta(r)} = \mu \frac{\partial}{\partial t}\left(\frac{\partial u_\theta}{\partial r}\right) + \eta \frac{\partial^{\alpha+1}}{\partial t^{\alpha+1}}\left(\frac{\partial u_\theta}{\partial r}\right) \tag{A.4}$$

$$A_r \frac{\partial \sigma_{r\theta(\theta)}}{\partial t} + \Omega_r \sigma_{r\theta(\theta)} = -\mu \frac{\partial u_\theta}{\partial t} - \eta \frac{\partial^{\alpha+1} u_\theta}{\partial t^{\alpha+1}} \tag{A.5}$$

$$a_z \frac{\partial \sigma_{\theta z(z)}}{\partial t} + \omega_z \sigma_{\theta z(z)} = \mu \frac{\partial}{\partial t}\left(\frac{\partial u_\theta}{\partial z}\right) + \eta \frac{\partial^{\alpha+1}}{\partial t^{\alpha+1}}\left(\frac{\partial u_\theta}{\partial z}\right) \tag{A.6}$$

Then, the FD expressions described in Section 3.3.3 are applied to approximate the above shown equations. Equation 3.27 for the spatial derivatives, Equation 3.28 for the first temporal derivatives, Equation 3.29 for the second temporal derivatives and Equation 3.30 for the fractional temporal derivatives. The derived expressions listed below are the discrete equations that are implemented in the MATLAB® code for the wave propagation model.

Equation A.1 yields the following discrete equation:

$$\begin{aligned} u_{\theta(r)}\big|_{i,j}^{n} = H_{u(r)}\, u_{\theta(r)}\big|_{i,j}^{n-1} - M_{u(r)}\, u_{\theta(r)}\big|_{i,j}^{n-2} \\ + M_{u(r)} \frac{\Delta t^2}{\rho a_r \Delta r}\left(\sigma_{r\theta}\big|_{i+\frac{1}{2},j}^{n-1} - \sigma_{r\theta}\big|_{i-\frac{1}{2},j}^{n-1}\right) \end{aligned} \tag{A.7}$$

with:

$$M_{u(r)} = \frac{1}{1 + \frac{w_r \Delta t}{a_r}} \tag{A.8}$$

$$H_{u(r)} = \left(2 + \frac{w_r \Delta t}{a_r}\right) M_{u(r)} \tag{A.9}$$

The notation $g|_{i,j}^{n}$ indicates that the g function is evaluated at the spatial (i, j) grid node for the n^{th} time step.

Equation A.2 yields the following discrete equation:

$$\begin{aligned} u_{\theta(\theta)}\big|_{i,j}^{n} = H_{u(\theta)}\, u_{\theta(\theta)}\big|_{i,j}^{n-1} - M_{u(\theta)}\, u_{\theta(\theta)}\big|_{i,j}^{n-2} \\ + M_{u(\theta)} \frac{\Delta t^2}{\rho A_r}\left(\sigma_{r\theta}\big|_{i+\frac{1}{2},j}^{n-1} + \sigma_{r\theta}\big|_{i-\frac{1}{2},j}^{n-1}\right) \end{aligned} \tag{A.10}$$

with:

$$M_{u(\theta)} = \frac{1}{1 + \frac{W_r \Delta t}{A_r}} \tag{A.11}$$

$$H_{u(\theta)} = \left(2 + \frac{W_r \Delta t}{A_r}\right) M_{u(\theta)} \tag{A.12}$$

Equation A.3 yields the following discrete equation:

$$\begin{aligned} u_{\theta(z)}\big|_{i,j}^{n} = H_{u(z)}\, u_{\theta(z)}\big|_{i,j}^{n-1} - M_{u(z)}\, u_{\theta(z)}\big|_{i,j}^{n-2} \\ + M_{u(z)} \frac{\Delta t^2}{\rho a_z \Delta z} \left(\sigma_{\theta z}\big|_{i,j+\frac{1}{2}}^{n-1} - \sigma_{\theta z}\big|_{i,j-\frac{1}{2}}^{n-1} \right) \end{aligned} \tag{A.13}$$

with:

$$M_{u(z)} = \frac{1}{1 + \frac{w_z \Delta t}{a_z}} \tag{A.14}$$

$$H_{u(z)} = \left(2 + \frac{w_z \Delta t}{a_z}\right) M_{u(z)} \tag{A.15}$$

Equation A.4 yields the following discrete equation:

$$\begin{aligned} \sigma_{r\theta(r)}\big|_{i+\frac{1}{2},j}^{n} = \quad & H_{\sigma(r)}\, \sigma_{r\theta(r)}\big|_{i+\frac{1}{2},j}^{n-1} \\ & + M_{\sigma(r)} \frac{\mu}{a_r \Delta r} \left(u_\theta\big|_{i+1,j}^{n} - u_\theta\big|_{i,j}^{n} \right) \\ & - M_{\sigma(r)} \frac{\mu}{a_r \Delta r} \left(u_\theta\big|_{i+1,j}^{n-1} - u_\theta\big|_{i,j}^{n-1} \right) \\ & + M_{\sigma(r)} \frac{\eta}{a_r \Delta r \Delta t^\alpha} \sum_{k=0}^{L} (-1)^k \binom{\alpha+1}{k} \left(u_\theta\big|_{i+1,j}^{n-k} - u_\theta\big|_{i,j}^{n-k} \right) \end{aligned} \tag{A.16}$$

with:

$$M_{\sigma(r)} = \frac{1}{1 + \frac{w_r \Delta t}{2 a_r}} \tag{A.17}$$

$$H_{\sigma(r)} = \left(1 - \frac{w_r \Delta t}{2 a_r}\right) M_{\sigma(r)} \tag{A.18}$$

Equation A.5 yields the following discrete equation:

$$\begin{aligned}\sigma_{r\theta(\theta)}\big|_{i+\frac{1}{2},j}^{n} = \quad & H_{\sigma(\theta)}\,\sigma_{r\theta(\theta)}\big|_{i+\frac{1}{2},j}^{n-1} \\ & - M_{\sigma(\theta)}\frac{\mu}{2A_r}\left(u_\theta|_{i+1,j}^{n} + u_\theta|_{i,j}^{n}\right) \\ & - M_{\sigma(\theta)}\frac{\mu}{2A_r}\left(u_\theta|_{i+1,j}^{n-1} + u_\theta|_{i,j}^{n-1}\right) \\ & - M_{\sigma(\theta)}\frac{\eta}{2A_r\Delta t^{\alpha}}\sum_{k=0}^{L}(-1)^k\binom{\alpha+1}{k}\left(u_\theta|_{i+1,j}^{n-k} + u_\theta|_{i,j}^{n-k}\right)\end{aligned} \tag{A.19}$$

with:

$$M_{\sigma(\theta)} = \frac{1}{1+\frac{W_r\Delta t}{2A_r}} \tag{A.20}$$

$$H_{\sigma(\theta)} = \left(1-\frac{W_r\Delta t}{2A_r}\right)M_{\sigma(\theta)} \tag{A.21}$$

Equation A.6 yields the following discrete equation:

$$\begin{aligned}\sigma_{\theta z(z)}\big|_{i,j+\frac{1}{2}}^{n} = \quad & H_{\sigma(z)}\,\sigma_{\theta z(z)}\big|_{i,j+\frac{1}{2}}^{n-1} \\ & + M_{\sigma(z)}\frac{\mu}{a_z\Delta z}\left(u_\theta|_{i,j+1}^{n} - u_\theta|_{i,j}^{n}\right) \\ & - M_{\sigma(z)}\frac{\mu}{a_z\Delta z}\left(u_\theta|_{i,j+1}^{n-1} - u_\theta|_{i,j}^{n-1}\right) \\ & + M_{\sigma(z)}\frac{\eta}{a_z\Delta z\Delta t^{\alpha}}\sum_{k=0}^{L}(-1)^k\binom{\alpha+1}{k}\left(u_\theta|_{i,j+1}^{n-k} - u_\theta|_{i,j}^{n-k}\right)\end{aligned} \tag{A.22}$$

with:

$$M_{\sigma(z)} = \frac{1}{1+\frac{w_z\Delta t}{2a_z}} \tag{A.23}$$

$$H_{\sigma(z)} = \left(1-\frac{w_z\Delta t}{2a_z}\right)M_{\sigma(z)} \tag{A.24}$$

Appendix B

MATLAB® FDTD model code

This appendix contains the MATLAB® codes from the different algorithms that have been employed for the wave propagation model described in Chapter 3.

Main code of the 2D FDTD wave propagation model

```
%%%%%%%%%%%%%%%%%%%%%%%%%%%%%%%%%%%%%%%%%%%%%%%%%%%%%%%%%%%%%%%%%%%%%%%%%%%%
% 2D KVFD wave propagation model in plane r-z with PML
% Antonio Gomez     2016-06-03
%%%%%%%%%%%%%%%%%%%%%%%%%%%%%%%%%%%%%%%%%%%%%%%%%%%%%%%%%%%%%%%%%%%%%%%%%%%%

%% Setting

% Loading input information
addpath([pwd '/dat']);
eval('setup');                          % geometry and device conf.
eval('mechanical_parameters');          % mechanical properties
eval('PML');                            % PML

% Time parameters
dt      = 2.0e-5;                           % time step
tD      = ceil(tt/dt);                      % number of time steps
time    = linspace(0,tt,tD);                % time vector
L       = ceil(2e-3/tt*length(time));       % effective memory length

%% Declaring variables (1==r, 2==theta, 3==z)

% Displacement and stress fields
u2          = 0.*o;
u2_r        = u2;       u2_a        = u2;   u2_z        = u2;
u2_old1_r   = u2;       u2_old1_a   = u2;   u2_old1_z   = u2;
u2_old2_r   = u2;       u2_old2_a   = u2;   u2_old2_z   = u2;
s12         = u2;       s12_r       = u2;   s12_a       = u2;
s23         = u2;       s23_z       = u2;

% Auxiliar variables for fractional derivative
D_u2_r      = u2;       D_u2_a      = u2;   D_u2_z      = u2;
```

```
32 u2_memory    = zeros(zD*(L+1),rD);
33
34 % Auxiliar variables
35 Mu_r = 1./(1+w_r.*dt./a_r);
36 Hu_r = (2+dt.*w_r./a_r).*Mu_r;
37 Mu_a = 1./(1+W_r.*dt./A_r);
38 Hu_a = (2+dt.*W_r./A_r).*Mu_a;
39 Mu_z = 1./(1+w_z.*dt./a_z);
40 Hu_z = (2+dt.*w_z./a_z).*Mu_z;
41 Ms_r = 1./(1+w_r.*dt./(2.*a_r));
42 Hs_r = (1-dt.*w_r./(2.*a_r)).*Ms_r;
43 Ms_a = 1./(1+W_r.*dt./(2.*A_r));
44 Hs_a = (1-dt.*W_r./(2.*A_r)).*Ms_a;
45 Ms_z = 1./(1+w_z.*dt./(2.*a_z));
46 Hs_z = (1-dt.*w_z./(2.*a_z)).*Ms_z;
47
48 % Output storage
49 u2_rec       = zeros(num_receiver,tD);
50
51 % Vector binomial coefficients for the fractional derivative
52 binomial_coeff_aux = zeros(zD*(L+1),rD);
53 for j=0:L
54     binomial_coeff_aux(zD*j+1:zD*(j+1),:) = ...
55         (-1).^j.*gamma(alfa+2)./(gamma(j+1).*gamma(alfa+2-j));
56 end
57
58 % Excitation signal - Gaussian Modulated Wave & Sine smoothed
59 fa = fa_rad.*rr(1);
60 ft_aux1      = fa.*gauspuls(time,ff,1.6);
61 ft_aux2      = fa.*gmonopuls(time,ff);
62 peri_dt_aux  = ceil(0.9*1/ff/dt);
63 ft1          = [fliplr(ft_aux1(2:peri_dt_aux+1))...
64                    ft_aux1(1:end-peri_dt_aux)];
65 ft2          = [-fliplr(ft_aux2(2:peri_dt_aux+1))...
66                    ft_aux2(1:end-peri_dt_aux)];
```

```
67
68 %% Discrete equations, iterative process
69
70 % Video setup for recording the simulation
71 plotfreq  = 5;  % frequency for capturing frames
72 fi        = figure (8);
73 writerObj = VideoWriter('eps/video_name');
74 open(writerObj);
75
76 % Setting the graphs
77 set(fi,'MenuBar','none','Color',[0.6 0.6 0.6],...
78     'NumberTitle','off','units','pixels');
79 colormap jet; iptsetpref('ImshowBorder','tight');
80 set(gca,'position',[0 0 1 1],'units','normalized');
81 tic; clear('signal','mov');
82
83 %% Discrete equations, iterative process
84
85 m = num_emitter;  % number of emitters
86 for n = 0:tD-1
87
88 if ~mod(n+1,plotfreq),...
89     fprintf('Time step %d / %d remaining: %dmin\n',...
90             n+1,tD,round((tD-n+1)/(n+1)*toc/60));
91 end
92
93 % Calculating the displacement field components at the time step n
94 u2_r     = Hu_r.*u2_old1_r   - Mu_r.*u2_old2_r...
95          + Mu_r.*(dt.^2./(rho.*a_r.*dr)).*diff([zeros(zD,1) s12]')';
96 u2_a     = Hu_a.*u2_old1_a   - Mu_a.*u2_old2_a...
97          + Mu_a.*(dt.^2./(rho.*A_r.*2)).*(s12+[zeros(zD,1)...
98          s12(:,1:end-1)]);
99 u2_z     = Hu_z.*u2_old1_z   - Mu_z.*u2_old2_z...
100         + Mu_z.*(dt.^2./(rho.*a_z.*dz)).*diff([s23; zeros(1,rD)]);
101 u2       = u2_r + u2_a + u2_z;
```

```
102
103 u2_old2_r   = u2_old1_r;    u2_old1_r   = u2_r;
104 u2_old2_a   = u2_old1_a;    u2_old1_a   = u2_a;
105 u2_old2_z   = u2_old1_z;    u2_old1_z   = u2_z;
106
107 % Boundary condition
108 u2(emitter_pos_z(m,:),ab_r1+1) = ft1(n+1); % excitation signal
109
110 % Storing in memory the displacement field
111 u2_memory(1:end-zD,:)      = u2_memory(zD+1:end,:);
112 u2_memory(end-zD+1:end,:)  = u2;
113
114 % Declaring and calculating the stress components at time step n ...
115 % that are involved in the fractional derivative approximation
116 D_u2_r = D_u2_r.*0;
117 D_u2_a = D_u2_a.*0;
118 D_u2_z = D_u2_z.*0;
119
120 if n < L,  J = n;  else,    J = L;  end
121 for j=0:J
122     u2_aux = u2_memory(end-zD*(j+1)+1:end-zD*(j),:);
123     D_u2_r = D_u2_r + binomial_coeff_aux(zD*j+1:zD*(j+1),:)...
124         .*diff([u2_aux zeros(zD,1)]')';
125     D_u2_a = D_u2_a + binomial_coeff_aux(zD*j+1:zD*(j+1),:)...
126         .*(u2_aux+[u2_aux(:,2:end) zeros(zD,1)]);
127     D_u2_z = D_u2_z + binomial_coeff_aux(zD*j+1:zD*(j+1),:)...
128         .*diff([zeros(1,rD); u2_aux]);
129 end
130
131 % Calculating the stress field components at the time step n
132 s12_r   = Hs_r.*s12_r...
133         + Ms_r.*(mo./(a_r.*dr)).*(diff([u2 zeros(zD,1)]')'...
134         - diff([u2_memory(end-2*zD+1:end-zD,:) zeros(zD,1)]')')...
135         + Ms_r.*(eta./(a_r.*dr.*dt.^alfa)).*D_u2_r;
136 s12_a   = Hs_a.*s12_a...
```

```
137         - Ms_a.*(mo./(A_r.*2)).*((u2+[u2(:,2:end) zeros(zD,1)])...
138         - (u2_memory(end-2*zD+1:end-zD,:)...
139         + [u2_memory(end-2*zD+1:end-zD,2:end) zeros(zD,1)]))...
140         - Ms_a.*(eta./(A_r.*2.*dt.^alfa)).*D_u2_a;
141 s23_z   = Hs_z.*s23_z...
142         + Ms_z.*(mo./(a_z.*dz)).*(diff([zeros(1,rD); u2])...
143         - diff([zeros(1,rD); u2_memory(end-2*zD+1:end-zD,:)]))...
144         + Ms_z.*(eta./(a_z.*dz.*dt.^alfa)).*D_u2_z;
145 s12     = s12_r + s12_a;
146 s23     = s23_z;
147
148 % Saving the displacement signal measured at the receiver's location
149 u2_rec(:,n+1) = sum(reshape(u2(receiver_pos_z,ab_r1+1)...
150     ,[receiver_th_z,num_receiver])./receiver_th_z;
151
152 % Plotting the frames and recording the video simulation
153 if ~mod((n+1),plotfreq)     % plot every plotfreq steps
154     imagesc((0:1:20),(0:1:40)...
155           ,u2(ab_z1+1:zD-ab_z2,ab_r1+1:rD-ab_r2),[-2e-5 2e-5]);
156     axis off; axis equal;
157     set(gcf, 'Name', sprintf('t=%.3f us FDTD',n*dt*1e6));
158     colorbar; drawnow;
159     frame=getframe; writeVideo(writerObj,frame);
160 end
161 end
162 toc, close(writerObj);
163
164 %% Saving output data
165 save('filename','time','u2_rec');
```

Code for setting the geometry and device configuration

```
%%%%%%%%%%%%%%%%%%%%%%%%%%%%%%%%%%%%%%%%%%%%%%%%%%%%%%%%%%%%%%%%%%%%%%%%
% 2D wave propagation model - Geometry and device setup
% Antonio Gomez     2015-01-22
%%%%%%%%%%%%%%%%%%%%%%%%%%%%%%%%%%%%%%%%%%%%%%%%%%%%%%%%%%%%%%%%%%%%%%%%

% Central frequency and max amplitude of excitation

ff      = 0.7e3;        % centre frequency of excitation (Hz)
fa_rad  = 1e-3/3.25e-3; % max angular amplitude excitation (radians)

% Grid configuration:
rS    = 20e-3;      % real radius of domain (m)
zS    = 40e-3;      % real size of domain at z direction (m)
tt    = 35.0e-3;    % total time (s)
dr    = 150e-6;     % spacing r (m), condition: dr < cs/ff/20
dz    = dr;         % spacing z (m), condition: dz < cs/ff/20
ab_r1 = 0;      % number of PML elements - layers urethral wall
ab_r2 = 60;     % number of PML elements - layers right contour
ab_z1 = 60;     % number of PML elements - layers top contour
ab_z2 = 60;     % number of PML elements - layers botton contour

% Configuration of emitters and receivers:
emitter_ra   = 3.25e-3;     % emitter radius (m)
emitter_th   = 1.0e-3;      % emitter thickness (m)
receiver_th  = 0.5e-3;      % receiver thickness (m)
num_emitter  = 1;           % number of emitters
num_receiver = 32;          % number of receivers;
emitter_pos  = [zS/(num_emitter+num_receiver+1)...
    ; (num_emitter+num_receiver)...
    *zS/(num_emitter+num_receiver+1)];  % emitters positions (m)
receiver_pos = [linspace(0,1,num_receiver/2)...
```

```
32      .*(zS/2-4*emitter_th)...
33      +2*emitter_th linspace(0,1,num_receiver/2)...
34      .*(zS/2-4*emitter_th)...
35      +zS/2+2*emitter_th ];                % receivers positions (m)
36
37  % Grid definition
38  rD  = round((rS/dr+ab_r1+ab_r2)/2)*2;    % elements in r direction
39  zD  = round((zS/dz+ab_z1+ab_z2)/2)*2;    % elements in z direction
40  o   = ones(zD,rD);                       % empty grid + PML
41  rr  = dr*(0:1:rD-1)+emitter_ra;          % vector radius
42  A_r = repmat(rr,zD,1);                   % vector inverse radius
43
44  % Positions of emitters and receivers in the grid
45  emitter_th_z   = round(emitter_th/dz);
46  receiver_th_z  = round(receiver_th/dz);
47  emitter_pos_z  = repmat(ceil(ab_z1+emitter_pos./dz)...
48      ,1,emitter_th_z)...
49      +repmat(-floor(emitter_th_z/2):floor(emitter_th_z/2)...
50      ,num_emitter,1);
51  receiver_pos_z = repmat(round(ab_z1+receiver_pos./dz)...
52      ,receiver_th_z,1)...
53      +repmat((-floor(receiver_th_z/2):ceil(receiver_th_z/2)-1)'...
54      ,1,num_receiver);
55  receiver_pos_z = reshape(receiver_pos_z...
56      ,[num_receiver*receiver_th_z,1]);
```

Code for setting the mechanical properties of the medium

```
%%%%%%%%%%%%%%%%%%%%%%%%%%%%%%%%%%%%%%%%%%%%%%%%%%%%%%%%%%%%%%%%%%%%%%%%%%%%
% 2D wave propagation model - Mechanical parameters
% Antonio Gomez     2016-12-15
%%%%%%%%%%%%%%%%%%%%%%%%%%%%%%%%%%%%%%%%%%%%%%%%%%%%%%%%%%%%%%%%%%%%%%%%%%%%

%% Mechanical parameters:

% Healthy prostatic tissue
prostate_KVFD   = [3000,35,0.35];   % [mo,eta,alfa] KVFD parameters
mo      = prostate_KVFD(1).*o;      % shear stiffness (Pa)
eta     = prostate_KVFD(2).*o;      % shear viscosity (Pa*s^alfa)
alfa    = prostate_KVFD(3).*o;      % fractional derivative order
rho_0   = 1e3;                      % mass density (kg/m^3)
rho     = rho_0.*o;

% Rounded tumour parameters:
tumour_KVFD     = [3,3,1].*prostate_KVFD;   % [mo,eta,alfa] tumour
diam            = 6.0e-3;           % diameter of the tumour (m)
diam_x          = ceil(diam/dr);
tumour          = tumour_rounded(diam_x);
tumour_coor     = [14.0e-3, 18.0e-3];   % [r,z] coordinates...
% of the centre of the tumour ([0,0] is the top left corner)
tumour_coor_x   = [ab_z1,ab_r1]+fliplr(ceil(tumour_coor./dr));
tumour_corner   = tumour_coor_x-ceil(diam_x/2);

% HIFU lesion parameters:
lesion_KVFD     = [5,3,1].*prostate_KVFD;   % [mo,eta,alfa] lesion
ellipse_diam    = [10e-3,3e-3]; % [diameter_mayor,diameter_minor]...
% diameters of the ellipse (mm)
ellipse_diam_x  = ceil([ellipse_diam(1),ellipse_diam(2)]./dr);
ellipse_angle   = 0*pi/180; % angle of the mayor axis...
```

```
% respecting a horizontal r line (rad)
lesion          = ellipse(ellipse_diam_x(1),ellipse_diam_x(2)...
                    ,ellipse_angle);
lesion_coor     = [14.0e-3, 20.0e-3];
lesion_coor_x   = [ab_z1,ab_r1]+fliplr(ceil(lesion_coor./dr));
lesion_corner   = lesion_coor_x-ceil(fliplr(ellipse_diam_x)./2);

for j=1:length(tumour)
    for i=1:length(tumour)
        if tumour(j,i) == 1
            mo(tumour_corner(1)+j-1,tumour_corner(2)+i-1) =...
                tumour_KVFD(1);
            eta(tumour_corner(1)+j-1,tumour_corner(2)+i-1) =...
                tumour_KVFD(2);
            alfa(tumour_corner(1)+j-1,tumour_corner(2)+i-1) =...
                tumour_KVFD(3);
        end
    end
end
for j=1:size(lesion,1)
    for i=1:size(lesion,2)
        if lesion(j,i) == 1
            mo(lesion_corner(1)+j-1,lesion_corner(2)+i-1) =...
                lesion_KVFD(1);
            eta(lesion_corner(1)+j-1,lesion_corner(2)+i-1) =...
                lesion_KVFD(2);
            alfa(lesion_corner(1)+j-1,lesion_corner(2)+i-1) =...
                lesion_KVFD(3);
        end
    end
end
```

```
function ellipse=ellipse(a,b,phi)
%% Ellipsoidal shape in a matrix of ones and zeros
```

```
% Unknown author and date of creation
% a and b are the major and minor diameters of the ellipse

% Diameters of the ellipse
theta_grid = linspace(0,2*pi,4000);
a_x = round(a/2);
b_x = round(b/2);
X0 = max(a_x,b_x);          % coordinate x
Y0 = max(a_x,b_x);          % coordinate y

% The ellipse in x and y coordinates centered at 0
ellipse_x_r = a_x*cos( theta_grid );
ellipse_y_r = b_x*sin( theta_grid );

% Defining a rotation matrix
R = [ cos(phi) sin(phi); -sin(phi) cos(phi) ];
n = length(ellipse_x_r);

% Rotating the ellipse an angle phi and...
% then translate it to (X0, Y0)
r_ellipse = R*[ellipse_x_r; ellipse_y_r]+repmat([X0; Y0],[1,n]);

% Transform into a matrix of ones with the ellipse
ellipse = zeros(max(a_x,b_x)*2+1);
for i=1:length(theta_grid)
    ellipse(1+round(r_ellipse(2,i)),1+round(r_ellipse(1,i))) = 1;
end
for i=1:length(ellipse)
    aux1 = find(ellipse(i,:));
    ellipse(i,min(aux1):max(aux1)) = 1;
end

% Deleting rows and colums of zeros
ellipse( ~any(ellipse,2), : ) = [];  % rows
ellipse( :, ~any(ellipse,1) ) = [];  % columns
```

Code for setting the PML

```
%%%%%%%%%%%%%%%%%%%%%%%%%%%%%%%%%%%%%%%%%%%%%%%%%%%%%%%%%%%%%%%%%%%%%%%%
% Perfectly Matched Layer for the 2D FDTD wave propagation model
% Antonio Gomez     2015-02-11
%%%%%%%%%%%%%%%%%%%%%%%%%%%%%%%%%%%%%%%%%%%%%%%%%%%%%%%%%%%%%%%%%%%%%%%%

%% Perfectly Matched Layers
w_max       = 3.2*pi*ff;
modifier_r  = (-4/ab_r2^2).*linspace(0,ab_r2,ab_r2).^2 ...
    +(4/ab_r2).*linspace(0,ab_r2,ab_r2)+1;
w_r_aux_r   = modifier_r...
    .*(exp(linspace(0,ab_r2,ab_r2)*log(w_max+1)/ab_r2)-1);
w_r_aux_1   = fliplr(w_r_aux_r);
a_r_aux_1   = fliplr(a_r_aux_r);
w_r         = w_r_aux_1(1)*o;
a_r         = a_r_aux_1(1)*o;

if ab_r1 == 0
    for s=2:ab_z1
        w_r(s:end+1-s,1:end+1-(round(ab_r2/ab_z1))*s) = w_r_aux_1(s);
        a_r(s:end+1-s,1:end+1-(round(ab_r2/ab_z1))*s) = a_r_aux_1(s);
    end
else
    for s=2:ab_z1
        w_r(s:end+1-s,s:end+1-s) = w_r_aux_1(s);
        a_r(s:end+1-s,s:end+1-s) = a_r_aux_1(s);
    end
end

W_r = w_r.*0;
w_z = w_r;
a_z = a_r;
```

Appendix C

MATLAB® particle tracking code

This appendix contains the MATLAB® code for the particle tracking method used for the experimental validation of the wave propagation model in Chapter 4.

Main code of the particle tracking method

```
%%%%%%%%%%%%%%%%%%%%%%%%%%%%%%%%%%%%%%%%%%%%%%%%%%%%%%%%%%%%%%%%%%%%%%%%%%%%
% Particle tracking method by digital image correlation
% Antonio Callejas, Antonio Gomez     2017-05-14
%%%%%%%%%%%%%%%%%%%%%%%%%%%%%%%%%%%%%%%%%%%%%%%%%%%%%%%%%%%%%%%%%%%%%%%%%%%%

%% Loading video data
addpath([pwd '/Videos/high_speed_camera_recording']);

%% Extracting frames from video file
fname       = 'high_speed_camera_recording.tif';
info        = imfinfo(fname);
numFrames   = numel(info);
frames      = zeros(768,768,2,'uint8');
frames(:,:,1) = imread(fname,1);

%% Declaring variables
Z = 76;          % number of radial points
angles_corr     = zeros(1,numFrames);
angles_r_corr   = zeros(Z,numFrames);
dt = 1/1e4;      % frame frequency
time = (1:numFrames).*dt;
pixel_mm = 0.0163;  % real lenght dimension of a pixel
rr = (2:77).*10.*pixel_mm;

%% Cross-correlation process
% Cross correlation process for capturing the angle that each...
% section of the frame has rotated respecting the initial...
% reference position
for z=1:Z
disp(z);

```

```
32 extra_radius    = 57;
33 centre(1)       = 1;
34 centre(2)       = 386;
35 radius_ext      = extra_radius+20+z*10;
36 radius_int      = extra_radius+z*10;
37 xyresolution    = 2*radius_ext+1;
38
39 [xx, yy]    = meshgrid(1:xyresolution,1:xyresolution);
40 mask_ext    = sqrt((xx-radius_ext).^2+(yy-radius_ext).^2)...
41                 <= radius_ext; % circular mask
42 mask_int    = sqrt((xx-radius_ext).^2+(yy-radius_ext).^2)...
43                 <= radius_int; % circular mask
44
45 mask = mask_ext+mask_int;
46 mask(mask==2) = 0;
47
48 image1 = imcrop(im2double(frames(:,:,1))...
49     ,[centre(1) centre(2)-radius_ext radius_ext-extra_radius...
50     2*radius_ext]); % disk emitter on the left side of the video
51
52 if centre(2)<radius_ext
53     addition1_up = radius_ext-centre(2)+1;
54     image1 = [zeros(addition1_up,size(image1,2)); image1];
55 end
56 if 768-centre(2)<radius_ext
57     addition1_bottom = radius_ext-768+centre(2);
58     image1 = [image1; zeros(addition1_bottom,size(image1,2))];
59 end
60 if size(image1,2)<2*radius_ext
61     addition2=2*radius_ext+1-size(image1,2);
62     image1 = [zeros(size(image1,1),addition2) image1];
63 end
64
65 for i=1:numFrames
66
```

```
67  frames(:,:,2) = imread(fname,i);
68  image2 = imcrop(im2double(frames(:,:,2))...
69      ,[centre(1) centre(2)-radius_ext radius_ext-extra_radius...
70      2*radius_ext]); % emitter on the left side of the frame
71
72  if centre(2)<radius_ext
73      addition1_up = radius_ext-centre(2)+1;
74      image2 = [zeros(addition1_up,size(image2,2)); image2];
75  end
76  if 768-centre(2)<radius_ext
77      addition1_bottom = radius_ext-768+centre(2);
78      image2 = [image2; zeros(addition1_bottom,size(image2,2))];
79  end
80  if size(image2,2)<2*radius_ext
81      addition2=2*radius_ext+1-size(image2,2);
82      image2 = [zeros(size(image2,1),addition2) image2];
83  end
84  image2 = im2double(image2).*mask;
85  size_ref = size(image2,1);
86
87  bandwidth = 200;
88  if size_ref>1.1*bandwidth
89      image2 = image2(floor(size(image2,1)/2)...
90          -bandwidth/2:floor(size(image2,1)/2)+bandwidth/2,:);
91  end
92  image2 = image2(:,end-bandwidth/4+1:end);
93
94  if z<30
95      vector_angles   = -2.5:0.05:2.5;
96  else
97      if z<40
98          vector_angles   = -1.25:0.025:1.25;
99      else
100          if z<60
101             vector_angles   = -0.8:0.02:0.8;
```

```
102          else
103              if z<65
104                  vector_angles   = -0.7:0.01:0.7;
105              else
106                  vector_angles   = -0.6:0.01:0.6;
107              end
108          end
109      end
110  end
111
112  vector_corr = vector_angles.*0;
113
114  j=1;
115  for angle=vector_angles
116  image1_rotated...
117      = im2double(imrotate(image1,angle,'bicubic','crop')).*mask;
118  if size_ref>1.1*bandwidth
119  image1_rotated = image1_rotated(floor(size(image1_rotated,1)/2)...
120      -bandwidth/2:floor(size(image1_rotated,1)/2)+bandwidth/2,:);
121  end
122  image1_rotated = image1_rotated(:,end-bandwidth/4+1:end);
123  vector_corr(j)  = corr2(image1_rotated,image2);
124  j=j+1;
125  end
126  angles_corr(i) = vector_angles(find(vector_corr==max(vector_corr)));
127  end
128  angles_r_corr(z,:)   = angles_corr;
129  end
130
131  %% Save output data
132  % angles_r_corr contains the reconstructed angles at each r node
133  save(high_speed_camera_recording.mat','angles_r_corr','time','rr');
```

Appendix D

MATLAB® RTM code

This appendix contains the MATLAB® codes from the different algorithms that have been employed in the RTM method for the reconstruction of the location of stiff lesions inside the prostate, shown in Chapter 5.

Main code of the RTM method

```
%%%%%%%%%%%%%%%%%%%%%%%%%%%%%%%%%%%%%%%%%%%%%%%%%%%%%%%%%%%%%%%%%%%%%%%%%%%%
% RTM method using the 2D FDTD wave propagation model
% Antonio Gomez     2017-01-09
%%%%%%%%%%%%%%%%%%%%%%%%%%%%%%%%%%%%%%%%%%%%%%%%%%%%%%%%%%%%%%%%%%%%%%%%%%%%

%% Declaring initial parameters
addpath([pwd '/dat']);
eval('setup_KVFD');     % Grid data
imag2_aux = oSd.*0;

% Matrix for containing the reconstructed image...
% according the different cross correlation methods
claerbout_stacked2      = zeros(zSd,rSd);
norm_source_stacked2    = zeros(zSd,rSd);
norm_receivers_stacked2 = zeros(zSd,rSd);
ratio_squared_stacked2  = zeros(zSd,rSd);
proposed_stacked2       = zeros(zSd,rSd);

%% Iterative process, according the number of emitters
fprintf('Iteration number'); disp(1);
for m=1:num_emitter; fprintf('Emitter number'); disp(m);

% 1) FDTD 2D model for measurement of...
% pseudo-experimental signal at receivers
eval('mechanical_parameters_tumour_and_lesion'); % loading...
                            % mechanical parameters of the medium
eval('pseudoexp_KVFD'); % simulation for obtaninig the...
        % pseudo-experimental measurements at receivers' location
close all;

% 2) FDTD 2D model for making the reverse migration of collected...
```

```
% signals from receivers
eval('mechanical_parameters_healthy_prostate'); % loading...
                            % mechanical parameters of the medium
imagfreq = 1;  % frames frequency to carry out the correlation
eval('forward_source_KVFD'); % forward propagation,...
        % output: stored displacement field according the frame...
        % frequency selected at each time step
close all;

% 3) Preprocessing signal for removing the direct wave
u2_rec = u2_rec-u2_rec_healthy;     % Removal the direct wave
eval('adding_noise_KVFD');          % Addition of white noise

% 4) Imagining condition using the reverse propopagation and...
% the forward propagation in a homogeneous model
eval('reversed_receivers_imaging_KVFD');    % reverse...
        % propagation, output: stored displacement field...
        % according the frame frequency selected at each time step
close all;

% 5) Stacking the correlation images
claerbout_stacked2      = claerbout_stacked2 + claerbout2;
norm_source_stacked2    = norm_source_stacked2 + norm_source2;
norm_receivers_stacked2 = norm_receivers_stacked2 + norm_receivers2;
ratio_squared_stacked2  = ratio_squared_stacked2 + ratio_squared2;
proposed_stacked2       = proposed_stacked2 + antonioB;
end

%% 6) Normalization of the reconstruction image
claerbout_stacked_aux2 = claerbout_stacked2;
claerbout_stacked_aux2(claerbout_stacked_aux2<0) = 0;
claerbout_stacked_norm2 = claerbout_stacked_aux2...
                            ./max(max(claerbout_stacked_aux2));
norm_source_stacked_aux2 = norm_source_stacked2;
norm_source_stacked_aux2(norm_source_stacked_aux2<0) = 0;
```

```
norm_source_stacked_norm2 = norm_source_stacked_aux2...
                            ./max(max(norm_source_stacked_aux2));
norm_receivers_stacked_aux2 = norm_receivers_stacked2;
norm_receivers_stacked_aux2(norm_receivers_stacked_aux2<0) = 0;
norm_receivers_stacked_norm2 = norm_receivers_stacked_aux2...
                            ./max(max(norm_receivers_stacked_aux2));
ratio_squared_stacked_aux2 = ratio_squared_stacked2;
ratio_squared_stacked_aux2(ratio_squared_stacked_aux2<0) = 0;
ratio_squared_stacked_norm2 = ratio_squared_stacked_aux2...
                            ./max(max(ratio_squared_stacked_aux2));
proposed_stacked_aux2 = proposed_stacked2;
proposed_stacked_aux2(proposed_stacked_aux2<0) = 0;
proposed_stacked_norm2 = proposed_stacked_aux2...
                                ./max(max(proposed_stacked_aux2));

clear('binomial_coeff_aux','u2_memory','u2_stored');

%% Saving data
save('eps/rtm_filename.mat');
```

Codes for the algorithms named ‘mechanical_parameters_tumour_and_lesion’, ‘pseudoexp_KVFD’, ‘mechanical_parameters_healthy_prostate’ and ‘forward_source_KVFD’ are adapted versions from the codes shown in Appendix B.

Code for adding white noise

```
%%%%%%%%%%%%%%%%%%%%%%%%%%%%%%%%%%%%%%%%%%%%%%%%%%%%%%%%%%%%%%%%%%%%%%%%%%%%
%% Addition of white noise to the simulated measurements
%% Guillermo Rus, Antonio Gomez     2017-01-09
%%%%%%%%%%%%%%%%%%%%%%%%%%%%%%%%%%%%%%%%%%%%%%%%%%%%%%%%%%%%%%%%%%%%%%%%%%%%

% Adding the noise to the recordings:
u2_rec_clean = u2_rec;
fpx_noise   = randn(size(time));
noise_level = 0.1;
aux1        = repmat(rms(rms(u2_rec')),num_receiver,length(time));
noise       = noise_level*repmat(rms(u2_rec')',1,length(time))...
    .*repmat(fpx_noise,num_receiver,1);
u2_rec = u2_rec + noise;
u2_rec_noisy = u2_rec;
```

Code for the reverse propagation and the cross-correlation process

```
%%%%%%%%%%%%%%%%%%%%%%%%%%%%%%%%%%%%%%%%%%%%%%%%%%%%%%%%%%%%%%%%%%%%%%%%
% Reverse propagation for the RTM and cross-correlation process
% Antonio Gomez     2017-01-09
%%%%%%%%%%%%%%%%%%%%%%%%%%%%%%%%%%%%%%%%%%%%%%%%%%%%%%%%%%%%%%%%%%%%%%%%

%% Declaring initial variables
% Displacement and stress fields
u2          = 0.*o;
u2_r        = u2;       u2_a        = u2;   u2_z        = u2;
u2_old1_r   = u2;       u2_old1_a   = u2;   u2_old1_z   = u2;
u2_old2_r   = u2;       u2_old2_a   = u2;   u2_old2_z   = u2;
s12         = u2;       s12_r       = u2;   s12_a       = u2;
s23         = u2;       s23_z       = u2;

% Auxiliar variables for fractional derivative
D_u2_r      = u2;       D_u2_a      = u2;   D_u2_z      = u2;
u2_memory   = zeros(zD*(L+1),rD);

% Auxiliar variables
Mu_r = 1./(1+w_r.*dt./a_r);
Hu_r = (2+dt.*w_r./a_r).*Mu_r;
Mu_a = 1./(1+W_r.*dt./A_r);
Hu_a = (2+dt.*W_r./A_r).*Mu_a;
Mu_z = 1./(1+w_z.*dt./a_z);
Hu_z = (2+dt.*w_z./a_z).*Mu_z;
Ms_r = 1./(1+w_r.*dt./(2.*a_r));
Hs_r = (1-dt.*w_r./(2.*a_r)).*Ms_r;
Ms_a = 1./(1+W_r.*dt./(2.*A_r));
Hs_a = (1-dt.*W_r./(2.*A_r)).*Ms_a;
Ms_z = 1./(1+w_z.*dt./(2.*a_z));
Hs_z = (1-dt.*w_z./(2.*a_z)).*Ms_z;
```

```
32
33 % Imaging correlation auxiliar variables
34 claerbout2          = 0*oSd;
35 proposed_aux        = 0*oSd;
36 source2             = 0*oSd;
37 source_squared2     = 0*oSd;
38 receivers_squared2  = 0*oSd;
39
40 % Excitation signal - Reversed in time measurements from receivers
41 rev_u2_exc = fliplr(u2_rec);
42
43 %% Discrete equations, iterative process
44 for n = 0:tD-1
45     if ~mod(n+1,plotfreq)...
46         ,fprintf('Time step %d / %d    remaining: %dmin\n',n+1 ...
47         ,tD,round((tD-n+1)/(n+1)*toc/60))
48     end
49
50 % Calculating the displacement field components at the time step n
51 u2_r     = Hu_r.*u2_old1_r   - Mu_r.*u2_old2_r...
52         + Mu_r.*(dt.^2./(rho.*a_r.*dr)).*diff([zeros(zD,1) s12]')';
53 u2_a     = Hu_a.*u2_old1_a   - Mu_a.*u2_old2_a...
54         + Mu_a.*(dt.^2./(rho.*A_r.*2)).*(s12+[zeros(zD,1)...
55         s12(:,1:end-1)]);
56 u2_z     = Hu_z.*u2_old1_z   - Mu_z.*u2_old2_z...
57         + Mu_z.*(dt.^2./(rho.*a_z.*dz)).*diff([s23; zeros(1,rD)]);
58 u2       = u2_r + u2_a + u2_z;
59
60 u2_old2_r   = u2_old1_r;    u2_old1_r   = u2_r;
61 u2_old2_a   = u2_old1_a;    u2_old1_a   = u2_a;
62 u2_old2_z   = u2_old1_z;    u2_old1_z   = u2_z;
63
64 % Boundary condition
65 u2(reshape(receiver_pos_z',num_receiver*receiver_co_z,1)...
66     ,ab_r1+1) = reshape(repmat(rev_u2_exc(:,n+1)'...
```

```
67      ,receiver_co_z,1),num_receiver*receiver_co_z,1);
68
69  % Storing in memory the velocity field
70  u2_memory(1:end-zD,:)       = u2_memory(zD+1:end,:);
71  u2_memory(end-zD+1:end,:)   = u2;
72
73  % Declaring and calculating the stress components at time step n ...
74  % that are involved in the fractional derivative approximation
75  D_u2_r = D_u2_r.*0;
76  D_u2_a = D_u2_a.*0;
77  D_u2_z = D_u2_z.*0;
78
79  if n < L,   J = n;   else,     J = L;   end
80  for j=0:J
81      u2_aux = u2_memory(end-zD*(j+1)+1:end-zD*(j),:);
82      D_u2_r = D_u2_r + binomial_coeff_aux(zD*j+1:zD*(j+1),:)...
83          .*diff([u2_aux zeros(zD,1)]')';
84      D_u2_a = D_u2_a + binomial_coeff_aux(zD*j+1:zD*(j+1),:)...
85          .*(u2_aux+[u2_aux(:,2:end) zeros(zD,1)]);
86      D_u2_z = D_u2_z + binomial_coeff_aux(zD*j+1:zD*(j+1),:)...
87          .*diff([zeros(1,rD); u2_aux]);
88  end
89
90  % Calculating the stress field components at the time step n
91  s12_r    = Hs_r.*s12_r...
92          + Ms_r.*(mo./(a_r.*dr)).*(diff([u2 zeros(zD,1)]')'...
93          - diff([u2_memory(end-2*zD+1:end-zD,:) zeros(zD,1)]')')...
94          + Ms_r.*(eta./(a_r.*dr.*dt.^alfa)).*D_u2_r;
95  s12_a    = Hs_a.*s12_a...
96          - Ms_a.*(mo./(A_r.*2)).*((u2+[u2(:,2:end) zeros(zD,1)])...
97          - (u2_memory(end-2*zD+1:end-zD,:)...
98          + [u2_memory(end-2*zD+1:end-zD,2:end) zeros(zD,1)]))...
99          - Ms_a.*(eta./(A_r.*2.*dt.^alfa)).*D_u2_a;
100 s23_z    = Hs_z.*s23_z...
101         + Ms_z.*(mo./(a_z.*dz)).*(diff([zeros(1,rD); u2])...
```

```
102         - diff([zeros(1,rD); u2_memory(end-2*zD+1:end-zD,:)])))...
103         + Ms_z.*(eta./(a_z.*dz.*dt.^alfa)).*D_u2_z;
104 s12     = s12_r + s12_a;
105 s23     = s23_z;
106
107 % Imaging conditions - Cross-correlation zero lag
108 if ~mod(n+1,imagfreq) % apply every plotfreq frames
109 u2_aux = u2_stored((q-1)*zSd+1:q*zSd,:);   % extracting the source...
110                                 % images from the previous storing
111 % Stacking in time the different image components
112 claerbout2          = claerbout2 + u2(ab_z1+1:zD-ab_z2...
113                     ,ab_r1+1:rD-ab_r2).*u2_aux;
114 proposed_aux        = proposed_aux + u2_aux.^2 ...
115                     .*u2(ab_z1+1:zD-ab_z2,ab_r1+1:rD-ab_r2).^2;
116 source_squared2     = source_squared2 + u2_aux.^2;
117 receivers_squared2  = receivers_squared2...
118                     + u2(ab_z1+1:zD-ab_z2,ab_r1+1:rD-ab_r2)...
119                     .*u2(ab_z1+1:zD-ab_z2,ab_r1+1:rD-ab_r2);
120 q = q-1;
121 end
122 end
123
124 %% Applying imaging conditions
125 norm_source2    = claerbout2./source_squared2;
126 proposed       = proposed_aux./source_squared2;
127 norm_receivers2 = claerbout2./receivers_squared2;
128 ratio_squared2  = receivers_squared2./source_squared2;
```

Appendix E

MATLAB® GA-based reconstruction method code

This appendix contains the MATLAB® codes from the different algorithms that have been employed in the GA-based method for the reconstruction of the location and mechanical properties of stiff lesions inside the prostate, shown in Chapter 5.

Main code of the GA-based reconstruction method

```
%%%%%%%%%%%%%%%%%%%%%%%%%%%%%%%%%%%%%%%%%%%%%%%%%%%%%%%%%%%%%%%%%%%%%%%%%%%%
% GA reconstruction method using the 2D FDTD wave propagation model
% Guillermo Rus Carlborg     2015-01-02
% Adapted by Antonio Gomez     2017-01-09
%%%%%%%%%%%%%%%%%%%%%%%%%%%%%%%%%%%%%%%%%%%%%%%%%%%%%%%%%%%%%%%%%%%%%%%%%%%%

% clear all;
format compact;
addpath([pwd '/lib']);        % initialize
addpath([pwd '/lib_ip'  ]);   ip_vars;  ip_init;
addpath([pwd '/lib_ea'  ]);   ea_vars;  ea_init;
addpath([pwd '/lib_fpx' ]);  fpx_vars;  fpx_init;

fpx_spes={'1234' '34' '12' '3'};
fpx_spe=fpx_spes{cpu()}; % choose parametrization depending on cpu
switch fpx_spe
 case '1234', fpx_modpar=[1 2 3 4]; whichpars={[1 2] [3 4]};
end; par=ones(1,length(fpx_modpar))*.5;
l2=sprintf('eps/prospod_noise_%2.0f%%_res%1i_%s'...
    ,100*ip_noise,l3,fpx_spe);

%% Cost function analysis
par_ref=[0.5973 0.363636 0.75 0.5];
ip_damag = fpx_model_prost(par_ref);
eval(nexperiment); pars=0:0.05:1;
funs_1 = zeros(length(pars)); funs_2 = funs_1;
models1_1 = zeros(length(pars),1);
models2_1 = models1_1; models1_2 = models1_1;
models2_2 = models1_1;
np=1; whichpar=whichpars{np}; fig2=figu(2);
 for np1=1:length(pars)
```

```
    for np2=1:length(pars), par=par_ref;
        par(whichpar)=pars([np1 np2]); disp([np1 np2])
        funs_1(np1,np2)=feval(nfun,par);
        model_1=feval(nmodel,par);
        modeln_1=model_1.*fpx_model_norm;
        models1_1(np1)=modeln_1(whichpar(1));
        models2_1(np2)=modeln_1(whichpar(2));
    end
end
[C_1,h_1]=contour(models2_1,models1_1,log10(funs_1+eps),20);
set(h_1,'ShowText','on','TextStep',get(h_1,'LevelStep')*2 ...
   ,'Color','k'); colormap(1-bone);
hold on;
plot(ip_damag(whichpar(2))*fpx_model_norm(whichpar(2))...
    ,ip_damag(whichpar(1))*fpx_model_norm(whichpar(1)),'k+');
hold off;
xlabel(fpx_model_labels{whichpar(2)}{1});
ylabel(fpx_model_labels{whichpar(1)}{1});
title('Cost functional, {\it -log(f)}');
print('-depsc',sprintf('%s_CF_%01i_%01i.eps',l2,whichpar));
np=2; whichpar=whichpars{np}; fig3=figu(3);
for np1=1:length(pars)
    for np2=1:length(pars), par=par_ref;
       par(whichpar)=pars([np1 np2]); disp([np1 np2])
        funs_2(np1,np2)=feval(nfun,par);
        model_2=feval(nmodel,par);
        modeln_2=model_2.*fpx_model_norm;
        models1_2(np1)=modeln_2(whichpar(1));
        models2_2(np2)=modeln_2(whichpar(2));
    end
end
[C_2,h_2]=contour(models2_2,models1_2,log10(funs_2+eps),20);
set(h_2,'ShowText','on','TextStep',get(h_2,'LevelStep')*2 ...
   ,'Color','k'); colormap(1-bone);
hold on;
```

```
 plot(ip_damag(whichpar(2))*fpx_model_norm(whichpar(2))...
     ,ip_damag(whichpar(1))*fpx_model_norm(whichpar(1)),'k+');
 hold off;
 xlabel(fpx_model_labels{whichpar(2)}{1});
 ylabel(fpx_model_labels{whichpar(1)}{1});
 title('Cost functional, {\it -log(f)}');
 print('-depsc',sprintf('%s_CF_%01i_%01i.eps',l2,whichpar));

%% Search (inverse problem)
par_ref=[0.5973 0.363636 0.75 0.5];
ip_damag = fpx_model_prost(par_ref);
eval(nexperiment);
ip_damag = fpx_model_prost(par_ref);
ea_init; ea_opt={round(8/1) round(100/2)};
eval(nsear);        % do single search

%% Saving data
save('GA_namefile.mat');
```

```
% init
% Guillermo Rus Carlborg     2007-10-08
% Antonio Gomez              2016-06-10

% initialize general
nmea              ='fpx_mea_prost';
new_nmea        = 'fpx_newmea_prost';
nmodel            ='fpx_model_prost';

fpx_design       =[.5 .5 .5];
fpx_design_range =[1e-3 1e-3;2.0e-3 38.0e-3;0.7e3 0.7e3];
fpx_design_labels={'Transmitter length [mm]'...
    ,'Receiver separation [mm]','Frequency [kHz]'};
fpx_design_norm  =[1e3 1e3 1e-3]';
fpx_model_range  =[5.1e-3 20.0e-3; 6.0e-3 28.0e-3; 2 6; 2 4];
```

```
% [lesion_r,lesion_z,mo_ratio,eta_ratio] (lesion parameter ranges)
fpx_model_labels ={{'r  [mm]','r=%3.2f[mm]'}...
    ,{'z  [mm]','z=%3.2f[mm]'},{'ratio \mu  [kPa]'...
    ,'ratio \mu=%3.2f[mm]'},{'ratio \eta  [Pa*s^\alfa]'...
    ,'ratio \eta=%3.2f[a*s^\alfa]'}};
fpx_model_norm   =[1e3 1e3 1 1]';
ip_noise         =0.1;
l3               =4; % speedup (exact = 1, speed >= 4)

fpx_spe='1234'; fpx_modpar=[1 2 3 4];
par=ones(1,length(fpx_modpar))*.5;
```

```
% simulate experiment
% Guillermo Rus Carlborg     2007-03-18

function ip_meax
ip_vars;
fpx_init;

ip_meax = feval(nmea,ip_damag,1);

end
```

```
% model=fpx_model_prost(par)
% Guillermo Rus Carlborg     2007-12-04

function model=fpx_model_prost(par)
fpx_vars; ip_vars;

par_complete=fpx_model_norm*0+.5;
par_complete(fpx_modpar)=par;

model=par_complete*0; % below: mapping log or linear
```

```
model([1 2])=fpx_model_range([1 2],1)+((fpx_model_range([1 2],2)...
    -fpx_model_range([1 2],1)).*par_complete([1 2]));
model([3 4])=fpx_model_range([3 4],1)+((fpx_model_range([3 4],2)...
    -fpx_model_range([3 4],1)).*par_complete([3 4]));

end
```

```
% simulate
% [meas time]=fpx_mea_prost(model,ex)
% Guillermo Rus Carlborg     2012-04-15
% Antonio Gomez              2016-06-10

function [meas time]=fpx_mea_prost(model_tis,ex)
fpx_vars; ip_vars;

% compute model_design from fpx_design and their ranges
lesion_coor_r       = model_tis(1);
lesion_coor_z       = model_tis(2);
mo_ratio_lesion     = model_tis(3);
eta_ratio_lesion    = model_tis(4);

[time,meas]=fdtd(lesion_coor_r,lesion_coor_z,mo_ratio_lesion...
    ,eta_ratio_lesion,l3);

% Add experimental noise
if ex, nois=real(ip_noise);
else
    nois=imag(ip_noise);
end
if ~(length(fpx_noisreal)==length(meas))
    fpx_noisreal=randn(size(meas));
end
meas=meas+real(nois)*fpx_noisreal*rms(meas); % add noise
end
```

The ‘fdtd’ function refers to the forward model. The code of the forward model can be seen in Appendix B.

```
% residual
% residual=ip_residual(par)
% Guillermo Rus Carlborg     2007-03-18

function residual=ip_residual(par)
ip_vars;

model    =feval(nmodel,par);                    % model
meas     =feval(new_nmea,model,0);              % observation
residual=(ip_meax(:)-meas(:))/rms(ip_meax);     % residual

end
```

```
% cost functional
% f=ip_fun(par)
% Guillermo Rus Carlborg     2007-03-18

function f=ip_fun(par)
ip_vars;

residual=feval(nresidual,par);  % residual
f=.5*mean(mean( residual.^2 )); % cost functional

end
```

```
% initialize for evolutionary algorithms
% Guillermo Rus Carlborg     2008-03-16

% if exist('ea_opt')~=1, ea_opt={20 50}; end;
```

```
% population generations
ea_opt={20 50};
nsear='ea_sear';
% if exist('ea_type')~=1, ea_type='ga_finland'; end;
ea_type='ga_finland';
ea_box={zeros(size(par)) ones(size(par))};  % box constraints
l1=sprintf('ea_%s_%s',ea_type,nsear);
```

```
% search GA
% requires nfun (name of cost functional) and par
% Guillermo Rus Carlborg     2008-03-16

ea_vars; rand('state',sum(100*clock));

% search
switch ea_type

case 'ga_finland'
 addpath([pwd '/lib_ea/ga_finland']);
 crossoverProb = 0.8 ;
 mutationProb  = 0.3;
 tournamentProb= 0.7 ;
 mutationScale = 0.1 ;
 initPopulation={};
 for individual=1:ea_opt{1}
     initPopulation{individual}=ea_box{1}+(ea_box{2}-ea_box{1})...
     .*rand(size(ea_box{1}));
 end
 [endpop endvalues stats] = gaSim_paralelized('ea_fun',ea_box{1}...
     ,ea_box{2},initPopulation,crossoverProb,mutationProb...
     ,tournamentProb,mutationScale,ea_opt{2});
 fval = max(endvalues);
 par = endpop{find(endvalues == fval,1,'first')};
 figure(1);
```

```
 plot(1:ea_opt{2},stats(:,1),'k-',1:ea_opt{2},stats(:,2),'k--');
 xlabel('Generation');ylabel('Cost functional, {\it -log(f)}');
 legend('Best value','Mean');
```

```
function [pop,values,stats] = gaSim(fun,low,up,initpop,crossprob,...
  mutprob,p_tour,mut_scale,gNr)
%
% Matlab function for simulating a simple real-coded
% genetic algorithm.
%
%  ------------------------------------------------------------------
%<<        Juha Haataja, Development Manager, Science Support       >>
%<<    Center for Scientific Computing, Box 405, FIN-02101 Espoo    >>
%<<           Phone +358 9 457 2731. Fax +358 9 457 2302            >>
%<<                 Internet: Juha.Haataja@csc.fi                   >>
%  ------------------------------------------------------------------

pop = initpop;                % Initial population
npop=length(pop);             % Number of individuals
nvar=length(pop{1});          % Number of variables
low=low(:)';up=up(:)';

% Evaluate initial function values:
%funstring = [fun '(pop(:,:))']; values = eval(funstring);
for j=1:npop; values(j)=eval([fun '(pop{j})']); end;

% Find the best individuals
maxval = max(values);
bestgen = pop{find(values == maxval,1)};
disp(['best value: ',num2str(maxval)]);

for i = 1:gNr
  stats(i,:) = [max(values) mean(values) std(values)];
  oldpop = pop;
```

```
31    oldvalues = values;
32    d = up - low;
33  % Recombine individuals
34    for j = 1:npop
35      % Select two parents
36      for k = 1:2
37        % Pick individuals for the tournament
38        idx = []; idx = 1 + floor(rand(2,1)*npop);
39        tour_val = oldvalues(idx);
40        % Select a parent
41        if (rand < p_tour)
42          tmp = find(tour_val == max(tour_val));
43        else
44          tmp = find(tour_val == min(tour_val));
45        end
46        pnt(k) = idx(tmp(1));
47      end
48      % Use box crossover
49      parent1 = oldpop{pnt(1)}(:)';
50      parent2 = oldpop{pnt(2)}(:)';
51      child = parent1;
52      mask = rand(1,nvar) <= crossprob;
53      idx = []; idx = find(mask);
54      if (length(idx) > 0)
55        coeff = 2*rand(size(idx))-0.5;
56        child(idx) = (1-coeff).*parent1(idx) + coeff.*parent2(idx);
57      end
58      % Mutations
59      for ii = 1:nvar
60        if (rand <= mutprob)
61         child(ii) = child(ii) + mut_scale*d(ii).*randn;
62        end
63      end
64      % Restore box constraints
65      child = min([max([child; low]); up]);
```

```
66      % Save the result
67      pop{j} = reshape(child,size(pop{1}));
68    end
69    %values = eval(funstring);     % Compute fitnesses
70    for j=1:npop; values(j)=eval([fun '(pop{j})']); end;
71    % Use elitism to restore the previous best solution
72    old_idx = find(max(oldvalues) == oldvalues);
73    % Select a random individual
74    new_idx = 1 + floor(rand*npop);
75    % Replace if the new individual is better
76    if (oldvalues(old_idx(1)) > values(new_idx))
77      pop{new_idx}    = oldpop{old_idx(1)};
78      values(new_idx) = oldvalues(old_idx(1));
79    end
80    % Find the best individuals in this generation
81    maxval = max(values);
82    bestgen = pop{find(values == maxval,1,'first')};
83    disp(['generation: ',num2str(i),'   best value: '...
84        ,num2str(maxval),'   best gen: ',num2str(bestgen(:)')]);
85  end
```

Appendix F

Publications

14th Anglo-French Physical Acoustics Conference (AFPAC2015) IOP Publishing
Journal of Physics: Conference Series **684** (2016) 012006 doi:10.1088/1742-6596/684/1/012006

Use of shear waves for diagnosis and ablation monitoring of prostate cancer: a feasibility study

A Gomez[1], G Rus[2] and N Saffari[1]

[1] UCL Mechanical Engineering, University College London, Torrington Place, London WC1E 7JE, UK
[2] Department of Structural Mechanics, University of Granada, Politécnico de Fuentenueva, Granada 18071, Spain

E-mail: aj.gomez@ucl.ac.uk

Abstract. Prostate cancer remains as a major healthcare issue. Limitations in current diagnosis and treatment monitoring techniques imply that there is still a need for improvements. The efficacy of prostate cancer diagnosis is still low, generating under and over diagnoses. High intensity focused ultrasound ablation is an emerging treatment modality, which enables the non-invasive ablation of pathogenic tissue. Clinical trials are being carried out to evaluate its long-term efficacy as a focal treatment for prostate cancer. Successful treatment of prostate cancer using non-invasive modalities is critically dependent on accurate diagnostic means and is greatly benefited by a real-time monitoring system. While magnetic resonance imaging remains the gold standard for prostate imaging, its wider implementation for prostate cancer diagnosis remains prohibitively expensive. Conventional ultrasound is currently limited to guiding biopsy. Elastography techniques are emerging as a promising real-time imaging method, as cancer nodules are usually stiffer than adjacent healthy prostatic tissue. In this paper, a new transurethral approach is proposed, using shear waves for diagnosis and ablation monitoring of prostate cancer. A finite-difference time domain model is developed for studying the feasibility of the method, and an inverse problem technique based on genetic algorithms is proposed for reconstructing the location, size and stiffness parameters of the tumour. Preliminary results indicate that the use of shear waves for diagnosis and monitoring ablation of prostate cancer is feasible.

1. Background

Prostate Cancer (PCa) is the most common cancer in men in the UK. It is also the second cause of cancer death after lung cancer. It represents around 13% of all cases of cancer and accounts for 7% of all UK cancer deaths [1]. The incidence of PCa increases with age, affecting mainly men over 50 years of age [2]. The increase in longevity and awareness of the disease will lead to more men requesting screening, which will in turn increase the number of patients diagnosed with PCa in the future [3].

Prostate carcinoma is often suspected when the serum Prostate-Specific Antigen (PSA) is elevated or an abnormal digital rectal examination is noted. However, PSA screening leads to a substantial number of unnecessary biopsies in patients with no or indolent cancer, who do not need immediate treatment [4]. Histopathological evaluation of systematic biopsy cores is used to confirm or rule out cancer, and is normally carried out with conventional transrectal ultrasound as a guidance tool. Despite

14th Anglo-French Physical Acoustics Conference (AFPAC2015) IOP Publishing
Journal of Physics: Conference Series **684** (2016) 012006 doi:10.1088/1742-6596/684/1/012006

the low specificity of PSA testing and the uncertainty after negative systematic biopsies, these techniques remain the standard for PCa diagnosis.

Current research is investigating whether modern imaging techniques can identify the site of the tumour. There are two main streams that are showing promising preliminary results: Magnetic Resonance Imaging (MRI) and Elastography techniques.

Multi-parametric MRI (mpMRI) combines T2-weighted imaging with functional sequences. It has become an important modality for tumour detection and staging [5,6], however, mpMRI performance varies depending on which combination of features is selected [7]. Additional limitations include cost, limited availability, contra-indication to MRI and contrast agents, and the fact that the very large majority of biopsies are ultrasound guided [8].

Prostate Elastography is an emerging imaging modality, which consists of the evaluation of prostate stiffness. Analogous to the cellular processes of wound repair, it is generally believed that normal tissue stroma responds in an effort to repair damage due to carcinoma cell invasion [9]. It has been concluded that the stromal reaction is also characterized by elevated collagen deposition [10]. Since increasing collagen deposition leads to an increase in the tumour rigidity, this suggests that quantitative stiffness estimations may prove to be an effective biomarker for assessing PCa grade and identification of more aggressive cancers [11].

Real-Time Elastography is available on some ultrasound systems for prostate imaging [12,13] and a few other techniques are currently being developed [13]. There are two main approaches commercially available:

- Quasi-Static (or Strain) Elastography (SE);
- Shear Wave Elastography (SWE).

SE of the prostate is based on the comparative analysis of tissue deformation before and after applying a slight static mechanical compression through the rectal wall. Stiffer tissue experiences less deformation than normal tissue. No quantitative elasticity analysis is available. Relative changes in the strain rate between zones work as a guide to suspect pathologic nodules existence [14]. This technique is commercially available for many clinical ultrasonic platforms [12]. SE limitations include:

- The lack of uniform compression over the entire gland;
- The intra and inter-operator dependency;
- Penetration issues in large prostate glands;
- Artefacts due to slippage of the compression plane.

SWE in PCa detection has been tested mainly by the Aixplorer ultrasound system transrectally (SuperSonic Imagine, Aix-en-Provence, France). In Transrectal-SWE (TR-SWE) by the Aixplorer system, acoustic radiation force produces a shear wave in the shape of a cone with a small inclination, which travels away from the pushing beam. An ultrafast scanner allows shear waves to be followed in real time in 2D, and echo tracking produces a displacement recording from which a small map of elasticity can be created [15]. Spatial resolution is worse than in SE imaging but the elastograms are quantitative.

Recent studies on PCa diagnosis using TR-SWE have shown very promising results [16–20]. The use of a 35 kPa threshold for Young's modulus to separate lesions from normal tissue in the Peripheral Zone may provide additional information for PCa detection and biopsy guidance, enabling a substantial reduction in the number of biopsies [16,17]. TR-SWE limitations include:

- The pressure artefacts induced by the transducer, as the end-fire design of the probe requires bending to image the mid prostate and apex;
- The slow frame rate, i.e. one image per second;
- The limited size of the region of interest (concretely only half of the prostate is covered);
- The delay to stabilize the signals at each acquisition plane;
- The signal attenuation in large prostates making the evaluation of the anterior Transitional Zone difficult or impossible [8].

14th Anglo-French Physical Acoustics Conference (AFPAC2015) IOP Publishing
Journal of Physics: Conference Series **684** (2016) 012006 doi:10.1088/1742-6596/684/1/012006

The aim of this study is to evaluate the feasibility of using a Transurethral-SWE (TU-SWE) approach for diagnosis and High Intensity Focused Ultrasound (HIFU) ablation monitoring of PCa. This approach encompasses both the transmission and the detection of the shear wave propagation. Shear waves are propagated into the prostate as the result of applying torsional stress on the urethra wall at a localized point. If stiff lesions are presented in the prostate, the wavefront would suffer reflections due to the change in acoustic impedance. This reflection would travel back to the urethra where it could be detected (Figure 1). The parameters which define the tumour (location, size and stiffness) can be reconstructed from those recovered signals.

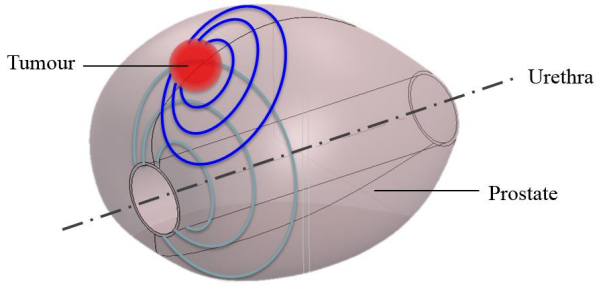

Figure 1. Conceptual idealization of the TU-SWE approach for diagnosis and ablation monitoring of PCa

The capability of transmitting shear waves into the prostate by mechanical contact through the urethra wall was evaluated in phantoms and *in vivo* canine experiments, by using a mechanical transurethral actuator as excitation force and MRI Elastography for measuring the displacement [21,22].

HIFU ablation is a promising focused technique for treating PCa, currently under clinical evaluation in several clinics around the world. As with other focused therapies it requires that the treated region be controlled and monitored to avoid damage of the surrounding healthy tissue. The TU-SWE approach allows the monitoring of HIFU ablation from the rectum, since the ultrasonic beam itself generates an alteration of the stiffness at the focal point and surroundings as the temperature increases during the surgery [23,24].

Inherent advantages of the TU-SWE approach proposed are listed below:

- The Transitional Zone and the Central Zone of the prostate (Figure 2) remain less accessible when using techniques that operate from the rectal passage. The urethral approach makes these zones more reachable. The Central Zone presents the lowest rate of PCa, but these cancers tend to be more aggressive and more likely to invade the seminal vesicles [25]. The TR-SWE studies are limited to the Peripheral Zone since this approach makes it difficult to reach the anterior zones of the prostate [16]. On the other hand, the reduction of tissue path is directly connected to the diminution of attenuation, which is a crucial matter in shear wave propagation.
- The possibility of using higher frequencies (above 500 Hz) than other techniques. This fact is related to the reduction in attenuation, which allows a slight increase of the excitation frequency, and therefore the spatial resolution, thus improving the imaging quality and the capacity of detecting smaller cancer nodules.
- Current techniques present difficulties in scanning the whole gland in a short time. TR-SWE covers only half of the prostate for every 2D scan. Although SE can cover complete 2D sections of the prostate, it presents problems covering the whole gland due to the challenge of keeping the pressure constant at every scan. Due to the geometrical configuration of the proposed TU-SWE approach, the whole gland volume may be covered simultaneously, permitting the opportunity of 3D real-time monitoring technique.

14th Anglo-French Physical Acoustics Conference (AFPAC2015) IOP Publishing
Journal of Physics: Conference Series **684** (2016) 012006 doi:10.1088/1742-6596/684/1/012006

- In comparison with techniques that use acoustic radiation force, lower levels of energy are expected, and therefore lower ultrasound thermal and mechanical indices.
- The use of the urethra as a channel for diagnosis keeps the rectal passage free for transrectal therapies such as HIFU ablation.

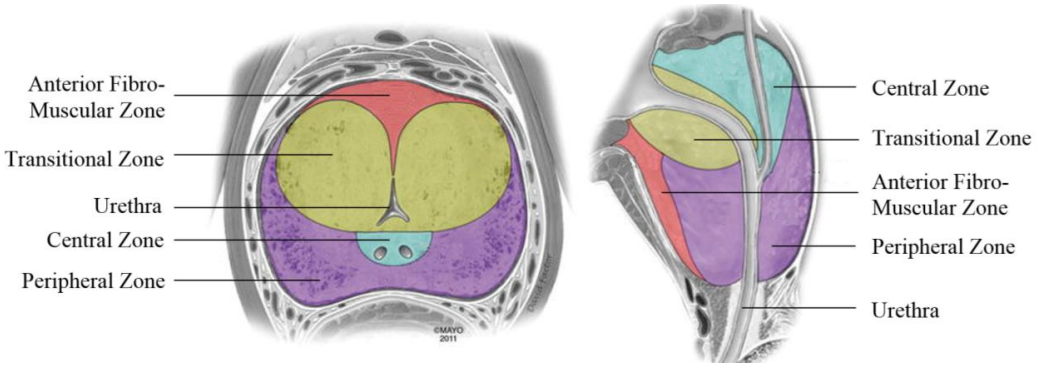

Figure 2. McNeal's anatomic division of the prostate. Source: Mayo Foundation for Medical Education and Research [26].

In this paper, a prostate-like medium is modelled using the Finite-Difference Time Domain (FDTD) method to investigate the PCa detection sensitivity of the proposed approach. An Inverse Problem (IP) based on genetic algorithms was developed for reconstructing the parameters that locate and size prostate nodules. Finally, the results from the reconstruction were analyzed to demonstrate the feasibility of the TU-SWE approach for diagnosis of PCa.

2. Methodology

2.1. Finite-Difference Time Domain model

A FDTD method is developed for simulating the propagation of shear waves into the prostate from the urethra. The FDTD method has been extensively used for modelling different physics phenomena in solid materials, mainly in electromagnetism and geophysics, but also for wave propagation in elastic and viscoelastic media [27,28]. Two aims are pursued with this model. One is to study, in a simple way, the feasibility of reflection detection in the PCa application. The other is to feed the reconstruction method, obtaining potential solutions which are tested iteratively in the inverse procedure.

The mechanical response of soft tissues is well known for a viscoelastic behaviour. In this study, an elastic model has been considered sufficient due to the absence of consensus about mechanical models and values for viscous parameters of prostatic tissue.

A cylindrical coordinate system is selected for establishing the discretization grid. The simplified prostate-like model is defined geometrically as a hollow cylinder, where the inner passage corresponds to the urethra (Figure 3).

Although the equations of motion can be formulated in several ways, a velocity-stress formulation was chosen [29], where time distributions of velocity and stress at spatial points are propagated along a regular grid to which material properties and the excitation source are assigned. Generally, a system of nine first-order hyperbolic equations are needed. Shear waves are generated by the application of torsional forces in the urethra wall in an axisymmetric configuration, and thus, together with the simplification of using a two dimensional approach, reduces the complexity to only one velocity component v_θ. The plane selected (in red colour Figure 3) contains the axis. The remaining three first-order hyperbolic equations (1-3) are expressed in terms of the stress tensor σ and velocity v_θ for an elastic medium. As a result of the simplification, the circular tumour in the plane becomes a torus in 3D.

14th Anglo-French Physical Acoustics Conference (AFPAC2015) IOP Publishing
Journal of Physics: Conference Series **684** (2016) 012006 doi:10.1088/1742-6596/684/1/012006

Although this geometrical distribution is not representative of PCa, it can be considered acceptable for a proof of principle approach.

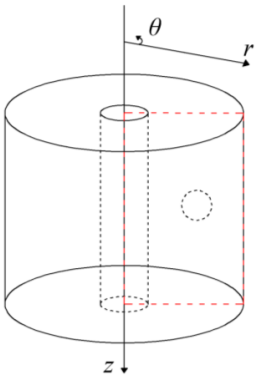

Figure 3. Simplified geometry for the model. 2D section of study in red. Spherical tumour.

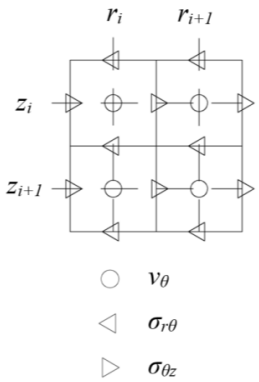

Figure 4. Diagram of the staggered grid discretization with positions of the variables.

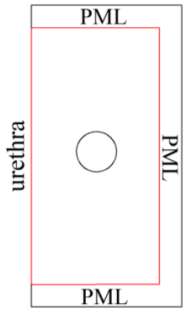

Figure 5. Spatial distribution of the model. Main domain in red. PML surrounding it. Urethra at left side.

$$\rho \dot{v}_\theta = \frac{\mathrm{d}\sigma_{r\theta}}{\mathrm{d}r} + \frac{\mathrm{d}\sigma_{\theta z}}{\mathrm{d}z} + \frac{2}{r}\sigma_{r\theta} \tag{1}$$

$$\dot{\sigma}_{r\theta} = \mu\left(\frac{\mathrm{d}v_\theta}{\mathrm{d}r} - \frac{v_\theta}{r}\right) \tag{2}$$

$$\dot{\sigma}_{\theta z} = \mu\frac{\mathrm{d}v_\theta}{\mathrm{d}z} \tag{3}$$

The mass density ρ and the shear modulus μ vary depending on whether they belong to the background tissue or to the cancer nodule. Spatial discretization is achieved with the staggered grid illustrated in Figure 4, i.e., the velocity component is specified at grid positions that are offset by a half-step from the corresponding stress components. Time is uniformly sampled via $t=n\Delta t$ for an integer n and interval Δt. Similarly, space is uniformly sampled, with $r=i\Delta r$ and $z=j\Delta z$ for integers i, j.

To propagate spatial quantities in time, the classical time-staggering approach is often used to estimate stress and velocity in alternating time intervals. In this case, an alternative method has been chosen, computing both magnitudes at each time interval starting from an initial situation at rest [27].

All temporal and spatial derivatives in equations (1), (2) and (3) are discretized using the following differencing schemes:

$$\dot{g}\big|_{r_i,t_{n+1}} = \frac{\mathrm{d}g}{\mathrm{d}t}\bigg|_{r_i,t_{n+1}} = \frac{g^{n+1}(i) - g^n(i)}{\Delta t} + \mathrm{O}(\Delta t) \tag{4}$$

$$g_{,r}\big|_{r_i,t_n} = \frac{\mathrm{d}g}{\mathrm{d}x}\bigg|_{r_i,t_n} = \frac{g^n\left(i+\frac{1}{2}\right) - g^n\left(i-\frac{1}{2}\right)}{\Delta r} + \mathrm{O}(\Delta r^2) \tag{5}$$

To reduce numerical dispersion we choose a minimum rate of 20 spatial intervals per wavelength λ as described in equation (6) although lower rates can be found in the literature. The temporal interval satisfies the stability condition (7) obtained from the Von Neumann condition [30].

14th Anglo-French Physical Acoustics Conference (AFPAC2015) IOP Publishing
Journal of Physics: Conference Series **684** (2016) 012006 doi:10.1088/1742-6596/684/1/012006

$$20\max(\Delta r, \Delta z) < \lambda_{\min} \tag{6}$$

$$\max(c_s)\Delta t < \left(\frac{1}{\Delta r^2} + \frac{1}{\Delta z^2} \right)^{-1/2} \tag{7}$$

The rotational excitation is introduced in the model by setting v_θ at the corresponding points in the grid within the urethra wall where the torsion is applied.

In order to avoid reflections at outer boundaries of the domain, a Perfectly Matched Layer (PML) absorber is incorporated surrounding the main domain, excepting the urethra wall (Figure 5), using an adaptation for cylindrical coordinates [31].

2.2. Inverse Problem based on Genetic Algorithms

A way to solve an IP is to use the forward problem to find a solution for a set of parameters that minimizes the difference between the predicted and the actual measurements by using an optimization algorithm [32]. For this study a genetic algorithm is proposed for the optimization. The tumour parameters are contained in a vector named p_c. These parameters are: the radial r_c and depth z_c coordinates of the centroid of the nodule, the diameter $\varnothing_c$ and the stiffness μ_c of the tumour.

Considering that this work is at a preliminary stage, experimental results are not yet available. To study the suitability of the proposed reconstruction method, pseudo-experimental signals u_{exp} were generated by adding white noise to signals simulated using the FDTD model.

The optimization algorithm will minimize the discrepancy between u_{exp} and the numerically predicted trial response $u(p_c)$, which is a function of the four-dimensional hyperspace formed by the four tumour parameters. To quantify the discrepancy, a cost functional f is designed, defined as the squared Euclidean distance between both measurements (8) [33].

$$f(p_c) = \left\| u_{\exp} - u(p_c) \right\|_2^2 \tag{8}$$

3. Results

3.1. Numerical model results

A numerical simulation was carried out by using the FDTD method described in Section 2.1. Figure 6 depicts the selected set-up. Note that the problem has been simplified after taking advantage of the axisymmetry of the cylindrical system shown in Figure 3.

The values corresponding to the labeled variables in Figure 6 are listed in Table 1. Those values and proportions are in agreement with those that can be found in a real human prostate. A rounded shape is selected to represent the cancerous nodule using an arbitrary, but realistic, value of 4 mm of diameter. The excitation source is located on the urethra wall, at centered depth. A set of 18 receivers is uniformly distributed for recording the signals coming from the interior of the domain.

Table 2 shows the values for mechanical parameters of both healthy and cancerous prostate, as well as the settings of the excitation source, which is implemented as a Gaussian modulated wave with central frequency of 1 kHz. Shear modulus values have been chosen in agreement with those found in the literature [16,17].

Table 3 lists the parameters for the numerical discretization. In order to guarantee an adequate visual resolution of the simulation, the discrete spatial values go beyond the stability condition described by equation (6), resulting in a total of 731,600 elements. The Von Neumann condition defined by equation (7) is applied to calculate the temporal discretization interval.

The simulation was performed using MATLAB® in conjunction with the Parallel Computing Toolbox™ (Release 2014b, MathWorks, Natick, United States). Run times lasted 406 seconds on a quad-core 3.60 GHz, 16 GB RAM, desktop computer.

14th Anglo-French Physical Acoustics Conference (AFPAC2015) IOP Publishing
Journal of Physics: Conference Series **684** (2016) 012006 doi:10.1088/1742-6596/684/1/012006

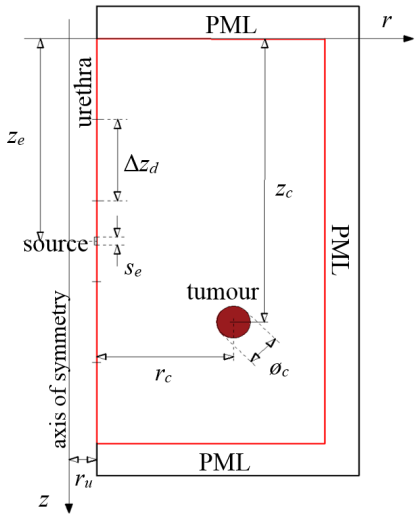

Figure 6. Schematic of set-up for numerical simulation. Tumour in red. Dimensions are described in Table 1.

Table 1. Dimension values for set-up of the numerical simulation.

Variable	Description	Value (mm)
r_d	Radial dimension of the domain	23.50
z_d	Depth dimension of the domain	50.00
r_u	Radius of urethra	3.25
z_e	Depth coordinate of excitation source	25.00
s_e	Thickness of excitation source	1.00
r_c	Radial coordinate of the tumour	14.00
z_c	Depth coordinate of the tumour	35.00
$\varnothing_c$	Diameter of the tumour	4.00
Δz_r	Distance between receivers	2.38

Table 2. Values for mechanical parameters and excitation [16,17]

Variable	Description	Value
ρ_h	Density of healthy tissue	1000 kg m^{-3}
μ_h	Shear modulus of healthy tissue	6.00 kPa
ρ_c	Density of cancerous tissue	1000 kg m^{-3}
μ_c	Shear modulus of cancerous tissue	18.00 kPa
f_c	Central frequency	1.00 kHz
t_T	Total time of simulation	25 ms
a	Source amplitude	10.00 µm

Table 3. Discretization parameters for FDTD simulation

Variable	Description	Value
Δr	Radial dimension interval	50 µm
Δz	Depth dimension interval	50 µm
Δt	Time interval	8.33 µs
n_{PML}	Number of PML elements	120

Figure 7 shows four snapshots of the simulated transient propagation of shear waves in a prostate-like medium containing a cancerous lesion, at different times when the wavefront hits and propagates across the tumour. It can be clearly seen how the reflections are generated traveling back to the urethra wall, as well as the ongoing wavefront accelerates while propagating across the tumour due to the higher velocity of the shear waves, 4.24 ms^{-1} against 2.45 ms^{-1} in the healthy tissue. A second reflection coming from the bottom of the tumour can be also visualized. The recordings at the receivers during the simulation are displayed in Figure 8.

3.2. Reconstruction IP-AG method results

In order to obtain a proof of feasibility for the IP-GA method, an example reconstruction is shown in this section.

As mentioned in Section 2.2, a simulated signal generated by the FDTD model with added white noise was used as an experimental signal to be reconstructed by the IP-GA method. The amplitude of the white noise signal corresponded to 10% of the root-mean-square of the simulated signal amplitude. The set-up for the pseudo-experimental signal was the same as the one in Section 2.1 (see Figure 6 and Tables 1 and 2). Table 4 shows the values of the parametrization. In this case, a coarser grid was chosen in order to speed up the iteration process and reduce the computational time. The pseudo-experimental

14th Anglo-French Physical Acoustics Conference (AFPAC2015) IOP Publishing
Journal of Physics: Conference Series **684** (2016) 012006 doi:10.1088/1742-6596/684/1/012006

signal was detected by a receiver located 12.5 mm below the source on the urethra wall. The reconstruction algorithm was implemented using MATLAB® and the Parallel Computing Toolbox™ (Release 2014b, MathWorks, Natick, United States), lasting for 1204 seconds on the computer mentioned above. A population of 10 candidate solutions was selected, to be updated during 13 generations.

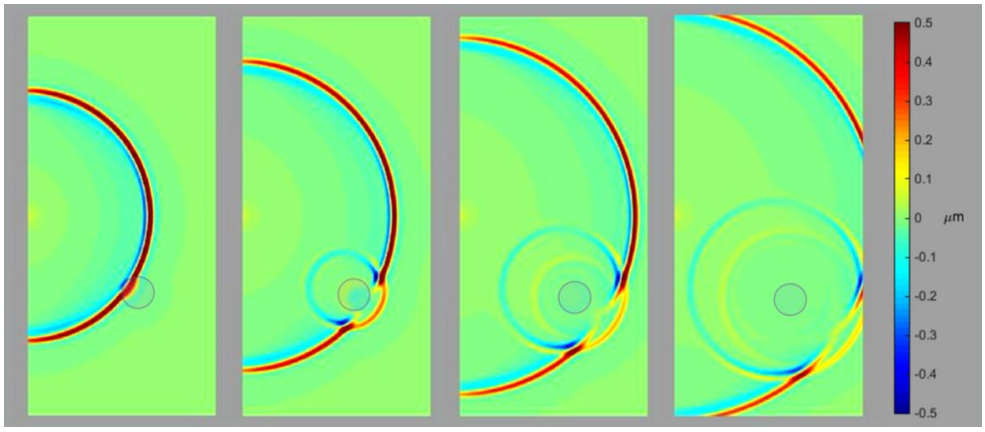

Figure 7. Snapshots of the FDTD simulation at 7.2, 8.7, 9.8 and 11.3 ms. The colour bar represents the amplitude of the displacement. The 4 mm rounded tumour is highlighted.

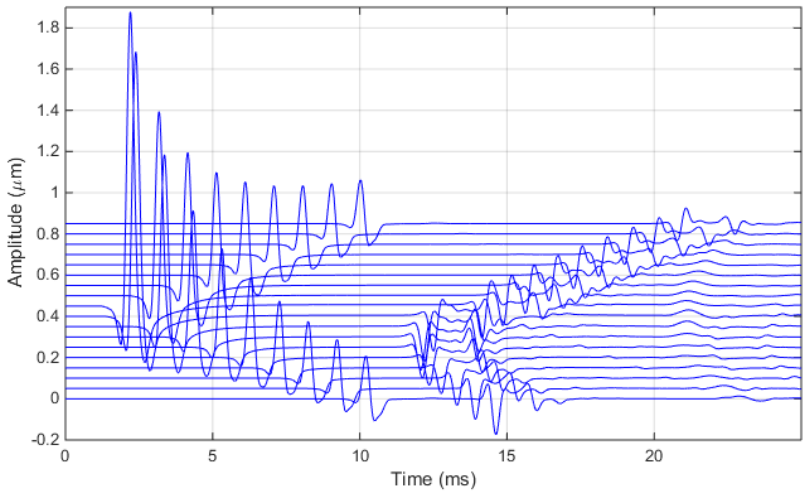

Figure 8. Recovered displacement signals at the 18 receivers. Distance between receivers 2.38 mm, with a 7.14 mm gap between receiver 9 and 10, where the excitation source is positioned.

Figure 9 depicts the reconstructed signal over the pseudo-experimental one. Recovered values for the tumour parameters and reconstruction errors are shown in Table 5. The errors were calculated over the search range established for each parameter. The algorithm showed good agreement between the reconstruction and the pseudo-experimental measurement.

14th Anglo-French Physical Acoustics Conference (AFPAC2015) IOP Publishing
Journal of Physics: Conference Series **684** (2016) 012006 doi:10.1088/1742-6596/684/1/012006

Table 4. Discretization parameters for IP-AG testing

Variable	Description	Value
Δr	Radial dimension interval	150 µm
Δz	Depth dimension interval	150 µm
Δt	Time interval	17.32 µs
n_{PML}	Number of PML elements	40

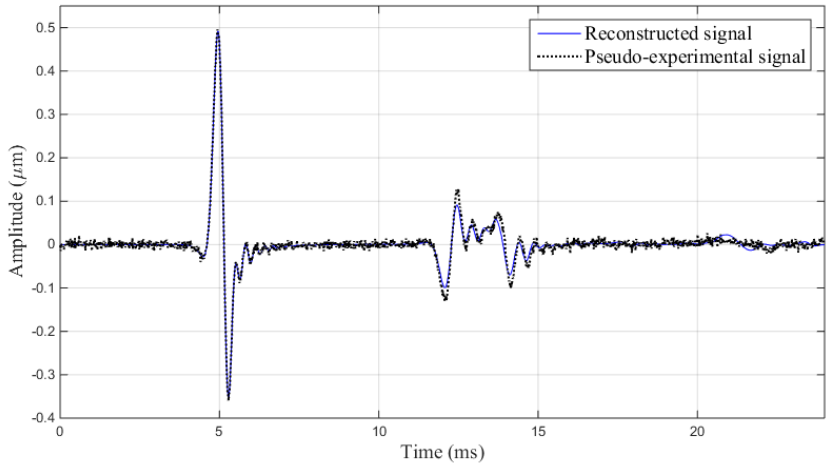

Figure 9. Reconstructed signal by using the IP-AG method (blue solid line) over the pseudo-experimental signal (black dotted line).

Table 5. Reconstructed values for the tumour parameters and reconstruction errors.

Parameter	Description	Original value	Reconstructed Value	Search Range	Error
r_c	Radial coordinate of the tumour	14.00 mm	13.7 mm	4 - 24 mm	3.10 %
z_c	Depth coordinate of the tumour	35.00 mm	36.98 mm	26 - 44 mm	3.96 %
$ø_c$	Diameter of the tumour	4.00 mm	3.63 mm	2 - 8 mm	6.16 %
μ_c	Shear modulus of cancerous tissue	18.00 kPa	16.61 kPa	16 - 21 kPa	9.56 %

4. Conclusion

A novel TU-SWE approach for diagnosis and ablation monitoring of PCa has been presented in this paper. It is based on the emission, detection and computational treatment of shear waves propagated into the prostate.

In order to study the feasibility of this approach, a FDTD model was developed to analyze the behavior of shear waves in a medium representative of prostatic tissue. Although the medium was assumed to be homogeneous and elastic, this was considered sufficient to simulate the mechanical behavior of the human prostate to a first approximation. The presence of cancerous nodules, which are usually stiffer than the surrounding healthy tissue, was also modelled. Reflections were generated when the wavefront hit the tumour, traveling back to the urethra where they were detected, demonstrating proof of principle and warranting further studies.

14th Anglo-French Physical Acoustics Conference (AFPAC2015) IOP Publishing
Journal of Physics: Conference Series **684** (2016) 012006 doi:10.1088/1742-6596/684/1/012006

The IP-AG reconstruction method was tested by using the FDTD model for generating a pseudo-experimental signal and also as a forward model for searching the solutions within the IP algorithm. The results from the test showed good agreement between the pseudo-experimental signal and the reconstructed one, with an admissible level of error in the recovery of tumour parameters.

In further studies, a more realistic 3D model will be required, taking into account the heterogeneity and mechanical complexity of the human prostate. Experimental tests in prostate phantoms will be also required. In the IP ambit, it is of interest to study the probability of producing a false positive diagnosis, as well as how the response of the system changes with increasing levels of noise.

5. Acknowledgements

The authors would like thank P. Gelat for constructive and illuminating discussions. This research was supported by the Ministry of Education DPI2014-51870-R and DPI2010-17065, and Junta de Andalucía for projects P11-CTS-8089 and GGI3000IDIB. First author was supported by Talentia Scholarship C2012F1-75146405T-1, Agencia del Conocimiento Junta de Andalucía.

References

[1] Cancer Research UK 2014 Prostate cancer Key Stats *Cancer Res. UK*
[2] The Prostate Cancer Charity UK 2015 What is my risk of prostate cancer? *Prostate Cancer UK*
[3] Abdellaoui A, Iyengar S and Freeman S 2011 Imaging in prostate cancer *Futur. Oncol.* 679–91
[4] Kelloff G J, Choyke P and Coffey D S 2009 Challenges in clinical prostate cancer: role of imaging *AJR. Am. J. Roentgenol.* **192** 1455–70
[5] Lemaitre L, Puech P, Poncelet E, Bouyé S, Leroy X, Biserte J and Villers A 2009 Dynamic contrast-enhanced MRI of anterior prostate cancer: Morphometric assessment and correlation with radical prostatectomy findings *Eur. Radiol.* **19** 470–80
[6] Lim H K, Kim J K, Kim K a. and Cho K S 2009 Prostate cancer: Apparent diffusion coefficient map with T2-weighted images for detection - A multireader study *Radiology* **35** 100–100
[7] Langer D L, Van Der Kwast T H, Evans A J, Trachtenberg J, Wilson B C and Haider M a. 2009 Prostate cancer detection with multi-parametric MRI: Logistic regression analysis of quantitative T2, diffusion-weighted imaging, and dynamic contrast-enhanced MRI *J. Magn. Reson. Imaging* **30** 327–34
[8] Correas J M, Drakonakis E, Isidori a. M, Hélénon O, Pozza C, Cantisani V, Di Leo N, Maghella F, Rubini a., Drudi F M and D'ambrosio F 2013 Update on ultrasound elastography: Miscellanea. Prostate, testicle, musculo-skeletal *Eur. J. Radiol.* **82** 1904–12
[9] Tuxhorn J a, Ayala G E and Rowley D R 2001 Reactive stroma in prostate cancer progression. *J. Urol.* **166** 2472–83
[10] Tuxhorn J a, Ayala G E, Smith M J, Smith V C, Dang T D and Rowley D R 2002 Reactive Stroma in Human Prostate Cancer : Induction of Myofibroblast Phenotype and Extracellular Matrix Remodeling Reactive Stroma in Human Prostate Cancer : Induction of Myofibroblast Phenotype and Extracellular **8** 2912–23
[11] Burns-Cox N, Avery N C, Gingell J C and Bailey a J 2001 Changes in collagen metabolism in prostate cancer: a host response that may alter progression. *J. Urol.* **166** 1698–701
[12] Bamber J, Cosgrove D, Dietrich C F, Fromageau J, Bojunga J, Calliada F, Cantisani V, Correas J-M, D'Onofrio M, Drakonaki E E, Fink M, Friedrich-Rust M, Gilja O H, Havre R F, Jenssen C, Klauser a S, Ohlinger R, Săftoiu A, Schaefer F, Sporea I and Piscaglia F 2013 EFSUMB guidelines and recommendations on the clinical use of ultrasound elastography. Part 2: Clinical applications. *Ultraschall Med.* **34** 238–53
[13] Doherty J, Trahey G, Nightingale K and Palmeri M 2013 Acoustic radiation force elasticity imaging in diagnostic ultrasound *IEEE Trans. Ultrason. Ferroelectr. Freq. Control* **60** 685–701
[14] Ophir J, Alam S K, Garra B S, Kallel F, Konofagou E E, Krouskop T, Merrit C R B, Righetti R, Souchon R, Srinivasan S and Varghese T 2002 Elastography : Imaging the Elastic Properties

of Soft Tissues with Ultrasound *J. Med. Ultrason.* **29** 155–71
[15] Bercoff J, Tanter M and Fink M 2004 Supersonic Shear Imaging : A New Technique for Soft Tissue Elasticity Mapping **51** 396–409
[16] Barr R G, Memo R and Schaub C R 2012 Shear wave ultrasound elastography of the prostate: initial results *Ultrasound Q.* **28** 13–20
[17] Correas J M, Tissier A-M, Khairoune A, Vassiliu V, Méjean A, Hélénon O, Memo R and Barr R G 2015 Prostate Cancer : Diagnostic Performance of Real-time Shear-Wave Elastography *Radiology* **275** 280–9
[18] Ahmad S, Cao R, Varghese T, Bidaut L and Nabi G 2013 Transrectal quantitative shear wave elastography in the detection and characterisation of prostate cancer *Surg. Endosc.* **27** 3280–7
[19] Woo S, Kim S Y, Lee M S, Cho J Y and Kim S H 2015 Shear wave elastography assessment in the prostate: an intraobserver reproducibility study *Clin. Imaging* **39** 484–7
[20] Boehm K, Salomon G, Beyer B, Schiffmann J, Simonis K, Graefen M and Budaeus L 2015 Shear Wave Elastography for Localization of Prostate Cancer Lesions and Assessment of Elasticity Thresholds: Implications for Targeted Biopsies and Active Surveillance Protocols *J. Urol.* **193** 794–800
[21] Chopra R, Arani A, Huang Y, Musquera M, Wachsmuth J, Bronskill M and Plewes D 2009 In vivo MR elastography of the prostate gland using a transurethral actuator. *Magn. Reson. Med.* **62** 665–71
[22] Arani A, Plewes D and Chopra R 2011 Transurethral prostate magnetic resonance elastography: prospective imaging requirements. *Magn. Reson. Med.* **65** 340–9
[23] Arnal B, Pernot M and Tanter M 2011 Monitoring of thermal therapy based on shear modulus changes: I. Shear wave thermometry *IEEE Trans. Ultrason. Ferroelectr. Freq. Control* **58** 369–78
[24] Arnal B, Pernot M and Tanter M 2011 Monitoring of thermal therapy based on shear modulus changes: II. Shear wave imaging of thermal lesions *IEEE Trans. Ultrason. Ferroelectr. Freq. Control* **58** 1603–11
[25] Cohen R J, Shannon B a., Phillips M, Moorin R E, Wheeler T M and Garrett K L 2008 Central Zone Carcinoma of the Prostate Gland: A Distinct Tumor Type With Poor Prognostic Features *J. Urol.* **179** 1762–7
[26] Bohyun K and Chan K K 2013 Embryology, Anatomy and Congenital Anomalies of the Prostate and Seminal Vesicles *Abdominal Imagin* pp 1797–812
[27] Orescanin M, Member S and Wang Y 2011 3-D FDTD Simulation of Shear Waves for Evaluation of Complex Modulus Imaging *IEEE Trans. Ultrason. Ferroelectr. Freq. Control* **58** 389–98
[28] Jiménez N, Picó R, Camarena F, Redondo J and Roig B 2012 Ultrasonic evaluation of the hydration degree of the orange peel *Postharvest Biol. Technol.* **67** 130–7
[29] Virieux J 1986 P-SV wave propagation in heterogeneous media: Velocity-stress finite-difference method *Geophysics* **51** 889–901
[30] Leutenegger T and Dual J 2004 Non-destructive testing of tubes using a time reverse numerical simulation (TRNS) method *Ultrasonics* **41** 811–22
[31] Liu Q H 1999 Perfectly matched layers for elastic waves in cylindrical and spherical coordinates *J. Acoust. Soc. Am.* **105** 2075–84
[32] Gallego R and Rus G 2004 Identification of cracks and cavities using the topological sensitivity boundary integral equation *Comput. Mech.* **33** 154–63
[33] Rus G, Wooh S C and Gallego R 2007 Processing of ultrasonic array signals for characterizing defects. Part II: Experimental work *IEEE Trans. Ultrason. Ferroelectr. Freq. Control* **54** 2139–45

Appendix G

Colophon

This document was set in the Times Roman typeface using LaTeX and BibTeX, composed with TeXmaker 5.0.2, a free cross-platform LaTeX editor since 2003, Copyright ©2003-2017 by Pascal Brachet.

TeXmaker contains code from these programs: Pdfium (BSD), QtPDF (The Qt Company Ltd - GPL), Hunspell (GPL), qpdfview (©Adam Reichold GPL), QtCreator (GPL), SyncTeX (©Jerome Laurens - License: GPL), Texworks (GPL), Tiled (Copyright Vsevolod Klementjev - License: GPL) and jsdifflib (©Chas Emerick - license : BSD).

Bibliography

Abdellaoui, A., Iyengar, S., and Freeman, S. Imaging in prostate cancer. *Futur. Oncol.*, 7(5):679–691, 2011.

Ahmad, S., Cao, R., Varghese, T., Bidaut, L., and Nabi, G. Transrectal quantitative shear wave elastography in the detection and characterisation of prostate cancer. *Surg. Endosc.*, 27(9):3280–7, 2013.

Ahmed, H. U., Freeman, a., Kirkham, a., Sahu, M., Scott, R., Allen, C., Van der Meulen, J., and Emberton, M. Focal therapy for localized prostate cancer: a phase I/II trial. *J. Urol.*, 185(4):1246–54, 2011.

Ahmed, H. U., Hindley, R. G., Dickinson, L., Freeman, A., Kirkham, A. P., Sahu, M., Scott, R., Allen, C., Van der Meulen, J., and Emberton, M. Focal therapy for localised unifocal and multifocal prostate cancer: a prospective development study. *Lancet Oncol.*, 13(6):622–32, 2012.

Ahmed, H. U., El-Shater Bosaily, A., Brown, L. C., Gabe, R., Kaplan, R., Parmar, M. K., Collaco-Moraes, Y., Ward, K., Hindley, R. G., Freeman, A., Kirkham, A. P., Oldroyd, R., Parker, C., and Emberton, M. Diagnostic accuracy of multi-parametric MRI and TRUS biopsy in prostate cancer (PROMIS): a paired validating confirmatory study. *Lancet*, 6736(16):1–8, 2017.

Aigner, F., Pallwein, L., Mitterberger, M., Pinggera, G. M., Mikuz, G., Horninger, W., and Frauscher, F. Contrast-enhanced ultrasonography using cadence-contrast

pulse sequencing technology for targeted biopsy of the prostate. *BJU Int.*, 103 (4):458–463, 2009.

Allen, J. P. *The art of medicine in ancient Egypt*. Metropolitan Museum of Art, 2005.

Amador, C., Kinnick, R. R., Urban, M. W., Fatemi, M., and Greenleaf, J. F. Viscoelastic tissue mimicking phantom validation study with shear wave elasticity imaging and viscoelastic spectroscopy. *2015 IEEE Int. Ultrason. Symp. IUS 2015*, pages 1–4, 2015.

An, L., Mills, B., Hah, Z., Mao, S., Yao, J., Joseph, J., Rubens, D. J., Strang, J., and Parker, K. J. Crawling wave detection of prostate cancer: Preliminary in vitro results. *Med. Phys.*, 38(5):2563–2571, 2011.

Andreev, V. G., Dmitriev, V. N., Pishchal'Nikov, Y. A., Rudenko, O. V., Sapozhnikov, O. A., and Sarvazyan, A. P. Observation of shear waves excited by focused ultrasound in a rubber-like media. *Acoust. Phys.*, 43(2):123–128, 1997.

Anquez, J., Corréas, J. M., Criton, A., Lacoste, F., and Yon, S. Assessment of HIFU lesions by shear-wave elastography: Initial in-vivo results. *AIP Conf. Proc.*, 1503 (2012):118–123, 2012.

Arani, A., Plewes, D., and Chopra, R. Transurethral prostate magnetic resonance elastography: prospective imaging requirements. *Magn. Reson. Med.*, 65(2): 340–9, feb 2011.

Arnal, B., Pernot, M., and Tanter, M. Monitoring of thermal therapy based on shear modulus changes: I. Shear wave thermometry. *IEEE Trans. Ultrason. Ferroelectr. Freq. Control*, 58(2):369–378, 2011a.

Arnal, B., Pernot, M., and Tanter, M. Monitoring of thermal therapy based on

shear modulus changes: II. Shear wave imaging of thermal lesions. *IEEE Trans. Ultrason. Ferroelectr. Freq. Control*, 58(8):1603–1611, 2011b.

Bamber, J., Cosgrove, D., Dietrich, C. F., Fromageau, J., Bojunga, J., Calliada, F., Cantisani, V., Correas, J.-M., D'Onofrio, M., Drakonaki, E. E., Fink, M., Friedrich-Rust, M., Gilja, O. H., Havre, R. F., Jenssen, C., Klauser, a. S., Ohlinger, R., Săftoiu, A., Schaefer, F., Sporea, I., and Piscaglia, F. EFSUMB guidelines and recommendations on the clinical use of ultrasound elastography. Part 2: Clinical applications. *Ultraschall Med.*, 34(3):238–53, 2013.

Barr, R. G. and Zhang, Z. Effects of precompression on elasticity imaging of the breast: Development of a clinically useful semiquantitative method of precompression assessment. *Journal of Ultrasound in Medicine*, 31(6):895–902, 2012.

Barr, R. G., Memo, R., and Schaub, C. R. Shear wave ultrasound elastography of the prostate: initial results. *Ultrasound Q.*, 28(1):13–20, 2012.

Bercoff, J., Pernot, M., Tanter, M., and Fink, M. Monitoring Thermally-Induced Lesions with Supersonic Shear Imaging. *Ultrason. Imaging*, 26:71–84, 2004a.

Bercoff, J., Tanter, M., and Fink, M. Supersonic Shear Imaging : A New Technique for Soft Tissue Elasticity Mapping. 51(4):396–409, 2004b.

Bercoff, J., Tanter, M., Muller, M., and Fink, M. The role of viscosity in the impulse diffraction field of elastic waves induced by the acoustic radiation force. *IEEE Trans. Ultrason. Ferroelectr. Freq. Control*, 51(11):1523–1536, 2004c.

Bernal, M., Gennisson, J.-L., Flaud, P., and Tanter, M. Correlation between classical rheometry and supersonic shear wave imaging in blood clots. *Ultrasound Med. Biol.*, 39(11):2123–36, 2013.

Boehm, K., Salomon, G., Beyer, B., Schiffmann, J., Simonis, K., Graefen, M., and Budaeus, L. Shear Wave Elastography for Localization of Prostate Cancer

Lesions and Assessment of Elasticity Thresholds: Implications for Targeted Biopsies and Active Surveillance Protocols. *J. Urol.*, 193(3):794–800, 2015.

Bouchard, R. R., Palmeri, M. L., Pinton, G. F., Trahey, G. E., Streeter, J. E., and Dayton, P. A. Optical tracking of acoustic radiation force impulse-induced dynamics in a tissue-mimicking phantom. *J. Acoust. Soc. Am.*, 126(5): 2733–2745, 2009.

Breasted, J. H. *The Edwin Smith Surgical Papyrus: published in facsimile and hieroglyphic transliteration with translation and commentary in two volumes*, volume 3. Chic. UP, 1930.

Brock, M., Von Bodman, C., Palisaar, R. J., Löppenberg, B., Sommerer, F., Deix, T., Noldus, J., and Eggert, T. The impact of real-time elastography guiding a systematic prostate biopsy to improve cancer detection rate: A prospective study of 353 patients. *J. Urol.*, 187(6):2039–2043, 2012.

Budelli, E., Brum, J., Bernal, M., Deffieux, T., Tanter, M., Lema, P., Negreira, C., and Gennisson, J.-L. A diffraction correction for storage and loss moduli imaging using radiation force based elastography. *Phys. Med. Biol.*, 62(1):91–106, 2017.

Burns-Cox, N., Avery, N. C., Gingell, J. C., and Bailey, a. J. Changes in collagen metabolism in prostate cancer: a host response that may alter progression. *J. Urol.*, 166(5):1698–1701, 2001.

Caenen, A., Shcherbakova, D., Verhegghe, B., Papadacci, C., Pernot, M., Segers, P., and Swillens, A. A versatile and experimentally validated finite element model to assess the accuracy of shear wave elastography in a bounded viscoelastic medium. *IEEE Transactions on Ultrasonics, Ferroelectrics, and Frequency Control*, 62(3):439–450, 2015.

Callejas, A., Gomez, A., Melchor, J., Riveiro, M., Massó, P., Torres, J., López-López, M. T., and Rus, G. Performance study of a torsional wave sensor and cervical tissue characterization. *Sensors (Switzerland)*, 17(9):1–19, 2017.

Cancer Research UK. Prostate cancer Key Stats. *Cancer Res. UK*, 2014.

Cao, R., Huang, Z., Varghese, T., and Nabi, G. Tissue mimicking materials for the detection of prostate cancer using shear wave elastography: a validation study. *Med. Phys.*, 40(2):022903, 2013.

Caputo, M., Carcione, J. M., and Cavallini, F. Wave simulation in biologic media based on the Kelvin-Voigt fractional-derivative stress-strain relation. *Ultrasound Med. Biol.*, 37(6):996–1004, 2011.

Carcione, J. M., Cavallini, F., Mainardi, F., and Hanyga, a. Time-domain Modeling of Constant- Q Seismic Waves Using Fractional Derivatives. *Pure and Applied Geophysics*, 159:1719–1736, 2002.

Chatelin, S., Gennisson, J.-L., Bernal, M., Tanter, M., and Pernot, M. Modelling the impulse diffraction field of shear waves in transverse isotropic viscoelastic medium. *Phys. Med. Biol.*, 60(9):3639–54, 2015.

Chaussy, C. and Thüroff, S. High-intensity focused ultrasound in the management of prostate cancer. *Expert Rev. Med. Devices*, 7(2):209–17, 2010.

Chaussy, C., Tilki, D., and Thüroff, S. Transrectal High-Intensity Focused Ultrasound for the Treatment of Localized Prostate Cancer: Current Role. *J. Cancer Ther.*, 04(04):59–73, 2013.

Chen, J., Daniel, B. L., Diederich, C. J., Bouley, D. M., Van Den Bosch, M. A. A. J., Kinsey, A. M., Sommer, G., and Pauly, K. B. Monitoring prostate thermal therapy with diffusion-weighted MRI. *Magn. Reson. Med.*, 59(6):1365–1372, 2008.

Chen, S., Fatemi, M., and Greenleaf, J. F. Quantifying elasticity and viscosity from measurement of shear wave speed dispersion. *J. Acoust. Soc. Am.*, 115(6):2781, 2004.

Chen, S., Urban, M. W., Pislaru, C., Kinnick, R., Zheng, Y., Yao, A., and Greenleaf, J. F. Shearwave Dispersion Ultrasound Vibrometry (SDUV) for Measuring Tissue Elasticity and Viscosity. *IEEE Trans. Ultrason. Ferroelectr. Freq. Control*, 56(1):55–62, 2009.

Chen, T. and He, B.-S. A normalized wavefield separation cross-correlation imaging condition for reverse time migration based on Poynting vector. *Appl. Geophys.*, 11(2):158–166, 2014.

Chen, W. and Holm, S. Modified Szabo's wave equation models for lossy media obeying frequency power law. *J. Acoust. Soc. Am.*, 114(5):2570–2574, 2003.

Chen, W. H., Sanghvi, N. T., Carlson, R., and Uchida, T. Real-time tissue change monitoring on the Sonablate 500 during high intensity focused ultrasound (HIFU) treatment of prostate cancer. *AIP Conf. Proc.*, 1359(2011):391–396, 2011.

Chen, W. H., Sanghvi, N. T., Carlson, R., Schatzl, G., and Marberger, M. Validation of tissue change monitoring (TCM) on the Sonablate 500 during high intensity focused ultrasound (HIFU) treatment of prostate cancer with real-time thermometry. *AIP Conf. Proc.*, 1481:53–58, 2012.

Cheng, M. Y., Lin, C. L., and Yang, Y. J. Tactile and shear stress sensing array using capacitive mechanisms with floating electrodes. *Proc. IEEE Int. Conf. Micro Electro Mech. Syst.*, 2:228–231, 2010.

Chin, J. L., Billia, M., Relle, J., Roethke, M. C., Popeneciu, I. V., Kuru, T. H., Hatiboglu, G., Mueller-Wolf, M. B., Motsch, J., Romagnoli, C., Kassam, Z., Harle, C. C., Hafron, J., Nandalur, K. R., Chronik, B. A., Burtnyk, M., Schlemmer, H. P., and Pahernik, S. Magnetic Resonance ImagingGuided Transurethral Ultrasound Ablation of Prostate Tissue in Patients with Localized Prostate Cancer: A Prospective Phase 1 Clinical Trial. *Eur. Urol.*, 70(3):447–455, 2016.

Chopra, R., Arani, A., Huang, Y., Musquera, M., Wachsmuth, J., Bronskill, M., and Plewes, D. In vivo MR elastography of the prostate gland using a transurethral actuator. *Magn. Reson. Med.*, 62(3):665–71, sep 2009.

Chopra, R., Colquhoun, A., Burtnyk, M., Kobelevskiy, I., Boyes, A., Siddiqui, K., Foster, H., Sugar, L., Haider, M. A., Bronskill, M., and Klotz, L. MR Imaging – controlled Transurethral Ultrasound Therapy for Conformal Treatment of Prostate Tissue : Initial Feasibility in Humans. *Radiology*, 265(1):303–313, 2012.

Cohen, R. J., Shannon, B. a., Phillips, M., Moorin, R. E., Wheeler, T. M., and Garrett, K. L. Central Zone Carcinoma of the Prostate Gland: A Distinct Tumor Type With Poor Prognostic Features. *J. Urol.*, 179(5):1762–1767, 2008.

Correas, J., Drakonakis, E., a.M. Isidori, Hélénon, O., Pozza, C., Cantisani, V., Di Leo, N., Maghella, F., Rubini, a., Drudi, F., and D'ambrosio, F. Update on ultrasound elastography: Miscellanea. Prostate, testicle, musculo-skeletal. *Eur. J. Radiol.*, 82(11):1904–1912, 2013a.

Correas, J.-M., Khairoune, A., Tissier, A.-M., and Vassiliu, V. Trans-rectal quantitative Shear Wave Elastrography : application to prostate cancer - A feasibility study, 2011.

Correas, J.-M., Tissier, A.-M., Khairoune, A., Khoury, G., Eiss, D., and Hélénon, O. Ultrasound elastography of the prostate: state of the art. *Diagnostic and interventional imaging*, 94(5):551–60, 2013b.

Correas, J. M., a M Tissier, Khairoune, a., Vassiliu, V., Méjean, A., Hélénon, O., Memo, R., and Barr, R. G. Prostate Cancer : Diagnostic Performance of Real-time Shear-Wave Elastography. *Radiology*, 275(1):280–289, 2015.

Crouzet, S., Chapelon, J. Y., Rouvière, O., Mege-Lechevallier, F., Colombel, M., Tonoli-Catez, H., Martin, X., and Gelet, A. Whole-gland ablation of localized

prostate cancer with high-intensity focused ultrasound: oncologic outcomes and morbidity in 1002 patients. *Eur. Urol.*, 65(5):907–14, 2014.

Curiel, L., Souchon, R., Rouvière, O., Gelet, A., and Chapelon, J. Y. Elastography for the follow-up of high-intensity focused ultrasound prostate cancer treatment: Initial comparison with MRI. *Ultrasound Med. Biol.*, 31(11):1461–1468, 2005.

Czernuszewicz, T. J., Streeter, J. E., Dayton, P. A., and Gallippi, C. M. Experimental validation of displacement underestimation in ARFI ultrasound. *Ultrason. Imaging*, 35(3):196–213, 2013.

Dewhirst, M. W., Viglianti, B. L., Lora-Michiels, M., Hanson, M., and Hoopes, P. J. Basic principles of thermal dosimetry and thermal thresholds for tissue damage from hyperthermia. *Int. J. Hyperth.*, 19(3):267–294, 2003.

Dickinson, L., Hu, Y., Ahmed, H. U., Allen, C., Kirkham, A. P., Emberton, M., and Barratt, D. Image-directed, tissue-preserving focal therapy of prostate cancer: A feasibility study of a novel deformable magnetic resonance-ultrasound (MR-US) registration system. *BJU Int.*, 112(5):594–601, 2013.

Dietrich, C. F., Barr, R. G., Farrokh, A., Dighe, M., Hocke, M., Jenssen, C., Dong, Y., Saftoiu, A., and Havre, R. F. Strain Elastography - How To Do It? *Ultrasound international open*, 3(4):E137–E149, 2017.

Doherty, J., Trahey, G., Nightingale, K., and Palmeri, M. Acoustic radiation force elasticity imaging in diagnostic ultrasound. *IEEE Trans. Ultrason. Ferroelectr. Freq. Control*, 60(4):685–701, 2013.

Donaldson, I., Hamid, S., Barratt, D., Hu, Y., Rodell, R., Villarini, B., Bonmati, E., Martin, P., Hawkes, D., McCartan, N., Potyka, I., Williams, N., Brew-Graves, C., Moore, C., Emberton, M., and Ahmed, H. Mp33-20 the Smarttarget Biopsy Trial: a Prospective Paired Blinded Trial With Randomisation To Compare Visual-Estimation and Image-Fusion Targeted Prostate Biopsies. *J. Urol.*, 197 (4):e425, 2017.

Dunmire, B., Kucewicz, J. C., Mitchell, S. B., Crum, L. A., and Sekins, K. M. Characterizing an Agar/Gelatin phantom for image guided dosing and feedback control of high-intensity focused ultrasound. *Ultrasound Med. Biol.*, 39(2): 300–311, 2013.

Eri, L. M., Thomassen, H., Brennhovd, B., and Håheim, L. L. Accuracy and repeatability of prostate volume measurements by transrectal ultrasound. *Prostate cancer and prostatic diseases*, 5(4):273–278, 2002.

Farmer, P., Jones, I., Zhou, H., Bloor, R., and Goodwin, M. Application of reverse time migration to complex imaging problems. *First Break*, 24(September):64–73, 2006.

Farmer, P., Zhou, Z. Z., Jones, D., and Services, I. G. I. The role of reverse time migration in imaging and model estimation. *Lead. Edge Offshore Technol.*, pages 436–441, 2009.

Fisher, R. A. *Statistical Methods for Research Workers*. Ed., Hafner, 13th edition, 1958.

Franck, A. Understanding instrument inertia corrections in oscillation. Technical report, 2005.

Frehner, M., Schmalholz, S., H. Saenger, E., and Steeb, H. Comparison of finite difference and finite element methods for simulating two-dimensional scattering of elastic waves. 171:112–121, 12 2008.

Gallego, R. and Rus, G. Identification of cracks and cavities using the topological sensitivity boundary integral equation. *Comput. Mech.*, 33(2):154–163, 2004.

Garra, B. S. Elastography: history, principles, and technique comparison. *Abdom. Imaging*, 40(4):680–697, 2015.

Giannarini, G., Autorino, R., and di Lorenzo, G. Saturation Biopsy of the Prostate: Why Saturation Does Not Saturate. *Eur. Urol.*, 56(4):619–621, 2009.

Ginat, D. T., Destounis, S. V., Barr, R. G., Castaneda, B., Strang, J. G., and Rubens, D. J. US elastography of breast and prostate lesions. *Radiographics*, 29(7): 2007–2016, 2009.

Gladwell, G. M. L. The Calculation To an Indenter of Mechanical Relating Vibrating on the Surface of a Semi- Infinite Elastic Body. *J. Sound Vib.*, 8(2): 215–228, 1968.

Goldberg, S. N., Grassi, C. J., Cardella, J. F., Charboneau, J. W., Dodd, G. D., Dupuy, D. E., Gervais, D. A., Gillams, A. R., Kane, R. A., Lee, F. T., Livraghi, T., McGahan, J., Phillips, D. A., Rhim, H., Silverman, S. G., Solbiati, L., Vogl, T. J., Wood, B. J., Vedantham, S., and Sacks, D. Image-guided Tumor Ablation: Standardization of Terminology and Reporting Criteria. *Radiology*, 2235(3): 728–739, 2009.

Gomez, A., Rus, G., Suarez, F., Arcoya, D., Bochud, N., Melchor, J., Peralta, L., Chiachio, J., and Chiachio, M. Biomechanical shear moduli recovery from ultrasound in multilayered half-space media. *ICU 2013 Proceedings*, pages 626–631, 2013.

Gomez, A., Rus, G., and Saffari, N. Use of shear waves for diagnosis and ablation monitoring of prostate cancer: a feasibility study. *Journal of Physics: Conference Series*, 684:012006, 2016.

Good, D. W., Stewart, G. D., Hammer, S., Scanlan, P., Shu, W., Phipps, S., Reuben, R., and McNeill, A. S. Elasticity as a biomarker for prostate cancer: a systematic review. *BJU Int.*, 113(4):523–34, 2014.

Graff, K. *Wave Motion in Elastic Solids*. Dover Publications, Inc., Mineola, N.Y., 1991.

Grohmann, M., Niederleithinger, E., and Buske, S. Geometry determination of a foundation slab using the ultrasonic echo technique and geophysical migration methods. *J. Nondestruct. Eval.*, 35(1):1–13, 2016.

Grzesikiewicz, W., Wakulicz, A., and Zbiciak, A. Non-linear problems of fractional calculus in modeling of mechanical systems. *Int. J. Mech. Sci.*, 70(May):90–98, 2013.

Gsell, D., Leutenegger, T., and Dual, J. Modeling three-dimensional elastic wave propagation in circular cylindrical structures using a finite-difference approach. *J. Acoust. Soc. Am.*, 116(6):3284–3293, 2004.

Haataja, J. Matlab function for simulating a simple real-coded genetic algorithm. Center for Scientific Computing, Box 405, FIN-0210. Technical report, 2000.

Hall, T. J., Bilgen, M., Insana, M. F., and Krouskop, T. A. Phantom materials for elastography. *IEEE Trans. Ultrason. Ferroelectr. Freq. Control*, 44(6): 1355–1365, 1997.

Hazard, C., Hah, Z., Rubens, D., and Parker, K. Integration of Crawling Waves in an Ultrasound Imaging System. Part 1: System and Design Considerations. *Ultrasound Med. Biol.*, 38(2):296–311, 2012.

Hazle, J. D., Diederich, C. J., Kangasniemi, M., Price, R. E., Olsson, L. E., and Stafford, R. J. MRI-guided thermal therapy of transplanted tumors in the canine prostate using a directional transurethral ultrasound applicator. *J. Magn. Reson. Imaging*, 15(4):409–417, 2002.

Holland, J. *Adaptation in Natural and Artificial Systems*. University edition, 1975.

Holm, S. and Näsholm, S. P. A causal and fractional all-frequency wave equation for lossy media. *J. Acoust. Soc. Am.*, 130(4):2195, 2011.

Holm, S. and Näsholm, S. P. Comparison of fractional wave equations for power law attenuation in ultrasound and elastography. *Ultrasound Med. Biol.*, 40(4): 695–703, 2014.

Holm, S. and Sinkus, R. A unifying fractional wave equation for compressional and shear waves. *J. Acoust. Soc. Am.*, 127(1):542–59, 2010.

Hoyt, K., Castaneda, B., Zhang, M., Nigwekar, P., Anthony, P., Agnese, S., Joseph, J. V., Strang, J., Rubens, D. J., and Parker, K. J. Tissue elasticity properties as biomarkers for prostate cancer. *Cancer Biomarkers*, 4:213–225, 2008.

Hristova, Y., Kuchment, P., and Nguyen, L. Reconstruction and time reversal in thermoacoustic tomography in acoustically homogeneous and inhomogeneous media. *Inverse Probl.*, 24(5), 2008.

Hu, Y., Gibson, E., Uddin, H., Moore, C. M., Emberton, M., and Barratt, D. C. Population-based prediction of subject-specific prostate deformation for MR-to-ultrasound image registration. *Med. Image Anal.*, 26(1):332–344, 2015.

Illing, R. and Emberton, M. Sonablate-500: transrectal high-intensity focused ultrasound for the treatment of prostate cancer. *Expert review of medical devices*, 3(6):717–729, 2006.

Junker, D., De Zordo, T., Quentin, M., Ladurner, M., Bektic, J., Horniger, W., Jaschke, W., and Aigner, F. Real-time elastography of the prostate. *Biomed Res. Int.*, 2014:180804, 2014.

Kelloff, G. J., Choyke, P., and Coffey, D. S. Challenges in clinical prostate cancer: role of imaging. *AJR. Am. J. Roentgenol.*, 192(6):1455–1470, 2009.

Kirkpatrick, S., Gelatt, C. D., and Vecchi, M. P. Optimization by Simulated Annealing. *Science (80-.).*, 220(4598):pp. 671–680, 1983.

Kiss, M. Z., Varghese, T., and Hall, T. J. Viscoelastic characterization of in vitro canine tissue. *Phys. Med. Biol.*, 49:4207–4218, 2004.

Kiss, M. Z., Daniels, M. J., and Varghese, T. Investigation of temperature-dependent viscoelastic properties of thermal lesions in ex vivo animal liver tissue. *J. Biomech.*, 42(8):959–966, 2009.

Klatt, D., Hamhaber, U., Asbach, P., Braun, J., and Sack, I. Noninvasive assessment of the rheological behavior of human organs using multifrequency

MR elastography : a study of brain and liver viscoelasticity. *Phys. Med. Biol.*, 52:7281–7294, 2007.

Klemuk, S. A. and Titze, I. R. Determining motor inertia of a stress-controlled rheometer. *Journal of Rheology*, 53(4):765, 2010.

Kohonen, J. A brief comparison of simulated annealing and genetic algorithm approaches. Technical report, 1999.

Kwiecinski, W., Bessière, F., Colas, E. C., N'Djin, A. W., Tanter, M., Lafon, C., and Pernot, M. Cardiac shear-wave elastography using a transesophageal transducer: application to the mapping of thermal lesions in ultrasound transesophageal cardiac ablation. *Phys. Med. Biol.*, 60(20):7829–46, 2015.

Langer, D. L., Van Der Kwast, T. H., Evans, A. J., Trachtenberg, J., Wilson, B. C., and Haider, M. a. Prostate cancer detection with multi-parametric MRI: Logistic regression analysis of quantitative T2, diffusion-weighted imaging, and dynamic contrast-enhanced MRI. *J. Magn. Reson. Imaging*, 30(2):327–334, 2009.

Lee, C. H., Akin-Olugbade, O., and Kirschenbaum, A. Overview of Prostate Anatomy, Histology, and Pathology. *Endocrinol. Metab. Clin. North Am.*, 40 (3):565–575, 2011a.

Lee, H.-k., Chung, J., Chang, S.-i., and Yoon, E. Normal and Shear Force Measurement Using a Flexible Polymer Tactile Sensor With Embedded Multiple Capacitors. *J. Microelectromechanical Syst.*, 17(4):934–942, 2008.

Lee, H.-K., Chung, J., Chang, S.-I., and Yoon, E. Real-time measurement of the three-axis contact force distribution using a flexible capacitive polymer tactile sensor. *J. Micromechanics Microengineering*, 21(3):035010, 2011b.

Lemaitre, L., Puech, P., Poncelet, E., Bouyé, S., Leroy, X., Biserte, J., and Villers, A. Dynamic contrast-enhanced MRI of anterior prostate cancer: Morphometric

assessment and correlation with radical prostatectomy findings. *Eur. Radiol.*, 19 (2):470–480, 2009.

Lepetit, J. A theoretical approach of the relationships between collagen content, collagen cross-links and meat tenderness. *Meat Sci.*, 76(1):147–159, 2007.

Lerner, R. M. and Parker, K. J. Sonoelasticity images, ultrasonic tissue charactertization and echographic imaging. In *7th European Communities Workshop; Nijmegen, The Netherlands.*, 1987.

Lerner, R. M., Parker, K. J., Holen, J., Gramiak, R., and Waag, R. C. Sono-elasticity: medical elasticity images derived from ultrasound singals in mechanically vibrated targets. *Acoust. Imaging*, 16:317–327, 1988.

Leutenegger, T. and Dual, J. Non-destructive testing of tubes using a time reverse numerical simulation (TRNS) method. *Ultrasonics*, 41(10):811–822, 2004.

Lewis, M. A., Staruch, R. M., and Chopra, R. Thermometry and ablation monitoring with ultrasound. *Int. J. Hyperth.*, 31(2):163–81, 2015.

Lim, H. K., Kim, J. K., Kim, K. a., and Cho, K. S. Prostate cancer: Apparent diffusion coefficient map with T2-weighted images for detection - A multireader study. *Radiology*, 35(1):100–100, 2009.

Lipman, S. L., Rouze, N. C., Palmeri, M. L., and Nightingale, K. R. Evaluating the improvement in shear wave speed image quality using multidimensional directional filters in the presence of reflection artifacts. *IEEE Transactions on Ultrasonics, Ferroelectrics, and Frequency Control*, 63(8):1049–1063, 2016.

Liu, F., Zhang, G., Morton, S. a., and Leveille, J. P. An effective imaging condition for reverse-time migration using wavefield decomposition. *Geophysics*, 76(1): S29, 2011.

Liu, Q. H. Perfectly matched layers for elastic waves in cylindrical and spherical coordinates. *J. Acoust. Soc. Am.*, 105(4):2075–2084, 1999.

Liu, Z. and Liu, L. Application of Iterative Reverse Time Migration Procedure on Transcranial Thermoacoustic Tomography Imaging. In *Soundscape Semiot. - Localization Categ.*, pages 47–64. InTech, 2014.

Liu, Z., Liu, L., Xu, Y., and Wang, L. V. Transcranial thermoacoustic tomography: a comparison of two imaging algorithms. *IEEE Trans. Med. Imaging*, 32(2): 289–94, 2013.

Madariaga, R. Dynamics of an expanding circular fault. *Bulletin of the Seismological Society of America*, 66(3):639 –666, 1976.

Madsen, E. L., Sathoff, H. J., and Zagzebski, J. A. Ultrasonic shear wave properties of soft tissues and tissuelike materials. *J Acoust Soc Am*, 75(5):1346–1355, 1983.

Madsen, E. L., Frank, G. R., Krouskop, T. a., Varghese, T., Kallel, F., and Ophir, J. Tissue-Mimicking Oil-in-Gelatin Dispersions for Use in Heterogeneous Elastography Phantoms. *Ultrason. Imaging*, 25(1):17–38, jan 2003.

Madsen, E. L., Hobson, M. a., Shi, H., Varghese, T., and Frank, G. R. Tissue-mimicking agar/gelatin materials for use in heterogeneous elastography phantoms. *Phys. Med. Biol.*, 50(23):5597–618, 2005.

Madsen, E. L., Hobson, M. A., Frank, G. R., Shi, H., Jiang, J., Hall, T. J., Varghese, T., Doyley, M. M., and Weaver, J. B. Anthropomorphic breast phantoms for testing elastography systems. *Ultrasound Med. Biol.*, 32(6):857–874, 2006a.

Madsen, E. L., Hobson, M. A., Shi, H., Varghese, T., and Frank, G. R. Stability of heterogeneous elastography phantoms made from oil dispersions in aqueous gels. *Ultrasound Med. Biol.*, 32(2):261–270, 2006b.

Mariani, A., Kwiecinski, W., Pernot, M., Balvay, D., Tanter, M., Clement, O., Cuenod, C. a., and Zinzindohoue, F. Real time shear waves elastography monitoring of thermal ablation: in vivo evaluation in pig livers. *J. Surg. Res.*, 188(1):37–43, 2014.

Marshall, S. and Taneja, S. Focal therapy for prostate cancer: The current status. *Prostate Int.*, 3(2):35–41, 2015.

McNeal, J. E. The Zonal Anatomy of the Prostate. *Prostate*, 2(1981):35–49, 1981.

McNeal, J. E., Redwine, E. A., Freiha, F. S., and Stamey, T. A. Zonal Distribution of Prostatic Adenocarcinoma. Correlation with Histologic Pattern and Direction of Spread. *Am. J. Surg. Pathol.*, 12(12):897–906, 1988.

Melchor, J. and Rus, G. Torsional ultrasonic transducer computational design optimization. *Ultrasonics*, 54(7):1950–1962, 2014.

Melchor, J., Muñoz, R., and Rus, G. Torsional Ultrasound Sensor Optimization for Soft Tissue Characterization. *Sensors*, 17(6):1402, 2017.

Melodelima, D., Bamber, J. C., Duck, F. a., and Shipley, J. a. Transient Elastography Using Impulsive Ultrasound Radiation Force: A Preliminary Comparison With Surface Palpation Elastography. *Ultrasound Med. Biol.*, 33(6):959–969, 2007.

Missinne, J., Bosman, E., Van Hoe, B., Verplancke, R., Van Steenberge, G., Kalathimekkad, S., Van Daele, P., and Jan, V. Ultra thin optical tactile shear sensor. *Procedia Eng.*, 25:1393–1396, 2011.

Missinne, J., Bosman, E., Van Hoe, B., Verplancke, R., Van Steenberge, G., Kalathimekkad, S., Van Daele, P., and Vanfleteren, J. Two axis optoelectronic tactile shear stress sensor. *Sensors Actuators, A Phys.*, 186:63–68, 2012.

Mitchell, M. *An introduction to genetic algorithms*. Cambridge, Massachusetts. London, England, fifth prin edition, 1998.

Mitri, F. G., Urban, M. W., Fatemi, M., Member, S., Greenleaf, J. F., and Fellow, L. Shear Wave Dispersion Ultrasonic Vibrometry for Measuring Prostate Shear Stiffness and Viscosity : An In Vitro Pilot Study. *IEEE Trans. Biomed. Eng.*, 58 (2):235–242, 2011.

Miyagawa, T., Tsutsumi, M., Matsumura, T., Kawazoe, N., Ishikawa, S., Shimokama, T., Miyanaga, N., and Akaza, H. Real-time elastography for the diagnosis of prostate cancer: Evaluation of elastographic moving images. *Jpn. J. Clin. Oncol.*, 39(6):394–398, 2009.

Muller, B. G., Fütterer, J. J., Gupta, R. T., Katz, A., Kirkham, A., Kurhanewicz, J., Moul, J. W., Pinto, P. A., Rastinehad, A. R., Robertson, C., De La Rosette, J., Sanchez-Salas, R., Jones, J. S., Ukimura, O., Verma, S., Wijkstra, H., and Marberger, M. The role of magnetic resonance imaging (MRI) in focal therapy for prostate cancer: Recommendations from a consensus panel. *BJU Int.*, 113(2): 218–227, 2014.

Müller, S., Niederleithinger, E., and Bohlen, T. Reverse Time Migration: A Seismic Imaging Technique Applied to Synthetic Ultrasonic Data. *Int. J. Geophys.*, 2012: 1–7, 2012.

Napoli, A., Anzidei, M., De Nunzio, C., Cartocci, G., Panebianco, V., De Dominicis, C., Catalano, C., Petrucci, F., and Leonardo, C. Real-time magnetic resonance-guided high-intensity focused ultrasound focal therapy for localised prostate cancer: Preliminary experience. *Eur. Urol.*, 63(2):395–398, 2013.

Nasseri, S., Bilston, L. E., and Phan-Thien, N. Viscoelastic properties of pig kidney in shear, experimental results and modelling. *Rheol. Acta*, 41(2002):180–192, 2002.

Nguyen, M. M., Zhou, S., Robert, J.-L., Shamdasani, V., and Xie, H. Development of oil-in-gelatin phantoms for viscoelasticity measurement in ultrasound shear wave elastography. *Ultrasound Med. Biol.*, 40(1):168–76, 2014.

Noble, B. and Sneddon, I. N. The solution of Bessel function dual integral equations by a multiplying-factor method. *Math. Proc. Cambridge Philos. Soc.*, 59(02): 351, 1963.

O'Donnell, M., Skovoroda, A. R., Shapo, B. M., and Emelianov, S. Y. Internal displacement and strain imaging using ultrasonic speckle tracking. *IEEE Transactions on Ultrasonics Ferroelectrics & Frequency Control*, 41(3): 314–325, 1994.

Ophir, J., Cespedes, I., Ponnekanti, H., Yazdi, Y., and Li, X. Elastography: A quantitative method for imaging the elasticity of biological tissues. *Ultrason. Imaging*, 13(2):111–134, 1991.

Ophir, J., Alam, S. K., Garra, B. S., Kallel, F., Konofagou, E. E., Krouskop, T., Merrit, C. R. B., Righetti, R., Souchon, R., Srinivasan, S., and Varghese, T. Elastography : Imaging the Elastic Properties of Soft Tissues with Ultrasound. *J. Med. Ultrason.*, 29(Winter):155–171, 2002.

Orescanin, M., Wang, Y., and Insana, M. F. 3-D FDTD Simulation of Shear Waves for Evaluation of Complex Modulus Imaging. *IEEE Trans. Ultrason. Ferroelectr. Freq. Control*, 58(2):389–398, 2011.

Palma, R., Rus, G., and Gallego, R. Probabilistic inverse problem and system uncertainties for damage detection in piezoelectrics. *Mech. Mater.*, 41(9): 1000–1016, 2009.

Pavan, T. Z., Madsen, E. L., Frank, G. R., Adilton O Carneiro, A., and Hall, T. J. Nonlinear elastic behavior of phantom materials for elastography. *Phys. Med. Biol.*, 55(9):2679–92, 2010.

Pavan, T. Z., Madsen, E. L., Frank, G. R., Jiang, J., Carneiro, A. a. O., and Hall, T. J. A nonlinear elasticity phantom containing spherical inclusions. *Phys. Med. Biol.*, 57(15):4787–804, 2012.

Pepe, P., Fraggetta, F., Galia, a., Grasso, G., and Aragona, F. Prostate cancer detection by TURP after repeated negative saturation biopsy in patients with persistent suspicion of cancer: a case-control study on 75 consecutive patients. *Prostate Cancer Prostatic Dis.*, 13(1):83–86, 2010.

Podlubny, I. *Fractional Differential Equations*. Academic Press, San Diego-Boston-New York-London-Tokyo-Toronto, 1999.

Reissner, E. and Sagoci, H. F. Forced Torsional Oscillations of an Elastic Half-Space. I. *J. Appl. Phys.*, 15(9):652, 1944.

Rieke, V. and Pauly, K. B. MR thermometry. *J. Magn. Reson. Imaging*, 27(2): 376–390, 2008.

Rouvière, O., Lyonnet, D., Raudrant, A., Colin-Pangaud, C., Chapelon, J. Y., Bouvier, R., Dubernard, J. M., and Gelet, A. MRI appearance of prostate following transrectal HIFU ablation of localized cancer. *Eur. Urol.*, 40(3): 265–274, 2001.

Rouvière, O., Souchon, R., Salomir, R., Gelet, A., Chapelon, J. Y., and Lyonnet, D. Transrectal high-intensity focused ultrasound ablation of prostate cancer: Effective treatment requiring accurate imaging. *European Journal of Radiology*, 63(3):317–327, 2007.

Rus, G., Lee, S. Y., Chang, S. Y., and Wooh, S. C. Optimized damage detection of steel plates from noisy impact test. *Int. J. Numer. Methods Eng.*, 68(7):707–727, 2006.

Rus, G., Wooh, S. C., and Gallego, R. Processing of ultrasonic array signals for characterizing defects. Part I: Signal Synthesis. *IEEE Trans. Ultrason. Ferroelectr. Freq. Control*, 54(10):2129–2138, 2007.

Rus, G., Bochud, N., Melchor, J., Peralta, L., Chiachio, J., Chiachio, M., Gomez, A., Ximenez, A., Alaminos, M., and Campos, A. In-biorreactor ultrasonic monitoring of tissue mechanical properties. *ICU 2013 Proceedings*, pages 657–661, 2013.

Sahebjavaher, R. S., Baghani, A., Honarvar, M., Sinkus, R., and Salcudean, S. E.

Transperineal prostate MR elastography: initial in vivo results. *Magn. Reson. Med.*, 69(2):411–20, 2013.

Salcudean, S. E., French, D., and Bachmann, S. Viscoelasticity Modeling of the Prostate Region Using Vibro-elastography. *Proceedings of MICCAI 2006*, pages 389–396, 2006.

Salomon, G., Köllerman, J., Thederan, I., Chun, F. K. H., Budäus, L., Schlomm, T., Isbarn, H., Heinzer, H., Huland, H., and Graefen, M. Evaluation of prostate cancer detection with ultrasound real-time elastography: a comparison with step section pathological analysis after radical prostatectomy. *Eur. Urol.*, 54(6): 1354–62, 2008.

Sanghvi, N., Fry, F., Bihrle, R., Foster, R., Phillips, M., Syrus, J., Zaitsev, A., and Hennige, C. Microbubbles during tissue treatment using high intensity focused ultrasound. *1995 IEEE Ultrason. Symp. Proceedings. An Int. Symp.*, 2:1571–1574, 1995.

Sapareto, S. A. and Dewey, W. C. Thermal dose determination in cancer therapy. *Int. J. Radiat. Oncol. Biol. Phys.*, 10(6):787–800, 1984.

Sapin-de Brosses, E., Gennisson, J. L., Pernot, M., Fink, M., and Tanter, M. Temperature dependence of the shear modulus of soft tissues assessed by ultrasound. *Phys. Med. Biol.*, 55:1701–1718, 2010.

Sapin-de Brosses, E., Pernot, M., and Tanter, M. The link between tissue elasticity and thermal dose in vivo. *Phys. Med. Biol.*, 56(24):7755–65, 2011.

Schneider, C. A., Rasband, W. S., and Eliceiri, K. W. NIH Image to ImageJ: 25 years of image analysis. *Nat. Methods*, 9(7):671–675, 2012.

Schroyen, B., Swan, J. W., Van Puyvelde, P., and Vermant, J. Quantifying the dispersion quality of partially aggregated colloidal dispersions by high frequency rheology. *Soft Matter*, 2017.

Sheriff, R. E. *Encyclopedic Dictionary of Applied Geophysics*. Society of Exploration Geophysicists, 4th edition, 2012.

Sheriff, R. E. and Geldart, L. P. *Exploration seismology*. Cambridge University Press, 2nd edition, 1995.

Shi, W., Anand, A., Sethuraman, S., Huang, S. W., Xie, H., Agarwal, H., Yan, P., Azevedo, J., Kruecker, J., Ng, G., Shamdasani, V., Pritchard, W., Karanian, J., and Wood, B. Monitoring of radiofrequency ablation with shear wave delay mapping. *2015 IEEE Int. Ultrason. Symp. IUS 2015*, pages 10–13, 2015.

SonacareMedical. Sonablate ® vs. Ablatherm ® Comparison Guide. Technical report, 2015.

Souchon, R., Rouvière, O., Gelet, A., Detti, V., Srinivasan, S., Ophir, J., and Chapelon, J. Y. Visualisation of HIFU lesions using elastography of the human prostate in vivo: Preliminary results. *Ultrasound Med. Biol.*, 29(7):1007–1015, 2003.

Suomi, V., Edwards, D., and Cleveland, R. Optical Quantification of Harmonic Acoustic Radiation Force Excitation in a Tissue-Mimicking Phantom. *Ultrasound Med. Biol.*, 41(12):3216–3232, 2015.

Tang, J., Yang, J. C., Li, Y., Li, J., and Shi, H. Peripheral zone hypoechoic lesions of the prostate: evaluation with contrast-enhanced gray scale transrectal ultrasonography. *J. Ultrasound Med.*, 26(12):1671–1679, 2007.

Tanter, M., Bercoff, J., Athanasiou, A., Deffieux, T., Gennisson, J.-L., Montaldo, G., Muller, M., Tardivon, A., and Fink, M. Quantitative assessment of breast lesion viscoelasticity: initial clinical results using supersonic shear imaging. *Ultrasound Med. Biol.*, 34(9):1373–86, 2008.

Taylor, L. S., Richards, M. S., Moskowitz, a. J., Lerner, a. L., Rubens, D. J.,

and Parker, K. J. Viscoelastic Effects in Sonoelastography: Impact on Tumor Detectability. pages 1639–1642, 2001.

ter Haar, G. Intervention and therapy. *Ultrasound Med. Biol.*, 26(00):s51–s54, 2000.

The Prostate Cancer Charity UK. What is my risk of prostate cancer? *Prostate Cancer UK*, 2015.

The Prostate Cancer Charity UK. High-intensity focused ultrasound (HIFU). Technical report, 2017.

Thörmer, G., Reiss-Zimmermann, M., Otto, J., Hoffmann, K.-T., Moche, M., Garnov, N., Kahn, T., and Busse, H. Novel technique for MR elastography of the prostate using a modified standard endorectal coil as actuator. *J. Magn. Reson. Imaging*, 37(6):1480–5, 2013.

Tsutsumi, M., Miyagawa, T., Matsumura, T., Endo, T., Kandori, S., Shimokama, T., and Ishikawa, S. Real-time balloon inflation elastography for prostate cancer detection and initial evaluation of clinicopathologic analysis. *Am. J. Roentgenol.*, 194(6):471–476, 2010.

Tuxhorn, J. a., Ayala, G. E., and Rowley, D. R. Reactive stroma in prostate cancer progression. *J. Urol.*, 166(6):2472–2483, 2001.

Tuxhorn, J. a., Ayala, G. E., Smith, M. J., Smith, V. C., Dang, T. D., and Rowley, D. R. Reactive Stroma in Human Prostate Cancer : Induction of Myofibroblast Phenotype and Extracellular Matrix. *Clin. Cancer Res.*, 8:2912–2923, 2002.

Virieux, J. P-SV wave propagation in heterogeneous media: Velocity-stress finite-difference method. *Geophysics*, 51(4):889–901, 1986.

Wall, M. S., Deng, X.-H., Torzilli, P. A., Doty, S. B., O'Brien, S. J., and Warren, R. F. Thermal modification of collagen. *J. Shoulder Elb. Surg.*, 8(4):339–344, 1999.

Wang, L. and Yuan, F. G. Damage Identification in a Composite Plate using Prestack Reverse-time Migration Technique. *Structura*, 4(3):195–211, 2005.

Wang, T. and Jing, Y. A fast marching method based back projection algorithm for photoacoustic tomography in heterogeneous media. *Med. Phys.*, pages 1–11, 2015.

Wang, Z., Ding, H., Lu, G., and Bi, X. Reverse-Time Migration Based Optical Imaging Reverse. *IEEE Trans. Med. Imaging*, 35(1):273–281, 2016.

Whitmore, N. Iterative depth migration by backward time propagation. pages 382–385, 1983.

Woo, S., Kim, S. Y., Cho, J. Y., and Kim, S. H. Shear wave elastography for detection of prostate cancer: a preliminary study. *Korean J. Radiol.*, 15(3): 346–355, 2014.

Woo, S., Kim, S. Y., Lee, M. S., Cho, J. Y., and Kim, S. H. Shear wave elastography assessment in the prostate: an intraobserver reproducibility study. *Clin. Imaging*, 39(3):484–487, 2015.

Wright, N. T. and Humphrey, J. D. Denaturation of Collagen via Heating: An Irreversible Rate Process. *Annu. Rev. Biomed. Eng.*, 4(1):109–128, 2002.

Wu, T., Felmlee, J. P., Greenleaf, J. F., Riederer, S. J., and Ehman, R. L. Assessment of thermal tissue ablation with MR elastography. *Magn. Reson. Med.*, 45:80–87, 2001.

Xia, R. and Thittai, A. K. Real-Time Monitoring of High-Intensity Focused Ultrasound Treatment Using Axial Strain and Axial-Shear Strain Elastograms. *Ultrasound in Medicine and Biology*, 40(3):485–495, 2014.

Yee, K. S. Numerical Solution of Initial Boundary Value Problems Involving Maxwell's Equations in Isotropic Media. *IEEE Trans. Antennas and Propag.*, 14(3):302 – 307, 1966.

Yoo, L., Gupta, V., Lee, C., Kavehpore, P., and Demer, J. L. Viscoelastic properties of bovine orbital connective tissue and fat: Constitutive models. *Biomech. Model. Mechanobiol.*, 10(6):901–914, 2011.

Yu, P., Liu, W., Gu, C., Cheng, X., and Fu, X. Flexible piezoelectric tactile sensor array for dynamic three-axis force measurement. *Sensors*, 16(816), 2016.

Yuste, S. B. and Acedo, L. An explicit finite difference method and a new Von Neumann-type stability analysis for fractional diffusion equations. *SIAM J. Numer. Anal.*, 42(5):1862–1874, 2005.

Zhai, L., Madden, J., Foo, W.-C., Mouraviev, V., Polascik, T. J., Palmeri, M. L., and Nightingale, K. R. Characterizing Stiffness of Human Prostates Using Acoustic Radiation Force. *Ultrason. Imaging*, 32(4):201–213, 2010a.

Zhai, L., Madden, J., Foo, W.-C., Palmeri, M. L., Mouraviev, V., Polascik, T. J., and Nightingale, K. R. Acoustic radiation force impulse imaging of human prostates ex vivo. *Ultrasound Med. Biol.*, 36(4):576–588, 2010b.

Zhai, L., Polascik, T. J., Foo, W. C., Rosenzweig, S., Palmeri, M. L., Madden, J., and Nightingale, K. R. Acoustic Radiation Force Impulse Imaging of Human Prostates: Initial In Vivo Demonstration. *Ultrasound Med. Biol.*, 38(1):50–61, 2012.

Zhang, M., Nigwekar, P., Castaneda, B., Hoyt, K., Joseph, J. V., di Sant'Agnese, A., Messing, E. M., Strang, J. G., Rubens, D. J., and Parker, K. J. Quantitative characterization of viscoelastic properties of human prostate correlated with histology. *Ultrasound Med. Biol.*, 34(7):1033–42, 2008.

Zhang, M., Fu, S., Zhang, Y., Tang, J., and Zhou, Y. Elastic modulus of the prostate: a new non-invasive feature to diagnose bladder outlet obstruction in patients with benign prostatic hyperplasia. *Ultrasound Med. Biol.*, 40(7):1408–13, 2013a.

Zhang, S.-j., Qian, H.-n., Zhao, Y., Sun, K., Wang, H.-q., Liang, G.-q., and Li, F.-h. Relationship between age and prostate size. *Asian Journal of Andrology*, 15(1): 116–120, 2013b.

Zhang, W. and Holm, S. Estimation of shear modulus in media with power law characteristics. *Ultrasonics*, 64:170–176, 2016.

Zheng, X., Ji, P., Mao, H., and Hu, J. A comparison of virtual touch tissue quantification and digital rectal examination for discrimination between prostate cancer and benign prostatic hyperplasia. *Radiol. Oncol.*, 46(1):69–74, 2012.

Zhou, L., Yuan, F. G., and Meng, W.-J. A pre-stack migration method for damage identification in composite structures. *Smart Struct. Syst.*, 3(4):439–454, 2007.

Zhu, J. and Lines, L. R. Comparison of Kirchhoff and reverse-time migration methods with applications to prestack depth imaging of complex structures. *Geophysics*, 63(4):1166–1176, 1998.

Zienkiewicz, O., Taylor, R., and Zhu, J. *The Finite Element Method: Its Basics and Fundamentals*. 1977.